

## A computational modeling approach to study the neuromechanics of terrestrial locomotion

Présentée le 18 juillet 2022

Faculté des sciences et techniques de l'ingénieur  
Laboratoire de biorobotique  
Programme doctoral en robotique, contrôle et systèmes intelligents

pour l'obtention du grade de Docteur ès Sciences

par

**Shravan TATA RAMALINGASETTY**

Acceptée sur proposition du jury

Prof. D. Floreano, président du jury  
Prof. A. Ijspeert, directeur de thèse  
Prof. J. Hutchinson, rapporteur  
Prof. B. Prilutsky, rapporteur  
Prof. M. Mathis, rapporteuse



**Nullius in Verba**  
— Royal Society

To all the scientists on whose shoulders I stand,

# Acknowledgements

My journey as a PhD student has been made possible because of a great number of people. I would like to thank each and everyone who has been part of this amazing journey and also express my deepest gratitude for their love and support.

If I were asked what qualities should my PhD supervisor have? I would have said, it should be someone who, has great scientific temper, is supportive, is sensitive and fun. And with Prof. Auke Ijspeert I was lucky to have found someone with all those qualities and more. I would like to thank him for providing me with the opportunity to be part of an exciting project at EPFL and introducing me to an amazing group of people at the BioRobotics laboratory. My interactions with him has truly enriched the way I think and approach things in life. And I really appreciate the effort he put in to make the lab environment scientifically exciting and socially fun!

I would like to thank my funding agency the Human Brain Project and the BioRobotics laboratory, who have allowed me to explore my scientific ideas with great freedom throughout my PhD. Also, special thanks to all the EPFL administrative staff for making my PhD a smooth experience.

I thank my jury members Prof. Dario Floreano, Prof. Mackenzie Mathis, Prof. John Hutchinson, Prof. Boris Prilutsky for their time and valuable insights into my research.

I would like to thank my scientific collaborators who have made it possible for me to work on diverse challenging and exciting projects. I thank Prof. Ilya Rybak, Prof. Pavan Ramdya, Prof. Marco Capogrosso, Prof. Grégoire Courtine, Dr. Claudia Kathe, Dr. Sergey Markin, Dimitri Rodarie, Gizem, Victor, Nathan and the Human Brain Project team. A special thanks to Dr. Simon Danner for his continued support all through my PhD.

At BioRob, I had the pleasure to have been around for three phases. I had the chance to meet people from all over the world. Exchanging scientific ideas, cultures, views on society. No topic was unexplored at one of our Eh! Coffee sessions :) From phase 1, thanks to Robin and Simon for giving me secret tips into the life of a Swiss. Tomislav



for his forever spirit to keep everyone around him smiling. Mehmet for a never say *NO* attitude to do anything (crazy!). Thanks to Behzad for dropping me home after the long evenings in the lab. And Hamed! my happiness score right now is a 10. And many more great moments with Peter, Amy, Salman, Florin, Jessica. A special mention to Kamilo Melo (KM) for having a long lasting impression on me with all his wisdom and life lessons.

In phase 2, thanks to Laura for her strong support and guidance. Thanks to Andrea for an always fun atmosphere and introducing me to be passionate about static art ;) Thanks to Alice for cheering me by baking cakes to celebrate every occasion and for inspiring and introducing me to the world of climbing. Many thanks for Luca, Iselin, Matt, Anne, Xiangxiao, Mohsen and Dimitar for many great moments as well.

Finally, a big thanks to new gen BioRob members Astha, Alex (Ale, Alessandro..??), Milad, Guillaume, Anastasia, Gizem and Ozge for making so many great moments in such a short span of time.

All through my PhD, Jonathan has been a pillar of support and inspiration for my work. My collaboration and friendship with him has allowed me to be a better researcher and a better person. Thanks Jon!

No BioRob member can get away from Ale! Thanks to him for putting up with my constant “how do I?” questions about everything and making sure I had the infrastructure I needed to successfully complete my PhD. Many thanks to Sylvie and François for all the support in the lab activities.

During the pandemic, a great deal of my time was spent at home. I would like to thank my flatmates for keeping a great atmosphere at home and providing a safe, fun and relaxing environment. My flatmates over the years, Mark, Paramvir, Laura, Saranya, Leticia and Lucille. A special thanks to Mohit Pundir for the time we spent during the pandemic and introducing me to the culture and cuisine of northern regions of India. A special thanks to my special flatmate Rumi ;)

Many thanks to the Indian community, friends and members of YUVA at EPFL for making me feel at home! Special thanks to Nitin for always being there for me. Many thanks to Preethi for always looking out for me. And Harshal for giving his valuable inputs being just around the corner.

Thanks to my friends from Manipal, whose group name I cannot mention here ;) and my friends from Delft who have kept me sane all through my PhD with their visits and online interactions.

My PhD would not have been possible without my special friend Sagar. He took my role for my family and supported them anytime they needed me. Living far away from family would not have been possible if not for him.

I thank Meghana for being that person I can go to anytime I want to share my feelings and always making sure I am in a good space.

My mom (Padmaja), my dad (Ramalingasetty) and grandparents (Shubashini and Subbarajanna) have been the sole reason I am able to successfully complete my PhD. My achievements are a result of the many sacrifices they have made for me and I am truly indebted to them for that. A special thanks to my sweet little sister (Shruthi) for everything she has silently done for me to make sure I achieve everything I wished for and more. She has been a pillar of support for both myself and my family.

I thank all my family and friends again, some of whom I might have not mentioned by name here (sorry about that). To express my gratitude to each of you and relive some of the special moments we shared during my PhD, scan the QR code.

Thank to every one of you!

PS: My sincere apologies if I forgot to mention someone! As you know all PhD submissions are done last minute.

*Madhugiri, 24 February 2022*

S.T. R.



[Click here](#)



# Abstract

Control of movements in limbed terrestrial animals, some rhythmic (e.g., locomotion, grooming) and some non-rhythmic (e.g., reaching and grasping, crouching, posture-control) involves complex interactions between the neural controllers, the body/limb biomechanics and the environment. Animal experiments are often subjected to several restrictions to study freely behaving animals due to technical and ethical reasons.

Computational modeling represents a powerful tool to complement animal experiments by capturing the dynamics of motor control. Particularly, neural control of locomotion cannot be fully understood without revealing feedforward and feedback interactions between the neural circuits in the brain and spinal cord and the body biomechanics.

A necessary stage in these studies is the development of comprehensive musculoskeletal models of the whole body. In this thesis, we focus on three important model organisms in studying animal movements. Namely, *Mus musculus* (mouse), *Drosophila melanogaster* (fly) and *Macaca fascicularis*. For all three animals, we first developed their biomechanical models.

With the mouse (*Mus musculus*) biomechanical model, we conducted a comprehensive study on the characteristics of limb musculature and the influence of joint moments and moment-arms on producing limb movements. Our results revealed the complex relationships between muscles and joints and highlighted the significant role of biomechanics in producing movements.

Next, we investigated the limb kinematics and kinetics of locomotion and grooming by developing a bio-realistic model of *Drosophila melanogaster* (fly). Using the fly biomechanical model driven by neural oscillator models, we found that tripod gaits were preferentially chosen when simultaneously optimized for wide ranges of speed and static stability.

In our third model, we developed a computational framework to estimate the spatiotemporal patterns of proprioceptive inputs to the cervical spinal cord during three-dimensional arm movements in *Macaca fascicularis*. Estimated maps show complex and markedly distinct patterns of neural activity for each of the fiber populations spanning the spinal

cord rostro-caudally. Our results indicate that reproducing the proprioceptive information flow to the cervical spinal cord requires complex spatio-temporal modulation of each spinal root. Our model can support the design of neuroprosthetic technologies as well as in-silico investigations of the primate sensorimotor system.

Finally, from the culminated experience of developing neuromechanical models, we propose a framework for modeling and simulating of animals and robots (FARMS). The FARMS aims to standardize neuromechanical simulations for studying animal motor control. Our work shows how neuromechanical simulations can be used to investigate the different aspects of animal motor control and complement animal experiments.

Key words: neuromechanical, simulations, spatiotemporal afferent maps, simulation framework, musculoskeletal, insect locomotion, multi-legged locomotion, inverse dynamics

# Résumé

Le contrôle des mouvements chez les animaux terrestres membrés, rythmiques (par ex. locomotion, toilettage) et non rythmiques (par ex. accroupi, contrôle de la posture) implique des interactions complexes entre les contrôleurs neuronaux, la biomécanique du corps/des membres et l'environnement. Les expérimentations animales pour étudier leur comportement sont souvent soumises à des restrictions strictes pour des raisons techniques et éthiques.

La modélisation informatique représente donc un outil puissant pour compléter ces expériences animales en capturant la dynamique du contrôle moteur. En particulier, le contrôle neuronal de la locomotion ne peut pas être entièrement compris sans révéler les boucles de commandes prédictives et de rétroaction qui prennent place entre les circuits neuronaux du cerveau et de la moelle épinière et la biomécanique du corps.

Une étape nécessaire de ces études est le développement de modèles musculo-squelettiques complets du corps entier. Dans cette thèse, nous nous focalisons sur trois des organismes pour l'étude des mouvements des animaux. A savoir, la *Mus musculus*, la *Drosophila melanogaster* et le *Macaca fascicularis*. Pour ces trois animaux, nous avons en premier lieu développé leurs modèles biomécaniques.

Avec le modèle biomécanique de la *souris* (*Mus musculus*), nous avons mené une étude approfondie sur les caractéristiques de la musculature des membres et son influence sur la production de leurs mouvements en termes de couples appliqués aux articulations et de bras de levier. Nos résultats ont révélé les relations complexes entre les muscles et les articulations et ont mis en évidence le rôle important de la biomécanique dans la production des mouvements.

Ensuite, nous avons étudié la cinématique et la cinétique de la locomotion attachée et du toilettage ("grooming" en anglais) en développant un modèle bio-réaliste de la *Drosophila melanogaster*. En utilisant ce modèle biomécanique commandé par des modèles d'oscillateurs neuronaux, nous avons constaté que le déplacement en était favorisé lorsqu'il était optimisé pour de larges plages de vitesse et de stabilité statique.

Dans notre troisième modèle, nous avons développé un cadre computationnel pour estimer les caractéristiques spatio-temporelles de l'information proprioceptive vers la moelle

épineière cervicale lors des mouvements tridimensionnels des bras chez les singes. Les relations estimées montrent des modèles d'activité neuronale complexes et nettement distinctes pour chacune des populations de fibres couvrant la moelle épinière de manière rostro-caudale. Nos résultats indiquent que la reproduction du flux d'informations proprioceptives vers la moelle épinière cervicale nécessite des modulations spatio-temporelles de chaque racine spinale. Notre modèle peut apporter un soutien à la conception de technologies neuroprothétiques ainsi qu'aux investigations *in silico* du système sensorimoteur des primates.

Enfin, à partir de l'expérience aboutie en développant des modèles neuromécaniques, nous proposons un environnement computationnel pour la modélisation et simulation d'animaux et de robots (FARMS). FARMS vise à standardiser les simulations neuromécaniques pour l'étude du contrôle moteur animal. Notre travail démontre comment les simulations neuromécaniques peuvent être utilisées pour étudier les différents aspects de contrôle de la motricité animale et complimenter les expérimentations animales.

Mots clefs : neuromécanique, simulations, cartes afférentes spatio-temporelles, environnement de simulation informatique, musculo-squelettique, locomotion d'insectes, locomotion multi-pattes, dynamique inverse, contrôle moteur, modèle biomécanique

# Contents

<b>Acknowledgements</b>	<b>i</b>
<b>Abstract (English/Français)</b>	<b>v</b>
<b>List of figures</b>	<b>xiii</b>
<b>List of tables</b>	<b>xvii</b>
<b>1 Introduction</b>	<b>1</b>
<b>2 A whole-body musculoskeletal model of the mouse</b>	<b>11</b>
2.1 Abstract . . . . .	13
2.2 Introduction . . . . .	14
2.3 Methods . . . . .	16
2.3.1 Simulation tools . . . . .	16
2.3.2 Skeletal system . . . . .	16
2.3.3 Muscle System . . . . .	20
2.3.4 Analysis of sensitivity of joint moment-arms and moments to changes in muscle parameters and attachment points . . . . .	24
2.4 Results . . . . .	26
2.4.1 Moment-arm analysis for the hindlimb muscles . . . . .	30
2.4.2 Description of muscle function based on moment-arms and moments	30
2.4.3 Operational range of muscle-fiber length . . . . .	33
2.4.4 Sensitivity analysis . . . . .	35
2.5 Discussion . . . . .	40
2.5.1 Muscle system development . . . . .	40
2.5.2 Muscle moment-arms and moments . . . . .	42
2.5.3 Range of normalized muscle-fiber lengths . . . . .	44
2.5.4 Sensitivity analysis . . . . .	45
2.5.5 Model limitations . . . . .	46
2.5.6 Model use and future work . . . . .	47
	ix



<b>3</b>	<b>Neuromechfly</b>	<b>49</b>
3.1	Abstract . . . . .	51
3.2	Introduction . . . . .	52
3.3	Methods . . . . .	55
3.3.1	Constructing an adult <i>Drosophila</i> biomechanical model . . . . .	55
3.3.2	Kinematic replay and analysis . . . . .	59
3.3.3	Neural network parameter optimization . . . . .	67
3.4	Results . . . . .	73
3.4.1	Constructing a data-driven biomechanical model of adult <i>Drosophila</i> . . . . .	73
3.4.2	Identifying minimal joint degrees-of-freedom required to accurately replay real 3D leg kinematics . . . . .	74
3.4.3	Using NeuroMechFly to estimate joint torques and contact forces through kinematic replay of real fly behaviors . . . . .	76
3.4.4	Using NeuroMechFly to explore locomotor controllers by optimizing CPG-oscillator networks and muscles . . . . .	79
3.5	Discussion . . . . .	84
3.5.1	Limitations and future extensions of the biomechanical module . . . . .	85
3.5.2	Limitations and future extensions of the neuromuscular modules . . . . .	85
<b>4</b>	<b>Spatiotemporal Maps of Proprioceptive Inputs to the Cervical Spinal Cord During Three-Dimensional Reaching and Grasping</b>	<b>87</b>
4.1	Abstract . . . . .	89
4.2	Introduction . . . . .	90
4.3	Methods . . . . .	92
4.3.1	Biomechanical model . . . . .	92
4.3.2	Afferent fiber model . . . . .	93
4.3.3	Experimental dataset: kinematics . . . . .	95
4.3.4	Experimental dataset: electromyography . . . . .	96
4.3.5	Estimation of Spatiotemporal maps . . . . .	96
4.4	Results . . . . .	98
4.4.1	Model Validation . . . . .	98
4.4.2	Sensory Afferent Firing rates . . . . .	99
4.4.3	Spatiotemporal maps of proprioceptive inputs . . . . .	100
4.5	Discussion . . . . .	103
4.5.1	A realistic primate arm model . . . . .	103
4.5.2	Sensory afferent firing dynamics . . . . .	104
4.5.3	Spatiotemporal patterns of proprioceptive input to the cervical spinal cord . . . . .	104
4.5.4	Insights for the design of neuroprosthetic systems . . . . .	106
4.5.5	Model limitations . . . . .	106
4.6	Conclusion . . . . .	108

<b>5</b>	<b>FARMS: Framework for Animal Robot Modeling and Simulation</b>	<b>109</b>
5.1	Introduction . . . . .	111
5.2	Framework . . . . .	113
5.3	Data . . . . .	115
5.4	Modeling . . . . .	115
5.4.1	Scene . . . . .	115
5.4.2	Actuation . . . . .	116
5.4.3	Import/Export . . . . .	118
5.5	Simulation . . . . .	119
5.5.1	Physics . . . . .	119
5.5.2	Sensors . . . . .	120
5.5.3	Controller . . . . .	120
5.5.4	Actuators . . . . .	120
5.5.5	Logging . . . . .	120
5.6	Analysis . . . . .	121
5.7	Conclusion . . . . .	122
<b>6</b>	<b>Conclusion</b>	<b>123</b>
6.1	Mouse : Musculoskeletal model . . . . .	123
6.2	Drosophila melanogaster : Kinematic replay and feed-forward locomotion . . . . .	125
6.3	Macaca fascicularis : Sensory predictions . . . . .	125
6.4	A framework for neuromechanical simulations . . . . .	126
6.5	Challenges in performing animal simulations . . . . .	126
6.6	Future work . . . . .	127
<b>A</b>	<b>Supplementary Information : Mouse BioMechanics</b>	<b>131</b>
A.1	Hill-type muscle model . . . . .	131
A.2	Hindlimb muscle parameter scaling . . . . .	132
A.3	Muscle-tendon slack length estimation . . . . .	134
<b>B</b>	<b>Supplementary Figures and Tables : NeuroMechFly</b>	<b>137</b>
B.1	Supplementary Figures . . . . .	140
B.2	Supplementary Videos . . . . .	153
B.3	Code and data availability . . . . .	155
B.4	Funding . . . . .	155
B.5	Acknowledgments . . . . .	155
<b>C</b>	<b>Supplementary Information : Non-human Primate</b>	<b>157</b>
C.1	Muscle spindle and golgi tendon model equations . . . . .	157
	<b>Bibliography</b>	<b>178</b>
	<b>Curriculum Vitae</b>	<b>179</b>



# List of Figures

1.1	A representative view of the neuro-musculo-skeletal systems involved to produce locomotion. . . . .	3
2.1	Focus of the mouse modeling study . . . . .	12
2.2	Components of a closed-loop neuromechanical simulation . . . . .	14
2.3	Reference frames for model description . . . . .	17
2.4	Representation of skeletal model poses . . . . .	20
2.5	Hill-type muscle model describing the force generation by the muscles . .	21
2.6	Muscle attachment and polyline approximation of muscle paths . . . . .	22
2.7	Lateral view of the musculoskeletal system of the mouse's hindlimb and forelimb . . . . .	23
2.8	Validation of hindlimb moment-arms . . . . .	29
2.9	Comprehensive view of muscle moment-arm and moment over each degree-of-freedom . . . . .	31
2.10	Range of normalized muscle-fiber length . . . . .	34
2.11	Sensitivity of joint moment-arms to changes in muscle attachment points and of joint moments to changes in muscle parameters. . . . .	38
2.12	Perturbation of muscle moment-arms and moments . . . . .	39
2.13	Moment and moment-arm of hip flexor muscles . . . . .	43
3.1	Focus of the NeuroMechfly study . . . . .	50
3.2	Data-driven development and applications of NeuroMechFly. . . . .	53
3.3	biomechanical . . . . .	73
3.4	Adding a CTr roll DoF to base DoFs enables the most accurate kinematic replay of real walking and grooming. . . . .	76
3.5	Kinematic replay of forward walking allows the estimation of ground contacts and reaction forces. . . . .	78
3.6	Kinematic replay allows the estimation of self-collisions and reaction forces during foreleg/antennal grooming. . . . .	80

3.7	Using evolutionary optimization to identify oscillator network and muscle parameters that achieve fast and stable locomotion. . . . .	82
3.8	Modules that can be independently modified in NeuroMechFly. . . . .	84
4.1	Focus of the <i>Macaca fascicularis</i> study . . . . .	88
4.2	Overview of modeling and simulation pipeline . . . . .	94
4.3	Evolution of the principal joint angles during the three-dimensional reaching and grasping task for Mk-Sa, recorded and simulated . . . . .	98
4.4	Averaged and normalized EMG envelopes, compared to computed muscle activity for Mk-Br . . . . .	99
4.5	Decomposition of sensory modalities . . . . .	100
4.6	Spinal map of the three different sensory feedbacks during a standardized reaching and grasping task . . . . .	101
4.7	Comparison of spatiotemporal maps of sensory inputs in the cervical spinal cord for Ia- and II-type afferents . . . . .	102
4.8	Spinal map of combined estimated proprioceptive feedbacks . . . . .	105
5.1	Focus of the FARMS framework . . . . .	110
5.2	FARMS Architecture . . . . .	114
5.3	Overview of modeling steps in FARMS . . . . .	117
5.4	Example of neural network generation and visualization in FARMS . . . .	118
5.5	Visualization of simulation in FARMS . . . . .	121
6.1	Overview of the focus of individual chapters in this thesis with respect to neuromechanical control loop . . . . .	124
B.1	Leg segment lengths for real female <i>Drosophila melanogaster</i> and NeuroMechFly. . . . .	140
B.2	Position error for every joint in the distal leg during walking as a function of kinematic chain configuration. . . . .	141
B.3	Position error for every joint in the distal leg during grooming as a function of kinematic chain configuration. . . . .	142
B.4	Mean squared error between tracked and simulated joint positions and velocities as a function of position and velocity gain values. . . . .	143
B.5	Sensitivity of estimated joint torques and contact forces to proportional and derivative gains. . . . .	144
B.6	Leg joint degrees-of-freedom and their rotational axes. . . . .	145
B.7	The ‘zero pose’ of NeuroMechFly. . . . .	145
B.8	Sensitivity of simulated spherical treadmill rotation prediction accuracy during tethered walking to ERP and CFM constraint parameters. . . . .	146
B.9	Comparing real to simulated spherical treadmill rotational velocities during tethered walking. . . . .	147

B.10 Comparing real and simulation predictions for gait diagrams during tethered walking. . . . .	148
B.11 The impact of the morphological realism on estimates of leg-leg and leg-antenna contact during grooming. . . . .	149
B.12 Comparison of walking paths and velocities for real tethered walking versus kinematic replay in a tethered or untethered model. . . . .	150
B.13 Measured joint angles during real forward walking. . . . .	151
B.14 Objectives, penalties, and individual solutions over generations when optimizing for fast and statically stable tethered walking. . . . .	152



# List of Tables

2.1	Mouse skeletal segments grouping, joint names and joint ranges . . . . .	19
2.2	Hindlimb and forelimb muscle parameters . . . . .	28
4.1	Morphometric measurements of a subset of representative arm and forearm musculo-tendon units . . . . .	93
4.2	Proportional distribution of the motor pools . . . . .	101
A.1	Hill-type muscle model parameters . . . . .	133
B.1	Model body parts and degrees-of-freedom between each segment and its parent. . . . .	137
B.2	Matrix of p-values from pairwise comparisons of position errors after calculating forward kinematics for walking. . . . .	138
B.3	Matrix of p-values from pairwise comparisons of position errors after calculating forward kinematics for grooming. . . . .	138
B.4	Fixed angles for body joints during kinematic replay and optimization. . .	139
B.5	Fixed angles for leg joints during optimization (deg). . . . .	139
B.6	Lower and upper limits for the muscle parameters during optimization. . .	139





# Chapter 1

## Introduction

### Moving on (Locomotion). . .

*“A journey of a thousand miles begins with a single step!”* says the Chinese proverb. My time as a doctoral student has been to probe and investigate how this single step is achieved by animals. Life over the billions of years has evolved into this astronomically complex interactions of chemical building blocks. This level of sophistication would not have been possible if life did not interact with its environment. One of the outcomes of this interaction with the environment is the ability of life to move. Locomotion (loco: “from a place” and motion: “to move”) means to move from one place to another. Locomotion had profound impact on the evolution of life. Animals able to navigate in their environment increased their chances of survival by exposing themselves to newer resources. Locomotion also improved their ability to change habitat when their environment was not conducive anymore. From an evolutionary point-of-view locomotion has played a pivotal role in shaping life on earth to what we see today.

A key moment in the evolution of life was the transition of life from being purely water based to land based (Ashley-Ross et al., [2013](#)). Aquatic life moved to shallower waters and thereby getting closer to land. Once on land, different life forms evolved many strategies to navigate the new terrain. Some being an extension of their skills from their aquatic ancestors and some completely evolved for land (Grillner, [2018](#)). Eventually life took off and developed propelled flight. Over the eons, terrestrial, aquatic and aerial life forms have all evolved different locomotion strategies to navigate and flourish in their respective environments.

Over the years, the BioRobotics laboratory has been investigating aquatic and amphibious locomotion both using mathematical models and robotic platforms. Extending this line of evolution from amphibious animals, the next transition has been to study terrestrial locomotion.

Terrestrial locomotion predominantly evolved into three basic forms: (1) Legged: by moving its legged appendages; (2) Limbless: by using the body to propel itself with no additional appendages; (3) Rolling: by rotating the body over the surface. Among the three forms, legged locomotion is the most common form on land in both vertebrate and arthropods. Furthermore, not all animals that use legs to locomote are the same (Kubo and Benton, 2009). They differ in morphology, posture, number of legs and types of gaits they exhibit. Through the thesis I will explore these differences by studying three different terrestrial animals. Namely, *Macaca fascicularis*, *Mus musculus* (Mouse), and *Drosophila melanogaster*. The choice of the animal models were in part driven by funding choices (mouse model for the Human Brain Project), availability of experimental data (macaca with EMG and kinematic recordings) and collaborations (drosophila with Prof Pavan Ramdya).

Before we move to the specific studies, let me first briefly introduce the reader to the general understanding of animal locomotion in the literature.

## Studying locomotion

Locomotion being a primitive component of life, many a times it goes unnoticed as a tremendous feat of achievement that life has evolved. It may appear trivial due to its repetitive, rhythmic motion carried out by every animal. But the underlying principles which allow animals to do efficient, robust and versatile movements are more complex than it appears to be at first glance (Dickinson, 2000). It is a result of complex interactions between the body, the neural circuits and the environment (Figure 1.1). Each of these sub-systems are complex by themselves individually and posses emergent functional properties when they interact with each other and the environment. The coupling between these complex modules make it extremely challenging to come up with theories that can explain and capture how locomotion works in different in species (K. Pearson et al., 2006a).

Studying locomotion can be broadly classified into two popular approaches. One, a biomechanical perspective, wherein locomotion is studied as the interaction between the body and the environment with focus on the kinematics and the kinetics of the movement. Second approach is to study the behavior from a neural perspective, where in the main goal is to identify the circuitry responsible for producing appropriate body movements necessary for locomotion. An integrative approach, that merges neural and biomechanical investigations, has been attempted but is limited due to challenges in conducting experiments. We will get to that in a moment.

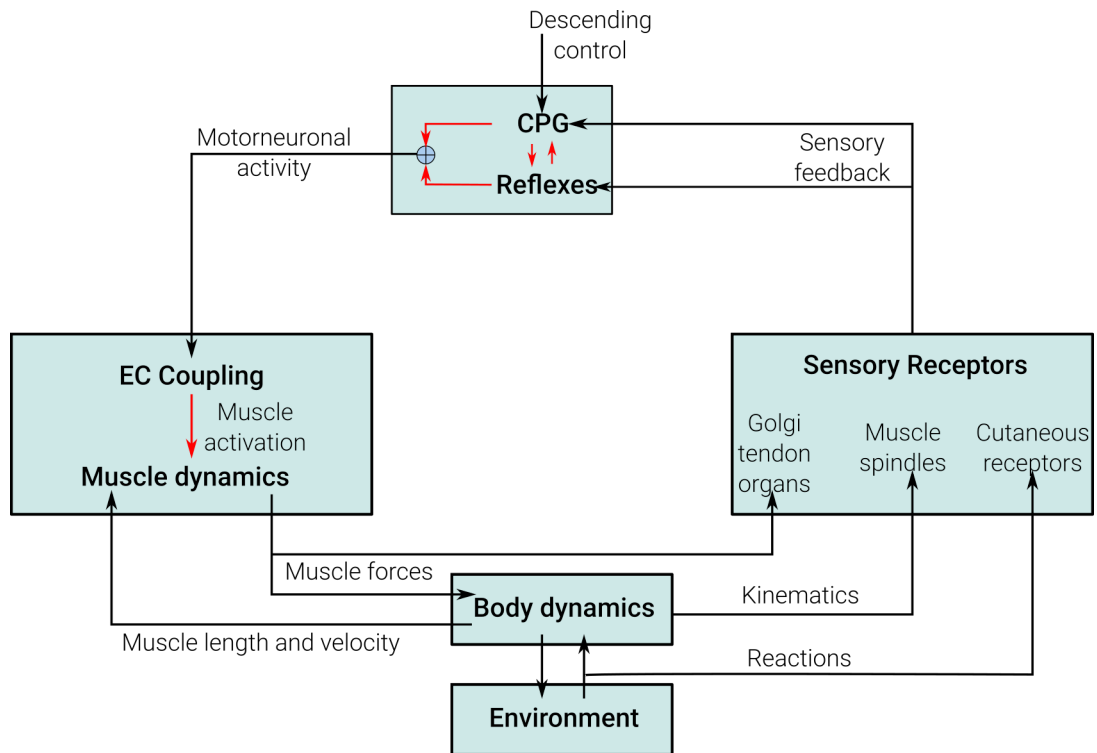


Figure 1.1: A representative view of the neuro-musculo-skeletal systems involved to produce locomotion. The neural component comprises of rhythm generating central pattern generators (CPG) working with reflexes and modulated by descending signals to produce motorneuronal activity. Excitation-contraction (EC) dynamics transform motorneuronal activity into muscle activation which produces appropriate muscle forces defined by its dynamics. The body then responds to the muscle forces to produce movement by interacting with the environment. The sensory receptors feedback the proprioceptive (muscle spindles and golgi tendon organs) and exteroceptive (cutaneous receptors) to the neural system. The figure has been edited and reproduced from the article of Paul et al. (2005) with kind permission of Springer Science and Business Media.

## A biomechanical perspective

The body of an animal has co-evolved along with the neural circuitry to best adapt to its environment. Movement is possible only when the body interacts with the environment to produce the necessary forces that propel itself in the desired direction. This body-environment interaction poses a strong coupling between the two and thereby resulting in developing bodies conducive to the environment. Of course, this observation is subjected to the survivorship bias. Nonetheless, it still highlights the importance of biomechanics in locomotion. Beal et al. (2006) have shown that a dead fish, under the proper conditions, can exhibit passive propulsion to move ahead in a stream of water. This is an excellent experiment to highlight the importance of biomechanics and to reflect how well the biomechanics of the animal is tuned with its environment to produce movement with

minimal neural inputs or in this particular case with no neural inputs.

For legged locomotion, as early as in 1685, Giovanni (1685) proposed the “compass gait” model to show that walking could be presented without need for active control of the swing leg. Over the centuries, many mathematical models and theories have been developed to describe how the body generates necessary forces to interact with the environment. These theories range from simple inverted pendulum model (Alexander, 1976; Mochon S., 1980) and Spring Loaded Inverted Pendulum (SLIP) (R., 1989; McMahon T., 1990) model to complex models that include more detailed biomechanical structures such as muscles and multi-articulate joints (Siegler et al., 1982; Geyer, Seyfarth, et al., 2006; F. E. Zajac et al., 2003; Geyer and Herr, 2010). Full and Koditschek (1999) introduced the terms *templates* for simple models such as the SLIP model and *anchors* for more elaborate models that include multiple joints and muscles from a perspective to understand the control strategies of the nervous system.

Using template models, Blickhan and Full (1993) showed that even among diverse animals such as cockroaches, quail and kangaroos, their locomotion can be generalized at the level of gait energetics and dynamics. Based on studies with simple template models, we can observe the global commonalities of a seemingly diverse locomotor behaviors. In more recent studies, experimental data from muscles during locomotor regime has revealed that muscles are more than just motors producing propulsive forces. From work-loop analysis, it can be observed that muscles can act as motors (produce positive work), as brakes (produce negative work), as springs (passive elastic elements) or as struts (force transmitters) and as dampers (energy dissipation). (Refer to the review by Dickinson (2000) for more details).

To summarize, animals gaits can be grouped and be modeled as templates. When more complex musculoskeletal models are considered, the biomechanics reveal that the body is more sophisticated than just executing the commands from the nervous system.

## A neural perspective

The most important contribution to this approach for mammalian locomotion started from Sir Charles Sherrington (Sherrington, 1910) and later extended by his student Thomas Graham Brown. Graham Brown showed 100 years ago from studies on decerebrated and spinal cats that in the absence of descending signals from higher brain centers and afferent sensory signals, it was still possible to produce rhythmic locomotion in flexor-extensor muscles of the hindlimb (T. G. Brown, 1911). Eventually, the proposition that special units in the spinal cord called central pattern generators (CPG's) emerged. This has been later confirmed in other vertebrates (Whelan, 2010). Ever since, several studies investigated spinal circuits responsible for producing rhythmic activity to control and execute coordinated movement of a large number of joints and muscles in the limbs and

the body.

Whelan (2010) defines CPG as “*A set of interneurons that are capable of producing rhythmic output without phasic input from afferent or descending projections*”. This means that the spinal cord has the necessary circuits to produce rhythmic locomotion activity, which is then regulated and modulated by sensory afferents and higher brain signals to ensure robust behavior. These results led Graham Brown to propose the “half-center hypothesis” and later extended by Lundberg et al. (1987) to explain the observed locomotor activity. The hypothesis was that every flexor-extensor antagonist muscle pairs in each limb were excited by mutually inhibiting half-centers. Though this model proved very powerful, a shortcoming was that it could not explain the complex motor-neuron activity apart from flexion-extension rhythmic patterns (McCrea and Ilya A. Rybak, 2008).

To better explain the experimentally measured neural activity several neural model structures have been proposed after the half-center model. A brief list of the proposed models are: (1) the ring model (Székely et al., 1969; Gurfinkel and Shik, 1974); (2) flexor burst model (K. G. Pearson and Duysens, 1976); (3) unit burst generators (UBG) (Grillner, 1981); (4) two-level CPG (Ilya A. Rybak et al., 2006). Among these models, the two-level CPG structure has been able to incorporate and explain the recent observations in animal experiments (Ausborn, Shevtsova, Caggiano, et al., 2019).

The advent of molecular and genetic tools in animal experiments, especially in mice has lead to the identification of several classes of interneurons involved in generation and regulation of locomotor motor patterns. Kiehn (2016) and Ausborn, Shevtsova, and Simon M. Danner (2021) summarize the experimental findings and the possible neural circuits based on the findings.

To summarize, since the time of Graham Brown we have come a long way in unraveling the specific interneurons and their connectivity in the black box locomotor neural system. It is now widely accepted that CPGs underlie rhythmic locomotor patterns.

## A sensory perspective

In the previous sections, we looked the feed-forward aspect of locomotor control with the central pattern generators. It is very important to take note that sensory/afferent feedback plays major role in locomotion too. It is the sensory information that tells the nervous system about the internal state of the body and the implications of the forces it generated against the environment to move. According to Kuo (2002), from a control perspective a mechanical system that dictates efficiency and stability is better accomplished with feedback versus purely feed-forward.

Akay et al. (2014) showed that in healthy mice proprioceptive feedback plays an important

role in shaping the locomotor activity during swing and stance phase. Removal of these feedbacks resulted in severe degradation of the patterns. Takeoka and Arber (2019) and Takeoka, Vollenweider, et al. (2014) showed that in rats after spinal cord injury it was proprioceptive afferent fibers that were essential in initiation and maintenance of locomotor recovery. The studies show how closely the feedback circuits are linked with locomotor circuits in the spinal cord.

To summarize, sensory feedbacks are necessary to generate efficient and robust locomotion but it still remains very hard to experimentally study them.

## An integrated, neuromechanical view

So far we have seen some of the insights gained into animal locomotion in terms of the individual components that are part of the locomotion loop. Individual perspectives give us a deeper understanding about the possible roles of each of these components in generating locomotion. However, from Figure 1.1 we can see that the biomechanics, the neural circuits, the sensory modalities and the environment are tightly coupled and influence the behavior of each other. An ideal scenario to study locomotion would thus be able to perturb and study each of the individual components while recording and monitoring the others. This is easier said than done. With the advent of genetic tools, we are getting closer to targeted animal experiments while observing the animal in a freely behaving environment. Still, this remains a challenging endeavor. In particular because it is very difficult to measure the activity of spinal circuits and sensory afferents during locomotion.

It is thus necessary to complement animal experiments with mathematical models that can fill the gaps in experimental setups. And also make predictions to refine the animal experiments to be specific and targeted. A promising up and coming solution mainly due to the advancement of computational ability of computers is to create mathematical models and computer simulations where the body and neural models interact with the environment to produce real animal like behaviors so that one can test and study the principles of locomotion more rigorously and systematically than what is possible with animals. In order to create these simulation models, data needs to be collected from the real animal. This establishes a dialogue between the modeling studies and the animal experiments. Where, observations from one paradigm can be validated<sup>I</sup> using the other and then use the validated experiments to deduce new findings and refine our existing understanding. There have been several important neuromechanical simulation studies in different animals and at various complexities that have been useful in pushing the field forward. These include studies in *C. elegans* (Szigeti et al., 2014), lamprey (Ekeberg, 1993a; Thandiackal et al., 2021), salamander (Ijspeert et al., 2007), cat (Ekeberg and

---

<sup>I</sup>confirm predictions by comparing direct or indirectly measurable quantities between experiments and simulations

K. Pearson, 2005; S. Yakovenko et al., 2004; Ivashko et al., 2003; Markin et al., 2016), *drosophila melanogaster* (Ramdya et al., 2017a), stick insect (Tóth and Daun, 2019), and humans (Geyer and Herr, 2010; Dzeladini et al., 2014)

## Tools for simulating neuromechanical models

A neuromechanical simulation comprises of developing mathematical models of each of the individual blocks represented in Figure 1.1 (K. Pearson et al., 2006a). It includes the neural and biomechanical components along with their interactions. Neural models (spinal and brain circuits) produce the necessary instruction signals (motorneuron activations) for a specific movement. Muscle models respond to the neural signals by producing forces that act on the skeletal model and cause movements. The skeletal model and the body interact with the environment to produce reaction forces. The sensory organ models encode the state of the movement (somatosensory afferent feedback signals) and transmit this information back to the nervous system which then adapts the instruction signals to sensed perturbations or external forces.

A complex component to model in a neuromechanical simulation is the computation of linear and angular accelerations (forward dynamics) of the articulated rigid bodies and its interaction with the environment (contacts) (K. Pearson et al., 2006a). In fact, neuromechanical simulations are often limited to 2D models due to the difficulties associated with modeling and simulating 3D forward dynamics and its interactions with the environment. With applications for articulated rigid body simulations in robotics and animations has resulted in many stand-alone packages that perform collision detection, forward dynamics and numerical integration. These packages are commonly termed as physics engines. Popular physics engines include Open Dynamics Engine (ODE) (Smith, 2001), Simbody (Sherman et al., 2011), Bullet (Coumans, 2015), Mujoco (Todorov et al., 2012), PhysX (NVIDIA, 2022), Webots (Michel, 2004) (a fork of ODE physics engine) and DART (J. Lee et al., 2018). The availability of different physics engines has provided an opportunity for simulating more complex animal morphologies. Each of the mentioned physics engines have their own advantages and disadvantages. Choosing the appropriate physics engine for a certain experiment is a difficult one. In this thesis, Webots, Bullet, Simbody and Mujoco are the three physics engines that are explored and used. For a comprehensive review on physics engines from a robotics perspective refer to Collins et al. (2021).

Neural circuits can be modeled at various levels of complexity. Ranging from spike based Hodgkin-huxley models with conduction based synapses to population based simple first-order phase oscillators models. The number of neurons and the number of synapses can increase the complexity of the networks exponentially. Neural libraries such as Neuron (T. Carnevale et al., 2006) allow for simulating detailed and complex neuron models. While libraries such as NEST (Gewaltig and Diesmann, 2007) or BRIAN (Stimberg et al., 2019)



offer a wider range of abstract neural models to be simulated.

Muscles are most often simulated as Hill-type muscle models formulated by F. Zajac (1989). For different variations of the Hill-type models refer to Romero and Alonso (2016). Simpler mechanistic muscle models such as the ones formulated by Ekeberg (1993a) are used to model antagonist muscle pairs. The geometrical route of the muscle along the skeleton and around the joints also dictates the dynamics of the muscle. Modeling the geometric paths of the muscle during a simulation is a complex and computationally demanding procedure. Currently, there are no standalone muscle libraries to simulate different muscle models. This is mainly because the dynamics of the muscles are dependent on the state of the rigid bodies and the neural activations. For neuromechanical simulations, people often implement their own muscle library plugins (Aoi et al., 2019; Dzeladini et al., 2014; Geyer and Herr, 2010; Ekeberg and K. Pearson, 2005).

Finally, sensory models are based on the states of the forward dynamics of the rigid bodies, the neural dynamics and the muscle dynamics. Thus the choices of the prior models influence the ability of modeling a sensory information in the neuromechanical simulation. A commonly used sensory model is that of the muscles spindles and golgi-tendon organs formulated by A. Prochazka and M. Gorassini (1998) and Arthur Prochazka and Monica Gorassini (1998).

Although, there exists many libraries to simulate the individual components required to build a neuromechanical simulation; there are very few that integrate all the blocks. OpenSim (Seth, Jennifer L. Hicks, et al., 2018b) is the most commonly used simulator that has integrated rigid-body physics (Simbody) and the muscle models and an option to interact with external libraries for modeling neural dynamics. SCONE (Thomas Geijtenbeek, 2019) is a free and open-source software for predictive simulation of biological motion. It is simulator agnostic and it currently supports bindings to work with OpenSim out-of-the-box. Animatlab (David Cofer et al., 2010) has gone further to integrate all the components of a neuromechanical simulation but has been used seldom in the community. Neurorobotics platform (Falotico et al., 2017) aims to combine the fields of neuroscience, computer science and biology to simulate realistic animals and robots models with spiking neural models. The final chapter 5 of this thesis discusses, FARMS, a novel framework for modeling, simulating and analyzing neuromechanical models. With FARMS, the goal is to connect the various works of researchers coming from different fields, including biomechanics, neuroscience and robotics.

## Thesis Organization and Main Contributions

This work utilizes the approach of creating neuromuscular simulation models and to study locomotion and limb movement in terrestrial animals. Namely, *Macaca fascicularis*, *Mus musculus*, and *Drosophila melanogaster*. The studies conducted among the three animals can be formulated in three folds:

- Develop animal models for neuromuscular simulations
- Investigate the biomechanical and neural components of motor control, particularly locomotion.
- Establish the bridge between animal experiments and simulations

The introduction chapter introduced reader to the context and the previous literature related to general terrestrial locomotion. The chapters that follow will cover the modeling and simulation of studies related to the three different animals. After which, a chapter is presented to discuss the framework for simulating neuromechanical models. And finally, a concluding chapter summarizes the studies, presents a reflection of the work and finally the possible future work to continue.

**Chapter 2** describes the development of the first whole body 3D *Mus musculus* (mouse) musculoskeletal model. Both the forelimbs and hindlimb musculature was modeled as Hill-type muscles with all the parameters appropriately estimated. We then describe the influence of muscle moments and moment-arms on joint motion in a comprehensive manner.

**Chapter 3** describes the development, analysis and simulation of a neuromechanical model of *Drosophila melanogaster*. We established a pipeline to transfer tethered kinematic gaits to 3D physics based simulation to estimate joint torques and contact forces. Further, we setup a tethered neuromechanical model driven by an open-loop central pattern generator to study the relationship between speed and static stability on gait generation.

**Chapter 4** describes a study to generate spatial afferent sensory maps in *Macaca fascicularis* during reaching and grasping tasks.

**Chapter 5** describes FARMS (A Framework for Animal and Robot Modeling and Simulation), a framework for modeling and simulating robots and neuromechanical models for studying animal motor control. The framework establishes a philosophy for simulating diverse animal and robot models and sharing the observations with the community.

**Main contributions**

- We developed a framework called FARMS (A Framework for Animal and Robot Modeling and Simulation) for neuromechanical simulations.
- We developed the first whole body 3D musculoskeletal model of mouse.
- We present comprehensive ways to present muscle-joint relationship in highly articulated models.
- We developed a tool chain (NeuroMechFly) for establishing a dialogue between animal experiments and simulation in *Drosophila Melanogaster*.
- We studied the relationship between speed and stability in tethered *Drosophila Melanogaster* using open-loop central pattern generator networks
- We estimated spatial sensory afferent maps of the spinal cord in *Macaca Fascicularis* for reaching and grasping task.

## Chapter 2

# A whole-body musculoskeletal model of the mouse

### Overview

*Mouse* has become an important model organism in studying locomotion and movement generation. The advent of molecular and genetic technologies has helped provide deep insights into the neural circuits of that are responsible for generating and controlling limb movements. But, there is very little known about the biomechanics of the *Mouse*. Partly due to the challenges in performing biomechanical experiments in *Mouse* due to their small size. In this chapter, we first aim to build a whole-body musculoskeletal model of *Mouse*. Then perform a comprehensive analysis on the relationship between muscle forces, moment-arms, and moments on the limb movement.

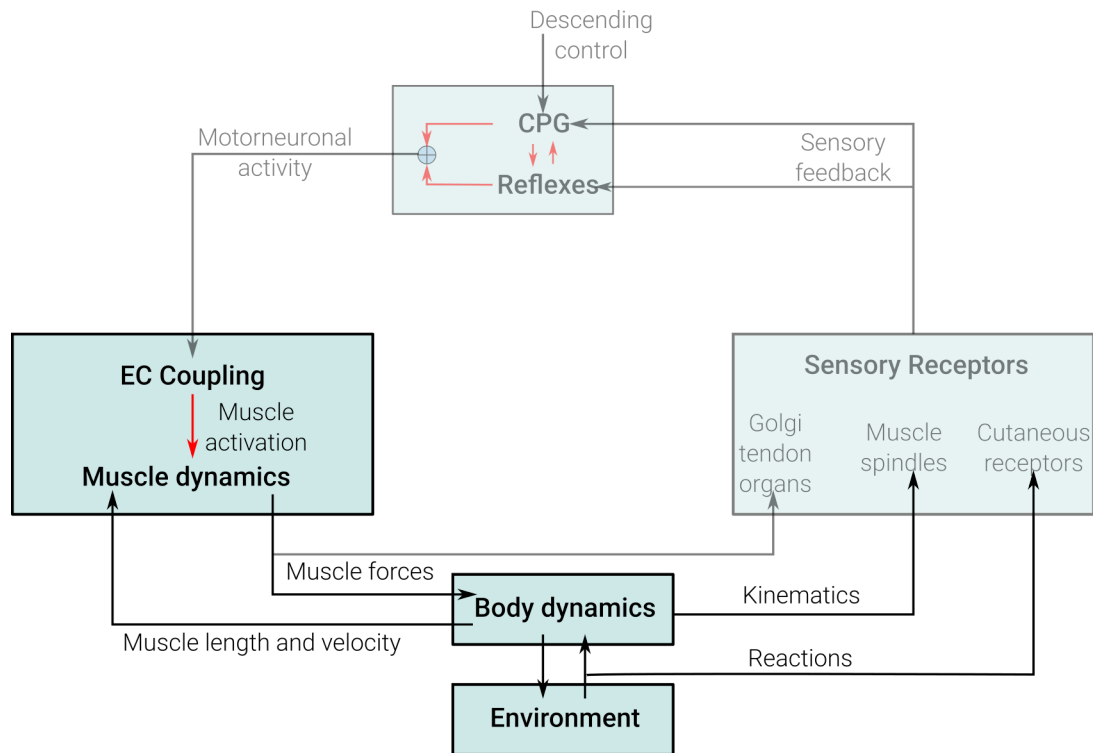


Figure 2.1: Focus of this chapter in the scheme of neuromechanical loop described in Figure 1.1 for movement generation

### Reference publication

*The following sections are based on our published article  
 “Shravan Tata Ramalingasetty, Simon M. Danner, Jonathan Arreguit,  
 Sergey N. Markin, Dimitri Rodarie, Claudia Kathe, Grégoire Courtine,  
 Ilya A. Rybak, and Auke Jan Ijspeert (2021). “A Whole-Body Musculoskeletal  
 Model of the Mouse”. In: IEEE Access 9, pp. 163861–163881. ISSN: 2169-3536.  
 DOI: [10.1109/ACCESS.2021.3133078](https://doi.org/10.1109/ACCESS.2021.3133078)”*

### My contributions

- Development and setup of the mouse skeletal model
- Development of the muscle simulation library (Now part of FARMS)
- Implementation of methodology to scale hindlimb parameters and estimate muscle parameters for the forelimb
- Computation and analysis of results and sensitivity study
- Preparation of the first draft of the original article

## 2.1 Abstract

Neural control of movement cannot be fully understood without careful consideration of interactions between the neural and biomechanical components. Recent advancements in mouse (*Mus musculus*) molecular genetics allow for the identification and manipulation of constituent elements underlying the neural control of movement. To complement experimental studies and investigate the mechanisms by which the neural circuitry interacts with the body and the environment, computational studies modeling motor behaviors in mice need to incorporate a model of the mouse musculoskeletal system. Here, we present the first fully articulated musculoskeletal model of the mouse. The mouse skeletal system has been developed from anatomical references and includes the sets of bones in all body compartments, including four limbs, spine, head and tail. Joints between all bones allow for simulation of full 3D mouse kinematics and kinetics. Hindlimb and forelimb musculature has been implemented using Hill-type muscle models. We analyzed the mouse whole-body model and described the moment-arms for different hindlimb and forelimb muscles, the moments applied by these muscles on the joints, and their involvement in limb movements at different limb/body configurations. The model represents a necessary step for the subsequent development of a comprehensive neuro-biomechanical model of freely behaving mice; this will close the loop between the neural control and the physical interactions between the body and the environment.

## 2.2 Introduction

Terrestrial animals exhibit a variety of complex motor behaviors, some rhythmic (e.g., locomotion, grooming) and some non-rhythmic (e.g., reaching and grasping, crouching, posture-control). These motor behaviors result from complex interactions between the neural circuits in the brain and spinal cord, the musculoskeletal system, and the environment (Figure 2.2) (Dallmann et al., 2021; Kiehn, 2016; Donald H. Edwards, 2010; Grillner and El Manira, 2019; Grillner, 2011). Investigating the underlying mechanisms of these motor behaviors in awake, behaving animals is highly challenging. Computational modeling is a powerful tool to complement experimental studies of neural control. It provides a platform to investigate the underlying neural mechanisms, allowing investigators to reproduce existing experimental observations, propose mechanistic explanations for the observed behaviors, suggest new experiments to test the proposed mechanisms, and propose possible approaches for treatment of different injuries or disorders (Morau et al., 2016; Ausborn, Shevtsova, and Simon M. Danner, 2021).

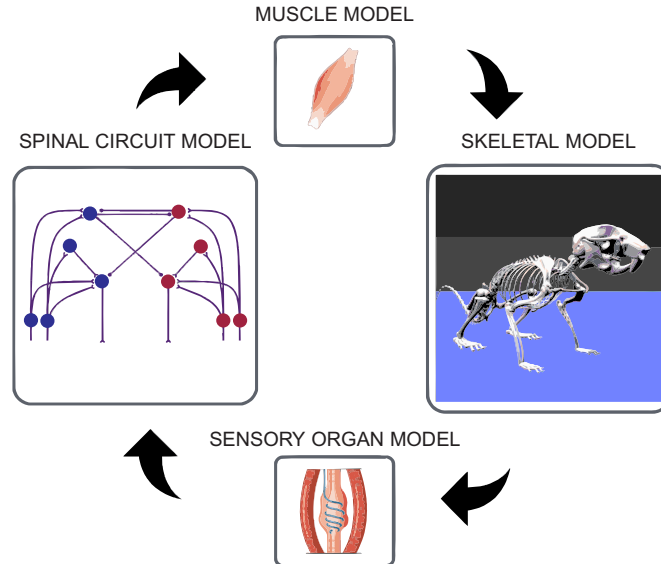


Figure 2.2: Components of a closed-loop neuromechanical simulation. Movements in animals arise due to complex interactions between the nervous system, the musculoskeletal system and the environment. A neuromechanical model includes the neural and biomechanical components along with their interactions. Neural models (spinal and brain circuits) produce the necessary instruction signals (motoneuron activations) for a specific movement. Muscle models respond to the neural signals by producing forces that act on the skeletal model and cause movements. The skeletal model and the body interact with the environment to produce reaction forces. The sensory organ models encode the state of the movement (somatosensory afferent feedback signals) and transmit this information back to the nervous system which then adapts the instruction signals to sensed perturbations or external forces.

Recent advances in mouse (*Mus musculus*) molecular genetic approaches have led to substantial progress in the studies of spinal and supra-spinal networks involved in motor control (Jessell, 2000; Goulding, 2009; Kiehn, 2011; Akay et al., 2014; Kiehn, 2016; Gosgnach et al., 2017; Ruder and Arber, 2019; Ruder, Schina, et al., 2021; Ausborn, Shevtsova, and Simon M. Danner, 2021; Ferreira-Pinto et al., 2018). Specifically, it is now possible to dissect the neural network by identifying and manipulating specific neural populations and to relate them to specific behavioral outcomes (Kiehn, 2016). The ubiquity of molecular genetic tools available for the mouse made it the preferred experimental animal for the study of neural control of movement.

Computational modeling of motor control in freely behaving mice, particularly modeling of locomotion, requires the development of detailed models of both the neural and biomechanical components and, importantly, their interactions during movements (Merel, Botvinick, et al., 2019) (Figure 2.2). Such detailed musculoskeletal models have been developed of the human (Cardona and Garcia Cena, 2019; S. Lee et al., 2019; Arnold, Ward, et al., 2010; Falisse et al., 2019; Rajagopal et al., 2016), the guinea fowl (Cox et al., 2019), the ostrich (Hutchinson, Rankin, et al., 2015), and the dog (Stark et al., 2021). Yet, no detailed whole-body three-dimensional musculoskeletal model of mouse currently exists; and most of the existing neuromechanical models (models incorporating neural controllers with the musculoskeletal system) of mammals have been limited to two-dimensional movements or had significantly simplified musculoskeletal or muscular components of the system (Ekeberg and K. Pearson, 2005; F. Young et al., 2019; Toeda et al., 2020; Aoi et al., 2019; S. Yakovenko et al., 2004; Markin et al., 2016; Ausborn, Shevtsova, and Simon M. Danner, 2021).

Here, we present an open-source, configurable whole-body musculoskeletal model of the mouse. We digitized all the bones of the mouse skeletal system and identified the corresponding joints to have a fully articulated rigid body model. Musculature for hindlimbs and forelimbs were modeled as Hill-type muscles. We compared and validated the hindlimb musculature of the model with the previously published single hindlimb model of mouse developed by Charles, Cappellari, Spence, Wells, et al. (2016). The three-dimensional (3D) model allowed us to explore the relationship of muscle moment-arms and moments on the hindlimb and forelimb joints in a comprehensive manner. Our analysis on the operational range of muscle-fibers for limb muscles give insights into the role of active and passive forces under isometric conditions. Finally, we evaluated the sensitivities of parameters to highlight a reduced set of crucial parameters in the complex whole-body mouse model.



## 2.3 Methods

### 2.3.1 Simulation tools

The mouse body was simulated as articulated rigid segments interacting with the environment. We used the Bullet v3.1.7 physics engine (Erwin Coumans and Yunfei Bai, 2016). Bullet was chosen because it is a fast and stable simulator of complex articulated rigid bodies. It employs Featherstone’s algorithm (Featherstone, 1983), which uses a reduced coordinate representation and an articulated-body inertia description to provide stability for models with long kinematic chains and links with larger mass differences. Furthermore, Bullet is available on most common operating systems and it has an application programming interface (API) for Python that allows for a full control of simulated behavior. To simulate muscle dynamics and their interactions with the skeletal system, we developed a simulator-agnostic muscle library and integrated it with Bullet.

### 2.3.2 Skeletal system

The mouse skeletal system was represented by a set of articulated rigid segments. The construction of this model involved obtaining skeletal scans, identifying joints, and computing inertial parameters.

#### Digitization

The skeletal model was based on several mouse skeletal scans and anatomical reference data. The model represents a generic mouse based on references from several specimens. All the bones of the mouse were digitized as individual mesh objects. This included 23 tail bones, 8 cervical bones, 13 thoracic bones, 6 lumbar bones, 4 sacral (merged together as Pelvis bone), 3 coccygeal, and 20 caudal vertebrae, 15 bones in each forelimb (including digits), 13 bones in each hindlimb (including digits), the pelvis, and the head. In total, the model consists of 108 bones (Table 2.1). The hind and forelimb bones are modeled to be symmetric across the sagittal plane.

#### Reference frames

The definition of the reference frames for the model followed the convention used in Simulation Description Format (SDF) (OSRF, n.d.); a widely used description format in the robotics community. Figure 2.3 shows the reference frames used to describe the model.

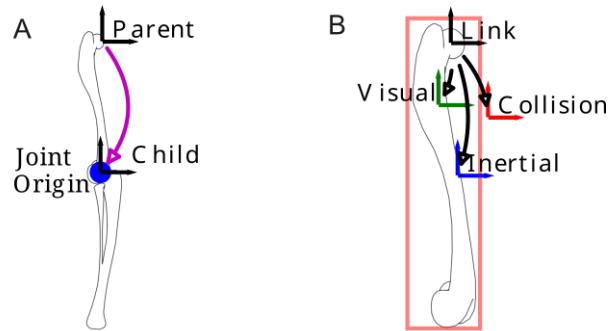


Figure 2.3: Reference frames. (A) For each bone (Femur in the example shown), a global reference frame (link frame; black) is used to define a set of reference frames: a visual reference frame (green) defines the position and orientation of visual shapes; a collision reference frame (red) defines the position and orientation of the collision shapes; an inertial reference frame (blue) defines the position of the center of mass and inertia of the link. These reference frames (visual, collision and inertial frames) are defined in local coordinates with respect to the link reference frame. (B) Joint reference frame is defined with respect to the child link frame in the parent-child relationship defining the joint. The position of the joint reference frame is the joint rotation center (Knee joint in the example shown).

### Identification of centers for joint rotation

Joint rotation centers for the model were chosen such that the rotations introduced minimal interference with neighboring bones within the range-of-motion of the joint. The rotation centers remain fixed throughout the range-of-motion.

Among the tail and spinal bones, we modeled two rotational degrees-of-freedom (DoFs) between each pair of consecutive bones: flexion-extension (rotation about the transversal axis) and lateral bending (rotation about the sagittal axis).

In the hindlimbs, the hip joints were modeled as spherical joints with three rotational DoFs: flexion-extension (rotation about the transversal axis), abduction-adduction (rotation about the coronal axis), and internal-external rotation (rotation about the sagittal axis). Knee joints were modeled with a single DoF, a flexion-extension (rotation about the transversal axis) joint. Ankle joints were modeled with three DoFs: plantarflexion-dorsiflexion (rotation about the transversal axis), abduction-adduction (rotation about the coronal axis) and inversion-eversion (rotation about the sagittal axis). Only a single DoF of flexion-extension (rotation about the transversal axis) was modeled between each digit in the hindpaws.

In the forelimbs, the shoulder joints were modeled as a spherical joint with three rotational DoFs: retraction-protraction (rotation about the transversal axis), abduction-adduction

(rotation about the coronal axis), and external-internal rotation (rotation about the sagittal axis). Elbow joints were modeled with two DoFs: extension-flexion (rotation about the transversal axis) and supination-pronation (rotation about the sagittal axis). Wrist joints were modeled with two DoFs: extension-flexion (rotation about the transversal axis), and abduction-adduction (rotation about the coronal axis). Only a single DoF of flexion-extension (rotation about the transversal axis) was modeled between each digit in the forepaws.

In total, the mouse model consists of 225 rotational joints. [Table 2.1](#) lists the joints in the model.

### Joint range-of-motion and limits

Joint range-of-motion defines the extent to which a joint can rotate between a minimal and a maximal angle. It is an important attribute for articulated rigid body simulations. For animals, joint ranges are imposed due to a combination of factors such as ligaments, muscles, and elastic forces of tissues. From previous experimental measurements on mice and rats (osteological ranges), we have compiled and reported the joint limits for the DoFs of the model in [Table 2.1](#). In this work, we modeled joint limits to mimic elastic ligaments that engage beyond the specified joint range by applying a resisting torque (modeled as a torsional spring and damper system as described in Opensim *v4.2* (Seth, Jennifer L. Hicks, et al., 2018b)).

### Zero-pose

Zero-pose defines the reference coordinate system. In the model, the zero-pose was defined as the pose at which all the joint angles are set to zero with respect to the corresponding coordinate frame. A non-anatomical pose in which some joints go beyond natural joint limits is chosen as the zero-pose to facilitate the coordinate frame transformations. Joint angles are measured with respect to the zero-pose. The model in the zero-pose is shown in [Figure 2.4A](#) and a possible rest-pose is shown in [Figure 2.4B](#).

### Estimating inertial properties

Inertial parameters are among the most important parameters for an accurate articulated rigid-body physics simulation. These parameters include the mass, the center-of-mass, and the inertia tensor for every bone (and surrounding soft tissues). To compute the inertial parameters, we assumed an uniform density of water ( $1000 \text{ kg/m}^3$ ) along the body (Bishop et al., 2020; Hutchinson, Ng-Thow-Hing, et al., 2007; Macaulay et al., 2017; Allen et al., 2009; Bates et al., 2009). The volume around the bones was estimated based on the convex hulls that represent the net volume encapsulated by the skin, soft-tissues, muscles,

Group	Bones	Joint	Degree-of-freedom (DoF)	Range-of-motion (degree)	Model
Hindlimb (left/right)	Femur	Hip	extension-flexion	[-30.0, 50.0]	Mouse <sup>1</sup>
			abduction-adduction	[-40.0, 20.0]	Rat <sup>2</sup>
			external-internal rotation	[-10.0, 30.0]	Rat <sup>2</sup>
	Tibia	Knee	flexion-extension	[-145.0, -40.0]	Mouse <sup>1</sup>
	Tarsus	Ankle	plantarflexion-dorsiflexion	[-50.0, -50.0]	Mouse <sup>1</sup>
			inversion-eversion	[-30.0, 50.0]	Rat <sup>2</sup>
			abduction-adduction	[-10.0, 30.0]	Rat <sup>2</sup>
	MetaTarsus{1-5}	MTP{1-5}	extension-flexion	[-5.0, -5.0]	-
	Phalange{1-5}	Phalange{1-5}	extension-flexion	[-5.0, 5.0]	-
	Forelimb (left/right)	Shoulder	retraction-protraction	[-45.0, 45.0]	-
			abduction-adduction	[-36.0, 3.0]	Rat <sup>3</sup>
			external-internal rotation	[-40.0, 14.0]	Rat <sup>3</sup>
	Ulna	Elbow	extension-flexion	[60.0, 153.0]	Rat <sup>3</sup>
	Radius	Elbow	supination-pronation	[-5.0, 30.0]	Rat <sup>3</sup>
	Carpus	Wrist	extension-flexion	[-20.0, 50.0]	Rat <sup>3</sup>
			abduction-adduction	[-10.0, 10.0]	
			extension-flexion	[-5.0, 5.0]	
	MetaCarpus{1-5}	MTC{1-5}	extension-flexion	[-5.0, 5.0]	
	Phalange	Phalange{1-5}	extension-flexion	[-5.0, 5.0]	
Pelvis	Pelvis	Pelvis	-	-	-
Spine	Lumbar{1-6}	Lumbar{1-6}	flexion-extension	[-6.0, 6.0]	Mouse <sup>4</sup>
			lateral bending	[-5.0, 5.0]	
	Thoracic{1-6}	Thoracic{1-6}	flexion-extension	[-5.0, 5.0]	Mouse <sup>4</sup>
			lateral bending	[-5.0, 5.0]	
	Cervical{1-6}	Cervical{1-6}	flexion-extension	[-9.0, 9.0]	Mouse <sup>5</sup>
Head	Upper jaw	Head	flexion-extension	[-50.0, 50.0]	-
	Lower jaw	Jaw	flexion-extension	[0.0, 30.0]	-
Tail	Tail{1-23}	Tail{1-23}	flexion-extension	[-10.0, 10.0]	-
			lateral bending	[-10.0, 10.0]	-

Table 2.1: **Mouse skeletal segments grouping, joint names and joint ranges**

The skeletal segments are grouped into six sparse groups to fully describe the model. Bones named  $\{1-n\}$  indicate  $n$  bones of the same name suffixed by its appropriate numeric position. A joint is formed between a parent and child (i.e., the bone that undergoes a transformation when the joint is rotated) bone. The table describes only the child bone for each joint. Degree-of-freedom (DoF) indicate the independent DoFs the joint has in the model. Joint range-of-motion for each DoF have been identified from several existing studies (see column ‘Model’). For joints where the information is not available for mice, we have resorted to works that are based on rats instead.

<sup>1</sup>(Charles, Cappellari, Spence, Wells, et al., 2016), <sup>2</sup>(Johnson et al., 2008), <sup>3</sup>(Bonnan et al., 2016), <sup>4</sup>(Dewan et al., 2010), <sup>5</sup>(Shahrokni et al., 2012)

and the bone(Sellers et al., 2012; Coatham et al., 2021). Masses were computed based on the density and volumes of the convex hulls. The center-of-mass and inertia tensors were computed based on the shape of the convex hulls and estimated mass assuming uniform density. The mouse model is 16.90 cm long from the head to the tip of the tail in the zero-pose and weighs 34.32 g.

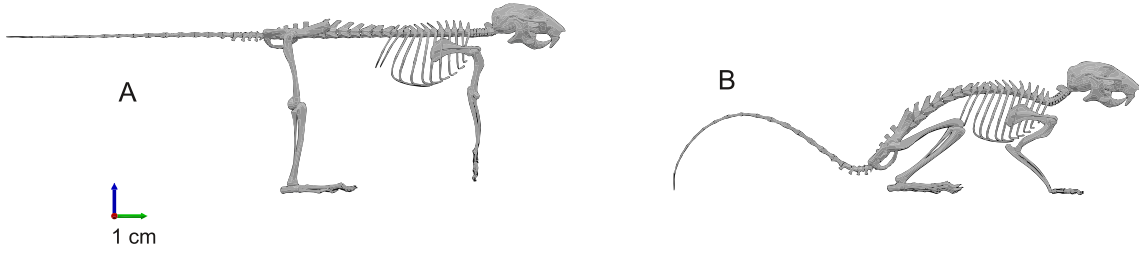


Figure 2.4: Representation of skeletal model poses. (A) The skeletal model of the mouse in zero-pose, i.e., when all the joint angles are set to zero. The zero-pose need not necessarily fall into the range-of-motion for a given joint. For example, the knee joint is defined to operate between -145.0 and -45.0 with respect to the zero position. (B) An example of the mouse in a sitting posture that is defined relative to the zero-pose.

### 2.3.3 Muscle System

Muscles were modeled using the Hill-type formalism (F. Zajac, 1989). Modeling each muscle required identification of attachment points in the hind and forelimbs and the estimation of their parameters.

#### Hill-type muscle model

Hill-type models make use of passive elements such as springs and dampers and experimental data to represent the active and passive dynamics of a muscle (F. Zajac, 1989). The contractile element (CE) and the parallel elastic element (PE) represent the muscle fibers; the series elastic element (SE) represents the total series elasticity of the muscle-tendon complex. It is important to keep in mind that due to this definition even muscles with short or no tendon still have non-zero tendon lengths in the parameterization of the Hill-type muscle model. Figure 2.5 shows the formulation of the muscle model used in this work. To simplify the dynamics of the muscle model, we assumed rigid tendons (Millard et al., 2013).

The Hill-type muscle model illustrated in Figure 2.5 was characterized by the following parameters: the optimal fiber length ( $l_m^o$ ; the length of muscle-fiber at which the muscle produces maximal active force), the tendon slack length ( $l_t^s$ ; the length of the tendon below which the muscle transfers no force to the attached bones), the maximum muscle-fiber velocity ( $v_m^{max}$ ), the pennation angle when the fiber length is at its optimal ( $\alpha_o$ ), and the maximum isometric force ( $F_m^0$ ). The formal description of the Hill-type muscle model used (Millard et al., 2013) is described in Appendix section A.1.

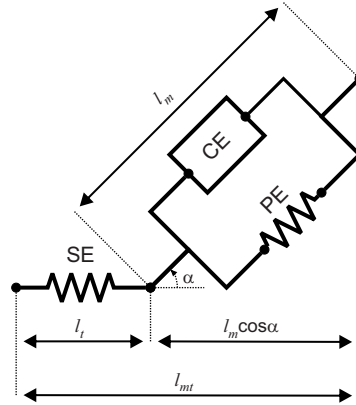


Figure 2.5: Hill-type muscle model describing the force generation by the muscles. The contractile element (CE) or the active element produces active contraction forces. The parallel element (PE) prevents the muscle from over stretching the muscle-tendon unit during normal operation. The series element (SE) represents the series elasticity of the muscle, including the muscle-tendon. Contractile element length or fiber-length ( $l_m$ ) is the length of muscles fibers. Pennate muscles are defined by the pennation angle  $\alpha_o$ . Series tendon-length ( $l_t$ ) is the length of series element. The total length of the muscle ( $l_{mt}$ ) is defined as  $l_{mt} = l_m \cos(\alpha) + l_t$

### Muscle attachment points

Muscles are attached to the bones via tendons. The attachment at the most proximal bone is called the origin (that bone tends to move less during muscle contraction) and the one at the most distal bone is called the insertion (that bone tends to move most during muscle contraction). The complex muscle paths were approximated as a polyline, a sequence of straight lines starting at the origin and ending with the insertion and are connected by *waypoints* in between (Figure 2.6). The polyline approximation is a common approach to describe the muscle paths (S. Lee et al., 2019; Seth, Jennifer L. Hicks, et al., 2018b; S. Delp et al., 1990; F. Young et al., 2019). (Refer to Figure 2.6 for an example showing the polyline muscle path description around the knee joint). The identification of the muscle attachment points and waypoints for hind and forelimbs used in this study is described below.

**Hindlimb attachment points** The attachment points for mouse hindlimb muscles have been previously identified by Charles et al. (Charles, Cappellari, Spence, Hutchinson, et al., 2016; Charles, Cappellari, Spence, Wells, et al., 2016). However, because of the differences in the bone geometry between our model and Charles, Cappellari, Spence, Wells, et al. (2016) model, it was necessary to transfer the muscle attachment points from Charles model to the bone surfaces of our mouse model. To automate the transfer process and limit the errors, we first performed mesh registration over the two bones from both

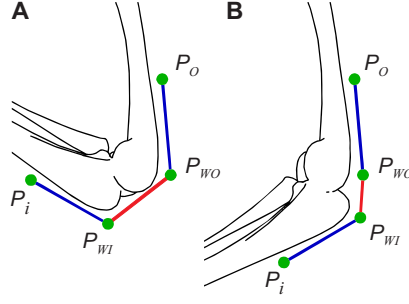


Figure 2.6: Polyline approximation of muscle paths. (A) and (B) show an example of an extensor muscle around the knee joint. Coordinates  $P_O$ (origin) through  $P_I$ (insertion) define the polyline muscle path. Coordinates  $P_O$  through  $P_{WO}$ (waypoint) are attached to the femur and coordinates  $P_{WI}$ (waypoint) through  $P_I$  are attached to the tibia. Thus,  $P_{WO} - P_{WI}$  is the only segment of the polyline that changes the muscle length when the joint is flexed or extended

models (mesh registration involves identifying appropriate landmarks between each bone segment of the hindlimb of our model and theirs.) Based on the chosen landmarks, a coordinate transformation matrix was computed to describe an affine transformation from the bone mesh in Charles model to our model. The affine transformation obtained from the mesh registration was then used to transfer the attachment points and waypoints between the models. The above-described process was carried out using the open-source mesh software CloudCompare ([CloudCompare - Open Source Project n.d.](#)). Identification of the landmarks on each bone from the two models was done manually. This process was carried out for the pelvis, femur, tibia, and pedal (tarsus, metatarsus, phalange) bones of the mouse hindlimb (Figure 2.7A).

**Forelimb attachment points** Modeling the forelimb muscles was challenging because of the lack of prior studies identifying attachment points of forelimb muscles. DeLaurier et al. (2008) has previously developed a 3D forelimb atlas of the mouse embryo at embryonic day 14.5 using Optical Projection Tomography and digital segmentation. Although the model was based on data from a mouse embryo, it still provides useful information on muscle attachments to the bones. This data allowed us to identify attachment points and necessary waypoints for 17 forelimb muscles (Figure 2.7B). To the best of our knowledge there is no published work that characterizes either the muscle properties or muscle attachments for forelimb muscles attaching to the scapula or the spine; neither for mice nor rats. Hence, these muscles were considered beyond the scope of this work.

### Estimation of muscle properties

As described above, the Hill-type muscle model is characterized by four parameters. Of these, the fiber velocity  $v_m^{max}$  is dependent on the fiber length and can be expressed as a

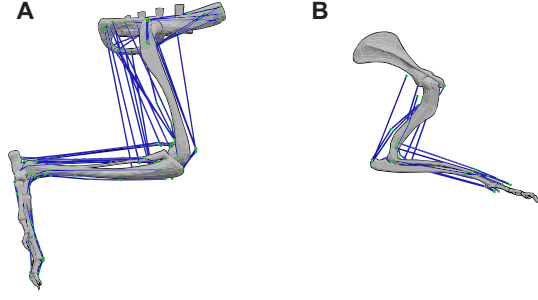


Figure 2.7: Lateral view of the musculoskeletal system of the mouse's (A) right hindlimb showing the attachment of 42 muscle-tendon units and (B) right forelimb showing the attachment of 17 muscle-tendon units. For all computations in this paper, the pose of the limbs shown in (A) and (B) are used unless mentioned otherwise

function of optimal fiber length  $l_m^o$ . As in Charles, Cappellari, and Hutchinson (2018), we set  $v_m^{max}$  to  $10 l_m^o/s$ . Thus,  $l_m^o$ ,  $l_t^s$ ,  $\alpha_o$  and  $F_m^0$  had to be identified for each muscle in the model.

**Hindlimb muscle properties** Transferring the attachment points from Charles model to our model meant that the muscle parameters had to be scaled accordingly. Maximum isometric force ( $F_m^0$ ) and pennation angle ( $\alpha_o$ ) were retained to be the same as in Charles model and only the length dependent parameters [optimal fiber length ( $l_m^o$ ) and tendon slack length ( $l_t^s$ )] were scaled. Since the length of the muscle varies over the DoFs it spans, we computed a scaling factor that is satisfied at all feasible joint poses. To achieve this, we employed a numerical optimization algorithm based on the one proposed by Modenese et al. (2016) to compute the scaling factors for each muscle. Refer to the Appendix section A.2 for further details.

**Forelimb muscle properties** Parameters  $l_m^o$  and  $F_m^0$  were extracted from measurements made by Mathewson et al. (2012) and used as preliminary approximations.  $l_m^o$  was scaled in proportion to the muscle-tendon lengths (i.e., the ratio of muscle-tendon length measured by Mathewson et al. (2012) to the muscle-tendon length in our model for each forelimb muscle was used as the scaling factor for  $l_m^o$ ). The scaling procedure used for hindlimb muscle parameters could not be employed here because there was no previous biomechanical model of the mouse forelimb.  $F_m^0$  was computed by multiplying the physiological cross-sectional area (PCSA) of the muscle by isometric stress ( $\sigma$ ) taken to be  $0.3 \text{ N/mm}^2$ , the same used in Charles, Cappellari, Spence, Wells, et al. (2016) for the hindlimb muscles.

The remaining muscle property,  $l_t^s$ , was estimated using an adaptation of the numerical optimization technique formulated by Manal and Buchanan (2004). We removed the restriction that muscle fibers only operate in the ascending region of the force-length



curve. We extended the algorithm to consider all the DoFs a muscle operates on while optimizing for  $l_t^s$ . Refer to the Appendix [section A.3](#) for further details.

### Computation of muscle-tendon length and moment-arm

Muscle-tendon length ( $l_{mt}$ ) is the distance from the origin of the muscle on the proximal bone to the insertion point on the distal bone. Based on the polyline approximation for describing the muscle paths ([Figure 2.6](#)),

$$l_{mt} = \sum_{n=0}^{N-1} \|P_{n+1} - P_n\| \quad (2.1)$$

where  $P_n$  are the muscle attachment points on the polyline with  $P_0$  being the origin,  $P_N$  the insertion point and waypoints in between  $P_i : i = 1 \dots (N - 1)$ .

Muscle moment-arms ( $r$ ) were computed using the perturbation method described in Sherman et al. (Sherman et al., [2013](#)),

$$r = \partial l_{mt} / \partial \theta \quad (2.2)$$

where  $\theta$  is generalized coordinate representing the DoF of interest across which the muscle moment-arm is to be computed.

#### 2.3.4 Analysis of sensitivity of joint moment-arms and moments to changes in muscle parameters and attachment points

Like any model, the mouse biomechanical model was developed based on several assumptions and simplifications. To highlight and study the influence of various characteristics of the biomechanical model on the overall motor behavior, we analyzed the sensitivity of joint moment-arms and moments to changes in muscle attachment points and model parameters.

For both analyses, we used the Sobol method (Sobol', [2001](#)), a variance-based global sensitivity method. The Sobol method decomposes the proportion of model output variance caused by each individual parameter (Qian and Mahdi, [2020](#)). This method also allows for the study of the inter-parameter effect on the model's output variance, but we restricted our analysis to first-order indices (main effects). First-order indices "measure the direct contribution of each input factor to the output variance" (Qian and Mahdi, [2020](#)). A value of 1.0 for the first-order indices indicates that the parameter is solely

responsible for all the variance in the models' output, whereas a value of 0.0 represents no influence on the models' output variance. We used the root-mean-square (RMS) value of the joint moment-arm or moment over the DoFs range-of-motion to represent the scalar value necessary to evaluate the sensitivities. The Sobol sensitivity analysis was performed using SALib v1.4 (Herman and Usher, 2017), an open source python library for the sensitivity analysis.

The polyline approximation of the muscle paths determines the computation of muscle-tendon length ( $l_{mt}$ ) and thereby the moment-arm (2.2). For the polyline approximation, change in  $l_{mt}$  can be reduced to just two attachment points of the segment that cross the DoF of interest (refer to Figure 2.6 showing an example). Therefore, for the analysis of sensitivities to muscle attachments, we referred to the proximal attachment point of the segment as  $P_{WO}$  and to the distal one as  $P_{WI}$ . The sensitivities to these attachment points were computed by varying their 3D position within a range of  $\pm 0.5$  mm in x, y, and z directions. With  $P_{WO}$  and  $P_{WI}$  we had six parameters (x, y, and z coordinates for each point) to study the sensitivity of the joint moment-arm. We limited our analysis to study how the 3D location of the two attachment points influence the joint moment-arms. As the total sum of the first-order indices is equal to 1.0, we reported the sum of the first-order indices along the individual 3D coordinates (x-y-z) for each attachment point. These values represent a direction-independent measure of moment or moment-arm sensitivity to the attachment points. Data on the individual sensitivities are available in the supplementary material.

Muscle force production depends not only on the geometric relationship defined by the muscle-path but also on the muscle dynamics. The Hill muscle dynamics are parameterized by four main parameters (as described in section 2.3.3).  $F_m^0$  linearly affects the overall force produced by the muscle.  $l_m^o$ ,  $l_t^s$  and  $\alpha_o$  determine the active and passive forces produced by the muscle and consequently affect the joint moments. Sensitivity of the joint moments to the changes in muscle parameters were analyzed within a range defined by  $\pm 10\%$  of their original parameter values.

## 2.4 Results

The parameters of all muscles in the model are specified in [Table 2.2](#). Because of the differences in the available experimental data, muscle parameters for the hindlimb and forelimb muscles were obtained using different approaches. For hindlimb muscles, the maximum isometric force ( $F_m^0$ ) and pennation angle ( $\alpha_o$ ) were directly taken from Charles, Cappellari, Spence, Wells, et al. (2016) while tendon slack length ( $l_t^s$ ) and optimal fiber length ( $l_m^o$ ) were scaled using the method described in Modenese et al. (2016) to account for the differences in model dimensions. For forelimb muscles,  $F_m^0$  and  $l_m^o$  were scaled from Mathewson et al. (2012) while keeping  $\alpha_o$  the same.  $l_t^s$  was optimized using a modified version of the algorithm originally described by Manal and Buchanan (2004) (see [Figure 2.3.3](#) for details). [Table 2.2](#), we reported the ratios between  $l_m^o$  and  $l_t^s$  for each muscle. The ratio shows the relationship between muscle-fiber length and tendon lengths. However, the definition of a tendon in the Hill-type muscle models include not only the external tendon but also the internal part of the tendon (i.e., the aponeurosis of the muscle) (F. Zajac, 1989). Thus, the ratios indicated necessarily imply muscles with shorter/longer external tendon physiologically and the has been shown to be true by in Charles, Cappellari, Spence, Wells, et al. (2016) by comparing the external tendon lengths of a few hindlimb muscles in the animal with the estimated  $l_t^s$  values.

Muscle-tendon Unit	Abbreviation	$F_m^{0(a)}$ (N)	$l_m^{o(b)}$ (mm)	$l_t^{s(c)}$ (mm)	$\alpha^{o(d)}$ (deg)	$\frac{l_t^s}{l_m^o}^{(e)}$	Group <sup>(f)</sup>
HINDLIMB							
Adductor brevis	AB	0.23	9.5	2.66	0.0	0.28	Hip
Adductor longus	AL	0.4	11.9	4.15	0.0	0.35	
Adductor magnus	AM	0.61	12.2	4.85	0.0	0.4	
Biceps femoris anterior	BFA	0.88	17.84	5.97	0.0	0.33	
Caudofemoralis	CF	0.55	17.85	4.82	0.0	0.27	
Gemellus	GEM	0.18	3.33	0.02	0.0	0.01	
Gluteus maximus(dorsal)	GM(dr)	0.94	14.99	5.75	20.42	0.38	
Gluteus maximus(mid)	GM(mi)	1.03	14.28	5.5	20.42	0.38	
Gluteus maximus(ventral)	GM(ve)	1.05	14.59	5.61	20.42	0.38	
Iliacus	ILI	0.55	9.67	3.1	0.0	0.32	
Obturator externus	OE	0.09	4.37	1.71	0.0	0.39	
Obturator internus	OI	0.31	6.3	0.72	0.0	0.12	
Pectineus	PECT	0.36	4.27	2.79	15.18	0.65	
Psoas major	PMA	1.34	8.01	5.76	15.54	0.72	
Psoas minor	PMI	1.09	6.79	4.58	12.57	0.67	
Quadratus femoris	QF	2.03	4.99	1.18	0.0	0.24	
Biceps femoris posterior(cranial)	BFP(cr)	0.72	16.46	8.02	0.0	0.49	Hip-Knee
Biceps femoris posterior(mid)	BFP(mi)	0.73	16.9	8.08	0.0	0.48	
Biceps femoris posterior(caudal)	BFP(ca)	0.61	19.81	6.72	0.0	0.34	
Gracilis anterior	GA	0.4	14.76	10.16	0.0	0.69	
Gracilis posterior	GP	0.34	15.92	7.68	0.0	0.48	
Rectus femoris	RF	4.16	9.87	15.77	15.89	1.6	
Semimembranosus	SM	1.92	20.14	7.07	0.0	0.35	
Semitendinosus	ST	1.3	19.1	8.25	0.0	0.43	
Popliteus	POP	0.31	3.3	3.26	0.0	0.99	Knee
Vastus intermedius	VI	0.37	10.08	11.68	10.92	1.16	
Vastus lateralis	VL	2.83	11.18	12.07	15.53	1.08	
Vastus medialis	VM	1.1	10.77	12.67	16.15	1.18	
Lateral gastrocnemius	LG	3.78	6.97	17.89	17.28	2.57	Ankle-Knee
Medial gastrocnemius	MG	1.75	7.29	18.5	14.24	2.54	
Plantaris	PLANT	0.88	5.75	20.23	17.1	3.52	
Extensor digitorum longus	EDL	0.37	8.12	30.42	12.39	3.74	Ankle
Extensor haliucis longus	EHL	0.07	7.71	23.32	9.56	3.02	
Flexor digitorum longus	FDL	1.9	5.71	36.6	15.2	6.41	
Peroneus brevis	PB	0.4	3.04	13.33	11.46	4.39	
Peroneus digiti quarti	PDQA	0.11	5.05	30.31	12.42	6.0	
Peroneus digiti quinti	PDQI	0.1	4.72	25.53	9.44	5.41	
Peroneus longus	PL	0.65	5.21	19.4	14.9	3.72	
Peroneus tertius	PT	0.46	4.78	15.81	12.46	3.31	
Soleus	SOL	0.59	4.5	10.53	11.43	2.34	
Tibialis anterior	TA	2.42	6.61	15.92	16.58	2.41	
Tibialis posterior	TP	0.55	4.72	19.71	15.44	4.18	

Continued on next page

Muscle-tendon Unit	Abbreviation	$F_m^{0(a)}$ (N)	$l_m^{o(b)}$ (mm)	$l_t^{s(c)}$ (mm)	$\alpha^{o(d)}$ (deg)	$\frac{l_t^s}{l_m^o}^{(e)}$	Group <sup>(f)</sup>
FORELIMB							
Coracobrachialis	COR	0.28	5.18	4.64	13.85	0.9	Shoulder
Biceps Brachii Long Head	BBL	0.78	11.63	7.52	21.68	0.65	Elbow-Shoulder
Triceps brachii lateral head	TBL	0.71	8.17	4.53	23.41	0.55	
Anconeus	AN	0.15	1.42	1.49	24.65	1.05	Elbow
Biceps brachii short head	BBS	0.84	9.08	6.07	28.27	0.67	
Brachialis	BRA	0.25	10.06	5.58	9.89	0.56	
Pronator teres	PTE	0.55	2.75	4.96	26.17	1.81	
Triceps brachii medial head	TBM	0.45	4.93	6.43	30.33	1.3	
Triceps brachii long head*	TBO	4.65	7.01	4.88	41.88	0.7	
Extensor carpi radialis brevis	ECRB	0.35	14.45	7.71	29.49	0.53	Elbow-Wrist
Extensor carpi radialis longus	ECRL	0.38	13.86	7.29	26.4	0.53	
Extensor carpi ulnaris	ECU	0.52	7.67	10.84	20.8	1.41	
Extensor indicis proprius 1	EIP1	0.07	5.05	2.99	19.0	0.59	
Extensor indicis proprius 2	EIP2	0.07	5.27	3.3	19.0	0.63	
Flexor carpi radialis	FCR	0.38	8.92	10.74	15.02	1.2	
Flexor carpi ulnaris	FCU	0.69	8.28	10.29	20.95	1.24	
Palmaris longus	PLO	0.27	10.9	9.12	24.65	0.84	

Table 2.2: **Hindlimb and forelimb muscle parameters**

<sup>(a)</sup> Maximum isometric force of the muscle. Hindlimb muscle forces are the same as reported in Charles, Cappellari, Spence, Wells, et al. (2016). Forelimb muscle forces are computed by multiplying the physiological cross-sectional area (PCSA) reported in Mathewson et al. (2012) by isometric stress ( $\sigma = 0.3 \text{ N/mm}^2$ ) (Charles, Cappellari, Spence, Wells, et al., 2016; Hutchinson, 2004).

<sup>(b)</sup> Optimal fiber length for hindlimb scaled to the current model from Charles, Cappellari, Spence, Wells, et al. (2016) using the scaling based on Modenese et al. (2016) and forelimb scaled to the current model (Mathewson et al., 2012).

<sup>(c)</sup> Tendon slack length is obtained in the same way as described for the optimal fiber length.

<sup>(d)</sup> Pennation angle for hindlimb is obtained from Charles, Cappellari, Spence, Wells, et al. (2016) and for forelimb from Mathewson et al. (2012).

<sup>(e)</sup> Ratio of optimal fiber length and tendon slack length.

<sup>(f)</sup> Sorting of muscles into groups based on the joints they span. For example, Biceps femoris posterior (BFP) belongs to Hip-Knee group as it spans over one or more hip and knee joints. The same order is used in the rest of this work.

### 2.4.1 Moment-arm analysis for the hindlimb muscles

Because of the differences in bone geometries, we transferred the muscle attachment points from the hindlimb model developed by Charles, Cappellari, Spence, Hutchinson, et al. (2016) and Charles, Cappellari, Spence, Wells, et al. (2016) to our model. The mesh registration technique described in Figure 2.3.3 was used to transfer the attachment points.

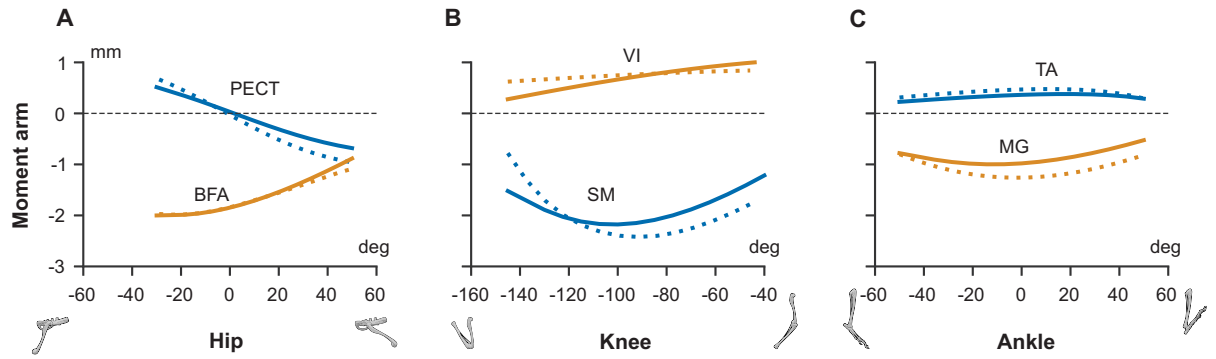


Figure 2.8: Comparison of moment-arms from (Charles, Cappellari, Spence, Wells, et al., 2016) (dotted lines) and current model (solid lines) for muscles (A) *pectineus* (PECT) and *biceps femoris anterior* (BFA) over hip flexion-extension range-of-motion (RoM) (B) *semimembranosus* (SM) and *vastus intermedius* (VI) over knee flexion-extension RoM (C) *medial gastrocnemius* (MG) and *tibialis anterior* (TA) over ankle flexion-extension RoM. The moment-arms are normalized by the respective thigh length ( $\text{thigh}_{\text{charles}} = 16.25$  mm and  $\text{thigh}_{\text{current}} = 24.5$  mm).

The attachment points of the muscle have a direct influence on the muscle moment-arms (Figure 2.6) and consequently on the moments on the joints they influence. To compensate for the lack of wrapping surfaces, additional waypoints were introduced along the muscle path when necessary. To validate the muscle attachment process, moment-arms of two flexor muscles of the hip, knee, and ankle joints from Charles model were compared with the moment-arms in our model (Figure 2.8). For this comparison, moment-arms were normalized to their respective thigh (femur) lengths, since the two models are of mice of different age and size. The moment-arms from the two models are in good quantitative and qualitative agreement throughout the range-of-motion for the three hindlimb joints.

#### 2.4.2 Description of muscle function based on moment-arms and moments

Figure 2.9 presents a comprehensive overview of each muscle’s influence over every DoF it spans. We present the functional grouping of the muscles based on the moment-arm and moment. Each DoF was sub-divided into two functions, representing the possible directions in which the muscle can influence the DoF. Thus, for every DoF it spans over, a muscle has the possibility to apply a moment either on one of the DoF functions’ or both (zero-crossing). Moment-arms were computed in the default pose shown in Figure 2.7; moments were computed assuming maximal muscle activation ( $a(t) = 1.0$ )

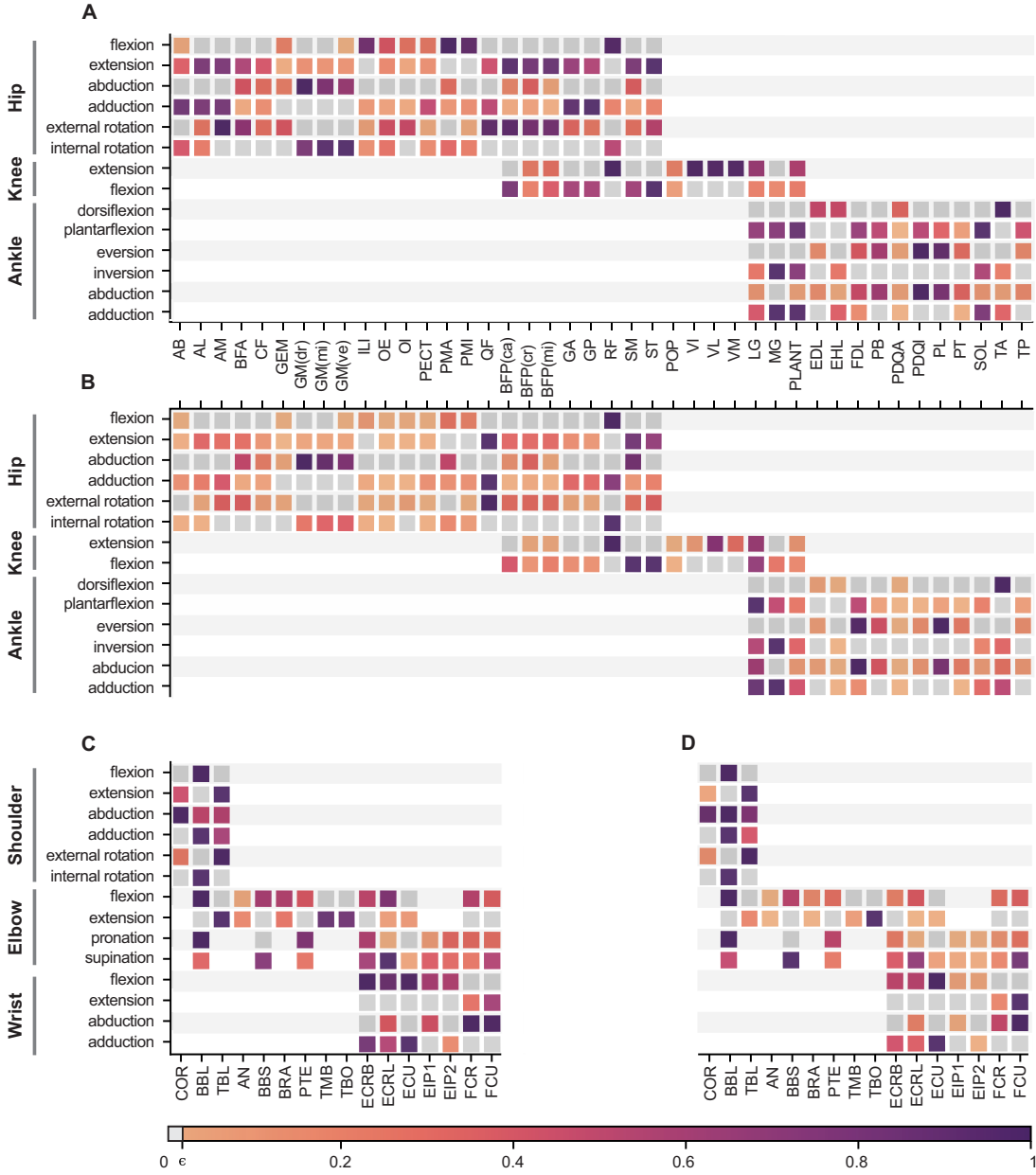


Figure 2.9: Maximum moment arms (A, C) and moments (B, D) for each muscle and joint function. Grey boxes indicate joint functions for joints the muscle spans but has zero influence over. For example, a pure hip flexor muscle is considered to be spanning over both hip flexion and extension joints, but the corresponding hip extension will be in grey to indicate that the muscle has no influence on hip extension. The moment-arms and moments are normalized by the muscle which has the maximum influence in the group.  $\epsilon$  indicates a very low non-zero positive value

### Hindlimb muscles

Figure 2.9A,B shows the functional grouping of hindlimb muscles based on the moment-arm and moment, respectively. For hip flexion, *iliacus*, *psaos major*, *psaos minor*, and

*rectus femoris* have the maximal moment-arms. However, since *rectus femoris* has the largest maximum isometric force, it exhibits the highest moment towards hip flexion. For hip extension, *adductor longus*, *adductor brevis*, *quadratus femoris*, *biceps femoris posterior*, *semimembranosus*, and *semitendinosus* have the dominant moment-arms. However, grouping them by moment reveals that *quadratus femoris*, *semimembranosus*, and *semitendinosus* are the dominant muscles. This classification also highlights that all hip flexors except *psoas major*, *psoas minor*, *iliacus*, and *rectus femoris* have zero-crossings (Figure 2.9A). While *gluteus maximus* muscle has the highest moment-arm to abduct the hip, *semimembranosus* along with *gluteus maximus* also strongly contributes to hip abduction moments as their maximum force is larger. For hip adduction, *adductor brevis*, *adductor longus*, *adductor magnus*, *gracilis anterior*, and *gracilis posterior* are the dominant adductors when we consider the moment-arms. Considering moments, *quadratus femoris* and *rectus femoris* dominate over other muscles because of their large  $F_m^0$ . For hip external rotators *quadratus femoris* has the most significant moment-arm and moment in the group. Also, *gluteus maximus* has the largest moment and moment-arm among the hip internal rotators.

For knee flexion, *semitendinosus*, *biceps femoris posterior*, *gracilis anterior*, *gracilis posterior*, and *semimembranosus* have the strongest moment-arms, but *semimembranosus* and *semitendinosus* show the largest moments followed by *lateral gastrocnemius*. For knee extension, *rectus femoris*, *vastus intermedius*, *vastus lateralis*, and *vastus medialis* have the largest moment-arms, while *rectus femoris* exerted the largest moment, followed by *vastus lateralis* and *lateral gastrocnemius*.

Several muscles show strong moment-arms for ankle plantarflexion with *soleus* and *plantaris* having the largest moment-arms. Considering the moments, *lateral gastrocnemius* overshadows all the other ankle plantarflexors. For ankle dorsiflexion, *tibialis anterior* exhibits the strongest moment-arm and moment. Among ankle evertors, *peroneus digiti quarti* and *peroneus longus* show the largest moment-arm but *flexor digitorum longus* and *peroneus longus*, due to their large maximum isometric force, also significantly contribute to the moments. For ankle inversion, *medial gastrocnemius* has the highest moment-arm and moment among all the muscles in its group. *Peroneus digiti quarti*, *peroneus longus*, and *peroneus brevis* have large moment-arms for ankle abduction, while *lateral gastrocnemius*, *flexor digitorum longus*, and *peroneus longus* can exert large moments for ankle abduction. *Medial gastrocnemius*, *plantaris*, and *soleus* have significant moment-arms for ankle adduction group, and *lateral gastrocnemius* and *medial gastrocnemius* have the highest moments.

### Forelimb muscles

Figure 2.9C,D show the functional grouping of forelimb muscles based on the moment-arm and moment, respectively. Anatomically, the forelimb is more complex than the



hindlimb, the scapula is a floating link with all six DoFs and elbow joints have complex joint rotations. The kinematic complexities are reflected in the identification of muscle functions. Most shoulder joint muscles originate from the axial skeleton and scapula. Here, we have not included those muscles that originate from the spinal segment due to the lack of available experimental data; the model only includes a limited number of proximal muscles in the forelimb. Shoulder retraction is actuated by the long head of *biceps brachii* whereas shoulder protraction is actuated by *coracobrachialis* and the lateral head of *triceps brachii*. Both latter muscles have similar maximum moment-arms, but the maximal isometric force of the lateral head of *triceps brachii* is much larger compared to *coracobrachialis*, resulting in a larger moment. *Coracobrachialis*, the long head of *biceps brachii*, and the lateral head of *triceps brachii* contribute similarly to shoulder abduction both in terms of moment-arm and moments, while the long head of *biceps brachii* and the lateral head of *triceps brachii* contribute to shoulder adduction. This shows that shoulder adduction is possible in the model only due to the zero-crossing of the long head of *biceps brachii* and the lateral head of *triceps brachii*. For shoulder external rotation, *coracobrachialis* and the lateral head of *triceps brachii* act on the joint function with the lateral head of *triceps brachii* dominating the joint function both in moment-arm and torque magnitudes. The long head of *biceps brachii* alone acts on the shoulder-internal-rotation joint function, leaving us to draw no further inferences about this joint function.

Among the many forelimbs muscles that span over the elbow joint, the elbow-flexors, the long head of *biceps brachii* and *extensor carpi radialis longus* have the largest moment-arms followed by short head of *biceps brachii*, *brachialis*, *extensor carpi radialis brevis*, and *flexor carpi radialis*. When we consider the moments, long head of *biceps brachii* has the largest maximal moment followed by short head of *biceps brachii*. Other muscles that had a large moment-arm are weak and exert smaller moments. For elbow-extension, all the triceps muscles (*triceps brachii lateral*, *triceps brachii medial*, and *triceps brachii long head*) have relatively strong moment-arms, with the long head of *triceps brachii* exerting the largest maximal moment. In the current model, we did not include any elbow-pronator muscles. For elbow supination, *extensor carpi radialis longus* has the largest moment-arm, followed by short head of *biceps brachii*, *extensor carpi radialis brevis*, and *flexor carpi ulnaris*. The short head of *biceps brachii* becomes the most dominant muscle for elbow supination when we consider moments, followed by *extensor carpi radialis longus* and *flexor carpi ulnaris*.

All the wrist flexor muscles have similar maximum moment-arms across the joint function, with *extensor carpi radialis brevis*, *extensor carpi radialis longus*, and *extensor carpi ulnaris* having the most dominant moment-arms. For moments, *extensor carpi ulnaris* has the strongest moment followed by *extensor carpi radialis longus* and *extensor carpi radialis brevis*. Three muscles act on wrist-flexion, of which *peroneus longus* has the highest moment-arm followed by *flexor carpi ulnaris*; when we consider moments, however, the dominance is flipped. While *flexor carpi radialis*, *flexor carpi ulnaris*, and *peroneus longus*

have the strongest moment-arms for wrist abduction, the strongest moments are exerted by the *flexor carpi ulnaris*, followed by *flexor carpi radialis*. Among the three muscles that influence wrist adduction, *extensor carpi ulnaris* has the strongest moment-arm followed by *extensor carpi radialis brevis* and *extensor carpi radialis longus*. *Extensor carpi radialis longus* has a zero-crossing such that it influences both wrist abduction and adduction. For moments, *extensor carpi ulnaris* has the highest moment followed by *extensor carpi radialis brevis*.

### 2.4.3 Operational range of muscle-fiber length

The muscle-fiber length ( $l_m$ ) determines the working region of the muscle in the force-length (FL) curve (Figure 2.10B). More specifically, the fiber-length determines if the muscle produces force purely based on muscle contractions or a combination of muscle contraction and passive forces. The range of operation in the FL relationship is determined by the muscle attachment points and parameters. Operational range of a muscle-fiber was computed by moving the joints it influences through its complete range-of-motion. Then minimum and maximum values of the fiber length for considering all the joints will determine the operational range of the muscle fibers. The range is then normalized by the muscles corresponding optimal fiber length ( $l_m^o$ ). In Figure 2.10A we show the working ranges of normalized muscle-fiber lengths ( $\tilde{l}_m$ ) across all the DoFs each muscle spans. Muscles that span over a single joint tend to have shorter range of operation in the FL relationship. Most muscles in the mouse forelimb and hindlimb operate within the active ( $\tilde{l}_m \leq 1.0$ ) and passive force ( $\tilde{l}_m > 1.0$ ) regions of the FL curve. *Gluteus maximus* in the hindlimb is the only muscle that operates completely in the active region of the FL curve. Short head of *biceps brachii*, *brachialis*, *extensor carpi radialis*, and *extensor indicis proprius* muscles in the forelimb exhibit operation only in the active region. These muscles in the hindlimb and forelimb have no passive/elastic force contributions during movement. In the hindlimb, *extensor digitorum longus*, *extensor hallucis longus*, *peroneus digiti quarti*, and *peroneus tertius* are the muscles that operate only in the passive region of the FL curve. All the mentioned muscles span over the ankle joint. *Pronator quadratus* is the only muscle in the forelimb that operates only in the passive region of the FL curve. This is because the optimization of the parameters of forelimb muscles was performed under the constraint that every muscle must have some operation range in the active section of the FL curve. A muscle whose operational range is only in the passive region always produces an elastic force on the joints and the force increases exponentially as the muscle is stretched. Passive forces are useful as they consume no energy to produce movement but if the desired movement is against the passive force, then it requires additional energy to overcome it. Hence, there is an interesting optimum that could be reached to minimize energy consumption. All the other muscles in the hindlimb and forelimb operate across the active and passive regions depending on the pose/configuration of the joints.

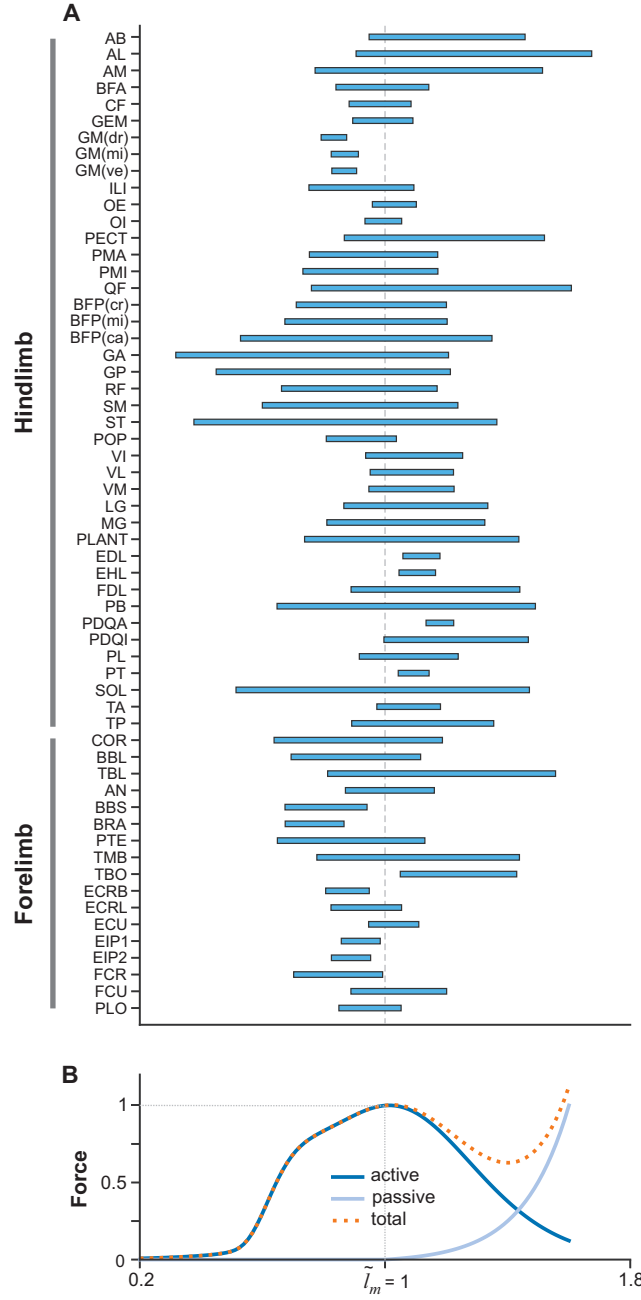


Figure 2.10: (A) Range of normalized muscle-fiber length (muscle-fiber length ( $l_m$ ) normalized by optimal fiber length ( $l_m^o$ );  $\tilde{l}_m = l_m/l_m^o$ ) for each muscle in the forelimb and the hindlimb. The range of  $\tilde{l}_m$  is computed considering the range-of-motion of all the degrees-of-freedom the muscle spans. (B) Hill-type muscle force-length relationship showing the normalized force produced by muscle contraction (active force), by series and parallel elastic forces, and the sum of both (total force) across the  $\tilde{l}_m$ . At  $\tilde{l}_m = 1.0$  the muscle produces maximum active force in the force length curve.

### 2.4.4 Sensitivity analysis

Muscle attachments and muscle parameters together determine the overall function and moments produced by the muscle. The high number of muscles and the DoFs each muscle influences makes it a challenging task to perform a comprehensive sensitivity analysis. Here, we use the Sobol method, a variance-based global sensitivity method to perform the analysis (see Section 2.3.4).

It is important to note that in Figure 2.11, results of two separate sensitivity analyses are displayed, one for the muscle attachments and one for the muscle parameters. Thus, sensitivity indices for the two cases should be interpreted independently.

#### Sensitivity of joint moment-arms to changes in muscle attachment points

The first observation we can make from the sensitivity analysis to variation in attachment points is that the majority of muscle joint moment-arms are highly sensitive to either  $P_{WO}$  (attachment to the parent bone of the joint) or  $P_{WI}$  (attachment to the child bone of the joint) and only very few to both. Figure 2.12(A-D) shows an example of the variation of moment-arms when the 3D positions of  $P_{WO}$  and  $P_{WI}$  are varied between  $\pm 0.5$  mm for gracilis anterior muscle across the 4 DoFs it spans over the hip and the knee joints. For hip flexion-extension and abduction-adduction, moment-arms of *gracilis anterior* are highly sensitive to  $P_{WO}$ . For hip internal and external rotation and knee flexion-extension DoF, the moment-arm of *gracilis anterior* is more sensitive to changes in  $P_{WI}$  than  $P_{WO}$ . The same observations are reflected in the comprehensive representation shown in Figure 2.11.

Referring to Figure 2.6, we can interpret the geometric reason for why a muscle-joint pair is sensitive to either  $P_{WO}$ ,  $P_{WI}$ , or sometimes both. When the attachment points are perturbed to perform the sensitivity analysis, points further away from the joint rotation centers will result in larger changes in muscle length within the range-of-motion of the joint. As we have seen from Equation 2.2, larger change in muscle-tendon length for the same change in DoF motion results in larger moment-arms. Thus, the proximity of the attachment point to the joint's center-of-rotation will influence its sensitivity. From the analysis (Figure 2.12), we can identify those attachment points that are most important and interesting to explore for a given muscle-DoF pair.

#### Sensitivity of joint moment to changes in muscle parameters

In addition to the muscle attachment points, the muscle parameters determine the dynamics of the muscle and the moments it generates on the joints. Estimation of muscle parameters is a challenging process that could potentially lead to modeling errors. This applies to our forelimb model, where the muscle parameters were estimated based on

several different data sources (See Section 2.3.3). The sensitivity analysis provides an overview of the parameters that have most influence on the moment generation for each muscle-joint pair. We performed this analysis for four muscle parameters [maximum isometric force ( $F_m^0$ ), optimal fiber length ( $l_m^o$ ), tendon slack length ( $l_t^s$ ), and pennation angle ( $\alpha_o$ )] within a range of  $\pm 10\%$  of their original values. The sensitivities of joint moments to changes in muscle parameters are reported in Figure 2.11. We do not show the results for  $\alpha_o$ , since no joint moment exhibited a significant sensitivity. plot with  $\alpha_o$ , refer to the correspondent figure in the supplementary material.

From the Hill-type muscle force (see Equation A.1 in the Appendix)  $F_m^0$  has a linear influence on the muscle force while  $l_m^o$  and  $l_t^s$  have complex, non-linear relationships.

Among the hindlimb muscles that span the hip joint,  $F_m^0$  is the parameter influencing the joint moments the most;  $l_m^o$  being the next parameter in a few muscles in this group. No muscle in this group exhibits sensitivity for the choice of  $l_t^s$  parameter. Next, sensitivity of moments caused by muscles that span hip and knee joints are equal due to the changes in  $F_m^0$ ,  $l_m^o$  and sometimes  $l_t^s$ . Muscles spanning only the knee joint exhibit sensitivity only for  $F_m^0$ . Moments of muscles that span knee and ankle or only ankle joint all have  $l_t^s$  as their most important parameter. Among the forelimb muscles, moments are most sensitive to the  $F_m^0$  parameter for almost all muscle-joint pairs. With just a few muscles for which moments are more sensitive to  $l_m^o$  or  $l_t^s$  parameters.

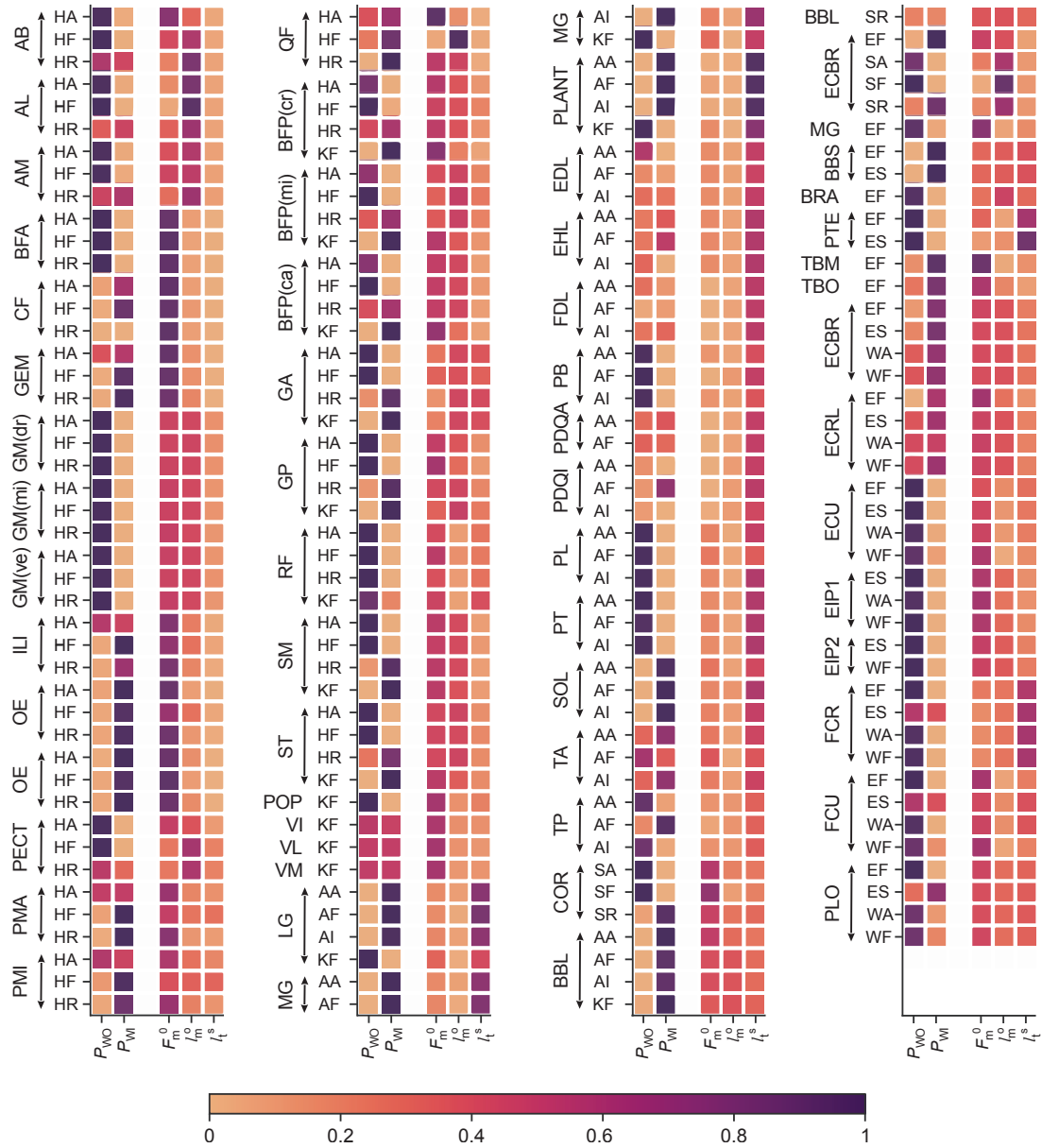


Figure 2.11: Sensitivity of joint moment-arms to changes in muscle attachment points and of joint moments to changes in muscle parameters. Analysis of muscle attachments and muscle parameters was done independently but is shown together in the figure. The colors indicate the first-order indices from the Sobol' analysis. A first-order index value of 0.0 indicates that the parameter under observation has no contribution to the output's (moment-arm/moment) variance and value of 1.0 indicates that the parameter is responsible for the total output's variance. Analyzed DoF pairs are: Hip abduction-adduction (HA), flexion-extension (HF), internal-external rotation (HR), Knee flexion-extension (KF), Ankle abduction-adduction (AA), flexion-extension (AF), inversion-eversion (AI). Shoulder abduction-adduction (SA), flexion-extension (SF), internal-external rotation (SR), Elbow flexion-extension (EF), pronation-supination (ES), Wrist abduction-adduction (WA), flexion-extension (WF)

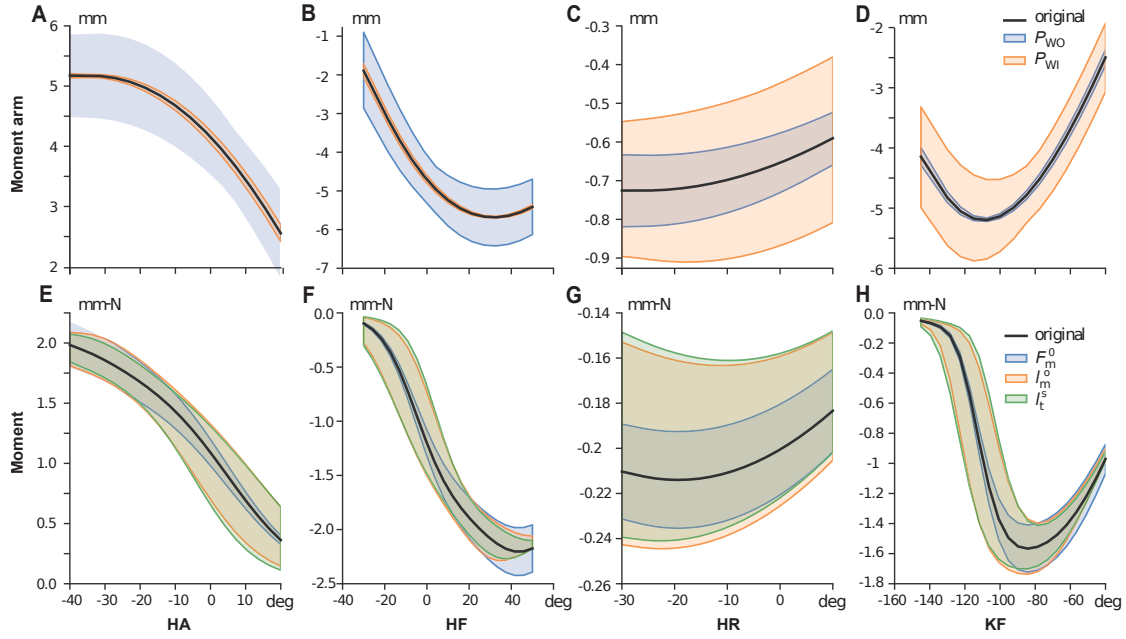


Figure 2.12: (A-D) Variation of *gracilis anterior* moment-arms for the variation of the 3D position of the attachment points  $P_{WO}$  (attachment point in the parent bone of the joint) and  $P_{WI}$  (attachment point in the child bone of the joint) within the range of  $\pm 0.5$  mm for hip flexion-extension (HF), hip abduction-adduction (HA), internal and external rotation (HR) and knee flexion-extension (KF). (E-H) Variation of Gracilis anterior moments for the variation of the muscle parameters (maximum isometric force ( $F_m^0$ ), muscle fiber length ( $l_m$ ), tendon slack length ( $l_t$ ) within the range of  $\pm 10\%$  of their default values for HF, HA, HR and KF.

## 2.5 Discussion

We presented a whole-body three dimensional (3D) musculoskeletal model of the mouse with a fully articulated skeletal system actuated by identified musculature for both hindlimbs and forelimbs. Using the model, we performed a systematic and comprehensive analysis of the limb musculature to study their influence on limb joints. We first studied how the muscles influence joint function based on the moment-arm and moments they exert. The analysis gives a comprehensive view to characterize muscle function. Our results reveal that many muscles that span multiple degrees-of-freedom (DoFs) tend to have zero-crossing (i.e., change their function over the DoFs range-of-motion). Examining the muscle-fiber length range showed how the limb muscles distribute their force production in terms of active and passive forces over the joints' complete range-of-motion. We then performed a sensitivity analysis to highlight the crucial parameters in the model and showed how different parameters affect on each muscle-DoF pair in the model. Although the model was based on a number of simplifications and assumptions, it is an important step in the direction of building complex biomechanical, and ultimately neuromechanical models to study motor behaviors and their underlying neuronal control.

### 2.5.1 Muscle system development

Identification and characterization of the muscles operating in complex musculoskeletal systems is a challenging task. It involves a laborious process of extracting individual muscles from the animal, carefully identifying the attachment landmarks such as origin and insertion locations of each muscle and identification of major muscle parameters.

These steps were traditionally performed directly on cadavers (Johnson et al., 2008); later studies, used microCT scans along with digital segmentation, which lead to more detailed identification about muscle geometry and attachments, especially for deep muscles (Charles, Cappellari, Spence, Hutchinson, et al., 2016). In this work, we developed the muscle system of both hindlimb and forelimbs by incorporating data from several studies on the mouse.

#### Transferring hindlimb muscle attachment points from Charles model

Development of the hindlimb musculature was largely based on the OpenSim single mouse hindlimb model of Charles, Cappellari, Spence, Hutchinson, et al. (2016) and Charles, Cappellari, Spence, Wells, et al. (2016). Since, this model was only of a single hindlimb, we had to transfer the muscle system to our full mouse model which had a different bone geometry. The first step in this process was to identify the appropriate landmarks of origin and insertion points of each muscle on the new model. To accomplish this task, we setup an automatic process to identify a coordinate transformation between the bones of two models using mesh-registration technique. With this, every attachment



point of a muscle defined in a particular coordinate of a bone was transferred to the coordinate frame of the same bone in the current model. The model in Opensim had incorporated muscle wrapping surfaces to better describe the muscle paths. However, in our current framework, muscle paths were approximated as linear polyline paths similar to S. Lee et al. (2019), S. Delp et al. (1990), and F. Young et al. (2019). To compensate for this approximation, we had to manually introduce additional waypoints to describe the muscle path closer to the original model. With the use of polyline method it was possible to faithfully describe muscle paths. In figure 2.8, we compared moment-arms of six hindlimb muscles from our current model with the model developed by Charles, Cappellari, Spence, Wells, et al. (2016) in OpenSim. Among the six muscles, five of them had used wrapping surfaces in Charles model (except *tibialis anterior* (TA)). The comparison showed excellent qualitative and quantitative agreement between the moment-arms of the two models, highlighting that the approximation of polyline method captured muscle paths well throughout range-of-motion.

### Scaling of hindlimb muscle parameters

After transferring the muscle attachments from Charles' model to our model, it was necessary to scale the muscle parameters appropriately to our model's geometry. Since our model is a whole-body 3D model, it was very important to consider the influence of the muscle parameters on all the DoFs the muscle spans. We used the numerical optimization based algorithm proposed by Modenese et al. (2016) to appropriately scale  $l_m^o$  and  $l_t^s$  parameters considering all the DoFs a muscle spans. While the method emphasizes on scaling the parameters such that the change in muscle length was preserved between the original and the scaled model, there is no constraint on preserving the ratios between  $l_m^o$  and  $l_t^s$ . In Charles model,  $l_t^s$  was estimated based on the numerical method proposed by Manal and Buchanan (2004). Thus, the  $l_t^s$  parameter has no direct measurable tendon property of the muscle. This is in accordance with the original formulation of the Hill-type muscle models (F. Zajac, 1989). Also, Charles, Cappellari, Spence, Wells, et al. (2016) showed that the measured tendon lengths were either longer or shorter than the estimated  $l_t^s$  values. Because of these observations, we did not impose any constraints to the algorithm to preserve the ratios between  $l_m^o$  and  $l_t^s$  of Charles' model. During future iterations of the model improvement,  $l_t^s$  parameter could be estimated from animal experiments (Cox et al., 2019).

### Modeling the mouse forelimb is more challenging than the hindlimb

Developing the forelimb muscle system was more challenging due to the lack of available biomechanical studies of the mouse or even rat forelimbs. To the best of our knowledge, Mathewson et al. (2012) was the only published work that measured some of the muscle properties necessary to model Hill-type muscles. But, since the goal of their work was not

building a simulation model of the mouse forelimb, information about muscle attachments were not reported.

DeLaurier et al. (2008) developed a 3D model of mouse embryonic forelimb using Optical Projection Tomography and digital segmentation. We transferred the attachment points for each muscle using their 3D atlas to our model. The choice of muscle was based on muscle data reported in Mathewson et al. (2012). This limited the forelimb model to mostly distal muscles. Proximal muscles around the shoulder that had origins from the spine were omitted from the model.

Mathewson et al. (2012) reported  $l_m^o$  and  $\alpha_0$  for the forelimb muscles. Unlike in the hindlimb case, we could not employ the algorithm to scale length related parameters from Modenese et al. (2016) because of a lack of information about muscle lengths at different model poses. The  $l_m^o$  parameter was thus scaled based on the ratio of average muscle-tendon length for while  $\alpha_0$  was used as reported.  $F_m^0$  was computed as by multiplying the physiological cross-sectional area by the same value of maximum isometric stress used for hindlimb muscles (0.3 N/mm<sup>2</sup>).

The final missing parameter  $l_t^s$  was estimated based on the extended algorithm by Manal and Buchanan (2004). (Refer to Appendix A.3 for details on the changes incorporated to the algorithm.) Determining  $l_t^s$  is one of the biggest bottlenecks in Hill-type muscle parameterization as there is no method to experimentally to estimate it (Charles, Cappellari, Spence, Wells, et al., 2016). The closest experimental method to estimate  $l_t^s$  is described by Cox et al. (2019). However, performing such experiments are extremely difficult in the mouse because of their relatively small size. The modifications we proposed to the numerical method by Manal and Buchanan (2004) should improve the reliability of these estimates for the mouse as well as for other musculoskeletal model of animals.

To the best of our knowledge there is no published work that characterizes either the muscle properties or muscle attachments for forelimb muscles attaching to the scapula or the spine; neither for mice nor rats. Hence, these muscles were considered beyond the scope of this work.

## 2.5.2 Muscle moment-arms and moments

The model includes 59 distinct forelimb and hindlimb muscles. It is a challenging task to provide a comprehensive analysis of a complex model such as this. Conventionally, the practice is to report and describe the relationship between moment-arm and joint movement for each muscle individually. This means that it is necessary to assume the function of a muscle *a priori*. Instead of making this assumption, we reported a global view of the possible roles of a muscle based on moment-arm and moment (Figure 2.9). With this representation one can quickly identify the function of a muscle and observe the contribution of different muscles to a particular degree of freedom.

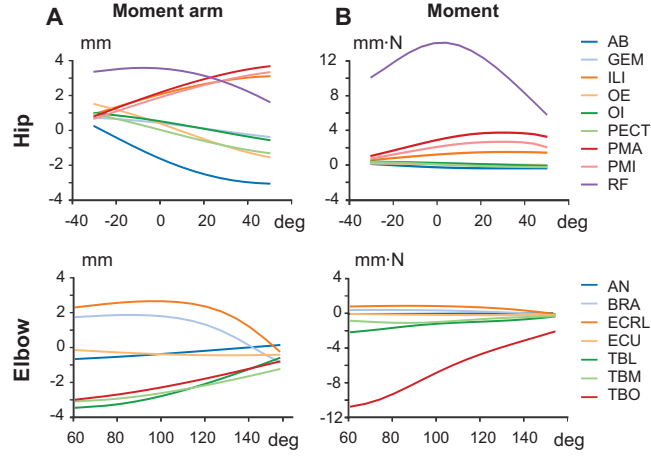


Figure 2.13: (A) Moment arm and (B) moment of hip flexor muscles *adductor brevis* (AB), *gemellus* (GEM), *iliacus* (ILI), *obturator externus* (OE), *obturator internus* (OI), *pectinus* (PECT), *psoas major* (PMA), *psoas minor* (PMI), *rectus femoris* (RF). (C) Moment arm and (D) moment of elbow flexor muscles *anconeus* (AN), *brachialis* (BRA), *extensor carpi radialis longus* (ECRL), *extensor carpi ulnaris* (ECU), *triceps brachii lateral head* (TBL), *triceps brachii medial head* (TBM), *triceps brachii long head* (TBO)

Previous musculoskeletal modeling studies have reported the behavior of zero-crossing of muscle moment arms in several animals such as cats (R. P. Young et al., 1993), mouse (Charles, Cappellari, Spence, Wells, et al., 2016), rat (Johnson et al., 2008) and ostrich (Hutchinson, Rankin, et al., 2015). R. P. Young et al. (1993) speculated that muscles with a zero-crossing moment-arms could intrinsically stabilize the joints around which they change sign without any need for extra neural commands. For the mouse hindlimb model from Charles, Cappellari, Spence, Wells, et al. (2016), several muscles were reported to have a zero-crossing. But their analysis was limited to the assumption of functional roles assigned to each muscle *a priori*. Here, we identified more muscles that have zero-crossings. For example, previously only *pectineus* muscle was reported to have a zero-crossing for hip flexion-extension. From Figure 2.13A,B we can observe that in addition to *pectineus* we have *adductor brevis*, *gemellus*, *gluteus maximus* (ventral), *obturator externus* and *internus* and *quadratus femoris* muscles have zero-crossing. Similarly for the different joints in forelimb and hindlimb, we can observe many muscles exhibiting the zero-crossing behavior.

A shortcoming of the representation we proposed is that it does not show joints' angle information: it is not possible to see at what joint angle the zero-crossing occurs. This limitation is only in the visual representation in this article, and detailed moment-arms of all the possible muscle and joint combinations are available. We encourage the readers to use the data and plotting tools in the code-repository (see [https://gitlab.com/paper\\_submissions/mouse\\_biomechanics\\_paper](https://gitlab.com/paper_submissions/mouse_biomechanics_paper)) to extract the detailed plots.

Along with moment-arms, we also reported the muscle moments across each DoF (Fig-

ure 2.9). By presenting both moment-arms and moments together, we can quickly observe how the role and importance of a muscle in actuating a particular DoF can change. Muscles with large maximum isometric force naturally become the dominating muscle for the DoF. While the moment-arm is only dependent on the muscle attachments and joint position, moments also depend on the dynamics of the muscle—most importantly muscle activation. From a neural control point of view this is very interesting: the nervous system can operate with a single strong muscle and/or utilize several different weaker muscles together to produce the same movement. Co-activation of multiple synergistic muscles with respect to a specific function could also result in a stabilization of the joint in the other DoFs.

The current muscle moment-arm and moment results were computed while the joint of interest was rotated within the range of motion and while keeping all other joints in their default position. This has a strong influence on the results. It limits the scope of the analysis to a particular pose of the model. This is often the case in biomechanical model analysis as it becomes very complex to interpret and represent the relationship of different joints with muscle moment and moment-arm. Young and colleagues (R. P. Young et al., 1993; F. Young et al., 2019) studied the coupled effect of a bi-articular muscle on joints. Also, we see from Figure 2.9 that many muscles operate on more than two degrees of freedom, especially muscles that span joints with multiple degrees of freedom (e.g., hip, ankle, shoulder, or wrist). With the condensed representation (Figure 2.9), it is possible to generate plots to study the relationships at various model poses.

### 2.5.3 Range of normalized muscle-fiber lengths

Muscle-fiber length ( $l_m$ ) is a state variable in describing the muscle dynamics (see Appendix A.1). It depends on the muscle-tendon length ( $l_{mt}$ ), the muscle contraction dynamics, and the muscle activation.  $l_m$  is thus a very interesting variable to study. In this paper, we reported the operational range of normalized muscle-fiber length ( $\tilde{l}_m$ ) for each muscle over all the joints it spans in Figure 2.10. (Unlike the moment-arm and moment representation in Figure 2.9, Figure 2.10 incorporates all the possible joint poses for a single muscle.) The range of  $\tilde{l}_m$  reflects the choice of the tendon slack length ( $l_t^s$ ) and optimal fiber length ( $l_m^o$ ) parameters. In future, if we can obtain experimental data of fiber-lengths at the different limb postures. This data can be used to validate the model by making sure that the experimental measurements fall within the predicted ranges of  $\tilde{l}_m$ .

Analyzing the  $\tilde{l}_m$  is also useful in understanding the behaviors by being able to characterize if a muscle is operating in the ascending, plateau or the descending region in the force-length curve (Figure 2.9B). In smaller animals, such as mice, due to their low weight and small inertias, the effect of gravity on the body is negligible (Hooper, 2012; Hooper et al., 2009). With lower influence of gravity, the forces produced by the passive elements

become more significant. This has two important consequences on the neural control circuits. One, it is less essential (compared to larger vertebrates) for the neural system to monitor the direction of gravity on the limbs during movements. Second, the momentum of the limbs is less useful during the swing phase during locomotion. For further discussion on the influence of body size on neural control refer to Hooper (2012). Thus, passive forces in mice play an important role in movement generation and it would be informative to use the muscle-fiber length range plots to explore it.

In Arnold, Hamner, et al. (2013), the authors reported the  $\tilde{l}_m$  of human leg muscles during different speeds of walking and running. They observed that the  $\tilde{l}_m$  has a wide range of operation in the force-length curve for different speeds of walking and running. Figure 2.10 for the mouse model also highlights that most muscles with the current muscle parameters operate both in the ascending and descending region of the force-length allowing for the kind of variability observed in humans.

#### 2.5.4 Sensitivity analysis

While developing a complex model like the one described here, it is important to identify the critical parameters that influence the overall performance of the model. To this aim, we performed a variance based global sensitivity analysis using the Sobol method to systematically study the influences of muscle attachment points and muscle parameters on the moment-arms and moments.

In our analysis of sensitivity of moment-arms to muscle attachment points, we considered only those attachment points ( $P_{WO}$  and  $P_{WI}$ ) that influence the muscle-length effect on the joint of interest. In Charles, Cappellari, Spence, Wells, et al. (2016), the analysis was performed directly at the origin and insertion points, and the perturbations applied to the attachments were along a particular direction. In contrast, in our work, we applied perturbations to the attachments in all three directions. Similar to the observations made by Charles, Cappellari, Spence, Wells, et al. (2016), we unsurprisingly observed that the attachment points located farther from the joint rotation centers had the greatest effect on the joint moment-arms. With the polyline approximation it therefore becomes very important to identify the intermediate points as accurately as possible to describe the muscle paths.

We further analyzed the sensitivity of joint moments to changes in  $F_m^0$ ,  $l_t^s$ ,  $l_m^o$  and  $\alpha_o$  parameters of the Hill-type muscle model. Based on (A.1), the formulation of Hill-type muscle models,  $F_m^0$  linearly affects the joint moments. However,  $l_t^s$ ,  $l_m^o$  and  $\alpha_o$  have a non-linear relationship with muscle force production (refer to Appendix A.1 for Hill model description). Unsurprisingly, moments across many muscle-DoF pairs were most sensitive to  $F_m^0$  with  $l_t^s$  being the next most significant parameters. Our observations presented in Section 2.4.4 agree with the sensitivity analysis by Charles, Cappellari, Spence, Wells,

et al. (2016). They observed that muscles with larger  $l_t^s$  compared to their  $l_m^o$  had their moments more sensitive to  $l_t^s$  than  $F_m^0$ . In Table 2.2 we reported the ratios of  $\frac{l_t^s}{l_m^o}$ . Muscles with smaller ratios ( $< 1.0$ ) for  $\frac{l_t^s}{l_m^o}$  have moments more sensitive to  $F_m^0$  and muscles larger  $\frac{l_t^s}{l_m^o} > 1.0$  ratios are more sensitive to  $l_t^s$ . This in accordance with the previous studies not only in mouse (Charles, Cappellari, Spence, Wells, et al., 2016) but also for chimpanzees (O'Neill et al., 2013) and humans (S. Delp et al., 1990; Redl et al., 2007).

The same applied to the forelimb muscles as well. Although, in the forelimb we have very few muscles whose ratios of  $\frac{l_t^s}{l_m^o}$  is greater than 1.0. The validation of our sensitivity analysis for the hindlimb muscle-joint pairs allows us to increase the confidence levels of our observations made for forelimb muscles.

Overall, with our comprehensive analysis we have highlighted the most important parameters in the model. This allows future researchers to identify and work with these important parameters more critically. The identification of the critical parameters also allows for adapting and fine tuning the model in case of numerical optimization for specific behaviors.

### 2.5.5 Model limitations

In this work, we present the most complete musculoskeletal model of the mouse. Yet, as with any model, the model construction was possible only because of some simplifications and assumptions. The skeletal model of the mice was developed from anatomical references rather than from an actual microCT scan. This allowed us to generate a more generic representation of the mouse skeleton but meant that not all anatomical features on the bones were captured. In future iterations, a skeletal model based on CT scans will further allow for better model validation. Here, we calculated the inertias of the bones using a bounding box method and assumed a uniform density of water along the body. We did not consider air cavities with different density in the lungs and head in our model. This introduces variation of inertial properties of certain bones and the overall center-of-mass of the mouse musculoskeletal model. Joint rotations were identified manually in this model and use joints such as revolute or spherical joints to represent the different DoFs in the model. However, in animals, joints are more complex and often difficult to model. Any studies that require validated joint movements should try to extend the current version of the model by including the necessary complexities in joint modeling for the particular study.

The Hill-type muscles were modeled as muscles with stiff/rigid tendons. This assumption allowed us to perform faster simulations due to the computational simplicity and thereby perform a comprehensive study of all the modeled muscles. The rigid-tendon model

assumption has implications on the changes in muscle-fiber lengths and muscle-forces. The variation of muscle-forces can be as high as 60% depending the ratio of  $l_m^o/l_t^s$  (Millard et al., 2013). The muscle model framework developed in this work also allows for simulating flexible tendon muscle models. In future iterations of this work, it is necessary to quantify the difference between the rigid-tendon and flexible tendon muscle models.

For the hindlimb muscles, we were able to build on, compare and validate our model with the previous mouse (Charles, Cappellari, Spence, Wells, et al., 2016) and rat (Johnson et al., 2008) hindlimb models. However, similar validation was not possible for the forelimb. Because of the lack of previous forelimb studies, we had to estimate both the attachment points and the muscle parameters ( $F_m^0$ ,  $l_m^o$ ,  $l_t^s$  and  $\alpha_o$ ). The comprehensive sensitivity analysis presented in this work provides information about the important parameters to be critically explored in the model. Further experimental measurements from the mouse forelimb are necessary to improve the forelimb model.

### 2.5.6 Model use and future work

A musculoskeletal model complements animal experiments by providing the data (EMG, afferent firings, interactions forces between the body and the environment) that is challenging to collect, and they are essential to setup and study closed-loop neuromechanical simulations (Figure 2.2). The whole-body model of the mouse presented in this work has the necessary components to contribute to both.

Locomotion is a result of whole-body movement with the neural circuits integrating feed-forward and sensory-driven strategies to generate the necessary muscle activation signals. The limb musculature modeled and analyzed in this work presents an excellent platform to use the model to setup predictive simulations to connect computational models of neural circuits to drive the musculoskeletal model (Note that the model is still missing axial muscles necessary for full 3D locomotion. For time being, they can be replaced by torque motors in the simulation). Alternatively, inverse kinematics and inverse dynamics approaches can be used to estimate kinematics (e.g., joint angles), kinetics (e.g., joint moments) and proprioceptive sensory information (e.g., activities of muscle spindles and Golgi tendon organs) from experimental whole-body trajectories made possible now by markerless pose estimation methods such as DeepLabCut (Mathis, Mamidanna, Kevin M. Cury, et al., 2018b).

The majority of the previous locomotion studies in mouse have been limited to straight forward locomotion. Exploring other locomotor regimes such as turning is now experimentally possible (Cregg et al., 2020) and the current 3D model has the necessary DoFs to replicate similar behaviors in simulation. The current model also allows to study motor behaviors that does not involve the whole-body movements like reaching and grasping.

While the possible use cases of our model are plenty, it still is only a preliminary step

towards a more robust computational model. As mice are one of the most significant experimental animal models to study normal and pathological motor behaviors, it is extremely important to develop computational models that can complement these studies.

The open-source and modular musculoskeletal model presented here offers an opportunity for a community driven approach that can collectively improve and rigorously validate the different components of the model with experimental data. In future iterations of the model, a systematic identification the full set of forelimb muscles along with the spinal muscles will increase the usability of the model in even more complex scenarios and grow towards a more complete model like the ones available for humans.

While the current work uses Bullet physics engine, most components developed here can be easily transferred to other physics simulation environments, for example OpenSim (Seth, Jennifer L Hicks, et al., [2018a](#)).





## Chapter 3

# Neuromechfly

### Overview

*Drosophila Melanogaster* commonly known as fruit-fly is the second model organism we focus on in this thesis. In an experimental setting, *Drosophila Melanogaster* has many unique advantages over *Mice*. *Drosophila Melanogaster* are easy to modify genetically, maintain, they reproduce fast, there are no ethical constraints and they have relatively simple nervous system and still exhibit complex motor behaviors. But there aspects such as the body dynamics that even harder to measure than with *Mice* or due to their size. In the following sections, we describe the development of a bio-realistic *in-silico* model of *Drosophila Melanogaster*. We then study mutli-legged gaits by first replaying recorded animal kinematics in a rigid-body physics environment and then driving the neuromechanical model by feed-foward central pattern generator (CPG) networks to generate animal like gaits.

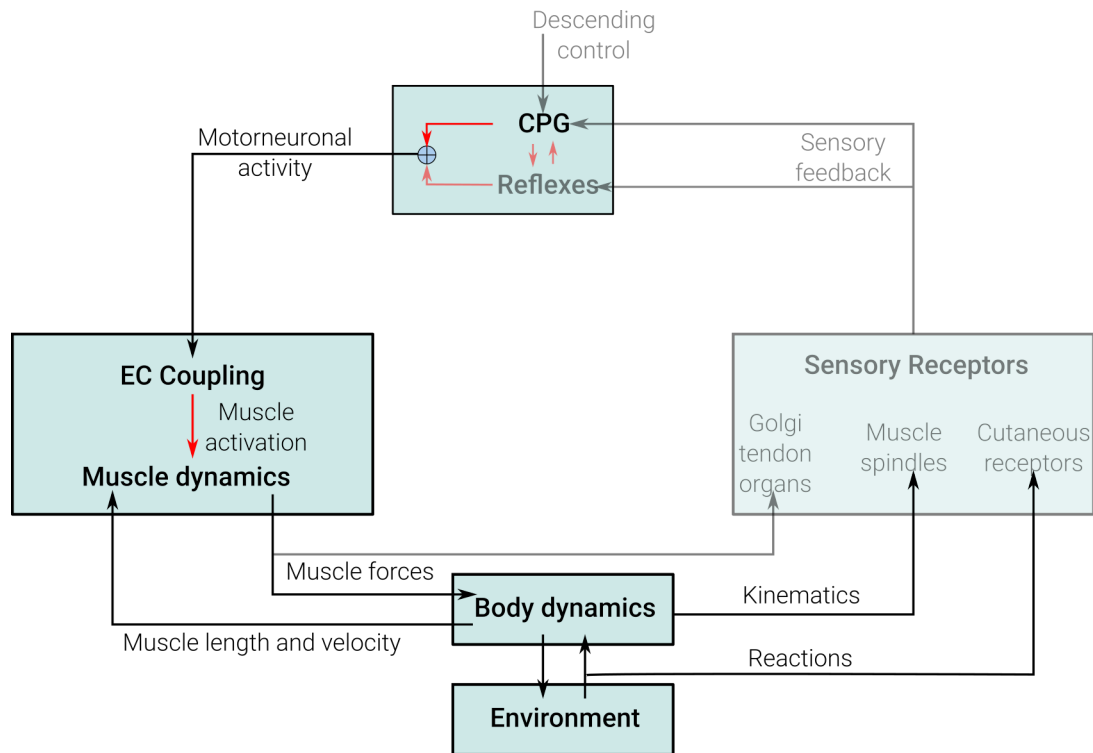


Figure 3.1: Focus of this chapter in the scheme of neuromechanical loop described in 1.1 for movement generation

### Reference publication

The following sections are based on our article which is currently under 2<sup>nd</sup> Accepted in Nature Methods “Victor Lobato Ríos, Shravan Tata Ramalingasetty, Pembe Gizem Özdil, Jonathan Arreguit, Auke Jan Ijspeert, and Pavan Ramdya (Nov. 2021). NeuroMechFly, a Neuromechanical Model of Adult *Drosophila melanogaster*. DOI: [10.1101/2021.04.17.440214](https://doi.org/10.1101/2021.04.17.440214)”<sup>a</sup>

### My contributions

- Development and setup of the *in-silico* model of *Drosophila melanogaster*
- Development of the neural simulation library
- Setting up of the original software framework
- Setup, evaluation and analysis of the multi-objective optimizations
- Revisions of the manuscript

<sup>a</sup>Second and third authors have equal contributions in this work

### 3.1 Abstract

Animal behavior emerges from a seamless interaction between neural network dynamics, musculoskeletal properties, and the physical environment. Accessing and understanding the interplay between these intertwined elements requires the development of integrative and morphologically realistic neuromechanical simulations. Until now, there has been no such simulation framework for the widely studied model organism, *Drosophila melanogaster*. Here we present NeuroMechFly, a data-driven model of the adult female fly within a physics-based simulation environment. NeuroMechFly combines a series of independent computational modules including a biomechanical exoskeleton with articulating body parts—legs, halteres, wings, abdominal segments, head, proboscis, and antennae—muscle models, and neural network controllers. To enable illustrative use cases, we first define minimal leg degrees-of-freedom by analyzing real 3D kinematic measurements during real *Drosophila* walking and grooming. Then, we show how, by replaying these behaviors using NeuroMechFly’s biomechanical exoskeleton in its physics-based simulation environment, one can predict otherwise unmeasured torques and contact reaction forces. Finally, we leverage NeuroMechFly’s full neuromechanical capacity to discover neural networks and muscle parameters that enable locomotor gaits optimized for speed and stability. Thus, NeuroMechFly represents a powerful testbed for building an understanding of how behaviors emerge from interactions between complex neuromechanical systems and their physical surroundings.

## 3.2 Introduction

Uncoupling the contributions to behavior of many neuronal and biomechanical elements is daunting. Systems-level numerical simulations can assist in this ambitious goal by consolidating data into a dynamic framework, generating predictions to be tested, and probing the sufficiency of prevailing theories to account for experimental observations (Chiel and Beer, 1997; Webb, 1999; K. Pearson et al., 2006b; Prilutsky and Donald H Edwards, 2015; Seth, Jennifer L Hicks, et al., 2018a; Einevoll et al., 2019). Computational models, including neuromechanical simulations, have long played a particularly important role in the study of movement control in vertebrates (Sigvardt and Miller, 1998; Lansner et al., 1998; Ijspeert, 2001; Ilya A Rybak et al., 2015) and invertebrates, including stick insects (Ekeberg, Blümel, et al., 2004; Toth, Schmidt, et al., 2013; Toth, Grabowska, et al., 2013; Schilling, Hoinville, et al., 2013), cockroaches (Szczecinski, A. E. Brown, et al., 2014; Proctor et al., 2010), praying mantises (Szczecinski, Martin, et al., 2015), and ants (Guo et al., 2018).

For animals like invertebrates with a relatively small number of neurons that can be identified across individuals, a mapping of real to simulated biomechanical or circuit elements might enable a cross-talk whereby models make predictions that can then be tested experimentally. However, for many of the animals for which neuromechanical models currently exist, there is a dearth or absence of genetic tools that would facilitate repeatedly recording, or perturbing the same neurons across animals. By contrast, for a few commonly studied ‘model’ organisms, a dialogue between experimental results and computational predictions represents an exciting but largely unrealized opportunity. This is recently enabled by advances in computing power, the realism of physics-based simulation environments, and improvements in numerical optimization approaches. Neuromechanical models of some commonly studied organisms have already been developed including for the nematode (*Caenorhabditis elegans* (Szigeti et al., 2014; Izquierdo and Beer, 2018)), maggots (larval *Drosophila melanogaster* (Loveless et al., 2019)), and rodents (Merel, Aldarondo, et al., 2019). However, for the adult fly, *Drosophila melanogaster*, only 2-dimensional (2D) (Isakov et al., 2016) and morphologically unrefined (Ramdya et al., 2017b) neuromechanical models exist.

Adult flies are an ideal organism for establishing a synergy between experimental and computational neuroscience. First, flies generate a large repertoire of complex behaviors including grooming (Seeds et al., 2014), courtship (Pavlou and Goodwin, 2013), flight (Fry et al., 2003), and walking (Mendes et al., 2013; Wosnitza et al., 2013) which they use to navigate complex environments (Pick and Roland Strauss, 2005). The kinematics of these behaviors can now be quantified precisely using deep learning-based computer vision tools (Pereira et al., 2019; Mathis, Mamidanna, Kevin M Cury, et al., 2018a) in 3-dimensions (3D) (Günel et al., 2019; Gosztolai et al., 2021). Second, flies have a relatively small number of neurons that can be repeatedly genetically targeted (Jenett et al., 2012) for recordings or perturbations in tethered, behaving animals (Seelig et al.,

2010; Maimon et al., 2010; Chin-Lin Chen et al., 2018; Hermans et al., 2021). These neurons can also be placed within their circuit context using recently acquired brain and ventral nerve cord (VNC) connectomes (Phelps et al., 2021; Scheffer et al., 2020). We previously developed a simple physics-based simulation of adult *Drosophila melanogaster* to investigate hexapod locomotor gaits (Ramdya et al., 2017b). However, this older model has a number of important limitations that restrict its widespread use: it lacks (i) the morphological accuracy needed to simulate mass distributions, compliance, and physical constraints, (ii) muscle models and their associated passive dynamical properties, as well as (iii) neural networks or other control architectures.

Here we describe NeuroMechFly, a neuromechanical model of adult *Drosophila* that fills this methodological gap by incorporating a new, open-source computational framework consisting of exchangeable modules which provide access to biomechanics, neuromuscular control, and parameter optimization approaches. These modules maintain the capacity for whole organism simulation while also facilitating further open source extensions and improvements by the scientific community. Thus, NeuroMechFly is a completely new modeling framework and not simply an improvement of an earlier model (Ramdya et al., 2017b).

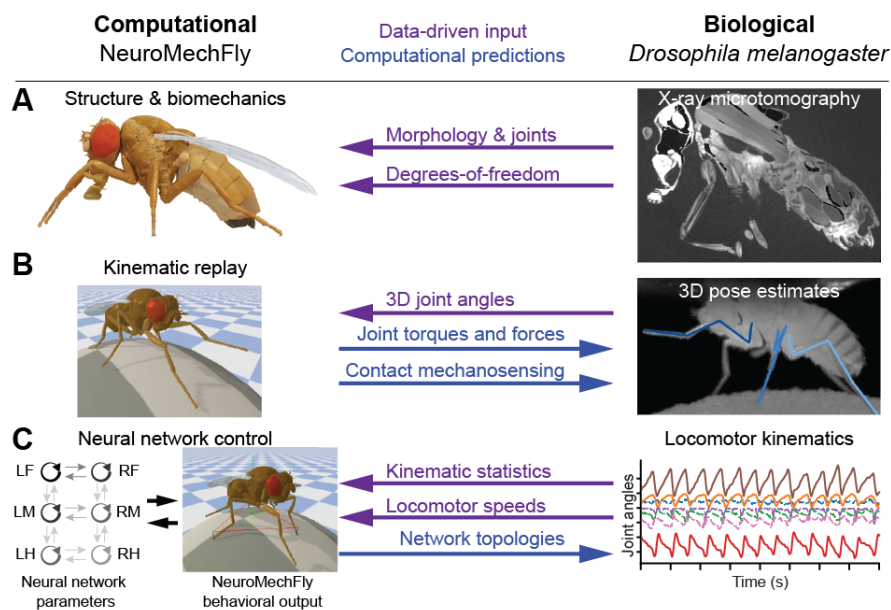


**Figure 3.2: Data-driven development and applications of NeuroMechFly.** (A) Body structures—morphology, joint locations, and degrees-of-freedom—were defined by x-ray microtomography and kinematic measurements. (B) Real 3D poses were used to replay kinematics in the model permitting the prediction of unmeasured contact reaction forces and joint torques. (C) Real limb kinematics were used to constrain the evolutionary optimization of neuromuscular parameters aiming to satisfy high-level objectives for walking—speed and static stability. The properties of optimized networks could then be more deeply analyzed.

The biomechanical exoskeleton of NeuroMechFly was obtained from a detailed CT-scan of an adult female fly which was then digitally rendered. We defined the model’s leg degrees-of-freedom based on an investigation of *Drosophila* 3D leg kinematics (Figure 3.2A), allowing us to discover that a previously unreported coxa-trochanter leg degree-of-freedom (DoF) is required to accurately recapitulate real fly walking and grooming. Using this biomechanical exoskeleton and replaying experimental leg kinematics within the PyBullet physics-based simulation environment (Figure 3.2B) (Coumans, 2015), we then explored how one can estimate quantities that cannot be experimentally measured in behaving flies—ground reaction forces (GRFs), joint torques, and tactile contacts. As a second use-case illustration of NeuroMechFly’s potential, we leveraged the full neuromechanical framework—now including neural and muscle models—to show how the parameters of a central pattern generator (CPG)-inspired coupled-oscillator network and associated torsional spring and damper muscle model could be optimized to discover and explore controllers for fast and stable walking (Figure 3.2C). Importantly, the NeuroMechFly framework is modular and open-source, enabling future extensions including the use of more detailed neural and muscle models that permit more interpretable experimental predictions that can inform our understanding of real *Drosophila* neural circuits. Thus, NeuroMechFly represents an important step towards comprehending how behaviors emerge from a complex interplay between neural dynamics, musculoskeletal biomechanics, and physical interactions with the environment.

### 3.3 Methods

#### 3.3.1 Constructing an adult *Drosophila* biomechanical model

##### Preparing adult flies for x-ray microtomography

The protocol used to prepare flies for microtomography was designed to avoid distorting the exoskeleton. We observed that traditional approaches for preparing insects for either archival purposes or for high resolution microscopy, including scanning electron microscopy (Chaffey, 2001), result in the partial collapse or bending of some leg segments and dents in the exoskeleton of the thorax and abdomen. These alterations mostly occur during the drying phase and while removal of ethanol by using supercritical carbon dioxide drying reduces these somewhat, it is still not satisfactory. We therefore removed this step altogether, and instead embedded flies in a transparent resin. This resulted in only a small surface artifact over the dorsal abdominal segments A1, A2, and A3.

Flies were heavily anaesthetized with CO<sub>2</sub> gas, then carefully immersed in a solution of 2% paraformaldehyde in phosphate buffer (0.1M, pH 7.4) containing 0.1% Triton 100, to ensure fixative penetration, and left for 24 h at 4°C. Care was taken to ensure the flies did not float on the surface, but remained just below the meniscus. They were then washed in 0.1M cacodylate buffer (2 x 3 min washes), and placed in 1% osmium tetroxide in 0.1M cacodylate buffer, and left at 4°C for an additional 24 h. Flies were then washed in distilled water and dehydrated in 70% ethanol for 48 h, followed by 100% ethanol for 72 h, before being infiltrated with 100% LR White acrylic resin (Electron Microscopy Sciences, US) for 24 h at room temperature. This was polymerised for 24 h at 60°C inside a closed gelatin capsule (size 1; Electron Microscopy Sciences) half-filled with previously hardened resin to ensure the insect was situated in the center of the final resin block, and away from the side.

##### X-ray microtomography

We glued the sample onto a small carbon pillar and scanned it using a 160 kV open type, microfocus X-ray source (L10711/-01; Hamamatsu Photonics K.K., Japan). The X-ray voltage was set to 40 kV and the current was set to 112 uA. The voxel size was 0.00327683 mm. To perform the reconstruction, we used X-Act software from the microtomography system developer (RX-solutions, Chavanod, France) obtaining a stack of 982 tiff images of 1046x1636 pixels each.

##### Building a polygonal mesh volume from processed microtomography data

First, we isolated cuticle and wings from the microtomography data using Fiji (Schindelin et al., 2012). We selected 360 images from the tiff stack as the region of interest (ROI)



beginning at slice 300. The tiff stack with the ROI was then duplicated. The first copy was binarized using a threshold value of 64 to isolate the cuticle. The second copy was cropped to keep the upper half of the image—where the wings are—and then binarized using a lower threshold value of 58. Finally, we applied a closing morphological operation to isolate the wings. Both binarized stacks were stored as tiff files.

We developed custom Python code to read the tiff stacks, and to fill empty holes within the body and wings. Finally, we used the Lewiner marching cubes algorithm (Lewiner et al., 2003) (implemented in the scikit-image package (van der Walt et al., 2014)) to obtain a polygon mesh for each stack. Both meshes were then exported to a standard compressed mesh storage format.

### Separating and reassembling articulated body parts

We used Blender (Foundation version 2.81 (Foundation, 2012)) to clean and manipulate polygon meshes obtained from microtomography data.

After importing these meshes into Blender, we removed noise by selecting all vertices linked to the main body (or wings), inverting the selection, and deleting these vertices. We explored the resulting meshes, looking for spurious features, and then manually selected and deleted the related vertices. We obtained 65 body segments (Table B.1) based on (Ferris, 1950). More recent literature corroborated these propositions for body morphology and joint degrees-of-freedom. We manually selected and deleted vertices from our imported 3D body and wing models. Segments were then separated at joint locations based on published morphological studies. We made some simplifications. Most notably, in the antennae, we considered only one segment instead of three because cutting this small element into a few pieces would alter its morphology.

Each wing was separated into an individual segment from the wing model. The body model was separated into 63 segments as described below. The abdomen was divided into five segments according to tergite divisions. The first and second tergites were combined as the first segment (A1A2), and the last segment (A6) included the sixth to tenth tergites. Each antenna was considered a single segment and separated from the head capsule at the antennal foramen. Both eyes and the proboscis were separated from the head. The latter was divided into two parts, the first containing the rostrum (Rostrum), and the second containing the haustellum and labellum (Haustellum). Each leg was divided in eight parts: the coxa, trochanter/femur, tibia, and five tarsal segments. The thorax was considered a single segment and only the halteres were separated from it.

Each segment was processed in Blender to obtain closed meshes. First, a remesh modifier was used in ‘smooth mode’, with an octree depth of 8, and a scale of 0.9 to close the gaps generated in the meshes after been separated from the original model. Smooth shading was enabled and all disconnected pieces were removed. Then, we used ‘sculpt mode’

to manually compensate for depressions/collapses resulting from the microtomography preparation, or from separating body segments.

Then, all segments were copied into a single \*.blend file and rearranged into a natural resting pose (Figure 3.3F). We made the model symmetric to avoid inertial differences between contralateral legs and body parts. For this, we used the more detailed microtomography data containing the right side of the fly. First, the model was split along the longitudinal plane using the bisect tool. Then the left side was eliminated and the right side was duplicated and mirrored. Finally, the mirrored half was repositioned as the left side of the model, and both sides of the head capsule, rostrum, haustellum, thorax, and abdominal segments were joined.

At this point, the model consisted of approximately nine million vertices, an intractable number for commonly used simulators. We therefore used the decimate tool to simplify the mesh and collapse its edges at a ratio of 1% for every segment. This resulted in a model with 87,000 vertices that conserved the most important details but eliminated small bristles and cuticular textures.

### Rigging the Blender model

We added an Armature object alongside our model to build the skeleton of the fly. To actuate the model, we created a 'bone'—a tool in Blender that is used to animate characters—for each segment. Bones were created such that the thorax would be the root of the skeleton and each bone would be the child of its proximal bone, as indicated in Table B.1. Then, the bones were positioned along the longitudinal axis of each segment with their heads and tails over the proximal and distal joints, respectively. Each joint was positioned at a location between neighboring segments. Each bone inherited the name of its corresponding mesh.

We used the FARMS modeling plugin (section 5.4) setup in Blender to modify the properties of each bone. These properties can be used later in a simulator to e.g., define the maximum velocity, or maximum effort of each link. Furthermore, we added a limit rotation constraint (range of motion) to each axis of rotation (DoF) for every bone. The range of motion for each rotation axis per joint was defined as  $-180^\circ$  to  $180^\circ$  to achieve more biorealistic movements. Because, to the best of our knowledge, there are no reported angles for these variables, these ranges of motion should be further refined once relevant data become available. The DoF of each bone (segment) were based on previous studies (Soler et al., 2004; Dickson et al., 2008; Geurten et al., 2014) (see Table B.1). Any bone can be rotated in Blender to observe the constraints imposed upon each axis of rotation. These axes are defined locally for each bone.

Finally, we defined a 'zero-position' for our model. Most bones were positioned in the direction of an axis of rotation (Figure B.7). Each leg segment and the proboscis were

positioned along the  $Z$  axis. Each abdominal segment and the labellum were positioned along the  $X$  axis. Wings, eyes, and halteres were positioned along the  $Y$  axis. The head and the antennae are the only bones not along a rotational axis: the head is rotated  $20^\circ$  along the  $Y$  axis, and the antennae are rotated  $90^\circ$  with respect to the head bone. Positioning the bones along axes of rotation makes it easier to intuit a segment's position with its angular information and also more effectively standardizes the direction of movements.

### Exporting the Blender model into the Bullet simulation engine

We used the FARMS modeling plugin in Blender to obtain the name, location, global rotation axis, range of motion, and custom properties for each bone. As mentioned above, the axes of rotation are defined locally for each bone. Therefore, our code also transforms this information from a local to a global reference system, obtaining the rotation matrix for each bone.

We used the Simulation Description Format (SDF, <http://sdformat.org/>) convention to store the model's information. This format consists of an \*.xml file that describes objects and environments in terms of their visualization and control. The SDF file contains all of the information related to the joints (rotational axes, limits, and hierarchical relations) and segments (location, orientation, and corresponding paths of the meshes) of the biomechanical model. We can modify this file to add or remove segments, joints, or to modify features of existing segments and joints. To implement joint DoFs, we used hinge-type joints because they offer more freedom to control individual rotations. Therefore, for joints with more than one DoF, we positioned in a single location as many rotational joints as DoFs needed to describe its movement. The parenting hierarchy among these extra joints was defined as roll-pitch-yaw. The mass and collision mesh were related to the segment attached to the pitch joint—present in every joint of the model. The extra segments were defined with a zero mass and no collision shape.

Our model is based upon the physical properties of a real fly. The full body length and mass of the model are set to  $2.8\text{ mm}$  and  $1\text{ mg}$ , respectively. To make the center of mass and the rigid-body dynamics of the model more similar to a real fly, rather than having a homogeneous mass distribution, we used different masses (densities) for certain body parts as measured in a previous study (Szczecinski, Bockemühl, et al., 2018). Specifically, these masses were: head ( $0.125\text{ mg}$ ), thorax ( $0.31\text{ mg}$ ), abdomen ( $0.45\text{ mg}$ ), wings ( $0.005\text{ mg}$ ), and legs ( $0.11\text{ mg}$ ).

In PyBullet, contacts are modeled based on penetration depth between any two interacting bodies. The contact parameters are set to 0.02 units of length (1 unit = 1 m in SI units). It is preferable to have the bodies of size larger than 0.02 units. Therefore, we performed a change of units of the physics simulator. Specifically, we changed the units of mass ( $kg$

to  $g$ ) and length ( $m$  to  $mm$ ) when setting up the physics of the simulation environment, and then converted back the calculated values to  $SI$  units when recording the results. Therefore, the physics engine was able to compute the physical quantities without numerical errors, and the model could also more accurately reflect the physics of a real fly. Notably, we are not compromising the dynamics of the simulated behaviors.

### Comparing leg sizes between NeuroMechFly and real flies

We dissected the right legs from ten wild-type female adult flies, 2-4 days-post-eclosion. Flies were cold anesthetized using ice. Then the legs were removed using forceps from the sternal cuticle to avoid damaging the coxae. Dissected legs were straightened onto a glass slide and fixed with UV-curable glue (Figure B.1A). We used a Leica M205 C stereo microscope to take images from the legs placed next to a 0.5 mm graduated ruler. Joints in the legs were manually annotated and then distances between them were measured in pixels and converted to mm using the ruler as a reference. Lengths between joints were compared to rigged bone lengths in NeuroMechFly.

## 3.3.2 Kinematic replay and analysis

### Forward walking data

We recorded spontaneous behaviors from wild-type females 3-4 days-post-eclosion. Flies were mounted on a custom stage and allowed to acclimate for 15 min on an air-supported spherical treadmill (Chin-Lin Chen et al., 2018). Experiments were conducted in the evening Zeitgeber time. Flies were recorded five times for 30 s at 5 min intervals. Data were excluded if forward walking wasn't present for at least five continuous seconds in 10 s windows. To record data, we used a 7-camera system as in (Günel et al., 2019). However, we replaced the front camera's InfiniStix lens with a Computar MLM3X-MP lens at 0.3x zoom to visualize the spherical treadmill. After the fifth trial of each experiment, we recorded an extra 10 s trial, having replaced the lens from a lateral camera with another Computar MLM3X-MP lens. We used these images to calculate the longitudinal position of the spherical treadmill with respect to the fly for the preceding five trials.

### Foreleg/antennal grooming data

Data for kinematic replay of foreleg/antennal grooming were obtained from a previous study describing DeepFly3D, a deep learning-based 3D pose estimation tool (Günel et al., 2019). These data consist of images from seven synchronized cameras obtained at 100 fps (<https://dataverse.harvard.edu/dataverse/DeepFly3D>). Time axes (Figure 3.6E, F) correspond to time points from the original, published videos. Data were specifically obtained from experiment #3, taken of an animal (#6) expressing aDN-GAL4 driving

UAS-CsChrimson.

### Processing 3D pose data

We used DeepFly3D v0.4 (Günel et al., 2019) to obtain 3D poses from the images acquired for each behavior. 2D poses were examined using the GUI to manually correct 10 frames during walking and 72 frames during grooming. DeepFly3D, like many other pose estimation softwares, uses a local reference system based on the cameras' positions to define the animal's pose. Therefore, we first defined a global reference system for NeuroMechFly from which we could compare data from experiments on different animals (see Figure B.7).

Aligning both reference systems consisted of six steps. First, we defined the mean position of each Thorax-Coxa (ThC) keypoint as fixed joint locations. Second, we calculated the orientation of the vectors formed between the hind and middle coxae on each side of the fly with respect to the global x-axis along the dorsal plane. Third, we treated each leg segment independently and defined its origin as the position of the proximal joint. Fourth, we rotated all data points on each leg according to its side (i.e., left or right) and previously obtained orientations. Fifth, we scaled the real fly's leg lengths for each experiment to fit NeuroMechFly's leg size: A scaling factor was calculated for each leg segment as the ratio between its mean length throughout the experiment and the template's segment length and then each data point was scaled using this factor. Finally, we used the NeuroMechFly exoskeleton as a template to position all coxae within our global reference system; the exoskeleton has global location information for each joint. Next, we translated each data point for each leg (i.e. CTr, FTi, and TiTa joints) with respect to the ThC position based on this template.

### Calculating joint angles from 3D poses

We considered each leg a kinematic chain and calculated the angle of each DoF to reproduce real poses in NeuroMechFly. We refer to this process as 'kinematic replay'. Angles were obtained by computing the dot product between two vectors with a common origin. We obtained 42 angles in total, seven per leg. The angles' names correspond to the rotational axis of the movement—roll, pitch, or yaw—for rotations around the anterior-posterior, mediolateral, and dorsoventral axes, respectively.

The thorax-coxa joint (ThC) has three DoFs. The yaw angle is measured between the dorsoventral axis and the coxa's projection in the transverse plane. The pitch angle is measured between the dorsoventral axis and the coxa's projection in the sagittal plane. To calculate the roll angle, we aligned the coxa to the dorsoventral axis by rotating the kinematic chain from the thorax to the FTi joint using the yaw and pitch angles. Then we measured the angle between the anterior-posterior axis and the projection of the rotated

FTi in the dorsal plane.

Initially, we considered only a pitch DoF for the CTr joint. This was measured between the coxa and femur’s longitudinal axis. Subsequently, we discovered that a CTr roll DoF would be required to accurately match the kinematic chain. To calculate this angle, we rotated the tibia-tarsus joint (TiTa) using the inverse angles from the coxa and femur and measured the angle between the anterior-posterior axis and the projection of the rotated TiTa in the dorsal plane.

The pitch angle for the FTi was measured between the femur and tibia’s longitudinal axis. The pitch angle for the TiTa was measured between the tibia and tarsus’s longitudinal axis. The direction of rotation was calculated by the determinant between the vectors forming the angle and its rotational axis. If the determinant was negative, the angle was inverted.

To demonstrate that the base six DoFs were not sufficient for accurate kinematic replay, we also compared these results to angles obtained using inverse kinematics. In other words, we assessed whether an optimizer could find a set of angles that could precisely match our kinematic chain using only these six DoFs. To compute inverse kinematics for each leg, we used the optimization method implemented in the Python IKPy package (L-BFGS-B from Scipy). We defined the zero-pose as a kinematic chain and used the angles from the first frame as an initial position (seed) for the optimizer.

### Calculating forward kinematics and errors with respect to 3D poses

To quantify the contribution of each DoF to kinematic replay, we used the forward kinematics method to compare original and reconstructed poses. Since 3D pose estimation noise causes leg segment lengths to vary, we first fixed the length of each segment as its mean length across all video frames.

We then calculated joint angles from 3D pose estimates with the addition of each DoF (see previous section). We formed a new kinematic chain including the new DoF. This kinematic chain allowed us to compute forward kinematics from joint angles, which were then compared with 3D pose estimates to calculate an error. We performed an exhaustive search to find angles that minimize the overall distance between each 3D pose joint position and that joint’s position as reconstructed using forward kinematics. The search spanned from  $-90^\circ$  to  $90^\circ$  with respect to the ‘zero pose’ in  $0.5^\circ$  increments.

The error between 3D pose-based and angle-based joint positions per leg was calculated as the average distance across every joint. We note that differences in errors can vary across legs and leg pairs because each joint’s 3D pose estimate is independent and each leg acts as an independent kinematic chain adopting its own pose. Thus, errors may also be asymmetric across the body halves. As well, errors integrate along the leg when using

forward kinematics (FK) for walking (Figure B.2) and for grooming (Figure B.3). By contrast, inverse kinematics (IK) acts as an optimizer and minimizes the error at the end of the kinematic chain (i.e., where the FK error is highest) for walking (Figure B.2D) and for grooming (Figure B.3D). This explains why errors using FK are generally higher than those using IK—with the exception of adding a roll degree-of-freedom at the Coxa-Trochanter joint. To normalize the error with respect to body length, we measured the distance between the antennae and genitals in our Blender model (2.88 mm). Errors were computed using 400 frames of data: frames 300-699 for forward walking from fly 1 and frames 0-399 for foreleg/antennal grooming.

We ran a Kruskal-Wallis statistical test to compare kinematic errors across the eight methods used. We then applied a posthoc Conover’s test to perform a pairwise comparison. We used the Holm method to control for multiple comparisons. The resulting p-value matrices for walking and foreleg/antennal grooming behaviors are shown in Table B.2 and Table B.3, respectively. Our statistical tests suggested that adding a CTr roll DoF uniquely improved kinematic replay compared with all other methods.

### Transferring real 3D poses into the NeuroMechFly reference frame

To incorporate the additional CTr roll DoF into NeuroMechFly, we enabled rotations along the  $z$  axis of CTr joints. Then, we created new SDF configuration files using utility scripts part of FARMS to include a CTr roll DoF for each leg. To simulate the fly tethering stage used in our experiments, we added three support joints (one per axis of movement) that would hold our model in place. We removed these supports for ground walking experiments (Videos 8 and 10).

We used position control for each joint in the model. We fixed the position of non-actuated joints to the values shown in Table B.4. The actuated joints (i.e. the leg joints) were controlled to achieve the angles calculated from 3D pose data. The simulation was run with a time step of 0.5 ms, allowing PyBullet to accurately perform numerical calculations. Since the fly recordings were only captured at 100 fps, we up-sampled and interpolated pose estimates to match the simulation time steps before calculating joint angles.

### Comparing real and simulated spherical treadmill rotations

We obtained spherical treadmill rotational velocities from real experiments using Fic-trac (Moore et al., 2014). We also obtained the relative inclination of each tethered fly ( $\Phi$ ) (Figure B.9A) as the angle between the ground plane and the axis between the hind leg ThC joint and the dorsal part of the neck. Finally, we estimated the position of the ball with respect to the fly from both front and lateral views (Figure B.9B-C) by identifying the ball and fly using a Hough transform and standard thresholding, respectively. For axes observed from both views, we averaged the expected position.

For the simulated environment we created a spherical body in PyBullet with three hinge joints along the  $x$ ,  $y$ , and  $z$  axes, allowing our sphere to rotate in each direction like a real spherical treadmill. Rolling and spinning frictions were set to zero to obtain virtually frictionless conditions similar to a real treadmill floating on air. The mass of the simulated spherical treadmill was set to  $54.6\text{ mg}$ : the measured mass of the real foam sphere. Finally, the sphere's diameter was measured and set into the simulation as  $9.96\text{ mm}$ .

We ran kinematic replay of walking by setting the simulated spherical treadmill position and fly inclination based on measurements from experimental images. We used predefined values for kinematic replay of grooming. Then, we empirically determined the following parameters:

- Global ERP = 0.0
- Friction ERP = 0.0
- Solver iterations = 1000
- Treadmill lateral friction = 1.3

After running the simulation, we compared the rotational velocities estimated for each axis with the real velocities obtained with Fictrac. First, we smoothed both Fictrac and estimated signals using a median filter with a window size of 0.1 s. Second, we interpolated Fictrac data from time steps of 0.1 s (100 fps) to the simulation time step. Then, we established each signal's baseline as the mean of the first 0.2 s of data. Finally, we computed the Spearman correlation coefficient ( $\rho$ ) to assess correlations of forward, lateral, and heading (yaw) velocities for both signals.

### Constraint parameter sensitivity analysis

Simulated spherical treadmill velocity estimates depend on constraint force mixing (CFM) and contact error reduction (contact ERP) parameters. These parameters change the 'softness' of joint and contact constraints in the physics engine. Therefore we performed a sensitivity analysis to determine the best combination of CFM and ERP. CFM values were swept from 0 to 10, and ERP from 0 to 1.0. Then, we ran a simulation for each of 121 combinations. We assessed their performance by calculating the Spearman correlation coefficient for each axis ([Figure B.8A-C](#)).

Finally, to select optimal parameter values, we applied a weighted sum to the results as shown in [Equation 3.1](#):

$$WS_i = \alpha * Fw(\rho_i) + \beta * Lat(\rho_i) + \gamma * Head(\rho_i) \quad (3.1)$$



where Fw, Lat, and Head are the rotational axes,  $\rho_i$  is the Spearman correlation coefficient obtained for each CFM-ERP combination, and  $\alpha$ ,  $\beta$ , and  $\gamma$  are the standard deviation contributions for each axis calculated as shown in Equations 3.2, 3.3, and 3.4, respectively. Therefore, we favored the axis with the largest amplitude of variation.

$$\alpha = \frac{std(Fw)}{std(Fw) + std(Lat) + std(Head)} \quad (3.2)$$

$$\beta = \frac{std(Lat)}{std(Fw) + std(Lat) + std(Head)} \quad (3.3)$$

$$\gamma = \frac{std(Head)}{std(Fw) + std(Lat) + std(Head)} \quad (3.4)$$

Finally, we normalized WS (NWS) with respect to its maximum and minimum values (Figure B.8D). Consequently, a combination with NWS equal to 1 was selected: CFM = 3 and ERP = 0.1.

### Controller gain sensitivity analysis

We performed kinematic replay using a built-in PD position controller in PyBullet (Coumans, 2015). A PD controller was used rather than the more widely known PID controller because the integral component ('I' in PID) is mainly used to correct steady state errors (e.g., while maintaining a fixed posture). Thus, it is not used for time-varying postures like those during locomotion. We used PyBullet's built-in position control method because it operates with proportional and derivative gains that are stable and efficient. This PD controller minimizes the error:

$$error = K_p(\theta_r - \theta_a) + K_d(\omega_r - \omega_a) \quad (3.5)$$

where  $\theta_r$  and  $\theta_a$  denote reference and actual positions,  $\omega_r$  and  $\omega_a$  are desired and actual velocities, and  $K_p$  and  $K_d$  are proportional and derivative gains, respectively, which provides some compliance in the model.

Because the outputs of our model—dynamics of motion—depend on the controller gains  $K_p$  and  $K_d$ , we first systematically searched for optimal gain values. To do this, we ran the simulation's kinematic replay for numerous  $K_p$  and  $K_d$  pairs, ranging from 0.1 to 1.0

with a step size of 0.1 (i.e., 100 simulations in total). Target position and velocity signals for the controller were set as the calculated joint angles and angular velocities, respectively. To compute joint angular velocities, we used a Savitzky–Golay filter with a first-order derivative and a time-step of 0.5 ms on the joint angles. Feeding the controller with only the joint angles could also achieve the desired movements of the model. However, including the velocity signal ensured that the joint angular velocities of the fly and the simulation were properly matched. We then calculated the mean squared error (MSE) between the ground truth—joint angles obtained by running our kinematic replay pipeline on pose estimates from DeepFly3D (Günel et al., 2019)—and joint angles obtained from PyBullet. Then, we averaged the MSE values across the joints in one leg, and summed the mean MSEs from each of six legs to obtain a total error. We made the same calculations for the joint angular velocities as well. Our results (Figure B.4) show that our biomechanical model can replicate real 3D poses while also closely matching real measured velocities. In particular, an MSE of  $360 \text{ (rad/sec)}^2$  for the six legs corresponds approximately to  $7.74 \text{ rad/sec}$  per leg, i.e.,  $1.27 \text{ Hz}$ . This is acceptable given the rapid, nearly 20 Hz, leg movements of the real fly.

After validating the accuracy of kinematic replay, we performed a sensitivity analysis to measure the impact of varying controller gains on the estimated torques and ground reaction forces. This analysis showed that torques and ground reaction forces are highly sensitive to changing proportional gains ( $K_p$ ) (Figure B.5) but are robust to variations in derivative gain ( $K_d$ ). These results are expected since high proportional gains cause “stiffness” in the system whereas derivative gains affect the “damping” in a system’s response. We observed rapid changes in estimated torques and ground reaction forces at high  $K_p$  values (Figure B.5). Notably, in principle there can also be internal forces affecting contact forces. For example, a fly’s legs can squeeze the spherical treadmill with different internal forces but have identical postures.

As shown in Figure B.4, our model can match the real kinematics closely for almost every controller gain combination except for the low  $K_p, K_d$  band. By contrast, varying the gains proportionally increased the torque and force readings. Because there are no experimental data to validate these physical quantities, we selected gain values corresponding to intermediate joint torques and ground contact forces (Figure B.5). Specifically, we chose 0.4 and 0.9 for  $K_p$  and  $K_d$ , respectively. These values were high enough to generate smooth movements, and low enough to reduce movement stiffness.

### Comparing tethered and flat ground walking

To test the ability to run NeuroMechFly in an untethered context, we replayed the kinematics of a tethered walking experiment (Figure 3.5) but removed body supports and placed the model on the floor. To remove body supports, we deleted the corresponding links from the model’s description (SDF configuration file). The physics engine parameters

remained the same. The lateral friction for the floor was set to 0.1.

### Application of external perturbations

To test the stability of the untethered model walking over flat ground, we set the floor's lateral friction to 0.5 and introduced external perturbations. Specifically, we propelled solid spheres at the model according to the following equation of motion,

$$\vec{p} = \vec{r}_0 + \vec{u}_0 t + \frac{1}{2} \vec{g} t^2 \quad (3.6)$$

where,  $\vec{p}$  is the 3D target position (fly's center of mass),  $\vec{r}_0$  is the initial 3D position of the sphere,  $\vec{u}_0$  is the initial velocity vector,  $\vec{g}$  is the external acceleration vector due to gravity in the z-direction,  $t$  is the time taken by the sphere to reach the target position  $\vec{p}$  from  $\vec{r}$  with an initial velocity  $\vec{u}$ . The mass of the sphere was 3 mg and its radius 50  $\mu m$ . Spheres were placed at a distance of 2 mm from the fly's center of mass in the y-direction. With  $t$  set to 20 ms, the initial velocity of the projectile was computed using Equation 3.6. The spheres were propelled at the model every 0.5 s. Finally, at 3 s into the simulation, a 3 g sphere with a radius of 150  $\mu m$  was propelled at the fly to topple it over (Video 10).

### Analyzing NeuroMechFly's contact and collision data

The PyBullet physics engine generates forward dynamics simulations and collision detections. We plotted joint torques as calculated from PyBullet. To infer ground reaction forces (GRFs), we computed and summed the magnitude of normal forces resulting from contact of each tarsal segment with the ball. Gait diagrams were generated by thresholding GRFs; a leg was considered to be in stance phase if its GRFs was greater than zero. These gait diagrams were compared with a ground truth (Figure B.10) obtained by manually annotating when the legs were in contact with the ball for each video frame. Gait prediction accuracy was calculated by dividing the frames correctly predicted as being in stance or swing over the total number of frames.

Self-collisions are disabled by default in PyBullet. Therefore, for kinematic replay of grooming, we enabled self-collisions between the tibia and tarsal leg segments, as well as the antennae. We recorded normal forces generated by collisions between (i) the right and left front leg, (ii) the left front leg and left antenna, and (iii) the right front leg and right antenna. Grooming diagrams were calculated as for gait diagrams: a segment experienced a contact/collision if it reported a normal force greater than zero.

### Comparing grooming behaviors as a function of NeuroMechFly’s morphological accuracy

We replayed foreleg/antennal grooming kinematics (Figure 3.6) for three conditions to assess the degree to which biomechanical realism is important for collision estimation. We tested two experimental conditions: one in which both front legs were modelled as sticks, and one in which the front legs as well as the antennae were modelled as sticks. Notably, multisegmented tarsi are not found in other published insect stick models (Daun-Gruhn, 2011). Thus, as for our previous model (Ramdya et al., 2017b), each stick leg consisted of four segments: coxa, trochanter/femur, tibia, and one tarsal segment. Each leg and antennal stick segment had a diameter equal to the average diameter of the corresponding segment in our more detailed NeuroMechFly model. These changes were accomplished by modifying the model’s description (SDF configuration file) and by changing the collision and visual attributes for each segment of interest.

### 3.3.3 Neural network parameter optimization

#### CPG network architecture

For evolutionary optimization of neuromuscular parameters, we designed a CPG-based controller composed of 36 nonlinear oscillators (Figure 3.7), as for a previous investigation of salamander locomotion (Ijspeert et al., 2007). These CPGs consisted of mathematical oscillators that represent neuronal ensembles firing rhythmically in the Ventral Nerve Cord (VNC) (Mantziaris, Bockemühl, and Büschges, 2020). The CPG model was governed by the following system of differential equations:

$$\dot{\theta}_i = 2\pi\nu_i + \sum_j r_j w_{ij} \sin(\theta_j - \theta_i - \phi_{ij}) \quad (3.7)$$

$$\dot{r}_i = a_i(R_i - r_i) \quad (3.8)$$

$$M_i = r_i(1 + \sin(\theta_i)) \quad (3.9)$$

where the state variables—phase and amplitude of the oscillator  $i$ —are denoted  $\theta_i$  and  $r_i$ , respectively;  $\nu_i$  and  $R_i$  represent oscillator  $i$ ’s intrinsic frequency and amplitude,  $a_i$  is a constant. The coupling strength and phase bias between the oscillator  $i$  and  $j$  are denoted  $w_{ij}$  and  $\phi_{ij}$ , respectively.

During optimization, for the entire network of coupled oscillators, we set the intrinsic frequency  $\nu$  as an open parameter ranging from 6 to 10 Hz, matching the frequencies of our measured *Drosophila* joint angle movements and reported stepping frequencies (DeAngelis et al., 2019). The intrinsic amplitude  $R$  was set to 1, and the constant  $a_i$  was set to 25. To ensure a faster convergence to a phase-locked regime between oscillators, we set coupling strengths to 1000 (Cohen et al., 1982).  $M_i$  represents the cyclical activity pattern of neural ensembles activating muscles. We solved this system of differential equations using the explicit Runge-Kutta method of 5th-order with a time step of 0.1 ms.

Each oscillator pair sends cyclical bursts to flexor and extensor muscles which apply antagonistic torques to the corresponding revolute joint. We considered three DoFs per leg that were sufficient for locomotion in previous hexapod models (Daun-Gruhn, 2011) and that had the most pronounced joint angles (Figure B.13). These DoFs were (i) ThC pitch for the front legs, (ii) ThC roll for the middle and hind legs, and (iii) CTr pitch and FTi pitch for all legs. Thus, there were three pairs of oscillators optimized per leg, for a total of 36. We coupled (i) the intraleg oscillators in a proximal to distal chain, (ii) the interleg oscillators in a tripod-like fashion (the ipsilateral front and hind legs to the contralateral middle leg from anterior to posterior), (iii) both front legs to each other, and (iv) coxa extensor and flexor oscillators to one another. Intraleg coordination is equally important to generate a fly-like gaits since stance and swing phases depend on intrasegmental phase relationships. For this reason, both interleg (phase relationships between ThC joints) and intraleg (phase relationships within each leg) couplings were optimized for one half of the body and mirrored on the other.

### Muscle model

We adapted an ‘Ekeberg-type’ muscle model (Ekeberg, 1993b) to generate torques on the joints. This model simulates muscles as a torsional spring and damper system, allowing torque control of any joint as a linear function of motor neuron (CPG output) activities driving antagonist flexor ( $M_F$ ) and extensor ( $M_E$ ) muscles controlling that joint. The torque exerted on a joint is given by the equation:

$$T = \alpha(M_F - M_E) + \beta(M_F + M_E + \gamma)\Delta\varphi + \delta\dot{\varphi} \quad (3.10)$$

where  $\alpha, \beta, \gamma$ , and  $\delta$  represent the gain, stiffness gain, tonic stiffness, and damping coefficient, respectively (Ijspeert, 2001).  $\Delta\varphi$  is the difference between the current angle of the joint and its resting pose.  $\dot{\varphi}$  is the angular velocity of the joint. This muscle model makes it possible to control the static torque and stiffness of the joints based on optimized muscle coefficients— $\alpha, \beta, \gamma, \delta$ , and  $\Delta\varphi$ .

### CPG network and muscle parameter optimization

To identify neuromuscular network parameters that could coordinate fast and statically stable locomotion, we optimized the phase differences for each network connection, the intrinsic frequency of the oscillators, and five parameters controlling the gains and resting positions of each spring and damper muscle (i.e.,  $\alpha, \beta, \gamma, \delta$ , and  $\Delta\varphi$ ). To simplify the problem for the optimizer, we (i) fixed ThC flexor-extensor phase differences to  $180^\circ$ , making them perfectly antagonistic, (ii) mirrored the phase differences from the right leg oscillators to the left leg oscillators, (iii) mirrored muscle parameters from the right joints to the left joints, and (iv) mirrored phase differences from ThC-ThC flexors to ThC-ThC extensors. Thus, a total of 63 open parameters were set by optimization: five phases between ThC CPGs (Figure 3.7, A), 12 phases between intraleg CPGs (ThC-FTi extensor/flexor, FTi-TiTa extensor/flexor per leg), 45 muscle parameters (five per joint), and one parameter ( $\nu$ ) controlling the intrinsic frequency of the oscillators. We empirically set the lower and upper bounds for the parameters so leg movements would stay stable along the boundaries (Table B.6). Upper and lower bounds for the resting positions of the joints used in the muscle model were set as the first and third quartiles of measured locomotor angles. Finally, we optimized the intrinsic frequency of CPGs, denoted by  $\nu$  in Eq. 3.7 to be between 6 and 10 Hz for the reasons described above.

For parameter optimization, we used NSGA-II (Deb et al., 2002), a multi-objective genetic algorithm implemented in Python using the jMetalPy library (Benitez-Hidalgo et al., 2019). We defined two objective functions. First, we aimed to maximize locomotor speed, as quantified by the number of spherical treadmill rotations (Equation 3.11) along the  $Y$  axis within a specific period of time. Second, we maximized static stability<sup>I</sup>. In small animals like *Drosophila*, static stability is a better approximation for overall stability than dynamic stability (Szczecinski, Bockemühl, et al., 2018). We measured static stability by first identifying a convex hull formed by the legs in stance phase. If there were less than three legs in stance and a convex hull could not be formed, the algorithm returned -1, indicating static instability. Then, we measured the closest distance between the fly's center of mass—dynamically calculated based on the fly's moving body parts—and the edges of the convex hull. Finally, we obtained the minimum of all measured distances at that time step. If the center of mass was outside the convex hull, we reversed the sign of the minimum distance to indicate instability. Because the optimizer works by minimizing objective functions, we inverted the sign of speed and stability values: the most negative values meant the fastest and most stable solutions, respectively.

Four penalties were added to the objective functions. First, to make sure the model was always moving, we set a moving lower and upper threshold for the angular rotation of the ball, increasing from  $-0.2\text{ rad}$  to  $1.0\text{ rad}$  and from 0 to  $7.2\text{ rad}$  in one second, respectively. These values were determined such that the lower moving boundary was slower than the

<sup>I</sup>The ability of the animal to remain upright at any given moment of the gait cycle

slowest reported walking speed of *Drosophila* ( $10 \text{ mm/s} = 2 \text{ rad}$  when the ball radius  $r$  is  $5 \text{ mm}$ ) (DeAngelis et al., 2019) and the upper moving boundary would exceed the highest reported walking speed ( $34 \text{ mm/s} = 6.8 \text{ rad}$ ) (Mendes et al., 2013). Second, to avoid high torque and velocities at each joint, we set joint angular velocities to have an upper limit of  $250 \text{ rad/s}$ , a value measured from the data collected from real fly experiments performed in the kinematic replay section. Third, because we do not introduce physical joint limits in the model, we emulated these joint limits by setting a penalty on the difference between the joint angle range observed during kinematic replay of walking and the joint angles of individual solutions. We used this penalty to prevent joint angles from generating unrealistic movements (e.g., one full rotation around a DoF). Fourth, because the optimizer can exploit the objective function by simply leaving all legs on the ground—the highest possible stability—or can rotate the ball by using as few as two legs while the remaining legs are constantly on the ground, we introduced a penalty on duty factors. Specifically, we computed the ratio of stance phase duration to the entire epoch and penalized solutions whose duty factors for each leg were outside of the range  $[0.4, 0.9]$ , based on (Mendes et al., 2013).

The optimization was formulated as follows

$$\begin{aligned} \min \quad & -10 \cdot R_b \cdot \theta_{b,\parallel} + 0.1 \cdot p_v + 0.05 \cdot p_{jl} + 0.1 \cdot p_m + 100 \cdot p_d \quad (\text{Distance \& penalty}) \\ \min \quad & -0.01 \cdot s + 0.1 \cdot p_v + 0.05 \cdot p_{jl} + 0.1 \cdot p_m + 100 \cdot p_d \quad (\text{Stability \& penalty}) \end{aligned} \tag{3.11}$$

with the following penalty terms

$$p_m^i = \begin{cases} p_t^{i-1} + 1 & \text{if } \theta_{b,\parallel} \leq (\frac{t}{t_{total}} \cdot 1.20 - 0.20) \text{ or } \theta_{b,\parallel} \geq (\frac{t}{t_{total}} \cdot 7.20) \\ p_t^{i-1} & \text{otherwise} \end{cases} \quad \text{(Moving boundary p)} \quad (3.13)$$

$$p_v^i = \begin{cases} p_v^{i-1} + 1 & \text{if } \omega > 250 \text{ rad/sec} \\ p_v^{i-1} & \text{otherwise} \end{cases} \quad \text{(Angular velocity p)} \quad (3.14)$$

$$p_{jl}^i = \begin{cases} p_{jl}^{i-1} + \sum_k \theta_k - \max(\text{joint limit}_k) & \text{if } \theta_k \geq \max(\text{joint limit}_k) \\ p_{jl}^{i-1} + \sum_k -\theta_k + \min(\text{joint limit}_k) & \text{if } \theta_k \leq \min(\text{joint limit}_k) \\ p_{jl}^{i-1} & \text{otherwise} \end{cases} \quad \text{(Joint limit p)} \quad (3.15)$$

$$p_d^i = \begin{cases} p_d^{i-1} + 1 & \text{if } \frac{t_{stance}^k}{t_{bout}^k} < 0.4 \text{ or } \frac{t_{stance}^l}{t_{bout}^l} > 0.9 \text{ for } l = 1, 2, \dots, 6 \\ p_d^{i-1} & \text{otherwise} \end{cases} \quad \text{(Duty factor p)} \quad (3.16)$$

where  $R_b$  is the ball radius (5 mm),  $\theta_{b,\parallel}$  is the angle of the ball in the direction of walking,  $t_{tot}$  is the maximum simulation duration,  $\theta_k$  is the angular position of the joint  $k$ ,  $t_{stance}^l$  and  $t_{bout}^l$  are the total times spent in stance and the entire walking epoch duration of the leg  $l$ . Every penalty was multiplied by its corresponding weight and added to the objective function. Objective functions were evaluated for 2 s ( $t_{total}$ ), a period that was sufficiently long for the model to generate locomotion. We ran 60 generations with the weights given in [Equation 3.11](#) and [Equation 3.12](#).

To avoid a high computational cost during optimization, we reduced the model's complexity by removing collision shapes, like the wings and head, that were not required for locomotion, and converting joints that are not used in the simulation (see [Table B.4](#)) from revolute to fixed. This model was saved as a new SDF file. Thus, we could reduce computational time and memory needed to check for collisions on unused body segments, and for the position controller to set unused joints to fixed positions. This simplification increased the speed of the simulation, allowing us to reduce the time step to 0.1 ms and to run optimization with larger populations. In the simulation, we used a spherical treadmill with a mass, radius, and friction coefficient of 54.6 mg, 5 mm, and 1.3, respectively. We additionally increased the friction coefficient of the leg segments from the default value of 0.5 to 1.0.



Each optimization generation had a population of 200 individuals. Optimization runs lasted for 60 generations, a computing time of approximately 20 hours per run on an Intel(R) Core(TM) i9-9900K CPU at 3.60GHz. Mutations occurred with a probability of 1.0 divided by number of parameters (63), and a distribution index of 20. We set the cross-over probability to 0.9 and the distribution index to 15 (for more details see (Benitez-Hidalgo et al., 2019)).

### Analysis of optimization results

After optimization, we selected three individual solutions from the last generation for deeper analysis. First, the objective functions were normalized with respect to their maximum and minimum values. Note that the signs of the objective functions were inverted. Then, solutions were selected as follows:

$$\begin{aligned} \text{Longest distance traveled (fastest):} & \quad i = \operatorname{argmin}(d_g) \\ \text{Highest stability coefficient (most stable):} & \quad i = \operatorname{argmin}(s_g) \\ \text{Distance-Stability minimum 2-norm (trade-off):} & \quad i = \operatorname{argmin}\left(\sqrt{d_g^2 + s_g^2}\right), \end{aligned}$$

where  $d_g$  and  $s_g$  are the vectors containing the distance and stability values, respectively, from all individuals in a given generation  $g$ .

We plotted CPG activity patterns (as represented by the couple oscillators' outputs), joint torques, joint angles, GRFs, and ball rotations from this final generation of solutions. GRFs were used to generate gait diagrams as previously described. Ball rotations were used to reconstruct the models' walking paths. The distances travelled along the longitudinal ( $x$ ) and transverse ( $y$ ) axes were calculated from the angular displacement of the ball according to the following formula:

$$\Delta x = \Delta\theta_t r \qquad \Delta y = \Delta\theta_l r,$$

where  $\Delta\theta_t$  and  $\Delta\theta_l$  denote the angular displacement around the transverse and longitudinal axes, respectively, and  $r$  is the radius of the ball.

## 3.4 Results

### 3.4.1 Constructing a data-driven biomechanical model of adult *Drosophila*

Behavior depends heavily on the body's physical constraints and its interactions with the environment. Therefore, morphological realism is critical to accurately model leg movements and their associated self-collisions, joint ranges of motion, mass distributions, and mechanical loading. To achieve this level of realism in our model, we first measured the morphology of an adult female fly using x-ray microtomography (**Video 1**). We first embedded the animal in resin to reduce blurring associated with scanner movements (**Figure 3.3A**). Then we processed the resulting microtomography data (**Figure 3.3B**) by binarizing it to discriminate between foreground (fly) and background (**Figure 3.3C**). Finally, we applied a Lewiner marching cubes algorithm (Lewiner et al., 2003) to generate a polygon mesh 3D reconstruction of the animal's exoskeleton (**Figure 3.3D**).

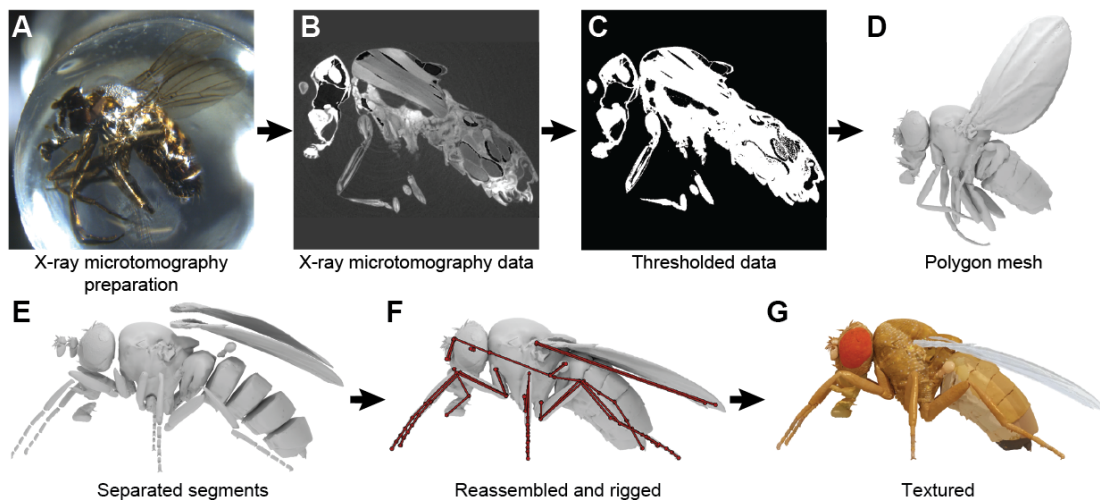


**Figure 3.3: Constructing a data-driven biomechanical model of adult *Drosophila*.** (A) An adult female fly is encased in resin for x-ray microtomography. (B) Cross-section of the resulting x-ray scan. Cuticle, muscles, nervous tissues, and internal organs are visible. (C) A threshold is applied to these data to separate the foreground (white) from the background (black). (D) A 3D polygon mesh of the exoskeleton and wings is constructed. (E) Articulated body parts are separated from one another. (F) These parts are reassembled into a natural resting pose. Joint locations are defined and constraints are introduced to create an articulated body (dark red). (G) Textures are added to improve the visual realism of the model.

Subsequently, to articulate appendages from this polygon mesh, we separated the body into 65 segments (see [Table B.1](#))(**Figure 3.3E**) and reassembled them into an empirically defined natural resting pose. Joints were added manually to permit actuation of the antennae, proboscis, head, wings, halteres, abdominal segments, and leg segments. Leg articulation points were based on observations from high-resolution videography (Günel

et al., 2019), and previously reported leg DoFs (Soler et al., 2004; Sink, 2006; Cruse et al., 2007)(Table B.1)(Figure 3.3F). By measuring leg segment lengths across animals ( $n = 10$ ), we confirmed that the model’s legs are within the range of natural size variation (Figure B.1).

To facilitate the control of each DoF in the physics engine, we used hinge-type joints to connect each of the body parts. We later show that this approximation permits accurate replay of leg end-effector trajectories. Therefore, to construct thorax-coxa joints with three DoFs, we combined three hinge joints along the yaw, pitch, and roll axes of the base link. Finally, we textured the model for visualization purposes (Figure 3.3G). This entire process yielded a rigged model of adult *Drosophila* with the morphological accuracy required for biomechanical studies as well as, in potential future work, model-based computer vision tasks like pose estimation (Loper et al., 2015; Zuffi et al., 2017; Li et al., 2020; Mu et al., 2020; Bolaños et al., 2021).

### 3.4.2 Identifying minimal joint degrees-of-freedom required to accurately replay real 3D leg kinematics

After constructing an articulating biomechanical model of an adult fly, we next asked whether the six reported and implemented leg DoFs—(i-iii) thorax-coxa (ThC) elevation/depression, protraction/retraction, and rotation, (iv) coxa-trochanter (CTr) flexion/extension, (v) femur-tibia (FTi) flexion/extension, and (vi) tibia-tarsus (TiTa) flexion/extension (Soler et al., 2004; Sink, 2006)—would be sufficient to accurately replay measured 3D leg kinematics. We did not add a trochanter-femur (TrF) joint because the *Drosophila* trochanter is thought to be fused to the femur (Sink, 2006). For the middle and hind legs, ThC protraction/retraction occurs along a different axis than similarly named movements of the front legs. Therefore, we chose to instead use the notations ‘roll’, ‘pitch’, and ‘yaw’ to refer to rotations around the anterior/posterior, medial/lateral, and dorsal/ventral axes of articulated segments, respectively (Video 2).

For our studies of leg kinematics, we focused on forward walking and grooming, two of the most common spontaneously-generated *Drosophila* behaviors. First, we used DeepFly3D (Günel et al., 2019) to acquire 3D poses from recordings of tethered flies behaving spontaneously on a spherical treadmill. Due to 3D pose estimation-related noise and some degree of inter-animal morphological variability (Figure B.1), directly actuating NeuroMechFly using raw 3D poses was impossible. To overcome this issue, we fixed the positions of base ThC joints as stable reference points and set each body part’s length to its mean length for a given experiment. Then, we scaled relative ThC positions and body part lengths using our biomechanical model as a template. Thus, instead of using 3D Cartesian coordinates, we could now calculate joint angles that were invariant across animals and that matched the DoFs used by NeuroMechFly. At first we calculated these joint angles for the six reported DoFs (Soler et al., 2004; Sink, 2006) by computing the

dot product between the global rotational axes and coxal joints and between adjacent leg segments joined by single-rotational joints (see Materials and Methods).

When only these six DoFs were used to replay walking and grooming, we consistently observed a large discrepancy between 3D pose-derived Cartesian joint locations and those computed from joint angles via forward kinematics (Figure 3.4, Base DoF Dot product). Visualization of these errors showed significant out-of-plane movements of the tibia and tarsus (Video 3, top-left). This was surprising given that each leg is thought to consist of a ball-and-socket joint (three DoFs in the ThC joint) followed by a series of one DoF hinge joints that, based on their orientations, should result in leg segments distal to the coxa residing in the same plane. Therefore, we next tried to identify alternative leg configurations that might better match 3D poses. First we performed an inverse kinematics optimization of joint angles rather than dot product operations. This would allow us to identify angle configurations that minimize error at the most distal tip of the kinematic chain—in this case, the pretarsus. Although inverse kinematics yielded a lower discrepancy (Figure 3.4, Base DoF Inverse kinematics), we still observed consistent out-of-plane leg movements (Video 3, top-middle).

We next examined whether an extra DoF might be needed at the CTr joint to accurately replicate real fly leg movements. This analysis was motivated by the fact that: (i) other insects use additional stabilizing rotations at or near the TrF joint (Watson et al., 2002; Frantsevich and Wang, 2009; Bender et al., 2010; Zill et al., 2017), (ii) unlike other insects, the *Drosophila* trochanter and femur are fused, and (iii) *Drosophila* hosts reductor muscles of unknown function near the CTr joint (Soler et al., 2004). To ensure that any improvements did not result simply from overfitting by increasing the number of DoFs, we also tested the effect of adding one roll or yaw DoF to each of the more distal hinge-type joints (CTr, FTi and TiTa)(Video 2). Indeed, for both walking (Video 3, top-right) and foreleg/antennal grooming (Video 4, top-right), we observed that adding a CTr roll DoF to the six previously reported (‘base’) DoFs significantly and uniquely reduced the discrepancy between 3D pose-derived and forward kinematics-derived joint positions, even when compared with improvements from inverse kinematics (Figure 3.4, Base DoF & CTr roll; for statistical analysis, see Table B.2 and Table B.3). This improvement was also evident on a joint-by-joint basis for walking (Figure B.2) and grooming (Figure B.3) and it was not achieved by any other kinematic chain tested—a result that argues against the possibility of over-fitting (Figure 3.4, Base DoF & CTr yaw, Base DoF & FTi roll, Base DoF & FTi yaw, Base DoF & TiTa roll, Base DoF & TiTa yaw). These findings demonstrate that accurate kinematic replay of *Drosophila* leg movements requires seven DoFs per leg: the previously reported six DoFs (Soler et al., 2004; Sink, 2006) as well as a roll DoF near the CTr joint. Thus, by default, NeuroMechFly’s biomechanical exoskeleton incorporates this additional DoF for each leg (Table B.1).

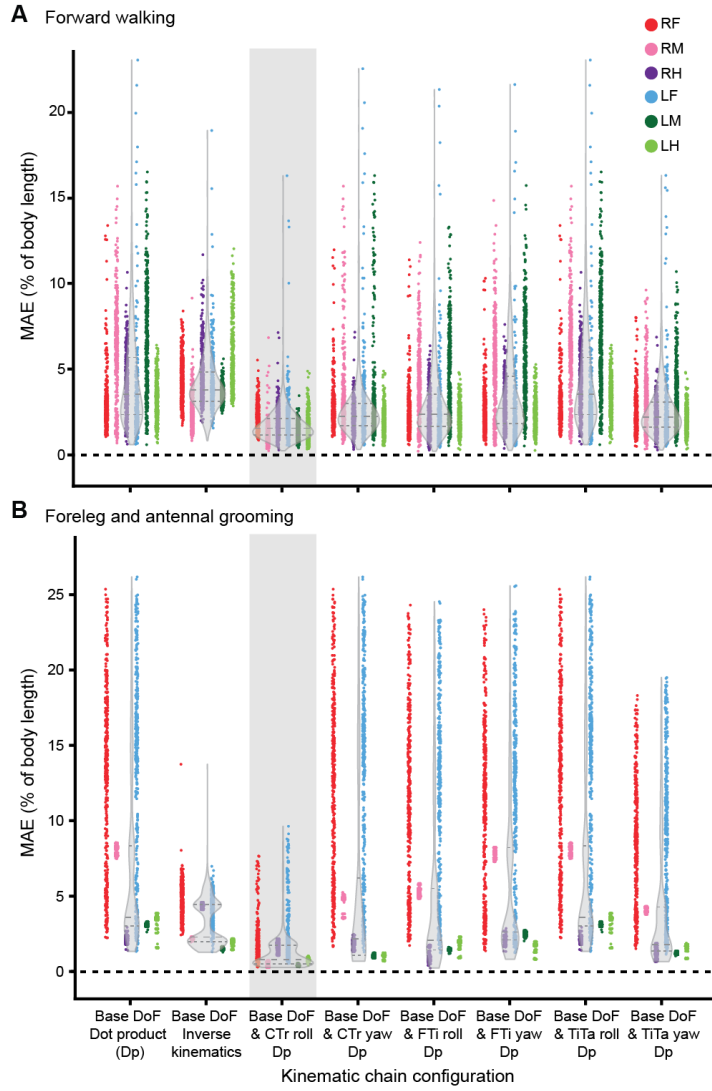


Figure 3.4: **Adding a CTr roll DoF to base DoFs enables the most accurate kinematic replay of real walking and grooming.** Body-length normalized mean absolute errors (MAE) comparing measured 3D poses and angle-derived joint positions for various DoF configurations. Measurements were made for representative examples of (A) forward walking, or (B) foreleg/antennal grooming. For each condition,  $n = 2400$  samples were computed for all six legs across 4 s of 100 Hz video data. Data for each leg are color-coded. ‘R’ and ‘L’ indicate right and left legs, respectively. ‘F’, ‘M’, and ‘H’ indicate front, middle, and hind legs, respectively. Violin plots indicate median, upper, and lower quartiles (dashed lines). Results from adding a coxa-trochanter roll DoF to based DoFs are highlighted in light gray.

### 3.4.3 Using NeuroMechFly to estimate joint torques and contact forces through kinematic replay of real fly behaviors

Having identified a suitable set of leg DoFs, we next aimed to illustrate the utility of NeuroMechFly as a biomechanical model within the PyBullet physics-based environment.

PyBullet is an integrative framework that not only gives access to collisions, reaction forces, and torques but also imposes gravity, time, friction, and other morphological collision constraints, allowing one to explore their respective roles in observed animal behaviors. Specifically, we focused on testing the extent to which one might use kinematic replay of real behaviors to infer torques, and contact forces like body part collisions and ground reaction forces (GRFs)—quantities that remain technically challenging to measure in small insects like *Drosophila* (D. Cofer et al., 2010; Guo et al., 2018). Although kinematic replay may not provide information about internal forces that are not reflected in 3D poses (e.g., how tightly the legs grip the spherical treadmill without changes in posture), estimates of collisions and interaction forces may be a good first approximation of an animal’s proprioception and mechanosensation.

We explored this possibility by using a proportional-derivative (PD) controller implemented in PyBullet to actuate the model’s leg joints, replaying measured leg kinematics during forward walking and foreleg/antennal grooming. We used joint angles and angular velocities as target signals for the controller. Because, when applying this kind of controller, there is no unique set of contact solutions that match forces and torques to prescribed kinematics (i.e., experimental validation of force estimates would ultimately be necessary), we first quantified how sensitive torque and force estimates were to changes in PD controller gains. Based on this sensitivity analysis, we selected gain values that optimized the precision of kinematic replay (Figure B.4, blue squares) and for which small deviations did not result in large variations in measured physical quantities (Figure B.5, red traces). We included all seven leg degrees-of-freedom from our error analysis (Figure B.6) and the model’s ‘zero-angle pose’ was selected to make joint angles intuitive (Figure B.7). We also set fixed values for the orientation of abdominal segments, wings, halteres, head, proboscis, and antennae to generate a natural pose (Table B.4).

When we replayed walking (Figure 3.5A-C)(Video 5) and foreleg/antennal grooming (Figure 3.6A-C) (Video 6), we observed that the model’s leg movements were largely identical to those measured from *Drosophila*. By measuring real ball rotations (Moore et al., 2014) and comparing them with simulated spherical treadmill rotations, for a range of soft constraint parameters (Figure B.8), we quantified high similarity between real and simulated spherical treadmill forward velocities (Figure B.9D), and to some extent, yaw velocities (Figure B.9F). Sideways velocities were smaller and, thus, difficult to compare (Figure B.9E). This was notable given that the ball’s rotations were not explicitly controlled but emerged from tarsal contacts and forces in our simulation. These observations support the accuracy of our computational pipeline in processing and replaying recorded joint positions.

Next, we more directly validated collisions and forces computed within the PyBullet physics-based simulation environment. From kinematic replay of joint angles during walking (Figure 3.5E, top), we measured rich, periodic torque dynamics (Figure 3.5E, middle). These were accompanied by ground reaction forces (GRFs) that closely tracked subtle



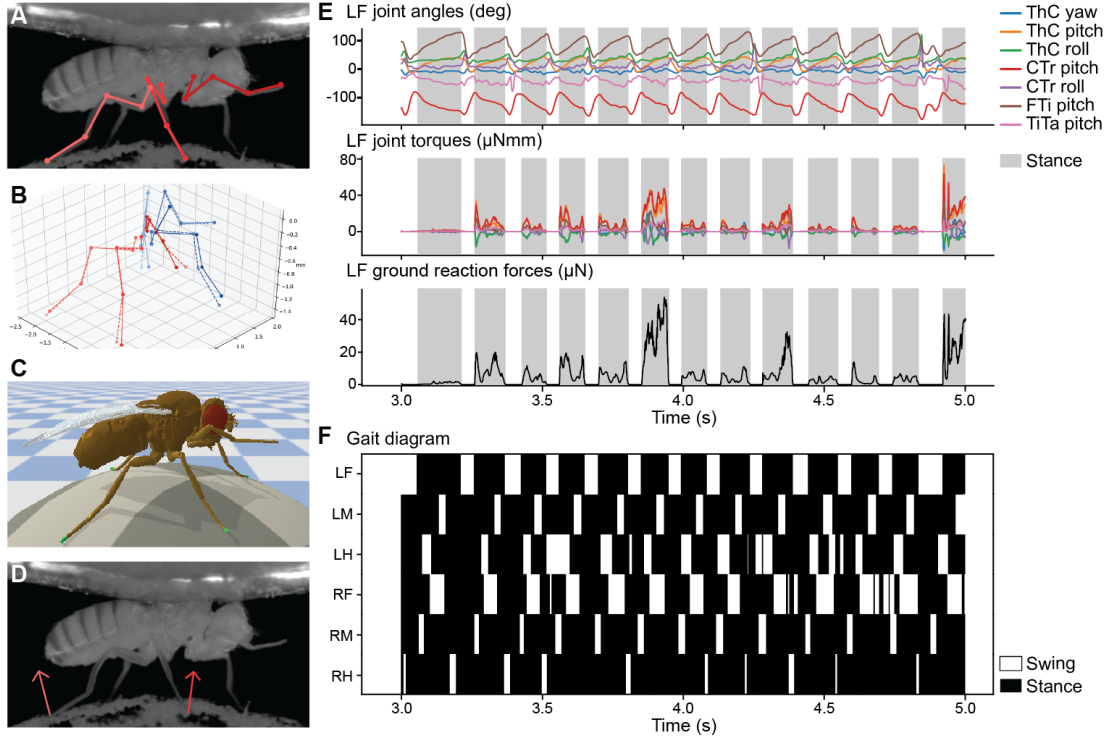


**Figure 3.5: Kinematic replay of forward walking allows the estimation of ground contacts and reaction forces.** (A) Multiple cameras and deep learning-based 2D pose estimation are used to track the positions of each leg joint while a tethered fly is walking on a spherical treadmill. (B) Multiview 2D poses (solid lines) are triangulated and processed to obtain 3D joint positions (dashed lines). These are further processed to compute joint angles for seven DoFs per leg. (C) Joint angles are replayed using PD control in NeuroMechFly. Body segments in contact with the ground are indicated (green). (D) Estimated ground reaction force vectors (red arrows) are superimposed on original video data. (E, top) Kinematic replay of real 3D joint angles permits estimation of unmeasured (E, middle) joint torques, and (E, bottom) ground reaction forces. Only data for the left front leg (LF) are shown. Grey bars indicate stance phases when the leg is in contact with the ground. Joint DoFs are color-coded. (F) A gait diagram illustrating stance (black) and swing (white) phases for each leg as computed by measuring simulated tarsal contacts with the ground.

differences in leg placement across walking cycles (Figure 3.5E, bottom). Superimposing these GRF vectors on raw video recordings of the fly allowed us to visualize expected tarsal forces (Figure 3.5D)(Video 5, top-left) which could also be used to generate predicted gait diagrams during tethered walking (Figure 3.5F). These predictions were highly accurate (83.5 - 87.3% overlap) when compared with manually labeled ground-truth gait diagrams for three different animals and experiments (Figure B.10). This result was notable given that the thorax is fixed and, in principle, subtle changes in attachment height could increase or decrease the duration of leg-treadmill contacts.

Similarly, for foreleg/antennal grooming (Figure 3.6A-C), we observed that measured joint angles (Figure 3.6E, top) could give rise to complex torque dynamics (Figure 3.6E, middle). Associated leg and antennal contact forces (Figure 3.6D, E, bottom) reached magnitudes about three times the fly’s weight. These fall within the range of previously observed maximum forces measured at the tip of the tibia ( $\sim 100\mu N$ ) for ballistic movements (Azevedo et al., 2020), but further experimental data will be required to fully validate these measurements. These leg and antennal contact forces were used to generate grooming diagrams—akin to locomotor gait diagrams—that illustrate predicted contacts between distal leg segments and the antennae (Figure 3.6F). During leg-leg grooming, we observed collisions that moved continuously along the leg segments in proximal to distal sweeps. These collision data provide a richer description of grooming beyond classifying the body part that is being cleaned and can enable a more precise physical quantification of many other behaviors including, for example, inter-animal boxing or courtship tapping. This approach also revealed the importance of having a morphologically accurate biomechanical model. When we replaced our CT scan-based leg segments and antennae with more conventional stick segments having similar diameters and lengths, we observed less rich collision dynamics including the elimination of interactions between the tarsi and antennae (Figure B.11) (Video 7).

Because our 3D pose estimates were made on a tethered fly behaving on a spherical treadmill, we also ‘tethered’ our simulation by fixing the thorax position. Next, we asked to what extent our model might be able to walk without body support (i.e., keeping its balance while carrying its body weight). To do this, we replayed 3D kinematics from tethered walking (Figure 3.5)(Video 5) while NeuroMechFly could walk freely (untethered) on flat terrain. Indeed, we observed that our model walked stably on the ground (Video 8). Although an animal’s legs would naturally be positioned differently on a curved versus a flat surface, the flexibility of NeuroMechFly’s tarsal segments allowed it to walk freely with a natural pose using 3D poses taken from tethered walking on a curved spherical treadmill. As expected, flat ground locomotion matched the velocities of tethered walking (Figure B.12) better than walking paths (Video 8): small deviations in heading direction yield large changes in trajectories.

In summary, we have shown how NeuroMechFly’s biomechanical exoskeleton—without muscle or neuron models—can be used to replay real 3D poses to estimate otherwise inaccessible physical quantities like joint torques, collisions, and reaction forces that are accessible from its physics-based simulation engine.

#### 3.4.4 Using NeuroMechFly to explore locomotor controllers by optimizing CPG-oscillator networks and muscles

As a full neuromechanical model, NeuroMechFly consists not only of biomechanical elements, like those used for kinematic replay, but also neuromuscular elements. In our



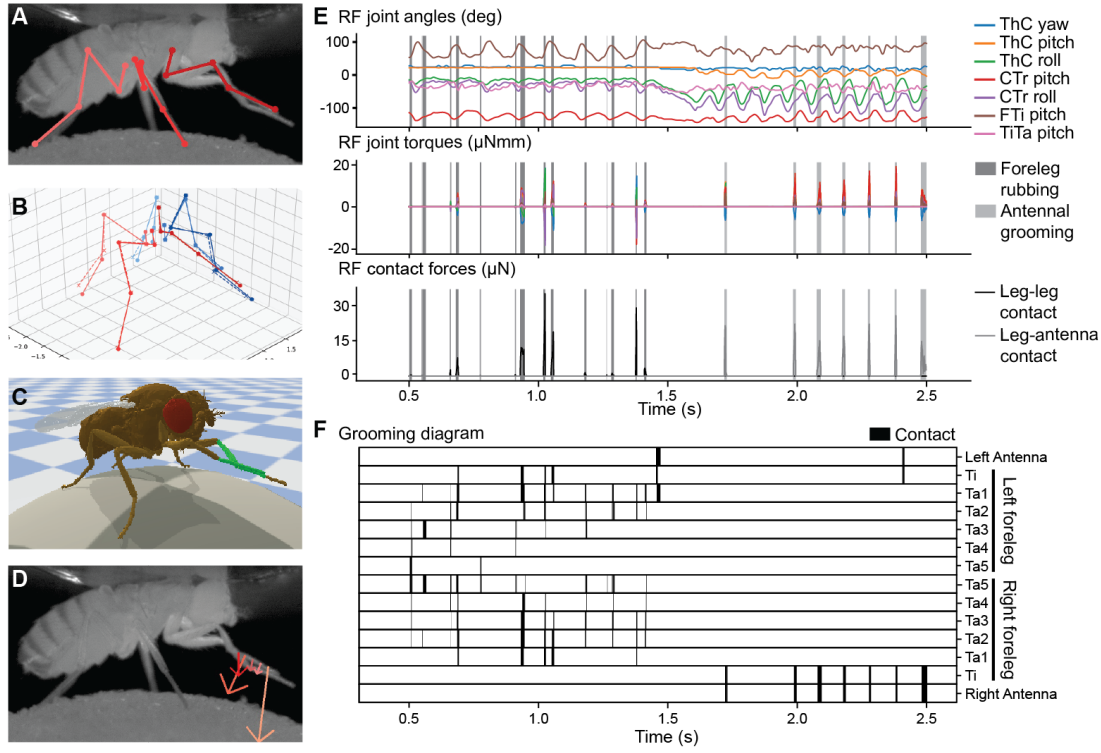


Figure 3.6: **Kinematic replay allows the estimation of self-collisions and reaction forces during foreleg/antennal grooming.** (A) Multiple cameras and deep learning-based 2D pose estimation are used to track the positions of each leg joint while a tethered fly grooms its forelegs and antennae. (B) Multiview 2D poses (solid lines) are triangulated and processed to obtain 3D joint positions (dashed lines). These are further processed to compute joint angles for seven DoFs per leg. (C) Joint angles are replayed using PD control in NeuroMechFly. Body segments undergoing collisions are indicated (green). (D) Estimated leg-leg and leg-antennae contact forces (red arrows) are superimposed on original video data. (E, top) Kinematic replay of real joint angles permits estimations of unmeasured (E, middle) joint torques, and (E, bottom) contact forces. Only data for the right front (RF) leg are shown. Dark grey bars indicate leg-leg contacts. Light grey bars indicate leg-antenna contacts. Joints are color-coded. (F) A grooming diagram illustrating contacts (black) made by the front leg's five tarsal segments ('Ta1' and 'Ta5' being the most proximal and the most distal, respectively), tibia ('Ti'), and both antennae ('Ant').

computational framework, these represent additional modules that the investigator can define to be more abstract—e.g., leaky integrate-and-fire neurons and spring-and-damper models—or more detailed—e.g., Hodgkin-Huxley neurons and Hill-type muscle models. Parameters for neural networks and muscles that maximize user-defined objectives and minimize penalties can be identified using evolutionary optimization.

Here, to provide a proof-of-concept of this approach, we aimed to discover neuromuscular controllers that optimize fast and statically stable tethered walking. Insect walking gaits

are commonly thought to emerge from the connectivity and dynamics of networks of CPGs within the ventral nerve cord (VNC) (Proctor et al., 2010; Fuchs et al., 2011; Szczecinski, A. E. Brown, et al., 2014; Mantziaris, Bockemühl, Holmes, et al., 2017). Although alternative, decentralized approaches have also been proposed (Schilling, Hoinville, et al., 2013; Schilling and Cruse, 2020), we focused on exploring a CPG-based model of locomotor control. First, we designed a neural network controller consisting of a CPG-like coupled oscillator (Ijspeert et al., 2007) for each joint (Figure 3.7A). For simplicity, we denote the output of each coupled oscillator as the activity of a CPG. These CPGs, in turn, were connected to spring-and-damper (‘Ekeberg-type’) muscles (Ekeberg, 1993b). This simple muscle model has been used to effectively simulate lamprey (Ekeberg, 1993b), stick insect (Ekeberg, Blümel, et al., 2004), and salamander (Ijspeert, 2001) locomotion.

We aimed to identify suitable neuromuscular parameters for walking in an reasonably short period of optimization time (less than 24 h per run on a workstation). Therefore, we reduced the number of parameters and, thus, the search space. Specifically, we limited controlled DoFs to those which (i) were sufficient to generate walking in other insect simulations (Daun-Gruhn, 2011) and (ii) had the most pronounced effect on overall leg trajectories in our kinematic analysis of real flies (Figure B.13). Thus, we used the following three DoFs per leg that satisfied these criteria: CTr pitch, and FTi pitch for all legs as well as ThC pitch for the forelegs and ThC roll for the middle and hind legs.

Each DoF was controlled by two coupled CPGs that drove the extensor and antagonistic flexor muscles. We assumed left-right body symmetry and optimized intraleg joint phase differences and muscle parameters for the right legs, mirroring these results for the left legs. In the same manner, we optimized the phase differences between the coxae flexor CPGs and mirrored them for the coxae extensor CPGs. Thus, we could connect 36 coupled oscillators in a minimal configuration to remove redundancy and reduce the optimization search space (Figure 3.7A). Finally, to permit a wide range of joint movements, each CPG’s intrinsic frequency was set as an open parameter, whose limits were constrained to biologically relevant frequencies observed from real fly joint movements during walking (Mendes et al., 2013; DeAngelis et al., 2019)(Figure B.13). In total, 63 open parameters were optimized including CPG intrinsic frequencies, CPG phase differences, and muscle parameters (see Materials and Methods).

We performed multi-objective optimization (Oliveira et al., 2011) using the NSGA-II genetic algorithm (Deb et al., 2002) to identify neuromuscular parameters that drove walking gaits satisfying two high-level objective functions: forward speed and static stability. Notably, these objectives can be inversely correlated: fast walking might be achieved by minimizing stance duration and reducing static stability. Forward speed was defined as the number of backward ball rotations within a fixed period of time and quantified as fictive distance traveled (Figure 3.7B, top). Static stability refers to the stability of an animal’s given pose if, hypothetically, tested while immobile. This metric can be quantified during walking as the minimal distance between the model’s center-of-

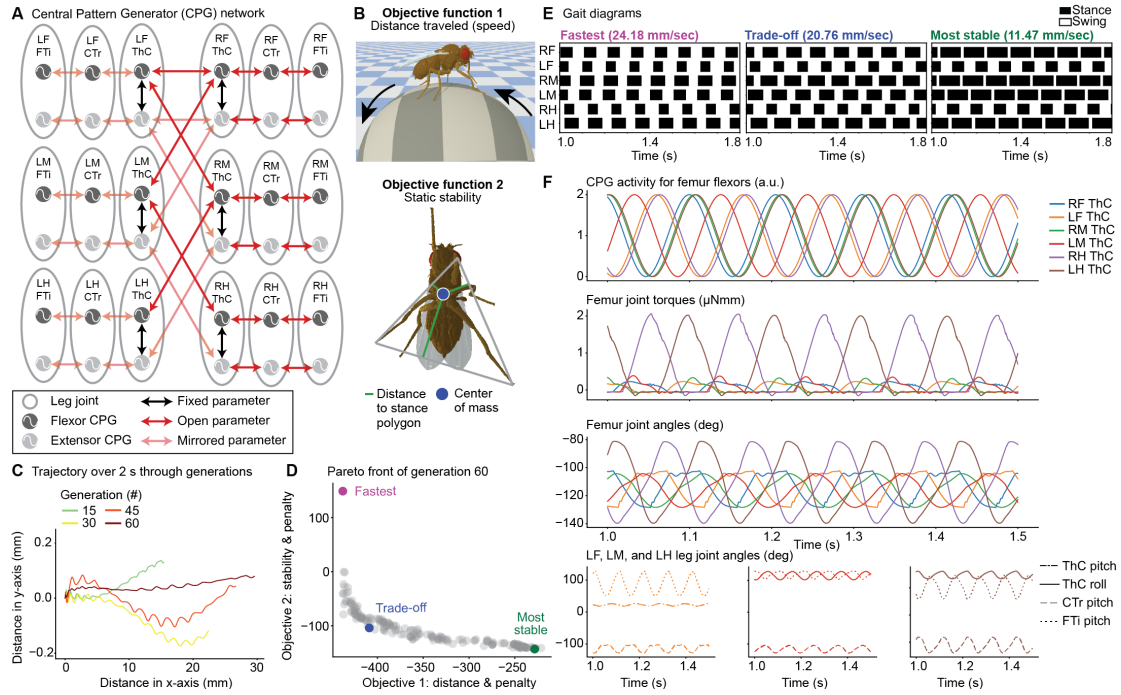


**Figure 3.7: Using evolutionary optimization to identify oscillator network and muscle parameters that achieve fast and stable locomotion.** (A) A network of coupled oscillators modeling CPG-based intra- and interleg circuits in the ventral nerve cord of *Drosophila*. Oscillator pairs control specific antagonistic leg DoFs (gray). Network parameter values are either fixed (black), modified during optimization (red), or mirrored from oscillators on the other side of the body (pink). (B) Multi-objective optimization of network and muscle parameters maximizes forward walking distance traveled (speed) and static stability. (C) A ‘trade-off’ solution’s locomotor trajectory (distance traveled over x and y axes) across 60 optimization generations. (D) Pareto front of solutions from the final (60th) optimization generation. Three individuals were selected from the population using different criteria: the longest distance traveled (fastest, purple), the most statically stable solution (‘most stable’, green), and the solution having the smallest 2-norm of both objective functions after normalization (trade-off). (E) Gait diagrams for selected solutions from generation 60. Stance (black) and swing (white) phases were determined based on tarsal ground contacts for each leg. Velocity values were obtained by averaging the ball’s forward velocity over 2 s. (F) Central Pattern Generator (CPG) outputs, joint torques, and joint angles of each leg’s femur for the ‘trade-off’ solution. Intraleg joint angles for the left front, middle, and hind legs are also shown. Legs are color-coded and joints are shown in different line styles.

mass (COM) and the closest edge of the support polygon formed by the legs in stance phase (i.e., in contact with the ground). This means that the closer the COM is to the center of the support polygon, the higher the static stability score. (Figure 3.7B, bottom). Additionally, we defined four penalties to discourage unrealistic solutions including those with excessive joint velocities (these cause jittering or muscle instability), speeds slower or

faster than real locomotion (a ‘moving boundary’), as well as joint angle ranges of motion and duty factors that violate those observed in real flies. Because the optimizer minimizes the objective functions, we inverted the sign for both functions. Thus, during optimization the Pareto front of best solutions evolved toward more negative values (Figure B.14A) and forward walking speeds became faster over generations (Figure 3.7C)(Video 9).

To more deeply investigate our optimization results, we examined three individual solutions from the final generation. These were: (i) the fastest solution, (ii) the most stable solution, and (iii) a ‘trade-off’ solution that was the best compromise between speed and static stability (see Methods for a precise mathematical definition) (Figure 3.7D). By generating gait diagrams for each of these solutions, we found a diversity of strategies—non-tripod gaits were observed in all generations (Figure B.14B) even after objectives were maximized and penalties minimized at generation 60 (Figure B.14C). However, the trade-off solution—a compromise between speed and static stability—closely resembled a typical insect tripod gait (Mendes et al., 2013; R. Strauss and Heisenberg, 1990), supporting the notion that tripod locomotion satisfies a need for stability during fast insect walking (Ramdya et al., 2017b).

Because NeuroMechFly provides access to neuromuscular dynamics and physical interactions, we could also analyze then further analyze how these underlying quantities give rise to optimized locomotor gaits. To illustrate this, we focused on the femur flexors of each leg for the ‘trade-off’ solution (Figure 3.7F). As expected for a tripod gait, stance and swing phases of the left front (LF) and hind (LH) legs were coordinated with those of the right middle (RM) leg. This coordination implies that the middle and hind legs CPG activities (Figure 3.7F, top, green and brown) are in phase with each other and phase shifted by  $180^\circ$  with respect to the front leg (Figure 3.7F, top, orange). This is because, during stance phases, the front legs flex while the middle and hind legs extend. However, for the tripod generated by other three legs, the CPG activity of the left, middle (LM) femur was phase shifted with respect to the right front (RF) and hind (RH) legs (Figure 3.7F, top, red). Torques were highest for the hind legs, suggesting an important role for driving ball rotations (Figure 3.7F, middle, purple and brown). Finally, we confirmed that the increased torque of the hind legs was associated with a larger range of motion as measured by joint angles (Figure 3.7F, bottom).

These results illustrate how, by combining our biomechanical exoskeleton with neuromuscular elements and an optimization framework, we could discover control strategies that maximize high-level behavioral objectives and minimize penalties informed by real measurements of *Drosophila*. For these solutions, neuromuscular dynamics, collisions, and forces could then be further examined because of their instantiation within a physics-based simulation environment.

### 3.5 Discussion

Here we have introduced NeuroMechFly, a computational model of adult *Drosophila* that can be used for biomechanical, and—by also including available neural and muscle models—neuromechanical studies. We first illustrated a biomechanical use case in which one can estimate joint torques and contact forces including ground-reaction forces and body part collisions by replaying real, measured fly walking and grooming. In the future, directly through force measurements (Takahashi et al., 2017; Elliott and Sparrow, 2012) or indirectly through recordings of proprioceptive and tactile neurons (Chin-Lin Chen et al., 2018; Mamiya et al., 2018), these estimates might be further validated. Next, we demonstrated a neuromechanical use case by showing how high-level optimization of a neural network and muscles could be used to discover and more deeply study locomotor controllers. Although here we optimized for speed and static stability during tethered locomotion, NeuroMechFly can also locomote without body support, opening up the possibility of optimizing neuromuscular controllers for diverse, untethered behaviors.

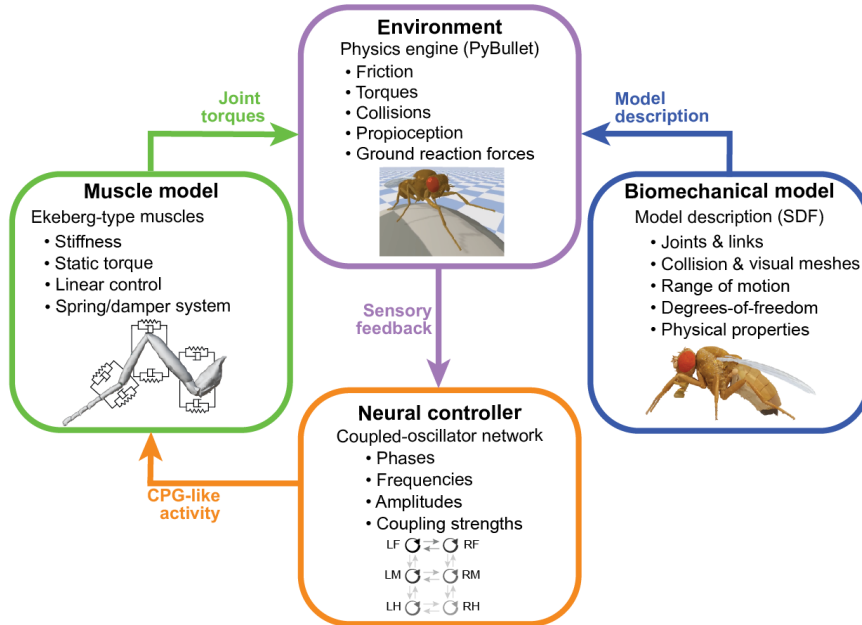


Figure 3.8: **Modules that can be independently modified in NeuroMechFly.** A neural controller’s output drives muscles to move a biomechanical model in a physics-based environment. Each of these modules can be independently modified or replaced within the NeuroMechFly simulation framework. The controller generates neural-like activity to drive muscles. These muscles produce torques to operate a biomechanical model embedded in PyBullet’s physics-based environment. When replacing any module it is only necessary to preserve the inputs and outputs (colored arrows).

### 3.5.1 Limitations and future extensions of the biomechanical module

The biomechanical exoskeleton of NeuroMechFly can benefit from several near-term extensions by the community. First, actuation is currently only implemented for leg joints. Additional effort will be required to actuate other body parts including the head, or abdomen by defining their DoFs, joint angle ranges and velocities based on 3D pose measurements. Second, the model currently achieves compliant joints during kinematic replay through position control (akin to a spring-and-damper) in PyBullet. However, future work may include implementing compliant joints with stiffness and damping based on measurements from real flies. Third, NeuroMechFly employs rigid bodies that do not reflect the flexibility of insect cuticle. Although our modeling framework could potentially include soft-bodied elements—these are supported by the underlying physics engine—we have chosen not to because it would first require challenging measurements of cuticular responses to mechanical stresses and strains (i.e. Young’s modulus) (Vincent and Wegst, 2004; Flynn and Kaufman, 2015), and this would increase the model’s computational complexity, making it less amenable to evolutionary optimization. NeuroMechFly currently supports flexibility in terms of compliance because the muscle model includes stiffness and damping terms. Additionally, the fact that kinematic replay is already accurate—with similar real and simulated joint angle and end-effector positions—suggests that modeling additional cuticular deformations might only have negligible effects. Therefore, we currently offer what we believe to be a practical balance between accuracy and computational cost. Finally, future iterations of our biomechanical model might also include forces that are observed at small scales, including Van der Waals and attractive capillary forces of footpad hairs (Kimura et al., 2020).

### 3.5.2 Limitations and future extensions of the neuromuscular modules

In addition to its biomechanical exoskeleton, NeuroMechFly includes modules for neural controllers, muscle models, and the physical environment (Figure 3.8). These interact with one another to generate rich *in silico* motor behaviors. Each of these modules can be independently modified in future work to improve biological interpretability, computational efficiency, and increase the range of possible experiments. First, more detailed neural controllers could already be implemented including Integrate-and-Fire, or Hodgkin-Huxley type neurons (Szczecinski, A. E. Brown, et al., 2014). This would aid in the comparison of discovered artificial neural networks and their dynamics with measured connectomes (Phelps et al., 2021; Scheffer et al., 2020) and functional recordings (Chin-Lin Chen et al., 2018), respectively. Second, to increase the realism of movement control, Hill-type muscle models that have nonlinear force generation properties could be implemented based on species-specific muscle properties—slack tendon lengths, attachment points, maximum forces, and pennation angles (Kuan et al., 2020; Azevedo et al., 2020). Third, to study more complex motor tasks, one can already use the PyBullet framework (Coumans, 2015) to increase the complexity of the physical environment. For example, one can study

locomotor stability by introducing external objects (**Video 10**), or locomotor strategies for navigating heightfield terrains.

In the near-term, we envision that NeuroMechFly will be used to test theories for neuromechanical behavioral control. For example, one might investigate the respective roles of feedforward versus feedback mechanisms in movement control (i.e., to what extent movements are generated by central versus sensory-driven signals). This can be tested by systematically modifying coupling strengths and sensory feedback gains in the simulation. Outcomes may then be experimentally validated. In the longer-term, this modeling framework might also be used in closed-loop with ongoing neural and behavioral measurements. Real-time 3D poses might be replayed through NeuroMechFly to predict joint torques and contact forces. These leg state predictions might then inform the delivery of perturbations to study how proprioceptive or tactile feedback are used to achieve robust movement control. In summary, NeuroMechFly promises to accelerate the investigation of how passive biomechanics and active neuromuscular control orchestrate animal behavior, and can serve as a bridge linking fundamental biological discoveries to applications in artificial intelligence and robotics.



## Chapter 4

# Spatiotemporal Maps of Proprioceptive Inputs to the Cervical Spinal Cord During Three-Dimensional Reaching and Grasping

### Overview

*Macaca fascicularis*, a nonhuman primate is the third model organism we focus on in this thesis. Due to their close genetic relationship with humans, *Macaca fascicularis* are extremely important in translating discoveries from nonhuman primates to humans for interventions in motor control treatments. A promising methodology in motor control recovery after spinal cord injury has been through epidural electrical stimulation (EES) of the spinal cord. But, for fine control of upper limb movements, Electrical stimulation of afferent fibers interfere with other neural activity. In this chapter, we developed a musculoskeletal framework of *Macaca fascicularis* upper limb to estimate spatiotemporal maps of individual afferent fibers for reaching and grasping task. Using our framework, researchers can design better EES strategies for multi-joint limb control rehabilitation.



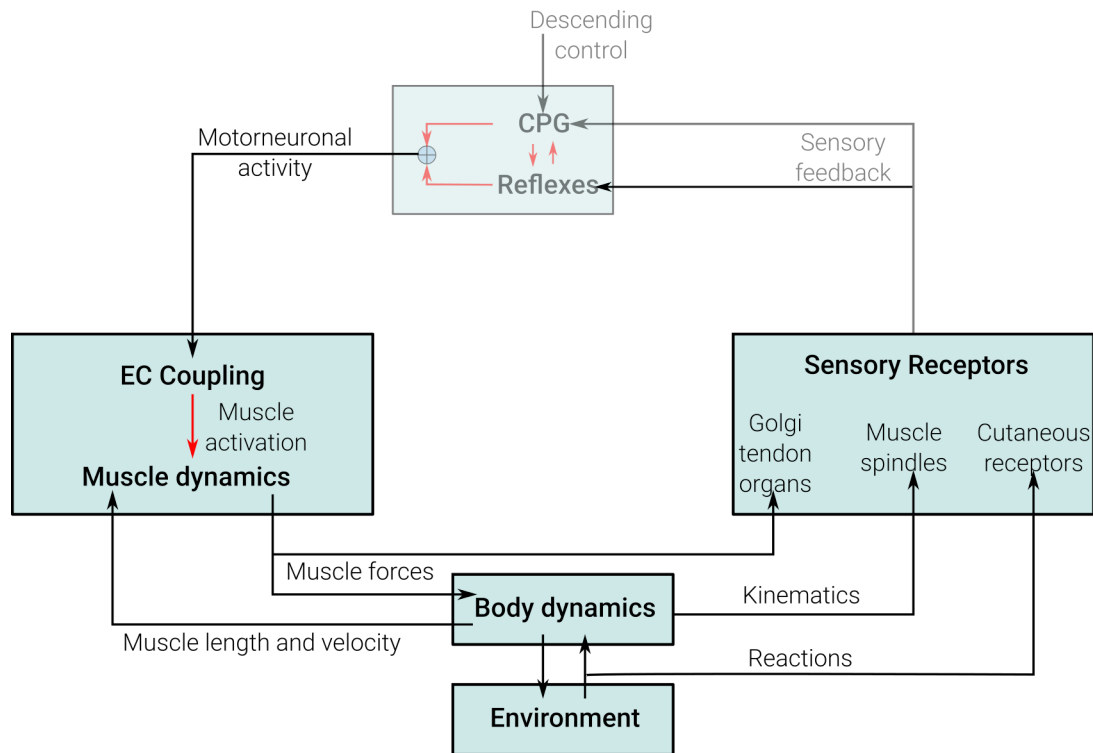


Figure 4.1: Focus of this chapter in the scheme of neuromechanical loop described in 1.1 for movement generation

### Reference publication

The following sections are based on our published article “Pierre Kibleur, Shravan R. Tata, Nathan Greiner, Sara Conti, Beatrice Barra, Katie Zhuang, Melanie Kaeser, Auke Ijspeert, and Marco Capogrosso (July 2020). “Spatiotemporal Maps of Proprioceptive Inputs to the Cervical Spinal Cord During Three-Dimensional Reaching and Grasping”. In: IEEE Transactions on Neural Systems and Rehabilitation Engineering 28.7, pp. 1668–1677. ISSN: 1558-0210. DOI: [10.1109/TNSRE.2020.2986491](https://doi.org/10.1109/TNSRE.2020.2986491) ” <sup>a</sup>

### My contributions

- Development and setup of the in-silico model of *Macaca fascicularis*
- Transferring the experimentally measured model parameters to simulation
- Evaluation and analysis of results
- Revisions of the manuscript

<sup>a</sup>Second and third authors have equal contributions in this work

## **4.1 Abstract**

Proprioceptive feedback is a critical component of voluntary movement planning and execution. Neuroprosthetic technologies aiming at restoring movement must interact with it to restore accurate motor control. Optimization and design of such technologies depends on the availability of quantitative insights into the neural dynamics of proprioceptive afferents during functional movements. However, recording proprioceptive neural activity during unconstrained movements in clinically relevant animal models presents formidable challenges. In this work, we developed a computational framework to estimate the spatiotemporal patterns of proprioceptive inputs to the cervical spinal cord during three-dimensional arm movements in monkeys. We extended a biomechanical model of the monkey arm with ex-vivo measurements, and combined it with models of mammalian group-Ia, Ib and II afferent fibers. We then used experimental arm kinematics and muscle activity of two monkeys performing a reaching and grasping task to estimate muscle stretches and forces with computational biomechanics. Finally, we projected the simulated proprioceptive firing rates onto the cervical spinal roots, thus obtaining spatiotemporal maps of spinal proprioceptive inputs during voluntary movements. Estimated maps show complex and markedly distinct patterns of neural activity for each of the fiber populations spanning the spinal cord rostro-caudally. Our results indicate that reproducing the proprioceptive information flow to the cervical spinal cord requires complex spatio-temporal modulation of each spinal root. Our model can support the design of neuroprosthetic technologies as well as in-silico investigations of the primate sensorimotor system.

## **4.2 Introduction**

Traumatic injuries of the central and peripheral nervous system interrupt the bi-directional communication between the brain and the periphery. Neuroprosthetic systems aiming at the recovery of motor function have been mainly focused on the restoration of motor control via direct muscle stimulation (Ethier et al., 2012; Bouton et al., 2016; Ajiboye et al., 2017), peripheral nerve stimulation (Schiefer et al., 2010; Brill et al., 2018; Raspopovic et al., 2011) and spinal cord stimulation (Sunshine et al., 2013; Zimmermann et al., 2011; Holinski et al., 2016; Angeli et al., 2018; Capogrosso, Milekovic, et al., 2016; Barra et al., 2018). For example, epidural electrical stimulation (EES) (Capogrosso, Wagner, et al., 2018) of the lumbar spinal cord has shown promising results for the recovery of multi-joint movements in animals (Capogrosso, Milekovic, et al., 2016; Courtine et al., 2009) and humans (Angeli et al., 2018; Wagner et al., 2018) with spinal cord injury (SCI). EES engages motoneurons pre-synaptically by directly recruiting large myelinated afferents in the posterior roots (Rattay et al., 2000; Capogrosso, Wenger, et al., 2013). In fact, the stimulation-induced information is processed by spinal circuitry and integrated with residual descending drive and sensory signals to produce coordinated movement (Moraud et al., 2016; Edgerton et al., 2008). These encouraging clinical results have produced a surge of interest in the application of spinal cord stimulation to the cervical spinal cord to restore also arm and hand movements (Barra et al., 2018; Kasten et al., 2013; D. C. Lu et al., 2016). However, restoration of voluntary control of arm and hand movements likely requires even finer integration between stimulation signals, descending drive and natural sensory feedback (Popovic et al., 2002). Unfortunately, electrical stimulation patterns interfere with natural afferent activity (Bensmaia, 2015) leading to impairment of movement execution and conscious perception of proprioception (Formento et al., 2018). Therefore, application of EES protocols to the complex control of the upper limb should rely on precise knowledge of cervical sensorimotor circuit dynamics. More generally, any application that aims at restoring limb function (Bouton et al., 2016; Ajiboye et al., 2017), or even at the control of external devices (Collinger et al., 2013; Pandarinath et al., 2017), might benefit from the restoration of proprioceptive feedback to enhance movement quality and control (Bensmaia, 2015; Bruns et al., 2013). In this view, experimental recordings of proprioceptive afferent dynamics are pivotal to future developments in neurotechnologies. Recordings of afferent activity in humans can be performed using microneurography (Edin and Vallbo, 1990; Birznieks et al., 2001), but this technique only allows the recording of single fibers in constrained experimental settings. Alternatively, extracellular recordings of dorsal root ganglion sensory neurons can be obtained in non-primate animal models during functional movements (Stein et al., 2004; Weber et al., 2006). However, although the latter allows recording multiple fibers simultaneously, it does not readily permit discrimination between the different fiber types, which requires a-priori knowledge of the firing dynamics of each cell type during movement. Moreover, studies addressing the human upper limb sensory dynamics require more pertinent animal models such as non-human primates, in which similar invasive recordings during unconstrained functional

movements still present formidable challenges. Here we sought to combine experimental recordings of kinematics and muscle activity in monkeys with a biomechanical model of the primate arm to produce in-silico estimates and characterize the firing rates of proprioceptive fiber ensembles during arm movements.

Using OpenSim (S. L. Delp et al., [2007](#)), we extended and scaled the biomechanical model of the *Macaca mulatta* upper limb developed by Chan and Moran (Chan and Moran, [2006](#)), with dedicated ex-vivo measurements, to the size and functional parameters of *Macaca fascicularis*. We then trained two monkeys to reach and grasp a spherical object while recording arm joint kinematics and electromyograms (EMGs) of the principal arm and hand muscles. We validated this biomechanical model by comparing simulated kinematics and muscle activity with experimental recordings, and used the model to extract muscle stretches and tendon elongation parameters.

Next, we fed simulated muscle and tendon states to empirical models of group Ia, Ib and II proprioceptive afferents (Arthur Prochazka and Monica Gorassini, [1998](#); A. Prochazka and M. Gorassini, [1998](#)). Finally, we projected the simulated activity of each of the fiber ensembles onto the spinal segments hosting their homonymous motor pools, thus obtaining spatiotemporal maps of the proprioceptive input to the cervical spinal cord during movement.

### 4.3 Methods

The computational framework to estimate the firing dynamics of proprioceptive sensory afferents of the upper limb in non-human primates is presented in Figure 4.2. It consists of a biomechanical model of the primate’s right arm, fine-tuned to the muscle mechanical properties and anatomy of *Macaca fascicularis*, and in a mathematical model linking muscle and tendon stretches to firing rates of group Ia, Ib and II afferent fibers. It is complemented with an experimental dataset of the three-dimensional arm joint kinematics and muscle activity of *Macaca fascicularis* during reaching and grasping movements, and a method to project the afferent activity onto the cervical spinal segments.

#### 4.3.1 Biomechanical model

The right arm model includes 39 musculo-tendon units (MTU), 8 bone structures, and 8 joints. We adapted a SIMM (Motion Analysis Corporation, USA) model of the right arm of the *Macaca mulatta* (Chan and Moran, 2006) to OpenSim (National Center for Simulation in Rehabilitation Research, USA) and scaled each bone separately to the dimensions of the *Macaca fascicularis* arm. The parametrization of each arm segment was complemented with mass (Cheng and S. H. Scott, 2000), and resulting inertia matrix coefficients calculated for each segment taken as a homogeneous cylinder. We obtained further anatomical measurements by dissecting an arm specimen of a female *Macaca fascicularis*. During the dissection, approximate muscle fiber and tendon lengths were also measured. From a dissected muscle, and after removing the tendons, we measured the fiber volume by submerging it in a graduated beaker. We estimated the fiber principal cross-sectional area (PCSA) as the muscle belly volume divided by the muscle fiber length. Subsequently, the maximal isometric force was estimated as

$$F_{max}^M = \sigma * PCSA \quad (4.1)$$

with  $\sigma = 0.3 \text{ N/m}^2$  (Charles, Cappellari, Spence, Wells, et al., 2016). We repeated such measurements for a total of 36 muscles of the arm, hand and shoulder. By combining this dataset with reported morphological measurements of macaques (Cheng and S. H. Scott, 2000; K. M. Graham and Stephen H. Scott, 2003; Singh et al., 2002), we complemented the model with novel data and adapted it to the *fascicularis* anatomy. However given the difficulty to measure it, we kept the pennation angle parameter at null (Cheng and S. H. Scott, 2000). Measurements from a subset of representative muscles is reported in Table 4.1. Moreover, following the observations made during the dissection (For more information refer to Kibleur (2020)), we adapted several MTU lines of action, and added wrapping surfaces when necessary to prevent MTUs from crossing bones. These adjustments preserved the operating ranges of normalized MTU length and moment arm. Finally, we added a joint to improve representation of the hand. The hand bone structure was split into two pieces around the first knuckles, in order to obtain the “fingers” and the

“palm” (with the thumb). For finger actuators such as the flexor digitorum superficialis muscle (FDS), the model already included a single MTU whose distal attachment point was located on the palm. However since we wanted to allow for the simulation of power grasps, we made adaptations to the FDS and its antagonist MTU, the extensor digitorum (EDC), so that together they could actuate the new finger joint. Both MTUs were stretched and the tendon lengths increased accordingly, in order to reach opposite sides of the middle finger’s distal phalanx. A degree of freedom was created to allow fingers flexion in the range (-10, 90) degrees, where the flat hand was taken to be the neutral fingers flexion. Reserve actuators (a mechanism of OpenSim) were de-activated for 4 out of 8 joints in the model, including the elbow and shoulder flexions, and heavily constrained on the remaining 4, such as the fingers flexion. The complete model is available online (<https://c4science.ch/diffusion/NHPOPENSIM/repository/master/>).

MTU	$l_{opt}^M$ [cm]	$l_S^T$ [cm]	V [cm <sup>3</sup> ]
Extensor digitorum	7.2	7.8	3.9
Extensor digiti	7.8	5.5	2.3
Flexor digitorum superficialis	9.4	2.7	9.4
Pronator quad	1.6	0.1	0.8
Pronator teres	6.2	0.1	7.8

Table 4.1: Morphometric measurements of a subset of representative arm and forearm musculo-tendon units (MTU): Optimal fiber length ( $l_{opt}^M$ ), Tendon slack length ( $l_S^T$ ), and fiber volume ( $V$ )

### 4.3.2 Afferent fiber model

The average firing rate of group Ia, Ib and II afferent fibers can be estimated from the state of a single MTU at time  $t$  using equations developed to fit experimental recordings of afferent firing rates in cats by Prochazka and colleagues (Morau et al., 2016; A. Prochazka and M. Gorassini, 1998; Arthur Prochazka and Monica Gorassini, 1998). MTU sizes are comparable between the cat hind limb and the *Macaca fascicularis* upper limb, therefore we expect such models to offer a reasonable approximation of sensory fiber dynamics in the *fascicularis* arm. Specifically, for a given MTU, we approximated the firing rate  $f_{Ia}$  of Ia afferents as:

$$f_{Ia} = \max\{0, k_v * \text{sign}(v^M) |v^M| p_v + k_{dI} (l^M - l_{opt}^M) + k_{nI} a + c_I\} \quad (4.2)$$

which is the sum of terms that depend on fiber contraction velocity  $v^M$  [mm/s], fiber stretch (obtained as the difference between fiber length  $l^M$  [mm] and optimal fiber length  $l_{opt}^M$  [mm], parsed from the model), the normalized muscle activity  $a$ , and a baseline firing rate  $c_I$ . Please note that the optimal fiber length, which is the length at which the force

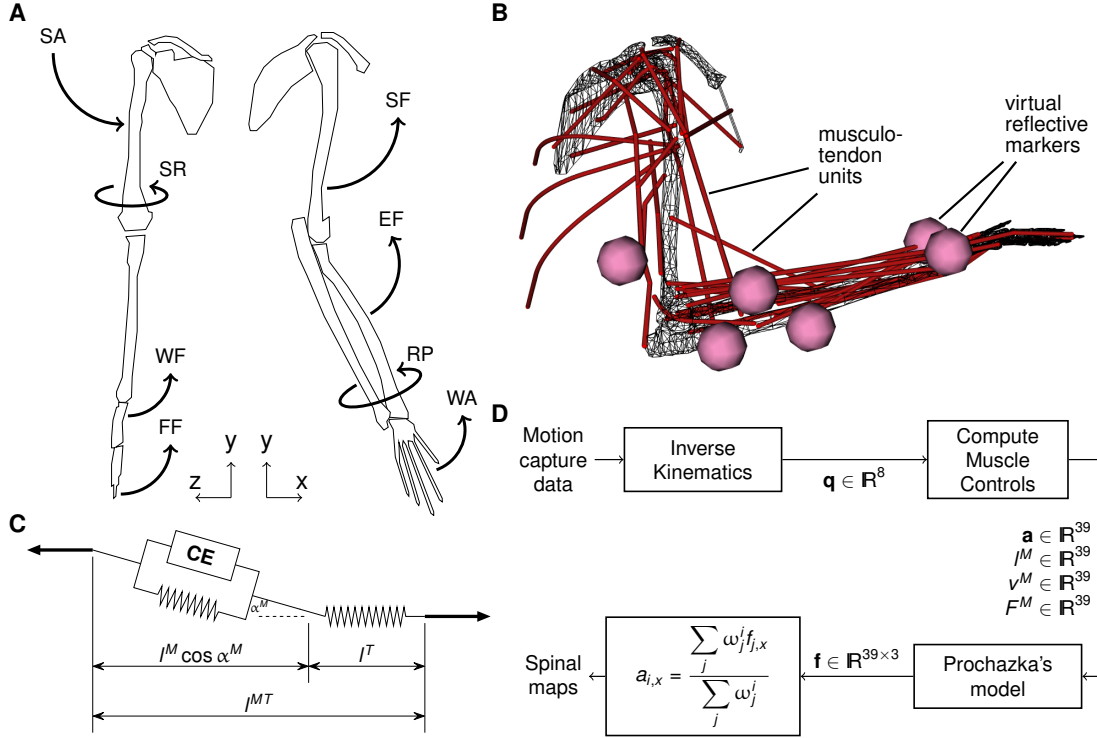


Figure 4.2: Modelling approach. A: the Macaca fascicularis right arm model of 8 bone structures, articulated around 8 degrees of freedom (SA: shoulder adduction, SR: shoulder rotation, SF: shoulder flexion, EF: elbow flexion, RP: radial pronation, WF: wrist flexion, WA: wrist abduction, FF: fingers flexion) B: 39 musculo-tendon units (MTU) allow dynamic activation of the joints. 6 virtual markers are added to the model, conform to the placement of real markers on the recorded animal. C: in the Hill muscle model, a MTU consists of a Contractile Element (CE) mounted in parallel with a passive element together representing the fiber, mounted in series with a passive element representing the tendon. D: Computational flowchart: the joint angles  $\mathbf{q}$  are produced by OpenSim's inverse kinematics, and are fed to OpenSim's CMC. The latter yields fiber properties such as the activity  $\mathbf{a}$ , the fiber length  $\mathbf{l}^M$  and its first derivative  $\mathbf{v}^M$ , as well as the fiber force  $\mathbf{F}^M$ . With linear models developed by Prochazka and Gorassini (A. Prochazka and M. Gorassini, 1998; Arthur Prochazka and Monica Gorassini, 1998), these properties are used to compute 3 types of sensory feedbacks for each of the 39 MTUs, sensory feedbacks which are then separately mapped to spinal segments to obtain spinal maps.

production can be maximal, is equivalent to the rest sarcomere length. All constants  $k_*$  and  $c_*$ , as well as  $p_v$  are numerical coefficients that have been previously determined (A. Prochazka, 1999). The numerical equations are given in Appendix. We finally enforced a lower bound firing rate of 0 [Hz] or [impulses/s] to each fiber population, to prevent negative firing rates. The firing rate of Ib afferents was estimated to be proportional to the ratio of the force exerted by the muscle fiber  $F^M$  [N] over the maximal isometric force  $F_{\max}^M$  [N]:

$$f_{Ib} = \max\{0, k_f \frac{F^M}{F_{\max}^M}\} \quad (4.3)$$

Finally, the firing of group-II spindle afferents was estimated as the sum of terms depending on fiber stretch, muscle activity, and a baseline firing:

$$f_{II} = \max\{0, k_{dII}(l^M - l_{opt}^M) + k_{nII}a + c_{II}\} \quad (4.4)$$

### 4.3.3 Experimental dataset: kinematics

Two females *Macaca fascicularis* (Mk-Sa, age 7 years, weight 4 kg and Mk-Br, age 4 years, mass 3.5 kg) were trained to reach with the left arm for a spherical object, grasp it, and pull it towards a return position to receive a food reward (Barra et al., 2018). Animals were housed within a group of five animals at the University of Fribourg, Switzerland. All experimental procedures were performed at the Platform for Translational Neuroscience at the University of Fribourg in agreement with the veterinary cantonal office of the Canton of Fribourg according to the license  $n^\circ 2017\_04\_FR$ .

We recorded three-dimensional arm-joint kinematics using the VICON Vero system (VICON, Oxford, U.K.) with 12 infrared cameras, 6 reflective markers attached to the arm joints, and 2 high definition video cameras. Two sets of  $n=9$  (Mk-Sa), and  $n=19$  (Mk-Br) reaching and grasping successful trials, each cut between the cue command and the return to start position, were extracted and used for the results of this study. Kinematic and video recordings were synchronized and sampled at 100Hz. The recordings of the reflective markers' positions in 3D were then resampled over 1000 time points. Given the constancy of the trial durations ( $1.62 \pm 0.26$  s for Mk-Sa,  $2.24 \pm 0.20$  s for Mk-Br), we proceeded to average in normalized time the marker positions across trials. The duration of this time-normalized average trial was finally scaled back to the real average trial duration in order to be fed to the chain of computations. The time point corresponding to the grasping event was manually identified in each video recording separately. The location of the markers on the arm is shown in Figure 4.2. Markers were placed at the middle of the upper arm, at the distal end of the humerus, at the elbow joint and at the proximal end of the ulna, and at the distal ends of the ulna and radius at the wrist. Finally, we artificially triggered a whole hand flexion of the model's "fingers" upon initiation of grasping by the animal. We simulated the fingers' flexions by making the fingers' joint angle follow a logistic function of time fitted to match the start and end angle values, with its step centered on the time point identified as the grasping onset. The key criterion in choosing the logistic function for this artificial joint evolution is that its first derivative is bell-shaped, which is the natural temporal profile of joint velocities



(Gribble and Ostry, 1999).

#### 4.3.4 Experimental dataset: electromyography

The monkeys were implanted with chronic bipolar teflon coated stainless steel wire electrodes in the deltoid (DEL), biceps (BIC), triceps (TRI), FDS and EDC muscles of the left arm (Cooner wires). The surgical procedures have been described elsewhere (Capogrosso, Wagner, et al., 2018). We recorded differential EMG signals at 12 kHz using a TDT RZ2 system with a PZ5 pre-amplifier (Tucker Davis Technology, USA) and synchronized them with the 3D kinematic recordings using analog triggers. Raw EMG recordings were band-passed filtered between 100 and 800 Hz (Butterworth order 3), and Notch filtered (Butterworth order 3, between 49 and 51 Hz). Then, to obtain signal envelopes for model validation purposes, the EMGs were high-pass filtered at 0.1Hz, rectified, and low-pass filtered at 10Hz (Butterworth order 3). EMG signal envelopes were normalized in amplitude (divided by their maximal value over the trial) independently for each muscle, and their time course was scaled similarly to that of the kinematic recordings.

#### 4.3.5 Estimation of Spatiotemporal maps

Proprioceptive sensory afferents, innervating muscles and tendons, converge towards the spinal cord in peripheral nerves bundled with their homonymous muscle motor axons. Therefore, we assumed that their organization within the dorsal roots matches that of their homonymous motor axons in the corresponding ventral roots. Following this assumption, the afferent activity stemming from each MTU was mapped to the dorsal roots and thus to the spinal segments using the rostro-caudal distribution of motor pools in the primate spinal cord (Jenny and Inukai, 1983). As data were missing for the deltoid in the mentioned publication, we approximated its motor pool localization using data available in humans (Schirmer et al., 2011). Table 4.2 shows the resulting proportions of motoneurons of each muscle in each cervical spinal segment, which we assumed to represent the proportions of afferent fibers of each muscle projecting to each segment as well. We estimated the input sensory activity  $a_{i,x}$  of type  $x$ , received by the  $i$ -th spinal segment, as:

$$a_{i,x} = \frac{\sum_{j=0}^{N_{mtu}} \omega_j^i f_{j,x}}{\sum_{j=0}^{N_{mtu}} \omega_j^i} \quad (4.5)$$

where  $f_{j,x}$  is the firing rate of the proprioceptive fibers of type  $x$  of the  $j$ -th MTU, and  $\omega_j^i$  the proportion of its afferent fibers projecting to the  $i$ -th spinal segment. The

considerations that led to the expression of  $a_{i,x}$  are addressed in the discussion.

The set of  $a_{i,x}$ 's can thus be represented as a color image summarizing the amount of input sensory activity of type  $x$  received by the cervical spinal cord over time, similarly to spatiotemporal maps of motoneuronal activity (Barra et al., [2018](#); Sergiy Yakovenko et al., [2002](#)).

## 4.4 Results

### 4.4.1 Model Validation

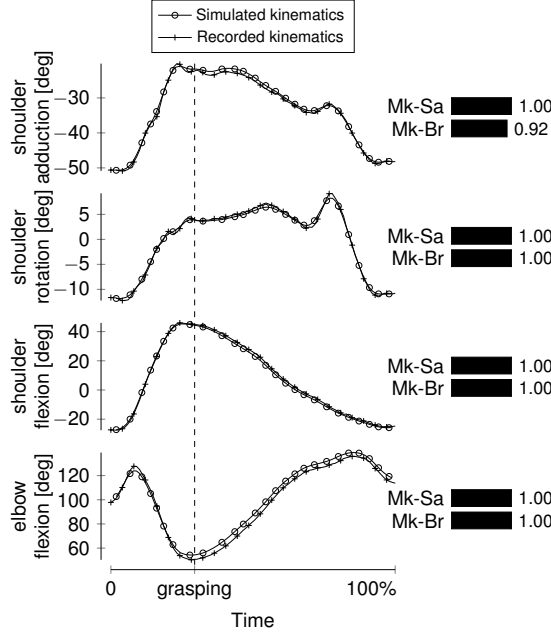


Figure 4.3: Evolution of the principal joint angles during the three-dimensional reaching and grasping task for Mk-Sa, recorded and simulated (resulting from the estimated muscle activities). The time of grasping was manually identified for each recording separately. Joint angles computed by forward dynamics, using estimated muscle activities, are in excellent agreement with experimental recordings as can be quantified with the cross-correlation between the two curves, presented in bars.

We recorded simultaneous 3D kinematics of the upper limb and EMGs of the principal upper limb muscles during an unconstrained three-dimensional reaching, grasping and pulling movement. To validate our biomechanical model, we fed averaged 3D trajectories of the joint markers to OpenSim, and computed joint angles with inverse kinematics. We then used the computed muscle control (CMC) tool to estimate a set of muscle activities, that represented a plausible solution to the inverse biomechanical problem, i.e.: what is the set of muscle activities, from which the recorded motion of the arm has originated?

Next we fed the simulated muscle activities to OpenSim's forward dynamics, thereby obtaining simulated kinematics solution to the forward biomechanical problem. Comparing the kinematics produced with this approach against the experimental joint angles (Figure 4.3) shows excellent similarity between simulated and recorded data. In particular, simulated joint angle trajectories are well within the experimental variability range of recorded data ( $R=0.90$  for Mk-Sa and  $R=0.81$  for Mk-Br). We then compared the computed muscle activities and the envelopes of recorded EMG signals from upper limb muscles. Qualitative analysis of activity patterns shows that the simulated muscle

activities match the recorded EMGs (Figure 4.4). In particular, upper arm muscles are activated in the first part of the reaching phase to lift the arm and initiate the whole limb movement. Successively, forearm and hand muscles are activated to shape the grasp, and grab the object. Finally, biceps and deltoid muscles are strongly activated during the pulling phase of the movement. Quantitative comparison between simulated muscle activities and EMG envelopes shows good correlation levels for almost all muscles in both animals (Figure 4.4). Results corresponding to cross-correlation values of about 0.50 correspond to model predictions that seem reasonably accurate. While the predictions realized for the finger actuators of Mk-Sa fall short of this accuracy, we observe outstanding accuracy for the elbow actuators of Mk-Sa, and for finger actuators of Mk-Br.

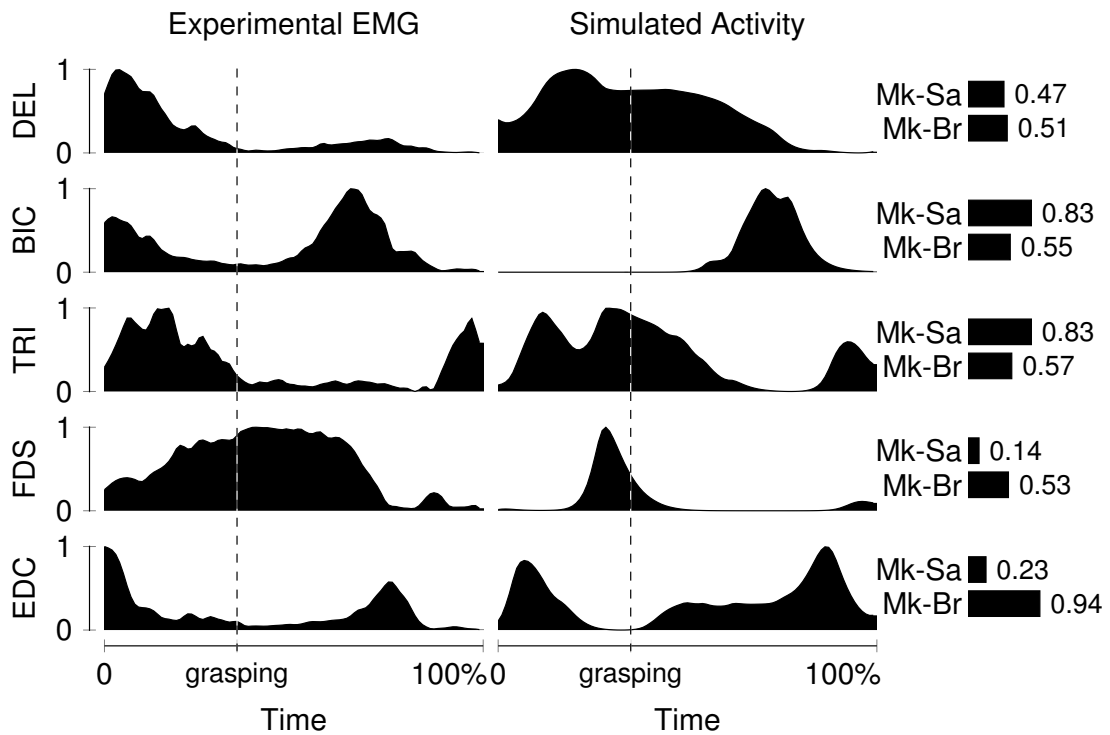


Figure 4.4: Averaged and normalized EMG envelopes, compared to computed muscle activity for Mk-Br. DEL: deltoid, BIC: biceps, TRI: triceps, FDS: flexor digitorum superficialis, EDC: extensor digitorum. Correlation between the two curves, for each monkey, are shown in bars.

#### 4.4.2 Sensory Afferent Firing rates

We estimated the firing rates of group Ia, Ib and group II afferent fibers by feeding the simulated muscle stretches and forces to the mathematical model of afferents firing rates Equation 4.2, Equation 4.4, Equation 4.3 (Note that according to A. Prochazka (1999), the velocity and length terms in the equations refer to the muscle-tendon unit length and not to fiber velocities and lengths). Given the uncertainties in the estimation of

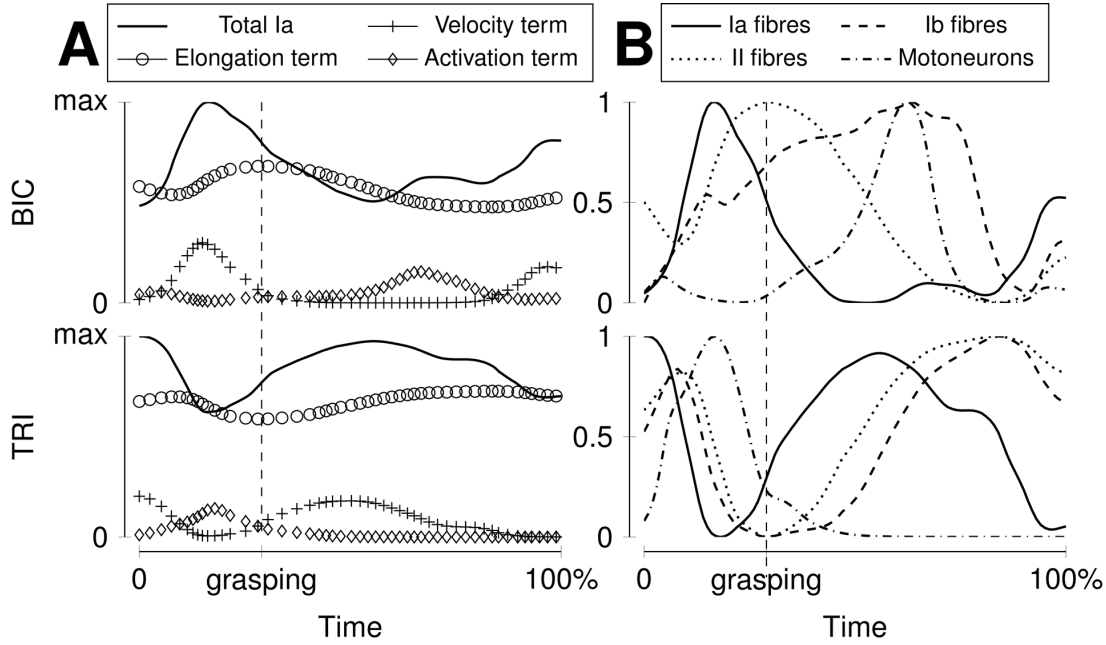


Figure 4.5: A: Decomposition of Ia sensory activity into the non-constant terms of equation 4.2, for two principal arm muscles in Mk-Sa. B: Profiles of normalized moto- and sensory-neurons activations, for two principal arm muscles in Mk-Sa.

muscle activities, it is important to evaluate the impact these can have on the outcomes of these mathematical models. Therefore, we decomposed the resulting afferent firing rates into single components. In Figure 4.5A we reported this decomposition for the agonist/antagonist of the elbow (i.e. biceps and triceps). As expected in NHPs, the muscular activity has a second-order impact on the total firing rates. Instead, it is the contraction velocity that dominates the Ia profile, which is coherent with the findings and predictions of A. Prochazka (1999). We then used our framework to compare the firing rate of each simulated sensory fiber ensemble with its homonymous muscle activity, during a whole limb three-dimensional movement (Figure 4.5B). As expected from intuition, antagonist's Ia afferents are anti-correlated. Instead, Group II and Ib afferents are not entirely anti-correlated between antagonists. Moreover, in the case of the triceps, afferents show almost complete anti-correlation with active muscle contraction. This is surprising, considered that group II and Ib afferents should respond more to active muscle force. However, this is likely resulting from the simultaneous occurrence of both passive and active tendon elongations, as well as muscle stretches, in multi-joint movements such as natural reaching.

#### 4.4.3 Spatiotemporal maps of proprioceptive inputs

Using (4.5), we projected the activity of proprioceptive sensory afferents over the spatial distribution of each fiber population along the cervical dorsal roots, thus obtaining

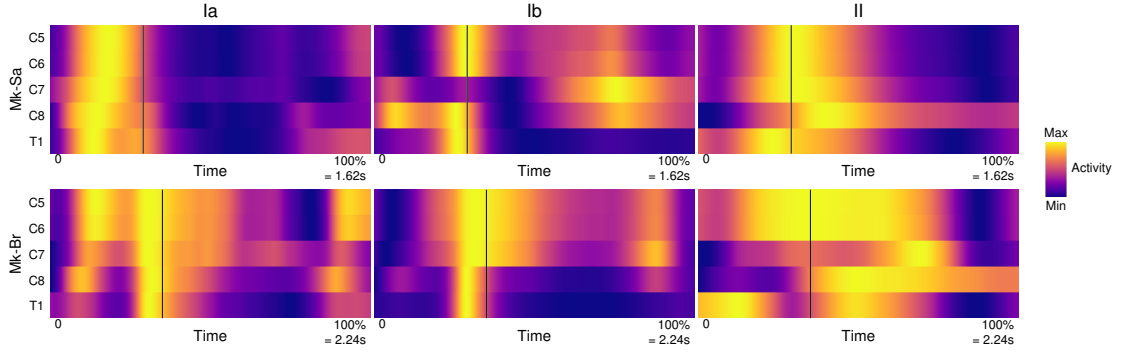


Figure 4.6: Spinal map of the three different sensory feedbacks during a standardized reaching and grasping task, for both animals. Here as well, the three identified phases present noticeably different patterns of afferent activity.

Spinal segment	DEL	BIC	TRI	FDS	EDC
C5	0.20	0.20	0.01	0.0	0.0
C6	0.47	0.47	0.05	0.0	0.0
C7	0.25	0.25	0.26	0.0	0.03
C8	0.08	0.08	0.53	0.26	0.65
T1	0.0	0.0	0.15	0.73	0.32

Table 4.2: Proportional distribution of the motor pools of Deltoid (DEL), Biceps (BIC), Triceps (TRI), Flexor digitorum superficialis (FDS) and Extensor Digitorum Communis (EDC)

spatiotemporal maps of each sensory ensemble (Table 4.2, Figure 4.6). These maps show very distinct patterns in both space and time for each of the fiber populations, across movement in both subjects. While Ia activity precedes the grasping phase, Ib, and group II activity are maximal during the pulling phase, when the animal applies maximal force. However, Ib activity shows sharp activations along the whole cervical enlargement, while group II has long bursts of activity that span the entire duration of the pulling phase. Furthermore, we performed a sensitivity analysis on the impact of muscle activation predictions, by computing spinal maps with and without the term in muscle activation terms ( $k_{nI} = 0$ ,  $k_{nII} = 0$ , in Equation 4.2 and Equation 4.4, respectively). Figure 4.7 displays maps that are remarkably similar, confirming that the most important parameters in NHPs Ia and II sensory firing rates are related to muscle stretch and stretch velocity. However, although such an analysis is not possible for the Ib afferents, we know that their firing rates uniquely depend on forces applied at the muscle, and thus they are more likely to be affected by a poor estimation of the muscle activity. Finally, we computed the total normalized proprioceptive sensory activity received by the cervical spinal cord, by summing the normalized activities of each fiber type. The resulting spatiotemporal map (Figure 4.8) shows how total proprioceptive inputs are conveyed in space and time to the cervical spinal cord during three-dimensional reaching movements. Proprioceptive activity first arises in the rostral segments, moves towards the caudal segments during

## Spatiotemporal Maps of Proprioceptive Inputs to the Cervical Spinal Cord

### Chapter 4      During Three-Dimensional Reaching and Grasping

grasp pre-shaping and finally peaks in both rostral and caudal segments during the pulling phase. In particular, it is sustained for the entire duration of the motor bursts responsible for the movement execution.

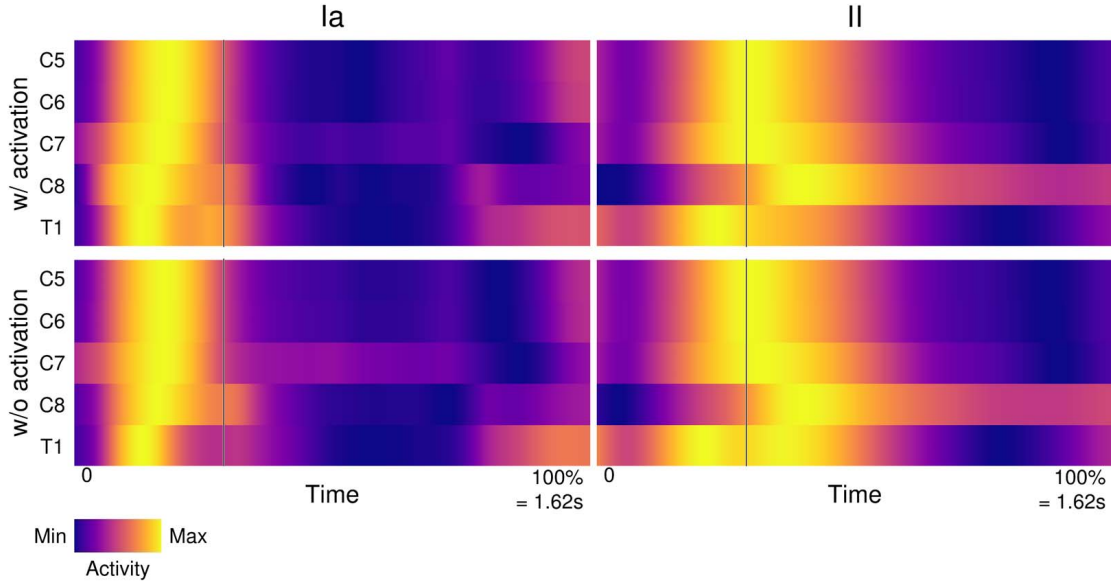


Figure 4.7: Comparison of spatiotemporal maps of sensory inputs in the cervical spinal cord for Ia- and II-type sensory activities computed by considering (top) and not considering (bottom) the muscle activation component estimated using OpenSim.

## 4.5 Discussion

We extended and validated a biomechanical model of the arm of *Macaca fascicularis* to predict the firing rates of ensembles of proprioceptive afferents during three-dimensional reaching and grasping.

### 4.5.1 A realistic primate arm model

We reworked a model of the rhesus monkey upper limb to fit the geometrical and mechanical properties of the *Macaca fascicularis* arm. We dissected most of the muscles of the arm, forearm and shoulder from a *fascicularis* arm specimen and extracted parameters such as fiber and tendon lengths, as well as fiber volume for each of the analyzed muscles, in order to refine and complement the initial model parametrization. As was the case in the original model, the joint angle space was constrained to physiological values. With forward dynamics, and with limited or de-activated (at the elbow and shoulder flexions) reserve actuators, our model was able to faithfully reproduce the recorded kinematics. This confirmed the quality of the skeletal model and its muscular parametrization. However, when comparing the computed muscle activity with the envelopes of the recorded EMG signals, we found a weaker correspondence. However, quantitative discrepancies between simulated and recorded muscle activities are common in biomechanical models ((Charles, Cappellari, and Hutchinson, 2018; Dzeladini et al., 2014)). Since we compute muscle activities from joint kinematics, our model cannot simulate the co-contraction of antagonist muscles (e.g. as occurs during stiffening of the arm). Indeed, CMC follows an optimization strategy that solves the inverse biomechanical problem by minimizing the sum of squared MTU activities, i.e. minimizing metabolic energy consumption ((Anderson and Pandy, 2001)). This generates a solution that might differ from the actual activation pattern, due to redundancy in muscle space. To bypass this limitation, other groups have resorted to EMG-driven modeling, i.e. directly using EMG recordings as inputs, instead of the result of an optimization algorithm ((Lloyd and Besier, 2003; Sartori et al., 2018)). However, calibrating such models requires long and specific protocols for each of the joints involved, protocols that are non-practical when working with NHPs. Indeed, due to the necessity of replicating diverse tasks, such studies have only been performed on human models, to the best of our knowledge. Despite these limitations, our sensitivity analysis showed that the estimation of Ia and II afferent firing rates remain unaffected by a poor estimation of muscle activation patterns, while Ib afferents could be more affected by a poor quantitative match. However, we believe that the qualitative results presented in this work remain pertinent. Indeed, the simulated muscle activity dynamics and kinematics are overall similar to those yielded by other investigations involving non-human primate upper limb models ((Chan and Moran, 2006)), strengthening our confidence in the validity of our approach ((Dzeladini et al., 2014; Sreenivasa et al., 2016)). Furthermore, the biomechanical model presented here constitutes a first step, and could later be embedded in a broader closed-loop simulation



environment. The estimated sensory activity could be used to compute motoneuronal activity, itself could be driving the evolution of arm kinematics, and in turn allow to estimate an updated distribution of sensory activity. Such an approach may enable testing for different hypotheses regarding the sensorimotor control of the upper limb.

#### **4.5.2 Sensory afferent firing dynamics**

The firing dynamics of primary sensory afferents during active functional movements is a key information to study sensorimotor integration during voluntary movement execution. Additionally, modern neuroprosthetic applications aiming at the recovery of both motor ((Formento et al., 2018)) and sensory ((Bensmaia, 2015; Valle et al., 2018)) functions in patients affected by neurological disorders often seek to design biomimetic stimulation protocols, with the underlying assumption that the most effective therapy depends on reproducing the natural activity in primary sensory afferents as closely as possible. For both these basic and translational applications, knowledge about the firing dynamics of various types of afferent fibers during functional voluntary movements is required. A sufficiently accurate computational model can be used to estimate these firing rates during multi-joint movements in dynamic tasks. Such estimates can support the interpretation of experimental data, as well as assist the design of neuroprosthetic systems that aim at reproducing these firing rates. Towards this goal, we describe a method to study sensory fiber ensembles from multiple muscles simultaneously during voluntary movements. The results that we reported show the importance of studying these signals during functional tasks. Indeed, when looking at the II and Ib afferent firing rates, we notice that in the triceps, the II, Ib afferents are not directly correlated with muscle activation (Figure 4.5). Ib afferents encode force information via tendon elongation and are thus commonly expected to be active during muscle contraction and consequent tendon elongation. However, during a multi-joint movement, active and passive tendon elongation can also occur due to the contraction of antagonist muscles, or gravity compensation. Therefore, large discrepancies from the expected firing patterns of this fiber populations may emerge as a result of complex bio-mechanical interactions, as it was likely the case in our simulations.

#### **4.5.3 Spatiotemporal patterns of proprioceptive input to the cervical spinal cord**

We assumed that the proprioceptive afferents are distributed along the rostrocaudal extent of the cervical spinal cord similarly to their homonymous motoneurons. Given the well-known strong monosynaptic connectivity between muscle spindle Ia afferents and motoneurons, this approximation seems reasonable ((Iles, 1976)). Using this assumption, we estimated the spatiotemporal distribution of the proprioceptive input to the spinal cord during arm movement. The total proprioceptive activity reaching the spinal cord

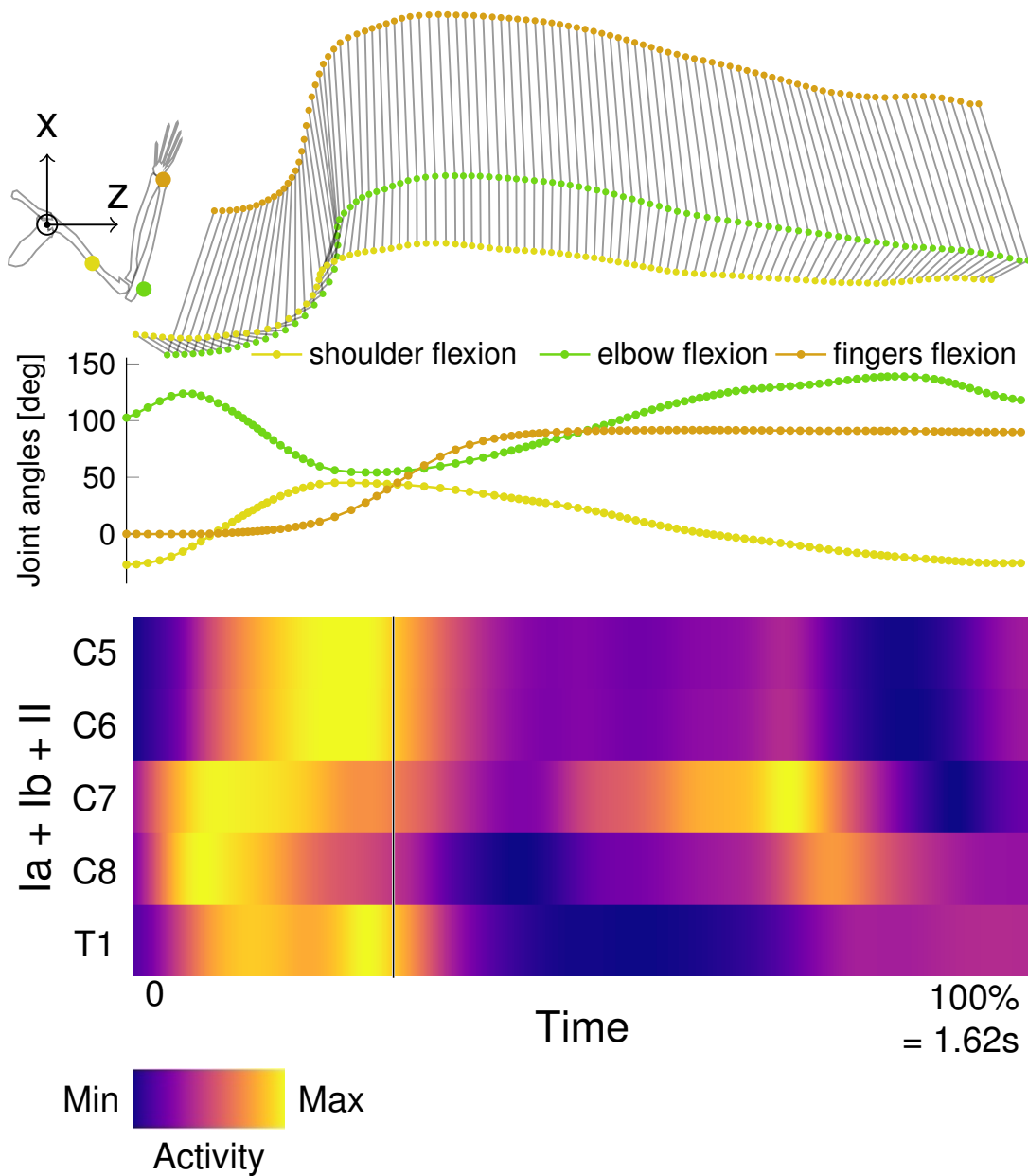


Figure 4.8: Spinal map of combined estimated proprioceptive feedbacks of Mk-Sa, during a standardized reaching and grasping task. The three identified phases present noticeably different patterns of general afferent activity.

during movement is a combination of both spindle and Golgi tendon fibers activity. This activity (Figure 4.8) arises in the form of clear bursts that span the spinal segments and are sustained across the entire duration of movement whilst being strongly modulated. This is in agreement with the well-known fact that the spinal cord receives large amounts of neural inputs during movement, and that spinal circuits are continuously fed with

information. Moreover, the neural input supplied by the different sensory fiber ensembles present markedly distinct spatiotemporal patterns, suggesting that a stimulation-based restoration of “proprioceptive” information and perception must target these three fiber populations independently.

#### **4.5.4 Insights for the design of neuroprosthetic systems**

Our results offer important insights for at least two applications in neuroprosthetics. The first important observation regards the distinct spatiotemporal patterns of each specific fiber population. Modern biomimetic strategies that aim at restoring sensation ((Valle et al., 2018)) employ electrical stimulation of the peripheral nerve to convey information to the central nervous system of amputees. However, this technology does not allow selectivity on fiber types ((Valle et al., 2018)) is particularly true for Ia and Ib fibers. Indeed, these afferents have similar diameters and thus similar recruitment thresholds making it challenging to independently control their firing rates. These fibers convey complementary information about movement and force, and our simulations show that they are active at markedly different moments during movement execution. This poses important questions on the theoretical limitations of electrical stimulation technologies to achieve realistic proprioceptive feedback in amputees. The second consideration concerns technologies aiming at the stimulation of the spinal roots such as EES. When active, electrical stimulation of a specific root will cancel the natural flow of information of each recruited afferent and substitute it with the imposed stimulation frequency ((Formento et al., 2018)). However spinal circuits require correct flow of sensory feedback to be able to produce functional movements. Therefore, development of epidural stimulation strategies of the spinal cord must take into account the spatiotemporal maps reported in Figure 4.8. For instance, the T1 spinal roots is supposed to have no input activity both at the beginning of reaching and at the end of the pulling phase. This means that stimulation targeting that root in these periods should be avoided to prevent delivery of aberrant proprioceptive information. Similar consideration can be made for the other roots.

#### **4.5.5 Model limitations**

Our model is limited by the data available for primates. Morphometric measurements, as well as live recordings, are scarce and scattered. The number of MTUs studied to obtain the spatiotemporal maps should be extended when data regarding motor pool distributions of additional muscles will be made available. Hence the reported spatiotemporal maps of proprioceptive input are built using a limited set of arm and forearm muscles. Yet, the actual proprioceptive input received by a spinal segment is the number of action potentials per unit time entering that spinal segment via all the proprioceptive fibers running in the corresponding dorsal root. However, the exact distribution of proprioceptive fiber

ensembles in the dorsal roots remains to date surprisingly unknown. We thus limited our analysis to the 5 MTUs shown in [Figure 4.4](#), for which we could estimate the relative proportions of fibers in the different spinal roots. We assigned identical weights to the Ia-afferent pools of every represented MTU (see  $a_i$ , [Equation 4.5](#)). This is equivalent to assuming that similar stretches and applied forces in these MTUs induce equal amounts of proprioceptive input to the spinal cord. This assumption may not hold if large differences in the absolute number of proprioceptive fibers exist between MTUs. The normalization introduced in [Equation 4.5](#) eases the interpretation of the spatiotemporal maps. Without this term, the input sensory activity estimated using [Equation 4.5](#) would be biased

towards those segments for which  $\sum_{j=0}^{N_{mtu}} \omega_j^i$  is larger (e.g. C6 compared to C5) and the temporal variations in the unfavored segments would have been obscured. In summary, the spatiotemporal maps shown in [Figure 4.7](#) and [Figure 4.8](#) are best interpreted in terms of normalized temporal variations of the combined proprioceptive input emerging from the selected MTUs and received by individual segments, rather than actual amounts of neural input expressed in impulses/sec.

Motion of the scapula is hard to track and was not incorporated in this study. This leads to some errors in the kinematics and the muscle activity. In future, incorporating the scapular motion will further improve the model's power of estimating spatiotemporal maps of the afferent activity in the spinal-cord.

## **4.6 Conclusion**

We presented a computational estimation of the spatiotemporal patterns of proprioceptive sensory afferent activity during three-dimensional arm movements in a clinically relevant animal model. We showed that the patterns of proprioceptive inputs during functional movements are surprisingly complex and do not necessarily match intuition. Additionally, we showed that different fiber populations have markedly distinct spatiotemporal patterns of activity, highlighting the need of recruiting these populations independently to restore the natural flow sensory information. Finally, our model can be integrated in a broader in-silico platform to simulate the effect of electrical stimulation of the sensory afferents on arm biomechanics, as well as support basic studies on sensory systems. These advancements can thus reduce the number of animals involved in invasive experiments.

## Chapter 5

# FARMS: Framework for Animal Robot Modeling and Simulation

### Overview

In the previous chapters we have seen how each of the three model organisms in experimental settings have unique advantages and disadvantages. With computational models we complemented the experimental paradigms by providing insights that are challenging to measure directly in animals. In this chapter, we propose a novel framework that aims to bring together diverse animal and robot studies in simulation. As such, FARMS could help bridge the gap to connect the various works of researchers coming from different fields, including biomechanics, neuroscience and robotics.

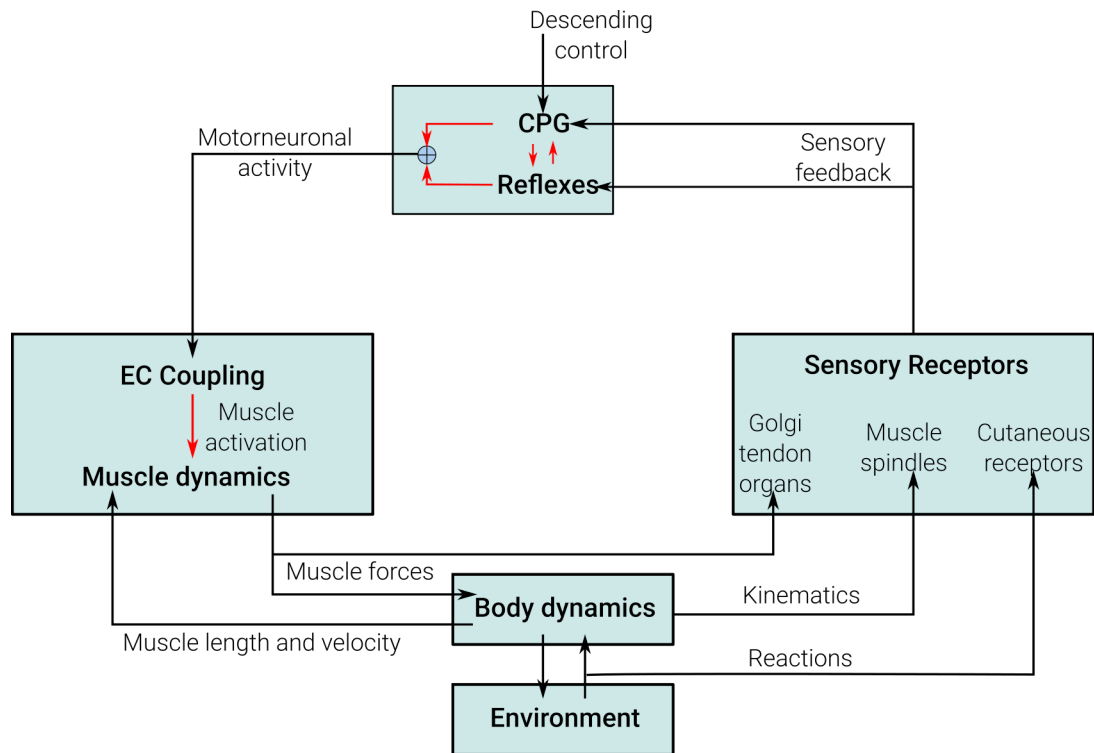


Figure 5.1: Focus of this chapter in the scheme of neuromechanical loop described in 1.1 for movement generation

### Reference publication

*The following sections are based on the article “Jonathan Arreguit, Shravan Tata Ramalingasetty and Auke Ijspeert “FARMS: Framework for Animal and Robot Modeling and Simulation” In preparation ”<sup>a</sup>*

### My Contributions

- Establishing the overall architecture of the framework
- Software development of the framework
- Drafting the original manuscript

<sup>a</sup>First and second authors have equal contributions in this work

## 5.1 Introduction

Animal movement is a result of the complex interactions between the body, the nervous system, the sensory modalities, and the environment. Each of the sub-systems have functional properties that emerge only when they interact with each other Dickinson, 2000. Studying individual components reveals only a part of the systems function. This makes studying animal movement a challenging and inter-disciplinary scientific endeavor.

The method of science simply put involves the following steps. First, make a guess<sup>I</sup> or construct an hypothesis, then compute the consequences based on the hypothesis and finally test the consequences against experimental observations. If the experimental observations do not match with the hypothesis then the hypothesis simply has to be replaced. This rigorous process of making experimental verification's and cross validations makes scientific advances slow and laborious (Capogrosso and Lempka, 2020). The process of making the initial guess is arduous. Once, the guess is made it is important to be able to make testable predictions based on the original idea. As the system of interest gets more complex, which is often the case in nature, computing testable predictions becomes as hard as making the hypothesis if not more.

To test the validity of the hypothesis, we need to collect relevant data from animal experiments. There are still several technical challenges associated with collecting animal data. These challenges vary depending on the animal species we are taking about. For example, we saw in chapter 3, in small animals such as *Drosophila melanogaster*, measuring ground reaction forces during locomotion is currently not possible. Another fundamental complication that comes up with animal experiments are the ethical restrictions. Depending on the animal, the ethical restrictions make data collection somewhere between hard to impossible. All these challenges associated with animal experiments makes it extremely important to be specific about the exact measurements needed to validate a hypothesis. It is thus important to be able to adapt the predictions to comply with measurements possible with the animal experiments.

Developing models based on existing understanding is an important way to systematically address the process of generating hypothesis and predictions to validate and further our understanding about animal movement. Models about animal movements can be of two types. One, theoretical or mathematical models and second, robots that mimic the behavior of animals. Both these approaches are essential to the field of studying animal movement motor control. Since, robotics is relatively a new technology by itself, there are several limitations associated to the replication of animal movements with robots.

Extending the meaning of theoretical or mathematical models we arrive at the idea of computer simulations. Computer simulation models of animals to study movement can be termed as neuromechanical simulations. A neuromechanical simulation integrates all

---

<sup>I</sup>The use of the word “guess” in this context is far more serious than the usual perception



## Chapter 5 FARMS: Framework for Animal Robot Modeling and Simulation

---

the fundamental blocks (as described in [Figure 5.1](#)) to reproduce animal movement. The idea of using neuromechanical simulations to study animal movement is not new. In 90's Karl Sims showed that diverse animal morphology's and locomotion behaviors can be systematically evolved using genetic algorithms (Sims, [1994b](#); Sims, [1994a](#)).

Currently, there is a strong need to contribute to the infrastructure of the neuromechanical simulation framework to further our understanding in animal motor control. A neuromechanical simulation can be either be with a model of the animal or that of a robot. The goal of this work is to setup an open-source modular framework that builds on existing tools to further the development of neuromechanical models.

To this aim, we developed FARMS (A Framework for Animal and Robot Modeling and Simulation). FARMS is a framework that is designed to be extendable and modular throughout its implementation. For example, by writing simple wrapper functions a user can integrate their favorite physics-engine to run with FARMS. The only requirement is to follow the conventions defined by FARMS while writing these wrappers. In essence, FARMS is a set principles upon which wrapper code is written to glue existing softwares. If a certain functionality is unavailable, then an agnostic plugin is written to cater to the need. For example, `farm-network` (used in [chapter 3](#)) to simulate sparse neural networks can be used independently as well as integrated with FARMS.

The most important aspect of FARMS is the data standard. By following a functional programming approach, we break down the neuromechanical simulation into modules that operate on data. This allows us to make FARMS extensively modular. Not only that, since data is saved throughout the simulation, it becomes natural and easy to catalog experiments to be easily shared with the community.

In the remainder of this chapter, we first briefly present related works that are used for neuromechanical simulations. Then, we define the core principles of FARMS in [section 5.2](#). Each of the core modules are then discussed in detail in the following sections. Finally, we present some concluding remarks about the framework.

## 5.2 Framework

FARMS is a modular framework written primarily in *Python* programming language, where various components can be used independently to accustom user needs. It is focused on reusing other available open-source projects wherever possible to take advantage and contribute back to existing infrastructure. By definition a Framework refers to the basic structure on top of which other things are built on. Establishing the fundamental structure allows (i) researchers to define neuromechanical experiments, (ii) developers to extend the functionality of existing framework, and (iii) share and exchange simulation results with the community. [Figure 5.2](#) establishes a common practice for modeling, simulating and analyzing neuromechanical simulations of animals and robots for studying movement control. According to FARMS framework, a neuromechanical simulation at top level can be broken down into four components ([Figure 5.2](#)); (i) modeling, (ii) simulation, (iii) analysis, and (iv) data being the bridge connecting the different components. Optimization and learning algorithms form the layer above all this as they need to be able to manipulate each component to produce the desired animal or robot movement.

- **Modeling:** Two basic necessities of any neuromechanical simulation are the descriptions of a robot or animal model and the control law one is interested in exploring to generate the movements. Modeling block covers the tools and aspects of generating these sub-blocks.
- **Simulation:** Once both the model and control are described, the next step is to be able to perform either a forward or inverse dynamics physics simulation with the controller in the loop. Simulation involves integrating (i) a physics engine to simulate articulated rigid bodies, interactions with the environment (land, water, or water) and (ii) the control laws to compute the actions to generate movements.
- **Analysis:** Finally, during and at the end of a simulation it is important to monitor the progress of an experiment. The analysis component deals with aspects of performing post-processing data, visualizing and replaying simulation data, and producing representations for scientific sharing and analysis.
- **Data:** At every step of the framework it is extremely important record and track the information. This is performed by the data block. Each module can read and write to the data block. This allows FARMS to be modular and the dependency between blocks is now data and it can be populated by any independent tool.

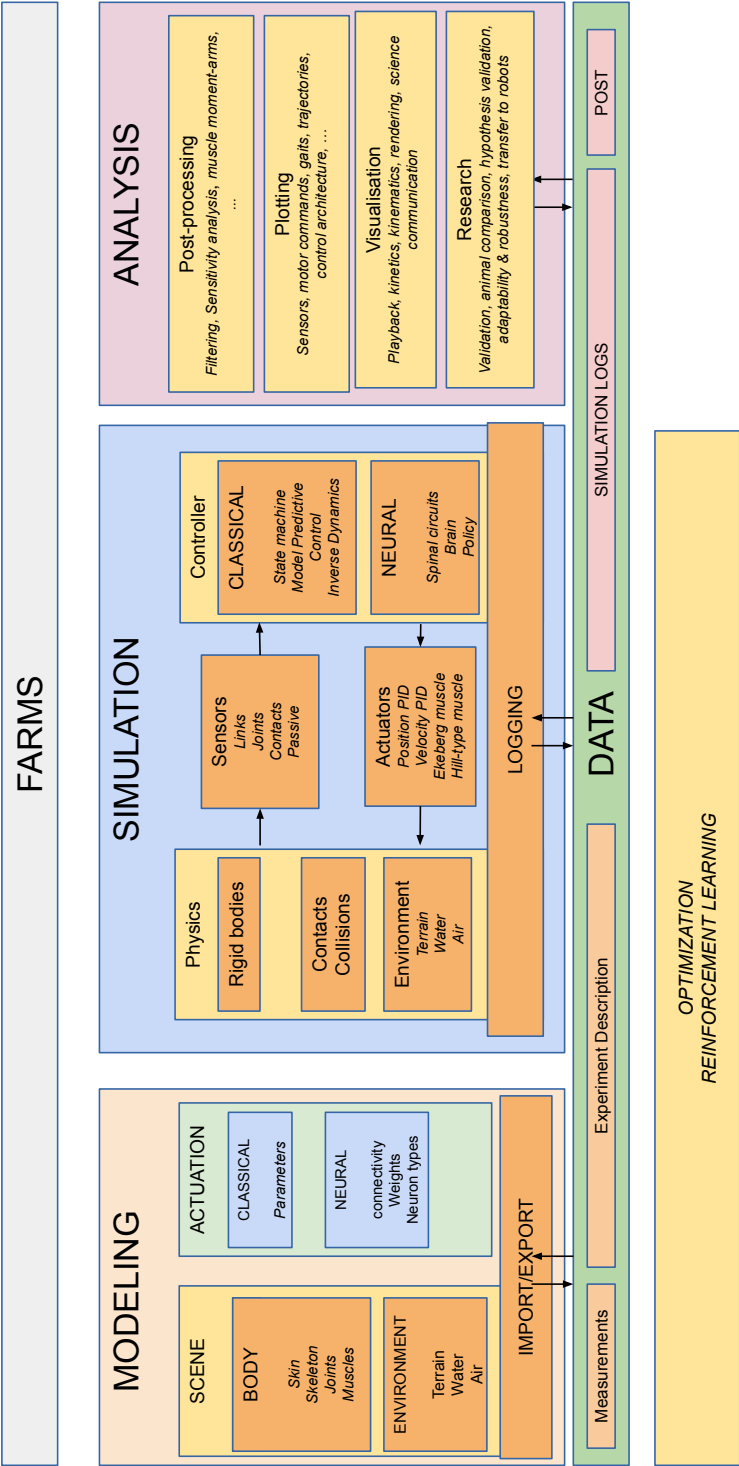


Figure 5.2: FARMS Architecture

### 5.3 Data

Data is the backbone of any numerical simulation. In FARMS, data block maintains and records information at every step of the simulation process. The data block in FARMS decouples the different steps in a neuromechanical simulation and makes FARMS a truly modular framework. There are several other advantages from this approach. By recording all the data, simulations become reproducible not only by the user but by the community. Any one who has access to the shared data can simply read the information and recreate the original experiment starting from modeling and until the analysis phase in any order. Currently, FARMS uses Hierarchical Data Format (HDF5) to store and organize the data. HDF5 format Application Programming Interface (API) for most of the common programming languages.

### 5.4 Modeling

For neuromechanical simulation, an experiment can be described by the following minimum elements: (i) Animal or robot bodies (In FARMS, we define body as an element that represents “lifeless” physical model of an animal or robot), (ii) Control law and (iii) the environment with which the animal or robot interacts. Modeling is often neglected when the conversation is about neuromechanical simulations. But, modeling each of the three elements is extremely important. Models need to be often modified when new experimental data is available. Not only that, generating models is an iterative process by itself. One can evaluate the model performance only after performing simulations. Which implies that there is a strong necessity to be able rapidly reconfigure models when the models in a simulation fail or do not agree with experimental data.

In FARMS, we regroup the three basic elements of an experiment description into scene and control. Scene comprises of the physical elements, the animal or robot model and the environment. Control defines the elements that decide how the physical elements move, for example the nervous system.

#### 5.4.1 Scene

A scene can comprise of one or more bodies, be it of animals, robots or both and an environment in which they live in. [Figure 5.3](#) shows an example of the different components of a scene while modeling a *Mouse*.

#### Body

In FARMS, we treat modeling of a robot or animal to be the same. We primarily use Blender Community, [2021](#) to develop and export bodies. Due to the modularity of the

framework this not a constraint. A user can use any other tool of their comfort to generate the necessary description files to setup the simulation. A body consists of the following elements,

- **Skin:** An external covering that interacts with the environment. In classical robotic simulations, a collision object can be considered as a skin. While modeling animals skin becomes important and for robots skin is often the same as the skeleton. An example for a robot with skin is described by Thandiackal et al. (2021), where the water-proof suit would be considered as the skin.
- **Skeleton:** The structural links that defines and supports the entire body. A skeleton is a collection of links that are described by their location and inertial elements (mass, center-of-mass, inertia).
- **Joints:** The articulation of the body emerges from the definition of joints in the body. They are define how any two links of a skeleton are allowed to move with respect to each other.
- **Muscles:** Muscles are “special” actuators that apply forces on the skeleton. They are defined by the locations at which they attach to the skeleton.

The information necessary to define the animal body and robot body are obtained differently. Robots are designed by humans in Computer aided design (CAD) softwares and are well defined. However, animal bodies are obtained usually from computerized tomography (CT) or magnetic resonance imaging (MRI) scans. They are then exported to CAD softwares. Thereon, an animal or a robot model is defined in the same way.

### Environment

With FARMS, we aim to support different medias as environment. This includes land, water, sand and air. Physics simulators are responsible to compute the interaction between the bodies and the environment. Most simulators only support rigid bodies, meaning one can only model land or rigid terrains. Some simulators support simplified hydrodynamic environments where bodies can interact with water. With FARMS, we fill this gap by developing physics simulator agnostic water, sand and air media using particle based simulations. While modeling the environment it is thus necessary to define the type of the medium and it's properties.

#### 5.4.2 Actuation

Once the bodies and the environment are defined, the next step is to model the actuation. To study animal movement, several different control strategies are possible. The possible actuation methods are (i) classical control and (ii) neural control.

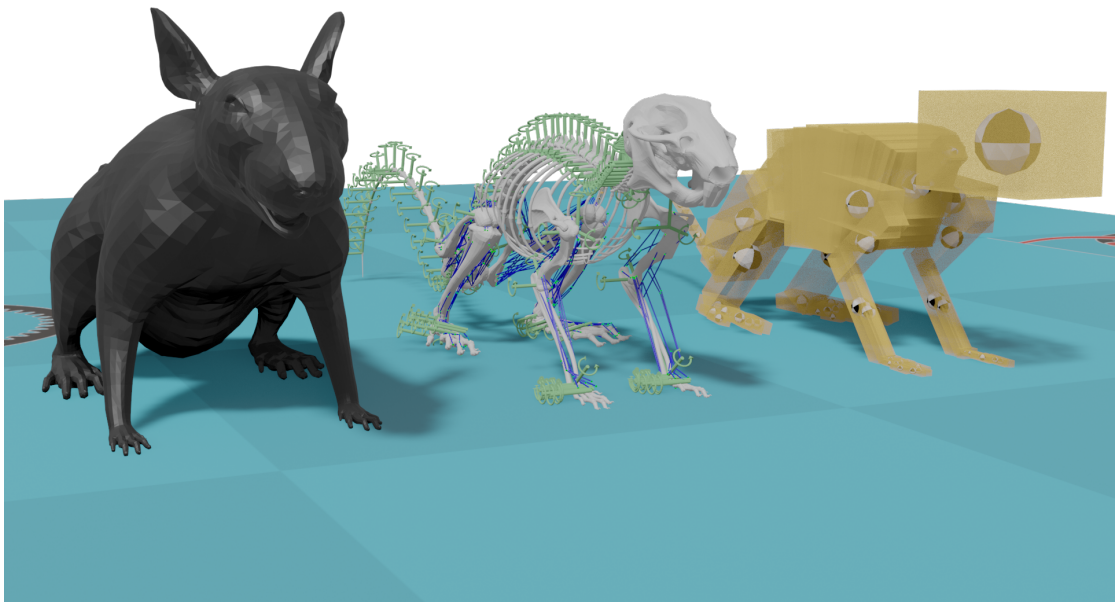


Figure 5.3: Scene modeling in FARMS with Blender. From left to right visualizes the following elements of a Mouse body (i) skin, (ii) skeleton, joints and muscles, (iii) inertials (inertia tensor, mass and center-of-mass)

Classical control methods include mainly come from control theory developed for robotics. These include methods like inverse dynamics, state-machines and model predictive control (MPC). From a modeling perspective, classical control mainly involves parameters that are later used by the controller to determine actions.

Neural control is more oriented towards neural networks either inspired from biology or machine learning techniques such as reinforcement learning. Modeling them involves describing the type of neurons, their properties and their connectivity. Currently, there is a lot of support for machine learning libraries and modeling them would mainly rely on those existing libraries. For biological networks, we could broadly classify them into spiking and non-spiking neural networks. For spiking networks, there are excellent open-source libraries such as NEST (Gewaltig and Diesmann, 2007), Brian (Stimberg et al., 2019) or Neuron (Hines and N. T. Carnevale, 1997). For sparse, non-spiking networks there is no library to the best of our knowledge that allows for easy modeling and simulation of locomotion networks. As part of FARMS, we developed a platform and simulator agnostic sparse neural network simulator called farms-network. farms-network provides commonly used neuron model types for locomotion circuits. The library can be access at [https://gitlab.com/farmsim/farms\\_network](https://gitlab.com/farmsim/farms_network). Figure 5.4 shows an example of sparse locomotor network based on Simon M. Danner, Wilshin, et al. (2016) modeling and visualized using the library developed as part of FARMS.

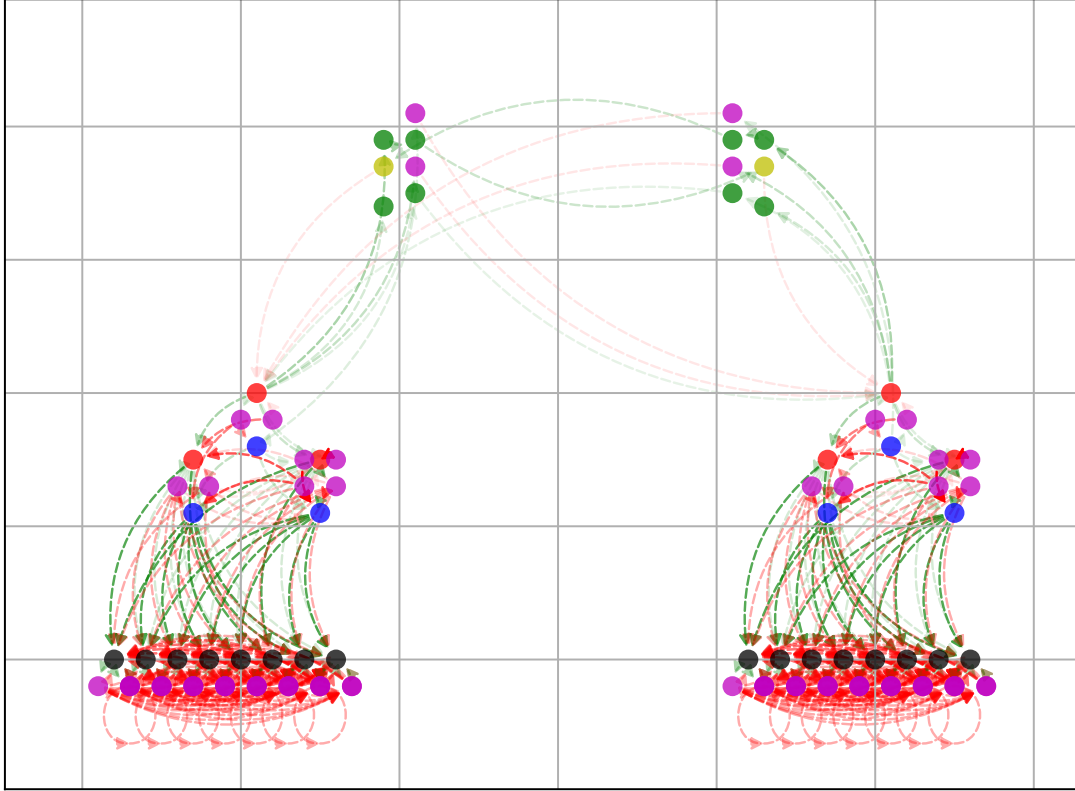


Figure 5.4: Example of neural network generation and visualization in FARMS. The two layered central pattern generator network is based on the computation model proposed by Simon M. Danner, Wilshin, et al. (2016)

### 5.4.3 Import/Export

At the end of the modeling step all the necessary data that defines the elements of the scene and actuation and written to the data block. Since, FARMS supports multiple physics engines and control libraries, it is important export the bodies and actuation data to relevant file formats that the respective libraries can process. For physics simulators, there have been several standards coming mainly from the robots community to describe the animal or robot bodies. *URDF*, *SDF*, *MJCF*, *OSIM*, *WBT* are some examples file-formats support by the physics engines.

The role of the import/export component is to read the relevant information in the data block and then generate the specific file-format necessary for the chosen physics simulator and neural simulator by the user. If a user wishes, the necessary description files can be generated independently of FARMS to directly continue to the simulation step.

## 5.5 Simulation

Once the scene and the actuation methods are fully described, the next step is to perform the numerical simulation. This step mainly involves performing forward simulation of the animal or robot model by the rigid body physics simulator, depending on the current state the controller then computes the necessary actuation signals to be fed back to the physics simulator to advance to the next time step. These steps are repeatedly performed to simulate the dynamics of an animal or robot with controller over time. FARMS provides wrappers that help bridge modalities of the simulation block.

### 5.5.1 Physics

The physics engine is the core of a neuromechanical simulation. The common steps performed by a physics engine are described by Geijtenbeek (2013) as:

- *Collision detection* checks if the body intersects with itself or other physical objects in the scene.
- *Forward dynamics simulations* computes the linear and angular accelerations of each simulated body.
- *Numerical integration* update positions, orientations and velocities of bodies, based on the previously computed accelerations.

The steps outlined above only simulate the articulated rigid bodies and its interactions with rigid terrain. Two important components are missing in the above formulation.

One, muscles are not commonly included as part of physics engines as most of the physics are in practice built for robotics communities. As part of FARMS we built a platform and simulator agnostic muscle library named farms-muscle ([https://gitlab.com/farmsim/farms\\_muscle](https://gitlab.com/farmsim/farms_muscle)). farms-muscle implements several types of Hill-type muscle models at various levels of abstractions in a computationally efficient manner.

Second, most physics engines do not commonly support any type of fluid or mixed media environments. As part of FARMS we provide access to both phenomenological models of fluid dynamics and more sophisticated fluid simulations based on Smoothed Particle Hydrodynamics (SPH) methods (Ramachandran et al., 2021).

The choice of physics simulator is extremely important for stable simulations of the specific experiment. And there are several simulators that employ different strategies to perform three steps described above to perform the numerical simulation. The unique prospective of FARMS is its ability to provide an interface to several of these simulators with little or medium effort. Currently, FARMS uses Bullet (Erwin Coumans and Yunfei



Bai, 2016) and MuJoCo (Todorov et al., 2012) as its primary physics simulators. For a comprehensive review on physics simulators from robotics perspective refer to Collins et al. (2021).

### 5.5.2 Sensors

At the end of time step of the numerical integration of the physics block, sensors implemented in the FARMS framework interface collect the complete information of the state of the simulation. This includes exteroceptive signals such as contact forces, ground reaction forces and proprioceptive signals such as muscle spindle feedbacks, joint angles, joint velocities.

### 5.5.3 Controller

Depending on the decisions made during the modeling phase, the simulation can either be running classical control or a neural control. For either of these approaches, the controller block will have complete access to the current state of the simulation through the sensors block. The controller can compute the necessary actions in the following time step of the simulation.

### 5.5.4 Actuators

The outputs of the controller block can be (i) muscle activation commands, (ii) desired joint positions and velocities or (iii) desired joint torques. FARMS will ensure the correct actuation is performed depending on the definitions of the body and control in the modeling phase.

### 5.5.5 Logging

At each of the four stages described above, the complete state of the block at every time step is logged into the data block. This ensures complete reproducibility of the simulation at any point of time. Logging simulation data is extremely important for further analysis and post-processing and this is seamlessly ensured by the FARMS framework.

## 5.6 Analysis

At the end of a successful or an unsuccessful simulation, it is important analyze the performance. Tools that help visualize and show data in a manner that allows for critical analysis will be part of the FARMS analysis toolbox. The analysis block can be subdivided into (i) post-processing, (ii) plotting, (iii) visualization and (iv) outreach. With the data containing the complete model information and the simulation logs, the analysis block can combine this information into useful ways to represent data for neuromechanical simulations.

Plotting and visualization aspects are mainly performed using Blender (Community, 2021). This includes replaying the simulation by overlaying additional data computed by the post-processing block to provide deeper insights to the researcher. High quality visualization tools go a long way in helping researchers in understanding the extremely high dimensional information gathered during the simulations. Figure 5.5 shows a snapshot of pleurobot robot locomotion replay rendered in FARMS.



Figure 5.5: An example of Pleurobot robot visualized in Blender with contact forces and center-of-mass

### 5.7 Conclusion

In this work we presented a new framework for performing neuromechanical simulations of animals and robots to study movement control. FARMS is a modular framework, where various components can be used independently to accustom user needs. It is focused on reusing other available open-source projects wherever possible to take advantage and contribute back to existing infrastructure. We have discussed the different components of the framework in-depth to provide the features and ability of FARMS.

FARMS is meant to serve as a platform which will facilitate the study of locomotion, and will feature a range of tools to help design models with realistic dynamics, running the controllers based on neuron models and for comparative studies between the animals and/or robots. It would also support optimisation methods for parameter tuning and 3D visualisation for debugging and rendering high quality videos for publication. We aim to make FARMS an open-source community-driven modular project in the future to accustom to the current needs of the scientific community. As such, FARMS could help bridge the gap to connect the various works of researchers coming from different fields, including biomechanics, neuroscience and robotics.

## Chapter 6

# Conclusion

Studying control of animal movement is a complex, inter-disciplinary area of research. Each animal model has its own advantage and disadvantage when it comes to performing experiments to study them. The availability of experimental animal data has been a big reason in this thesis which has driven me to work on three different animal models while focusing on different aspects of the modeling, simulation and analysis in each of these models. In this thesis, I studied three of the most important experimental animal models for studying legged motion, namely *Mus musculus* (Mouse), *Drosophila melanogaster* and *Macaca fascicularis*. In each of the model animals, we have explored the musculoskeletal, feed-forward motor control and sensory components using computational models in simulation. [Figure 6.1](#) shows the areas of research focused in each chapter in this thesis.

### 6.1 Mouse : Musculoskeletal model

*Mice*, due to the advent of molecular and genetic tools, have become an important animal model for movement control. Due to their small size, recording muscle activity (EMGs) from several, activity from afferent fibers, and ground reaction forces are challenging and often unavailable. Today, we have some exciting tools such as DeepLabCut by Mathis, Mamidanna, Kevin M. Cury, et al. ([2018b](#)) for markerless pose estimation. But due to the large volume of soft-tissues in mice, it still remains extremely difficult to capture accurate kinematics at the skeletal level in freely behaving animals. With the developed whole body biomechanical model of the mouse we can now address a few of these experimental shortcomings.

In [chapter 2](#) we developed a whole body musculoskeletal model of the mouse. Mouse is one of the most studied animal model for movement control. This ranges from studies in reaching and grasping to quadrupedal and bipedal locomotion. Yet, there has been

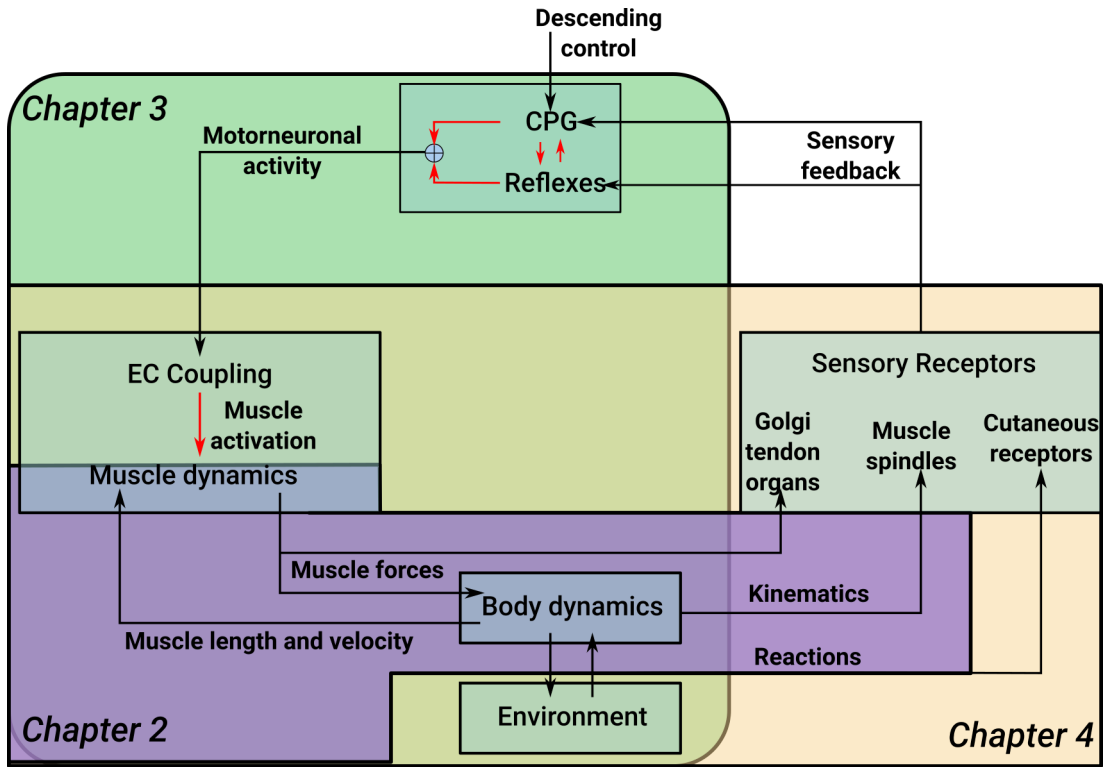


Figure 6.1: Overview of the focus of individual chapters in this thesis with respect to neuromechanical control loop

no complete musculoskeletal model of the mouse. The model developed in this thesis comprises of a fully articulated skeleton along with the musculature of both forelimbs and hindlimbs. Due to its small size, experiments related to estimating properties for forelimb musculature for musculoskeletal models have been limited. Using numerical optimization techniques we estimated those missing properties to provide a basis for future models. We then systematically explored the effects of the limb musculature on producing joint torques. We showed there are several muscles in the mouse hindlimb and forelimb that could have a zero-crossing of moment arms. Implying that the role of muscles of mouse might have much more interesting roles during movement generation. By not assuming a muscle functional role a-priori but rather infer them by computing their influence on joints using the developed model has revealed that many muscles in the limb influence more joints than what previous studies have shown. We also highlighted the range of active and passive muscle forces in the mouse limbs through their complete ranges of joint motion. Overall, the musculoskeletal model with limb musculature has provided a platform to integrate available neural controllers to study complex locomotion behaviors in *in-silico*. In future iterations of the model, addition of spinal muscles will further add to the completeness the model.

## 6.2 *Drosophila melanogaster* : Kinematic replay and feed-forward locomotion

*Drosophila melanogaster* commonly known as a fruit-fly, is yet another important species used in studying animal movement control. As model organisms, they have some very unique advantages; they have shorter lifecycles, they are inexpensive and easy to reproduce, availability of genetic tools for manipulation, and expression of diverse movement behaviors with a relatively simpler nervous system (Jennings, 2011). Compared to a mouse, a fruit-fly is around 30-50 times smaller. Making any kind of invasive or non-invasive recordings poses a bigger technical challenge. With the bio-realistic model of the fruit-fly developed in this thesis, we can now estimate internal and external forces of this model organism.

In chapter 3, we developed a bio-realistic model of *Drosophila melanogaster*. Using the model we setup a dialogue between the animal experiments and the developed model. Using the model we first established a pipeline to transfer the kinematics of tethered locomotion over a floating ball to the physics-based simulation model. While doing so, we observed that for a faithful reconstruction of the joint motion it was necessary to introduce a new degree-of-freedom in the limb than the conventionally identified degrees-of-freedom in the literature. The updated model was then used to replay the recorded kinematics with higher accuracy than before. By replaying the kinematics in a physics environment, we could estimate the internal and external forces generated in the body during the performed motion (locomotion and grooming). With this pipeline, we can now make predictions on the possible motor neuron activity during locomotion or grooming required to produce the necessary observed forces. Finally, we extended the model by including antagonist muscles (Ekeberg, 1993b) driven by an open-loop neural oscillator network (Central pattern generators). We hypothesized that there is a trade-off between gait speed and static stability during locomotion and investigated the relationship using multi-objective optimizations. From the results, we observed that the *drosophila* model by preferentially using a tripod gait could perform a wide range of walking speeds and at different static stability metrics. The convergence to a tripod gait was similar to the observations in the previous simulation study in flies by (Ramdya et al., 2017b).

## 6.3 *Macaca fascicularis* : Sensory predictions

A big part of understanding movement control is to finally be able to perform interventions in humans for rehabilitation and restoration of lost motor control. To this aim, genetically, physiologically and behaviorally nonhuman primates (NHP) are the closest animal models to humans (Harding, 2017).

Measuring activity of the sensory neurons in the dorsal root ganglion is important for understanding motor control and also for techniques such as Epidural Electrical

Stimulation (EES) for recovering lost motor behaviors. However, performing these recordings presents formidable challenges in nonhuman primates. And currently infeasible to do multi-fiber recordings of the same in humans. In [chapter 4](#), we presented a methodology to estimate spatiotemporal patterns of proprioceptive sensory afferent in *Macaca Fascicularis* for reaching and grasping task by projected the estimated afferent activity onto the spinal segments hosting their homonymous motor pools. With our methodology we isolated the spatiotemporal maps into specific fiber components (Ia, II and Ib). To our surprise, the spatiotemporal maps of sensory afferents were more complex than what we had expected.

## 6.4 A framework for neuromechanical simulations

In [chapter 5](#), we described a Framework for Animal and Robot Modeling and Simulation (FARMS). FARMS is a collaborative outcome of the BioRobotics lab. It is a culminated experience of developing diverse animal (*Mouse*, *Drosophila Melanogaster* and *Macaca Fascicularis* developed in the thesis) and robot models. FARMS is a modular, open-source framework that will facilitate the study of animal movement, and will feature a range of tools to help design models with realistic dynamics, running the controllers based on neuron models and for comparative studies between the animals and/or robots. Data is the back bone of FARMS. It is what allows the modules of FARMS to be independent. For example, one can easily switch between different physics engines such as Bullet or Mujoco. By standardizing data, (i) we decentralize and modularize components of neuromechanical simulations, (ii) we provide a stable platform for sharing and reusing models, (iii) promoting more reproducible research. Finally, we as humans are largely visual driven to build our intuition and draw inferences from our observations. FARMS focuses on this aspect by providing state-of-the-art tools and methods to visualize and represent data that will allow researchers to interpret their experimental data in newer ways. As such, FARMS could help bridge the gap to connect the various works of researchers coming from different fields, including biomechanics, neuroscience and robotics

## 6.5 Challenges in performing animal simulations

Neuromechanical simulations are a promising tool to complement animal experiments in many aspects as we have seen from the examples in this thesis. Since, it is a up and coming tool there are still several fundamental challenges that need to addressed. As we have seen in [section 5.5](#), the core component of a neuromechanical simulation is the numerical integration of rigid and soft body physics performed by the physics engines. Most of the current physics have been built around the idea of simulating robots and not animal models barring a few exceptions. And robots often are limited to small number of degrees-of-freedom and comprises of well defined rigid body elements. In this thesis, while

simulating the *Mouse* musculoskeletal model and the *Drosophila melanogaster* one of the primary challenges was addressing the numerical stability of the physics engines due to the extremely small size of the animals and their ability to produce large muscle forces relative to their body size. Along with that models with high number degrees-of-freedom are another concern as they increase the inaccuracy in the simulation and eventually lead to instability. Moreover, when the animals interact with the environment, modeling the contacts between the model and the environment becomes critical. Modeling contacts is challenging and often makes the simulation stiff and again hard to numerically integrate to perform forward simulations. Some of these problems can be partially addressed by simulating the models at a lower integration time-step. This solution is only adequate till a point where the simulations become so slow that are impractical to perform any kind of optimizations. Some of these problems haven't been addressed in the past because of the lack of such complex models. By developing complex models we will be able to systematically identify, report and then address them. FARMS, aims to provide the platform for such community driven improvements to the field.

Once we simulate an animal model *in-silico* the immediate question is, how do we validate our results?. With neuromechanical simulations we are predicting aspects of the movement control that are difficult or even currently impossible to measure in animal experiments. How does one then validate the observations from simulations? One method is to build robots that can replicate these observations. Currently, the robotic technology has limitations that make it a far fetched solution too. Another method is to rigorously validate every aspect of the simulation that is experimentally measurable. Similar to the methodology we described in validating the model of *Macaca fascicularis*. In the mouse model study, we performed a detailed sensitivity analysis of all the muscle parameters. The results from the analysis highlighted important parameters that need to be more critically looked into. Cox et al. (2019) described a detailed methodology to estimate and validate muscle parameters. Similar experimental studies in the mouse will aid in validating the model developed in this thesis. For the *Drosophila melanogaster* model, we were available to measure the animal kinematics during locomotion. We then used that data to compare and predict aspects of the gait to further validate the model. The need of the hour is collecting extensive amounts of experimental data from animals in a systematic manner and sharing it with the community. And then with frameworks such as FARMS, we could establish a better dialogue between animal experiments and simulations.

## 6.6 Future work

There are so many exciting avenues to take using neuromechanical simulations to explore control of animal movement. And the work we did during the thesis has been a great experience to learn and contribute to the field of animal movement.



Due to the diversity of the problems tackled in this thesis, each chapter is an opportunity to explore many more scientific questions. The idea of exploring the role of feed-forward and sensory afferents in the producing movements is a key question to be explored in each of the models organisms.

In [chapter 2](#), we developed a whole body musculoskeletal model of the mouse. Currently the musculoskeletal model has only limb musculature model. Due to the lack of experimental data, forelimb muscle parameters were numerically optimized. This needs to be validated by making experiments measurements in *Mouse*. Additionally, the model needs to be extended by characterizing and adding spinal musculature as well. This allow us to simulate the flexible bending of the spinal cord as well.

After the biomechanical analysis that we performed, the immediate next step is to connect the model to the neural network. In the literature there are several neural models of *Mouse* to study locomotion. Simon M. Danner, Wilshin, et al. ([2016](#)), Simon M Danner et al. ([2017](#)), and Simon M. Danner, Zhang, et al. ([2019](#)) describe computational models of neural circuits for quadrupedal locomotion based on available experimental data. These circuits have already been implemented in the FARMS framework and the preliminary results of coupling the circuits with the whole-body mouse model are showing promising results. Extending, it would be to interesting to include the sensory feedbacks with the circuits. This opens up a great number of open scientific questions on how to connect the sensory feedbacks to the circuits as we know very little about it. Typically, locomotion studies are limited to straight walking, both experimentally and *in-silico*. With the 3D model developed, we can now explore more complex locomotor problems such as turning and navigation. The methodology developed in [chapter 4](#) can be used with the mouse model to estimate spatiotemporal maps of sensory afferents during locomotion and reaching tasks. Combined with closed loop experiments this will allow us to expand our understanding on the role of sensory feedbacks in modulating central pattern generators in the spinal cord.

NeuroMechFly framework described in [chapter 3](#) provides a basis for a large set of new experiments. The immediate set questions to be explored are related to untethering the fly and performing free locomotion over ground. Due to the flexibility of the framework, we were able to already perform preliminary experiments in this direction with positive results. To further improve the bio-realism of the fly model, the natural future step would be to model the Hill-type muscles for the limbs. Soler et al. ([2004](#)) highlighted the limb musculature of the fly using GFP markers and confocal microscopy. Using their work, we can identify the attachments of the muscles on the exoskeleton. But, estimating the muscle parameters still remains to be challenging. Once we do that, we can perform a systematic and comprehensive biomechanical analysis of the fly; similar to the study described in [chapter 2](#).

With the powerful experimental toolkit available with the fly, one can perform targeted

excitation or suppression of specific neural populations. By closing the gap between the experiment and the simulation, in future we could perform real-time perturbations in the fly based on the additional information we can gather using simulations and simultaneously improve the simulation model with the new experimental data that is being recorded. This would reduce the overhead time of years of effort to bridge the gap between simulations and experiments.

The work described in [chapter 4](#) was limited to only the upper-limb model of *Macaca fascicularis*. In future, one should extend this to a full body musculoskeletal model like we did with the *mouse* in [chapter 2](#). With a whole body model of *Macaca fascicularis* we could first perform a systematic biomechanical analysis as described in [chapter 2](#). Further, the model can be used to prepare spatiotemporal maps of both the motor neurons pools and proprioceptive sensory afferents for locomotion. Such maps would be of great significance in setting up controllers for epidural stimulation technologies in humans to restore locomotion after spinal cord injuries.

FARMS in future could standardize how we perform neuromechanical simulations. By setting up environments such as OpenAI gym for complex neuromechanical models in FARMS, we could attract a large community of researchers from various disciplines. Currently, FARMS is in a early stage of development. Once we make it open-source, like many open-source projects the community could lead the development into avenues that are hard to foresee. A long term goal with FARMS would be to use neuromechanical simulations to train deep neural networks (DNNs). Currently, DNNs can generate kinematics from markerless animal movement videos. The captured kinematics could be fed into the simulations to replay the kinematics in a physics-based environment like we showed in [chapter 3](#). Then, the estimated proprioceptive and exteroceptive data can be used to train the DNNs to learn them. At the end of the pipeline, we could hope that one can estimate a feasible set of solutions of kinematics and kinetics from simple experimental videos of animals locomoting.



## Appendix A

# Supplementary Information : Mouse BioMechanics

### A.1 Hill-type muscle model

The force produced by the contractile and parallel elements was modeled as,

$$F = F_m^0(a(t)f_l(\tilde{l}_m)f_v(\tilde{v}_m) + f_{PE}(\tilde{l}_m) + \beta\tilde{v}_m) \quad (\text{A.1})$$

$F_m^0$  is the maximum isometric force the muscle is capable of producing.  $a(t)$  is the muscle activation.  $f_l(\tilde{l}_m)$  defines the force-length relationship curve during isometric contractions with  $\tilde{l}_m$  being the normalized muscle-fiber length.  $f_v(\tilde{v}_m)$  defines the force-velocity relationship curve during isotonic contractions with  $\tilde{v}_m$  being the normalized muscle-fiber length. Passive forces are generated in the muscle when stretched beyond a threshold length, this is represented by the passive-force-length given by  $f_{PE}(\tilde{l}_m)$ .  $\beta\tilde{v}_m$  represents the additional damping in the muscle with  $\beta$  being the damping coefficient, set to 0.1 by default.

The activation dynamics ( $a(t)$ ) and passive-force-length ( $f_{PE}$ ) are described based on the implementation from Opensim(Thelen, 2003).

$$\frac{da(t)}{dt} = \frac{u(t) - a(t)}{\tau_{act}} \quad (\text{A.2})$$

where  $u(t)$  is the neural-excitation input signal to the muscles bounded within a range of 0 and 1, and  $\tau_{act}$  is the time-constant (Note that we used a constant value for  $\tau_{act}$  instead

of varying it as a function of  $u(t)$  and  $a(t)$  as described by Thelen (2003).

$$f_{PE}(\tilde{l}_m) = \frac{\exp\left(k_{PE}(\tilde{l}_m - 1)/\epsilon_0^m\right) - 1}{\exp(k_{PE}) - 1} \quad (\text{A.3})$$

The active-force-length ( $f_l$ ) and force-velocity ( $f_v$ ) relationships described below are based on the description by De Groote et al. in (De Groote et al., 2016)

$$f_l(\tilde{l}_m) = \sum_{i=1}^3 b_{1i} \exp\left[\frac{-0.5(\tilde{l}_m - b_{2i})}{b_{3i} + b_{4i}\tilde{l}_m}\right]^2 \quad (\text{A.4})$$

$$f_v(\tilde{v}_m) = d_1 \log\left[(d_2\tilde{v}_m + d_3) + \sqrt{((d_2\tilde{v}_m + d_3)^2 + 1)}\right] + d_4 \quad (\text{A.5})$$

Since, the tendon is assumed to be rigid and inextensible, the force along the tendon ( $F_t$ ) equates to the force produced by the contractile element described in Equation A.1 as,

$$F_t = F \cos(\alpha) \quad (\text{A.6})$$

## A.2 Hindlimb muscle parameter scaling

Optimal muscle-fiber length ( $l_m^o$ ) and muscle-tendon slack length ( $l_t^s$ ) were scaled from Charles model (Charles, Cappellari, Spence, Wells, et al., 2016) (referred to as reference model) to our model (referred to as target model). To do the scaling, we used the algorithm proposed by Modenese et al. (2016), steps for which are described below,

- In the reference model, identify the  $N_q$  degrees-of-freedom spanned by the muscle. Discretize each joint into  $n_{dof}$  poses to create a set of  $n = (n_{dof})^{N_q}$  possible joint pose combinations.
- In the reference model, for each pose 1, 2, 3, .... $n$ , compute a vector of pennation angles ( $\alpha_{\text{ref}}$ ), normalized muscle-fiber length ( $\tilde{\mathbf{l}}_{\text{m,ref}}$ ) and normalized muscle-tendon lengths ( $\tilde{\mathbf{l}}_{\text{t,ref}}$ )

Table A.1: Hill-type muscle model parameters

Activation dynamics	$\tau_{\text{act}}(\text{s})$	0.001
Active force-length	$b_{11}$	0.815
	$b_{21}$	1.055
	$b_{31}$	0.162
	$b_{41}$	0.063
	$b_{12}$	0.433
	$b_{22}$	0.717
	$b_{32}$	-0.030
	$b_{42}$	0.200
	$b_{13}$	0.100
	$b_{23}$	1.00
	$b_{33}$	0.354
	$b_{34}$	0.0
Active force-velocity	$d_1$	-0.318
	$d_2$	-8.149
	$d_3$	-0.374
	$d_4$	0.886
Passive force-length	$k_{\text{PE}}$	4.0
	$\epsilon_0$	0.600
Tendon force-length	$k_{\text{T}}$	35
	$c_1$	0.200
	$c_2$	0.995
	$c_3$	0.250
Damping	$\beta$	0.100

- In the target model, for the same  $n$  poses, compute a vector of muscle-tendon lengths ( $\mathbf{l}_{\text{mt,targ}}$ )
- Solve for muscle-tendon slack length  $l_t^s$  in the target model by solving [Equation A.7](#) using a least-squares like numerical method.

$$\begin{bmatrix} l_{mt}^1 \\ l_{mt}^2 \\ \cdot \\ \cdot \\ l_{mt}^n \end{bmatrix}_{\text{targ}} = \begin{bmatrix} \tilde{l}_m^1 \cos(\alpha) & \tilde{l}_t^1 \\ \tilde{l}_m^2 \cos(\alpha) & \tilde{l}_t^2 \\ \cdot & \cdot \\ \cdot & \cdot \\ \tilde{l}_m^n \cos(\alpha) & \tilde{l}_t^n \end{bmatrix}_{\text{ref}} \begin{bmatrix} l_m^o \\ l_t^s \end{bmatrix}_{\text{targ}} \quad (\text{A.7})$$

We solved [Equation A.7](#) using the least squares method implemented in Scipy *v1.70*

### A.3 Muscle-tendon slack length estimation

Muscle-tendon slack length for the forelimb muscles were estimated based on the modified algorithm proposed by Manal and Buchanan (2004).

For the purpose of estimating the muscle-tendon slack length, we consider the tendons to be elastic and non-rigid whose force-tendon length ( $f_t(\tilde{l}_t)$ ) (with  $\tilde{l}_t = \frac{l_t}{l_t^s}$  being the normalized muscle-tendon length) characteristics are defined by the formulation by De Groote et al. (2016) as,

$$f_t(\tilde{l}_t) = c_1 \exp[k_T(\tilde{l}_t - c_2)] - c_3 \quad (\text{A.8})$$

Substituting Equation A.8 in Equation A.6,

$$F_m^0 f_t(\tilde{l}_t) = F_m^0 (a(t) f_l(\tilde{l}_m) f_v(\tilde{v}_m) + f_{PE}(\tilde{l}_m) + \beta \tilde{v}_m) \quad (\text{A.9})$$

The total length of the muscle-tendon unit is,

$$l_{mt} = l_m \cos(\alpha) + l_t \quad (\text{A.10})$$

Equation A.10 can be expressed in terms of normalized muscle-fiber length ( $\tilde{l}_m$ ) and normalized tendon ( $\tilde{l}_t$ ) as,

$$l_{mt} = \tilde{l}_m l_m^o \cos(\alpha) + \tilde{l}_t l_t^s \quad (\text{A.11})$$

From Equation A.11  $l_t^s$  can be written as,

$$l_t^s = \frac{l_{mt} - \tilde{l}_m l_m^o \cos(\alpha)}{\tilde{l}_t} \quad (\text{A.12})$$

Considering a maximal activation ( $a(t) = 1.0$ ) under isometric conditions ( $\tilde{v}_m = 0.0$ ),

from Equation A.8, Equation A.9 and Equation A.12,  $l_t^s$  can be written as,

$$c_1 \exp[k_T(\tilde{l}_t - c_2)] - c_3 = (f_l(\tilde{l}_m) + f_{PE}(\tilde{l}_m)) \cos(\alpha) \quad (\text{A.13})$$

$$\tilde{l}_t = \frac{c_2 + (\log[(f_l(\tilde{l}_m) + f_{PE}(\tilde{l}_m)) \cos(\alpha) + c_3]/c_1])}{k_T} \quad (\text{A.14})$$

$$l_t^s = \frac{l_{mt} - \tilde{l}_m l_m^o \cos(\alpha)}{c_2 + (\log[(f_l(\tilde{l}_m) + f_{PE}(\tilde{l}_m)) \cos(\alpha) + c_3]/c_1])/k_T} \quad (\text{A.15})$$

Here we use the tendon force-length relationship formulated by De Groote et al. (2016) instead of the one described by Manal and Buchanan (2004).

Given  $\tilde{l}_m$  at  $l_{mt}$  and knowing  $l_m^o$ , we can compute tendon slack length  $l_t^s$  from Equation A.15. But, we do not know  $\tilde{l}_m$  in practice. Manal et al. proposed to use numerical methods to estimate  $\tilde{l}_m$  at short, long and mid range of  $l_{mt}$  such that  $l_t^s$  is to be a constant, which was formulated as a minimization problem.

$$\begin{aligned} &\text{minimize} && [(l_t^{s1} - l_t^{s2})^2 + (l_t^{s1} - l_t^{s3})^2 + (l_t^{s2} - l_t^{s3})^2] \\ &\text{subject to,} && \tilde{l}_m \leq 1.0 \end{aligned}$$

We extended this formulation by Manal and Buchanan (2004) for  $l_t^s$  including the passive forces ( $f_{PE}(\tilde{l}_m)$ ) in Equation A.15 so that we include the complete force-length curve for estimation. The formalization described above is limited to the muscles' relationship with only a single degree-of-freedom. We extend this to all the degrees-of-freedom ( $ndof$ ) where the muscle has a significant moment-arm. This is done by estimating  $\tilde{l}_m$  at short, long and mid range of  $l_{mt}$  for each degree-of-freedom the muscle influences. The new minimization problem is defined as,

$$\begin{aligned} &\text{minimize} && \sum_{n=1}^{ndof} [(l_t^{s1} - l_t^{s2})^2 + (l_t^{s1} - l_t^{s3})^2 + (l_t^{s2} - l_t^{s3})^2]_n \quad (\text{A.16}) \\ &\text{subject to,} && 0.6 \leq \tilde{l}_m \leq 1.4 \quad (\text{A.17}) \end{aligned}$$

We used differential evolution, a stochastic population based optimization technique implemented in Scipy v1.70 to minimize the objective in Equation A.16 for each muscle in the forelimb. A population size of 20, maximum iterations of 1000 and relative and absolute tolerances were set to  $1e^{-10}$ .





## Appendix B

# Supplementary Figures and Tables : NeuroMechFly

Table B.1: Model body parts and degrees-of-freedom between each segment and its parent.

Body part	Segment	Parent	Degrees of freedom
Abdomen	A1A2	Thorax	1
	A3	A1A2	1
	A4	A3	1
	A5	A4	1
	A6	A5	1
Head	Head capsule	Thorax	3
	Eyes (x2)	Head	0
	Antennae (x2)		1
	Rostrum		1
	Haustellum	Rostrum	1
Legs	Coxa (x6)	Thorax	3
	Trochanter/Femur (x6)	Coxa	2
	Tibia (x6)	Femur	1
	Tarsus1 (x6)	Tibia	1
	Tarsus2 (x6)	Tarsus1	1
	Tarsus3 (x6)	Tarsus2	1
	Tarsus4 (x6)	Tarsus3	1
	Tarsus5-Claw (x6)	Tarsus4	1
Thorax	Halteres (x2)	Thorax	3
	Wings (x2)		3
	Thorax	-	0

Table B.2: Matrix of p-values from pairwise comparisons of position errors after calculating forward kinematics for walking. Numbers in bold (except in the case of identity) indicate that the p-value  $> 0.001$  (i.e., no statistical difference).

	Base	IK	Base & CTr roll	Base & CTr yaw	Base & FTi roll	Base & FTi yaw	Base & TiTa roll	Base & TiTa yaw
Base	1.00	5.42e-13	0.00	7.08e-184	2.28e-133	4.53e-50	<b>9.95e-01</b>	1.53e-197
IK	5.42e-13	1.00	0.00	4.48e-285	4.37e-222	6.82e-110	5.42e-13	8.62e-302
Base & CTr roll	0.00	0.00	1.00	5.49e-138	2.96e-189	0.00	0.00	1.57e-126
Base & CTr yaw	7.08e-184	4.48e-285	5.49e-138	1.00	2.52e-05	5.13e-45	7.83e-184	<b>5.38e-01</b>
Base & FTi roll	2.28e-133	4.37e-222	2.96e-189	2.52e-05	1.00	8.33e-22	2.44e-133	1.08e-07
Base & FTi yaw	4.53e-50	6.82e-110	0.00	5.13e-45	8.33e-22	1.00	4.53e-50	6.05e-52
Base & TiTa roll	<b>9.95e-01</b>	5.42e-13	0.0	7.83e-184	2.44e-133	4.53e-50	1.00	1.71e-197
Base & TiTa yaw	1.53e-197	8.63e-302	1.57e-126	<b>5.38e-01</b>	1.08e-07	6.05e-52	1.71e-197	1.00

Table B.3: Matrix of p-values matrix from pairwise comparisons of position errors after calculating forward kinematics for grooming. Numbers in bold (except in the case of identity) indicate that the p-value  $> 0.001$  (i.e., no statistical difference).

	Base	IK	Base & CTr roll	Base & CTr yaw	Base & FTi roll	Base & FTi yaw	Base & TiTa roll	Base & TiTa yaw
Base	1.00	4.34e-128	0.00	7.57e-149	2.59e-131	4.72e-32	<b>1.00</b>	2.47e-192
IK	4.34e-128	1.00	0.00	<b>2.02e-01</b>	<b>1.00</b>	4.30e-34	3.27e-126	1.11e-07
Base & CTr roll	0.00	0.00	1.00	0.00	0.00	0.00	0.00	0.00
Base & CTr yaw	7.57e-149	<b>2.02e-01</b>	0.00	1.00	<b>3.04e-01</b>	2.56e-45	8.05e-147	<b>1.08e-03</b>
Base & FTi roll	2.59e-131	<b>1.00</b>	0.00	<b>3.04e-01</b>	1.00	8.96e-36	2.08e-129	5.70e-07
Base & FTi yaw	4.72e-32	4.30e-34	0.00	2.56e-45	8.96e-36	1.00	3.84e-31	4.86e-71
Base & TiTa roll	<b>1.00</b>	3.27e-126	0.00	8.05e-147	2.08e-129	3.84e-31	1.00	4.85e-190
Base & TiTa yaw	2.47e-192	1.11e-07	0.00	<b>1.08e-03</b>	5.70e-07	4.86e-71	4.85e-190	1.00

Table B.4: Fixed angles for body joints during kinematic replay and optimization.

Body part	Joint	Fixed angle (deg)	Body part	Joint	Fixed angle (deg)
Abdomen	A1A2	0	Thorax	Left haltere roll	0
	A3	-15		Left haltere pitch	0
	A4	-15		Left haltere yaw	0
	A5	-15		Right haltere roll	0
	A6	-15		Right haltere pitch	0
Head	Head capsule roll	0		Right haltere yaw	0
	Head capsule pitch	10		Left wing roll	90
	Head capsule yaw	0		Left wing pitch	0
	Left antenna	35		Left wing yaw	-17
	Right antenna	-35		Right wing roll	-90
	Rostrum	90		Right wing pitch	0
	Haustellum	-60		Right wing yaw	17

Table B.5: Fixed angles for leg joints during optimization (deg).

Body Part	Side	ThC yaw	ThC pitch	ThC roll	CTr pitch	CTr roll	FTi	TiTa
Front	Left	0	actuated	10	actuated	0	actuated	-39
	Right	0	actuated	-10	actuated	0	actuated	-39
Middle	Left	7.45	-5	actuated	actuated	0	actuated	-54
	Right	-7.45	-5	actuated	actuated	0	actuated	-54
Hind	Left	3.45	6.2	actuated	actuated	0	actuated	-45
	Right	-3.45	6.2	actuated	actuated	0	actuated	-45

Table B.6: Lower and upper limits for the muscle parameters during optimization.

Body part	Joint	$\Delta\varphi$ [Lower limit, Upper limit]	$\alpha$ [Lower limit, Upper limit]	$\beta$ [Lower limit, Upper limit]	$\gamma$ [Lower limit, Upper limit]	$\delta$ [Lower limit, Upper limit]
Front leg	ThC pitch	[0.0, 0.47]	$[1 \times 10^{-10}, 5 \times 10^{-9}]$	$[1 \times 10^{-10}, 1 \times 10^{-9}]$	[1.0, 10.0]	$[5 \times 10^{-13}, 1 \times 10^{-11}]$
	CTr pitch	[-2.0, -1.68]	$[1 \times 10^{-10}, 1 \times 10^{-9}]$			
	FTi	[1.31, 2.05]	$[1 \times 10^{-10}, 1 \times 10^{-9}]$			
Middle leg	ThC pitch	[2.18, 2.01]	$[1 \times 10^{-10}, 5 \times 10^{-9}]$			
	CTr pitch	[-2.14, -2.01]	$[1 \times 10^{-10}, 1 \times 10^{-9}]$			
	FTi	[1.96, 2.22]	$[1 \times 10^{-10}, 1 \times 10^{-9}]$			
Hind leg	ThC pitch	[2.69, 2.53]	$[1 \times 10^{-10}, 5 \times 10^{-9}]$			
	CTr pitch	[-2.14, -1.55]	$[1 \times 10^{-10}, 1 \times 10^{-9}]$			
	FTi	[1.43, 2.26]	$[1 \times 10^{-10}, 1 \times 10^{-9}]$			

B.1 Supplementary Figures

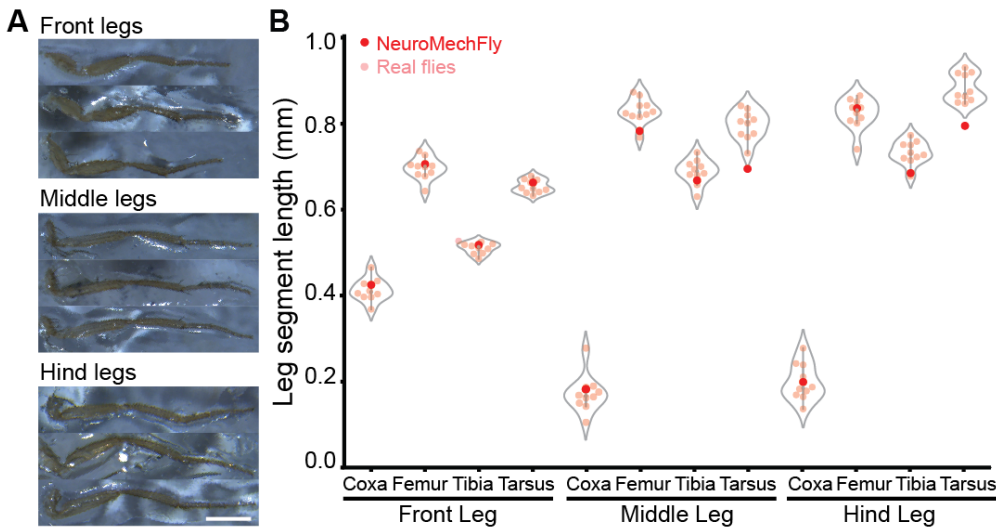


Figure B.1: **Leg segment lengths for real female *Drosophila melanogaster* and NeuroMechFly.** (A) Legs were dissected, straightened, and fixed onto a glass slide for measurements. Scale bar is 0.5mm. (B) The lengths of leg segments from 1-3 dpe animals (pink) and NeuroMechFly (red) are shown. Violin plots indicate median, upper, and lower quartiles.

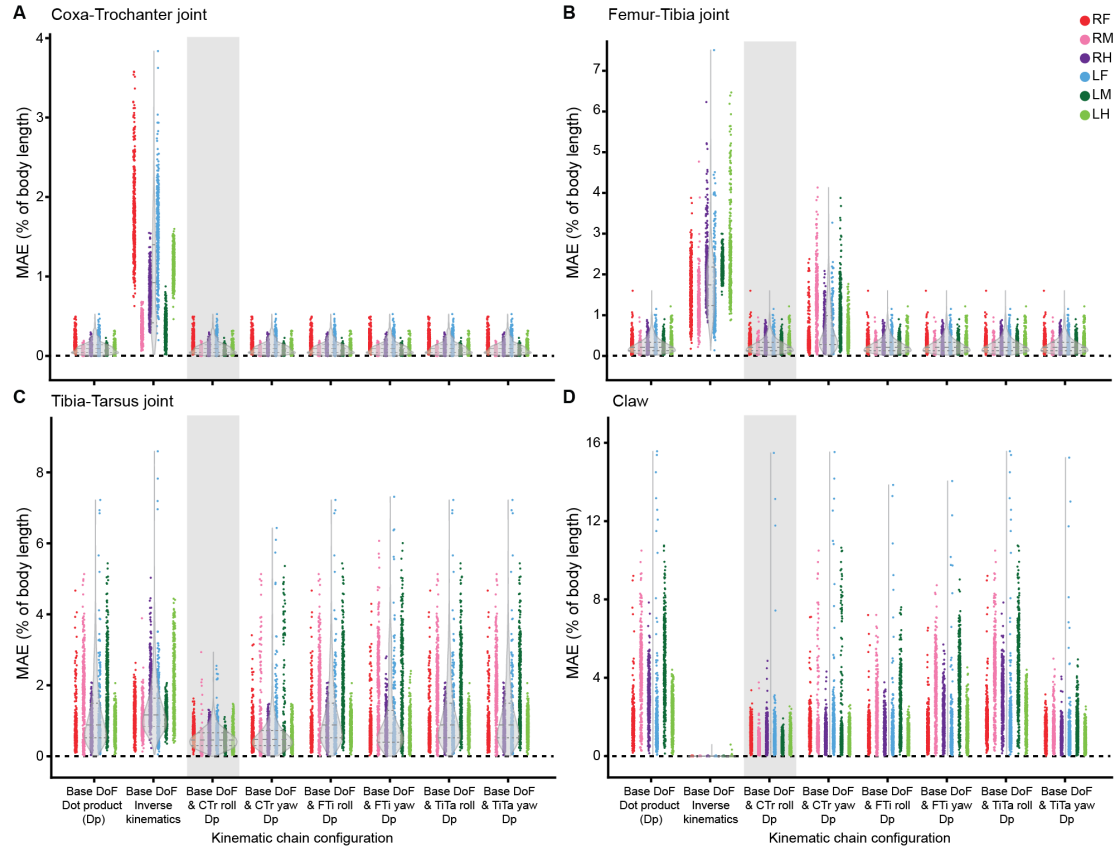


Figure B.2: The position error for every joint in the distal leg during walking as a function of kinematic chain configuration. Body-length normalized mean absolute errors (MAE) comparing measured 3D poses and angle-derived joint positions during walking. Errors are compared among different DoF configurations for (A) Coxa-Trochanter joints, (B) Femur-Tibia joints, (C) Tibia-Tarsus joints, and (D) Claw positions. For each condition,  $n = 2400$  samples were computed across all six legs from 4s of 100 Hz video data. Data for each leg are color-coded. ‘R’ and ‘L’ indicate right and left legs, respectively. ‘F’, ‘M’, and ‘H’ indicate front, middle, and hind legs, respectively. Violin plots indicate median, upper, and lower quartiles (dashed lines). Results from adding a coxa-trochanter roll DoF to based DoFs are highlighted in light gray.

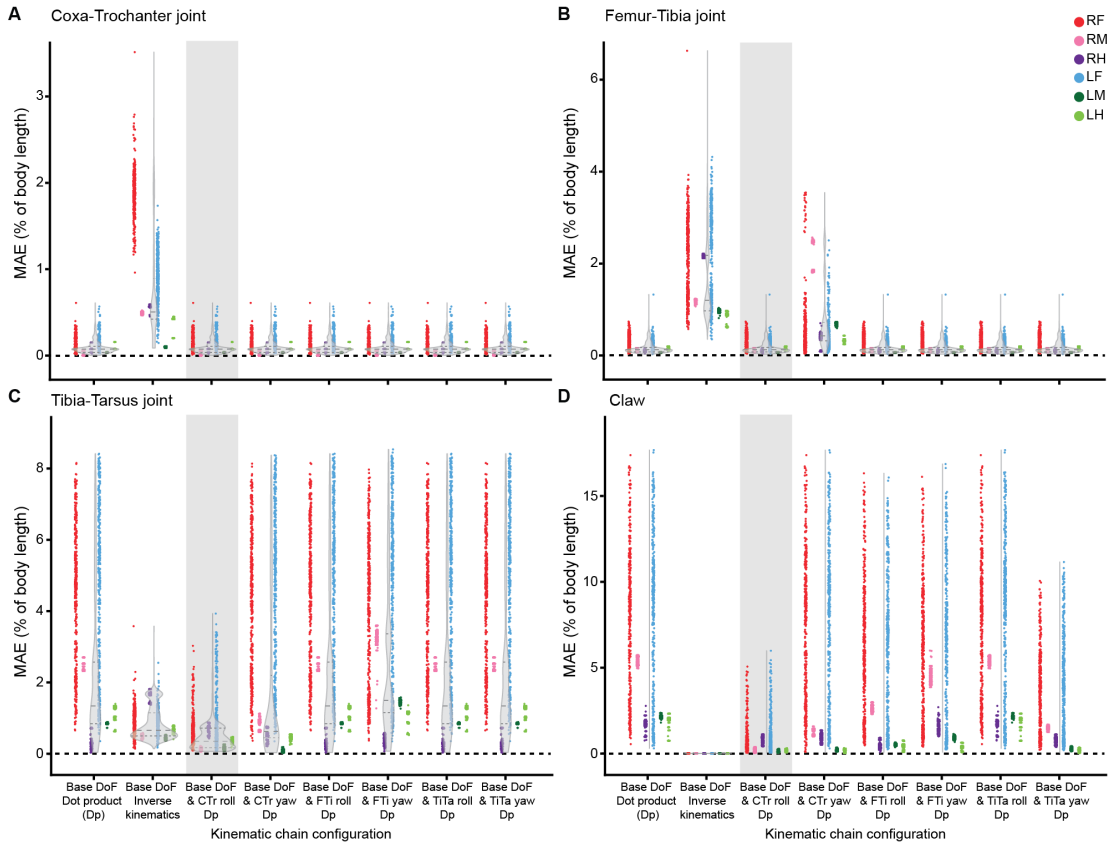


Figure B.3: **The position error for every joint in the distal leg during grooming as a function of kinematic chain configuration.** Body-length normalized mean absolute errors (MAE) comparing measured 3D poses and angle-derived joint positions during grooming. Errors are compared among different DoF configurations for **(A)** Coxa-Trochanter joints, **(B)** Femur-Tibia joints, **(C)** Tibia-Tarsus joints, and **(D)** Claw positions. For each condition,  $n = 2400$  samples were computed across all six legs from 4s of 100 Hz video data. Data for each leg are color-coded. ‘R’ and ‘L’ indicate right and left legs, respectively. ‘F’, ‘M’, and ‘H’ indicate front, middle, and hind legs, respectively. Violin plots indicate median, upper, and lower quartiles (dashed lines). Results from adding a coxa-trochanter roll DoF to based DoFs are highlighted in light gray.

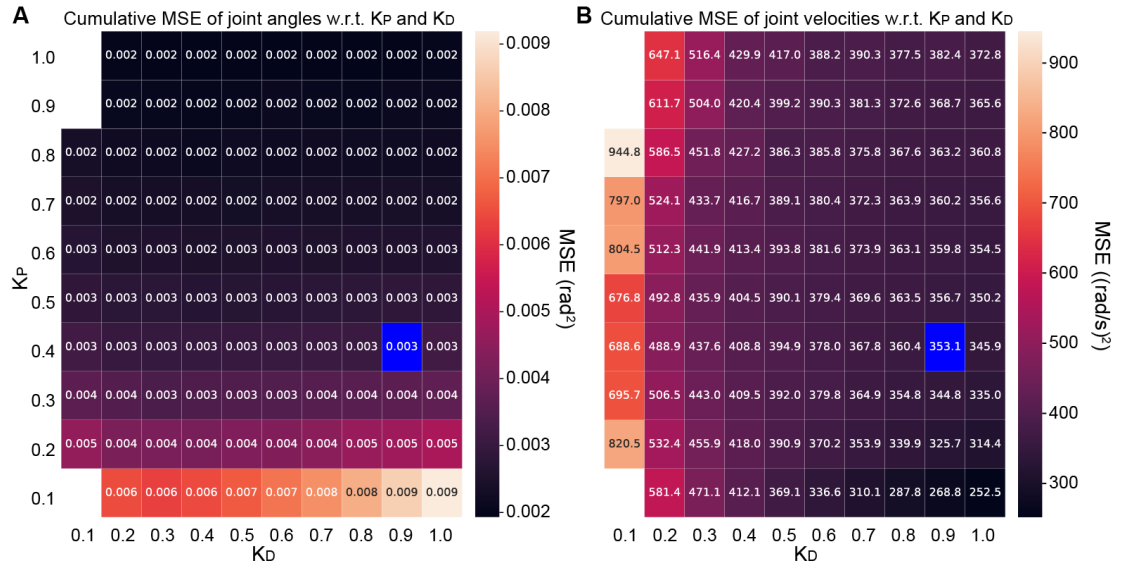
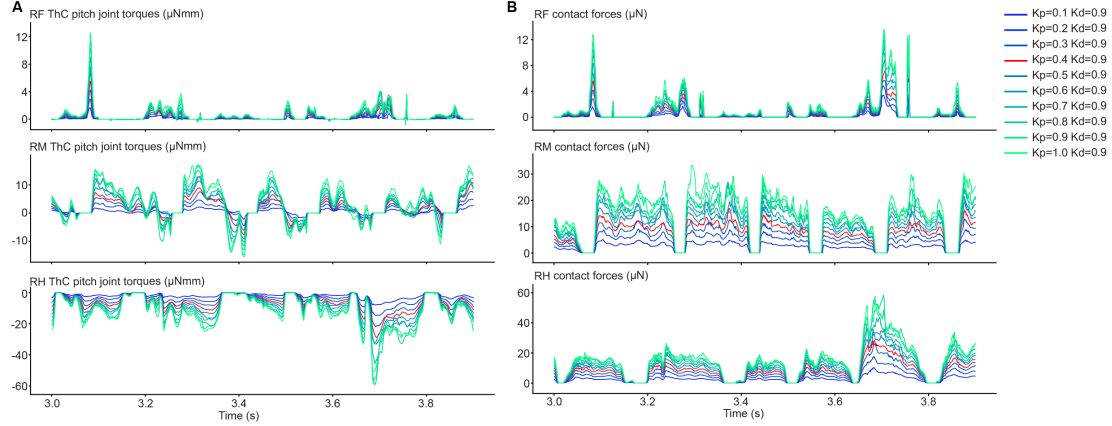


Figure B.4: Mean squared error between tracked and simulated joint positions and velocities as a function of position and velocity gain values. MSE of (A) joint angles and (B) joint velocities as a function of derivative ( $K_d$ ) and positional gain ( $K_p$ ). Selected  $K_p$  and  $K_d$  values are indicated in blue. White areas indicate  $K_p$  and  $K_d$  pairs rendering the simulation nonfunctional.



## Varying proportional gain with a fixed derivative gain



## Varying derivative gain with a fixed proportional gain

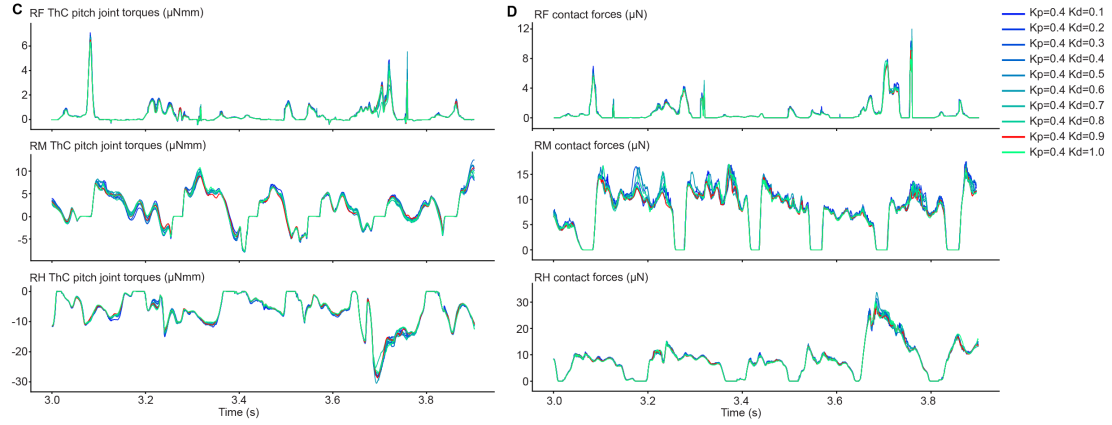


**Figure B.5: Sensitivity of estimated joint torques and contact forces to proportional and derivative gains.** (A) Estimated torques during forward walking as a function of proportional gain ( $K_p$ ). The derivative gain ( $K_d$ ) is fixed at 0.9. Shown are measurements of ThC pitch torques for the right legs. Measurements for the contralateral legs were nearly symmetrically identical and are not shown. (B) Contact force measurements of the right legs during forward walking as a function of  $K_p$  values. Results from the selected  $K_p$  and  $K_d$  values are shown in red. (C) Estimated torques during forward walking as a function of derivative gain ( $K_d$ ). The proportional gain ( $K_p$ ) is fixed at 0.4. Shown are measurements of ThC pitch torques for the right legs. Measurements for the contralateral legs were nearly symmetrically identical and are not shown. (D) Contact force measurements of the right legs during forward walking as a function of  $K_d$ . Results from the selected  $K_p$  and  $K_d$  values are shown in red.

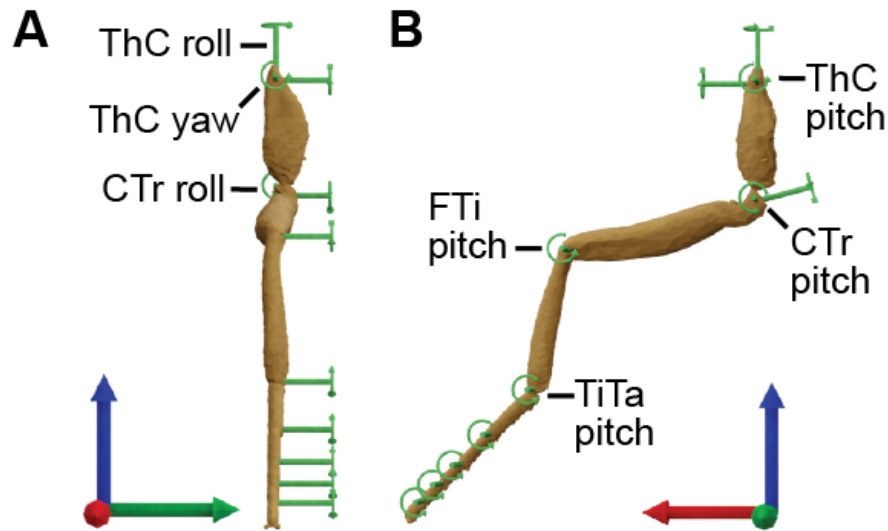


Figure B.6: **Leg joint degrees-of-freedom and their rotational axes.** Each leg is composed of 11 hinge joints. Joints with more than one DoF were modeled as a union of multiple hinge joints. The left foreleg observed from (A) front and (B) side views. The global coordinate system's x, y, and z axes are red, green, and blue, respectively.

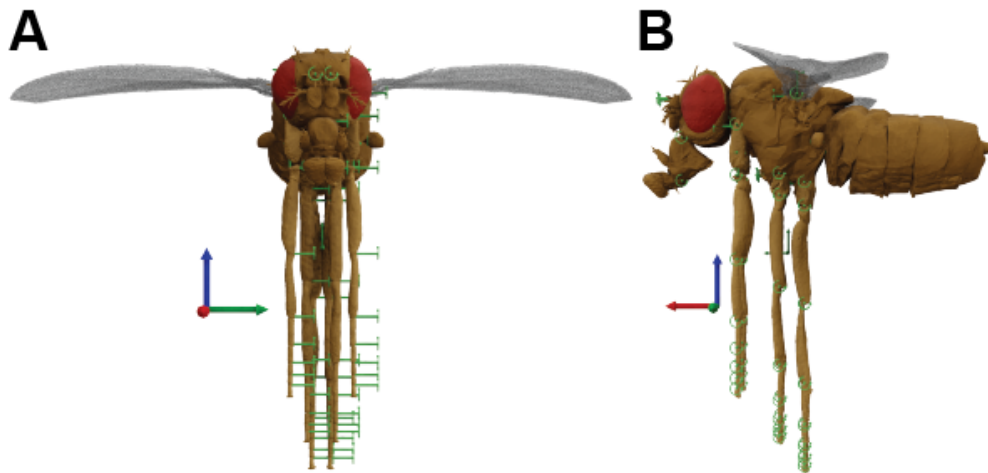


Figure B.7: **The 'zero pose' of NeuroMechFly.** Each body segment (Table B.1) is aggregated using hinge joints. Rotational axes of joints are shown. (A) Zero pose from (A) front and (B) side views. The global coordinate system's x, y, and z axes are shown (red, green, and blue, respectively).

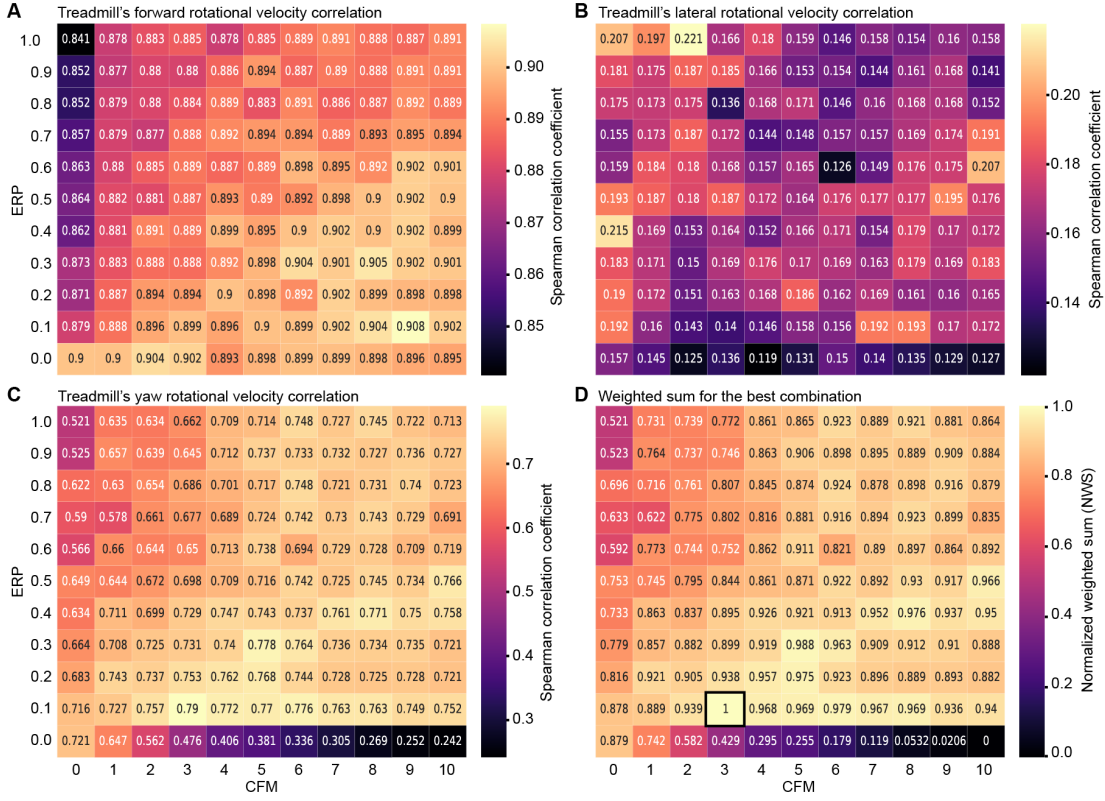


Figure B.8: Sensitivity of simulated spherical treadmill rotation prediction accuracy during tethered walking to ERP and CFM constraint parameters. Spherical treadmill rotational velocities resulting from Kinematic Replay of walking depend on simulation constraint parameters. Shown are Spearman correlation coefficients computed between measured and estimated treadmill rotational velocities for (A) forward, (B) lateral, and (C) yaw axes when varying the simulation's error reduction parameter (ERP), and the constraint force mixing (CFM). (D) The best combination of ERP and CFM—0.1 and 3, respectively (black outline)—was selected through a normalized weighted sum (NWS) of the correlation coefficients for each axis.

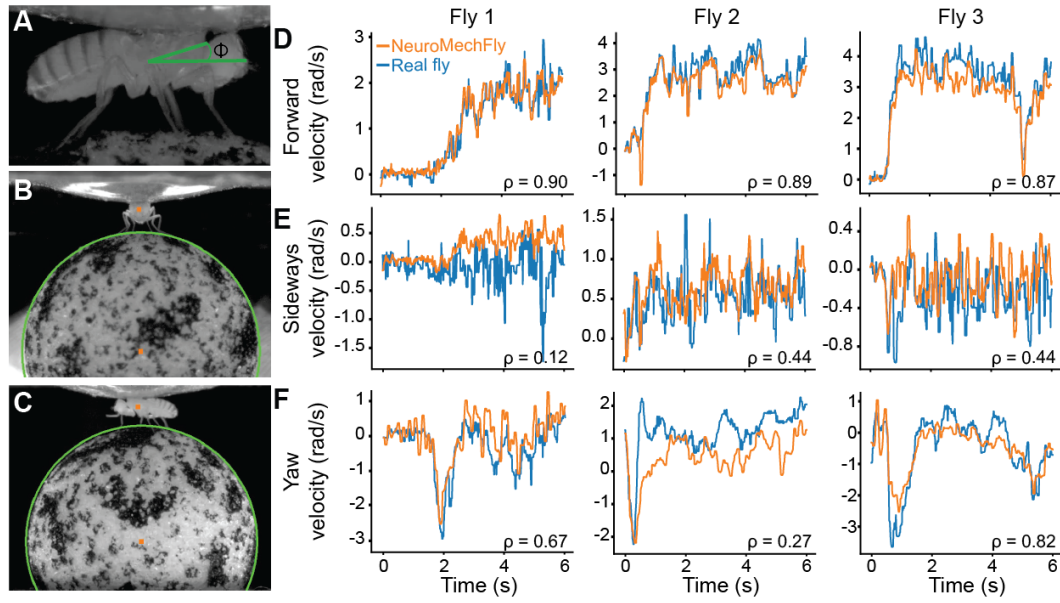


Figure B.9: **Comparing real to simulated spherical treadmill rotational velocities during tethered walking.** Spherical treadmill rotations depend on a tethered fly's (A) inclination ( $\Phi$ , green), (B) lateral, and (C) longitudinal positions with respect to the ball (green outlines). These positions (orange dots) were automatically detected and recreated in the simulation. Rotational velocities of the spherical treadmill generated by three real flies (blue) were compared with those generated by NeuroMechFly (orange) for (D) forward, (E) lateral, and (F) yaw axes. Spearman correlation coefficients ( $\rho$ ) comparing blue and orange traces are indicated.

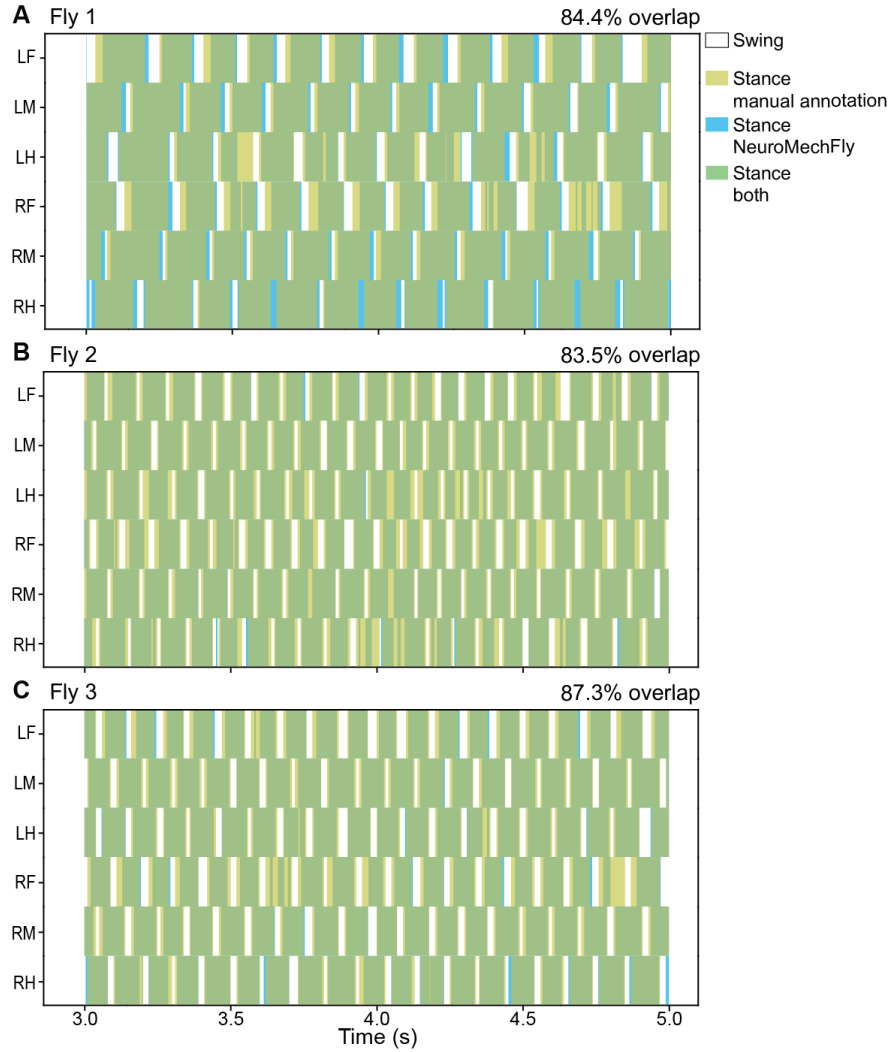


Figure B.10: **Comparing real and simulation predictions for gait diagrams during tethered walking.** Gait diagrams showing manually-annotated stance phases for three real flies (**A-C**, gold) as well as those obtained from estimated ground reaction forces in NeuroMechFly (blue). Percentage of overlap in real and simulated stance phases (green) is quantified. ‘R’ and ‘L’ indicate right and left legs, respectively. ‘F’, ‘M’, and ‘H’ indicate front, middle, and hind legs, respectively.

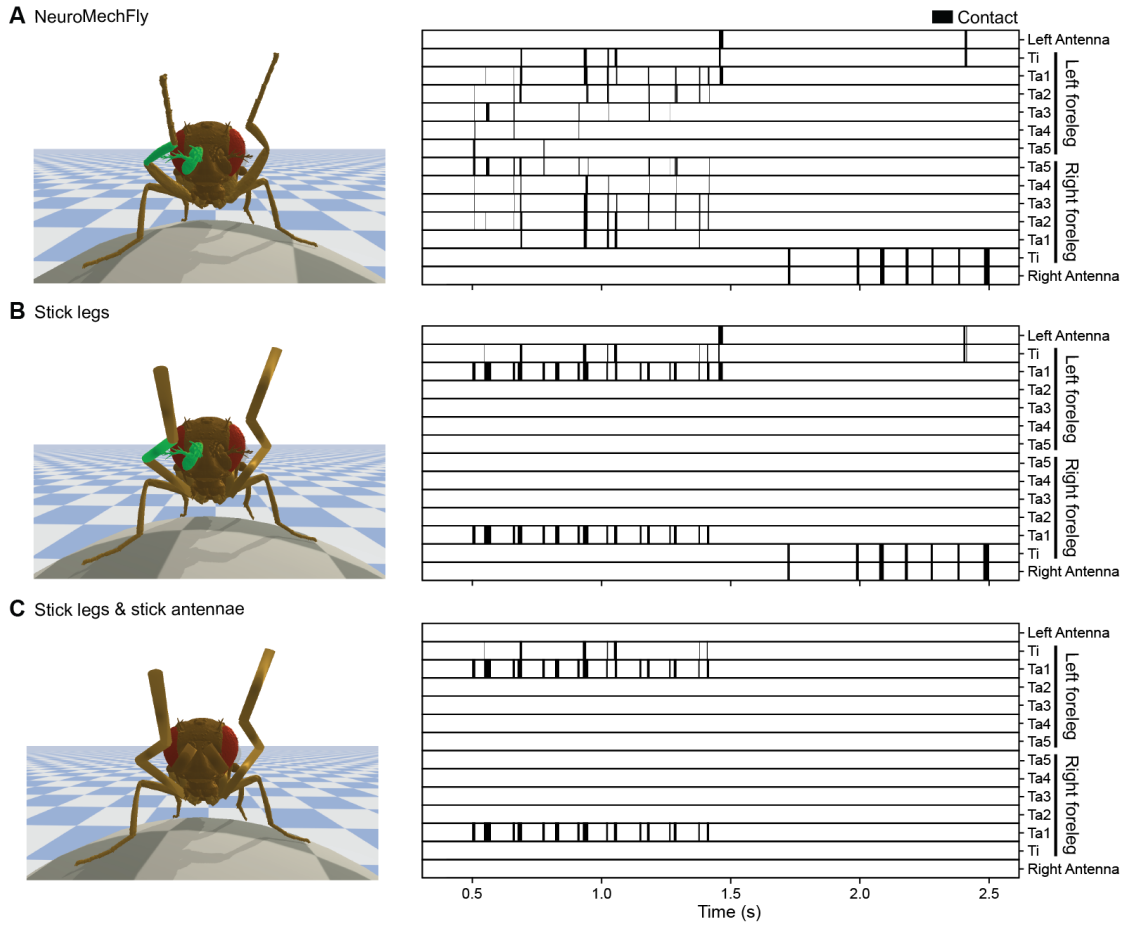


Figure B.11: **The impact of the morphological realism on estimates of leg-leg and leg-antenna contact during grooming.** Collision diagrams from kinematic replay of foreleg/antennal grooming when using either (A) NeuroMechFly's morphologically detailed legs and antennae, or after replacing its (B) forelegs, or (C) forelegs and antennae with simple cylinders, as in a conventional stick skeletal model.

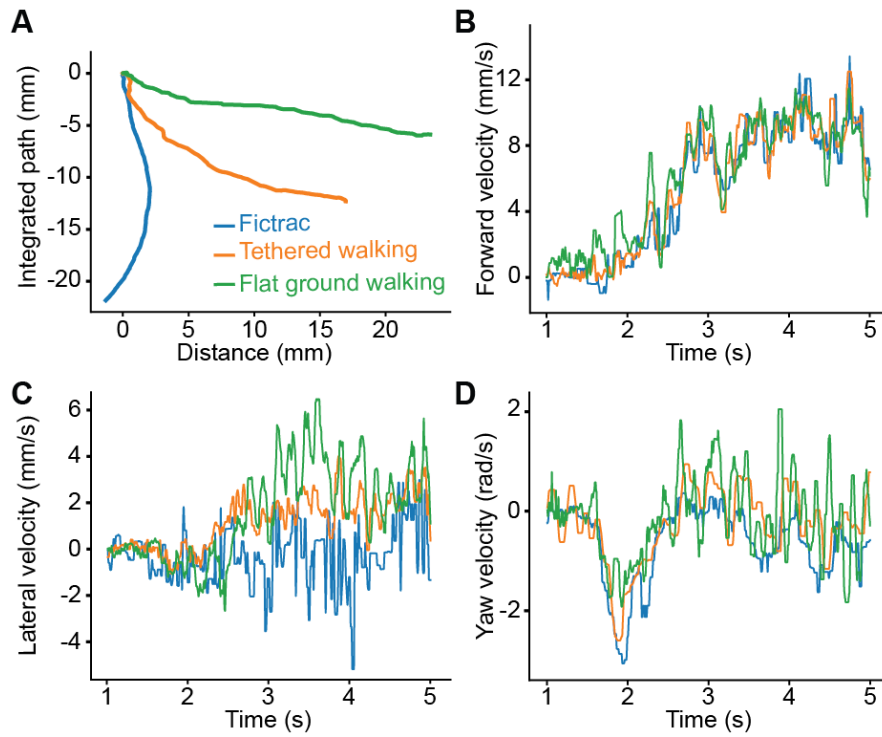


Figure B.12: **Comparison of walking paths and velocities for real tethered walking versus kinematic replay in a tethered or untethered model.** Leg kinematics from a tethered walking experiment (blue) were used for kinematic replay in NeuroMechFly either tethered on a simulated spherical treadmill (orange) or freely walking on flat ground (green). Shown are resulting (A) integrated walking paths, as well as associated (B) forward, (C) lateral, and (D) yaw velocities.

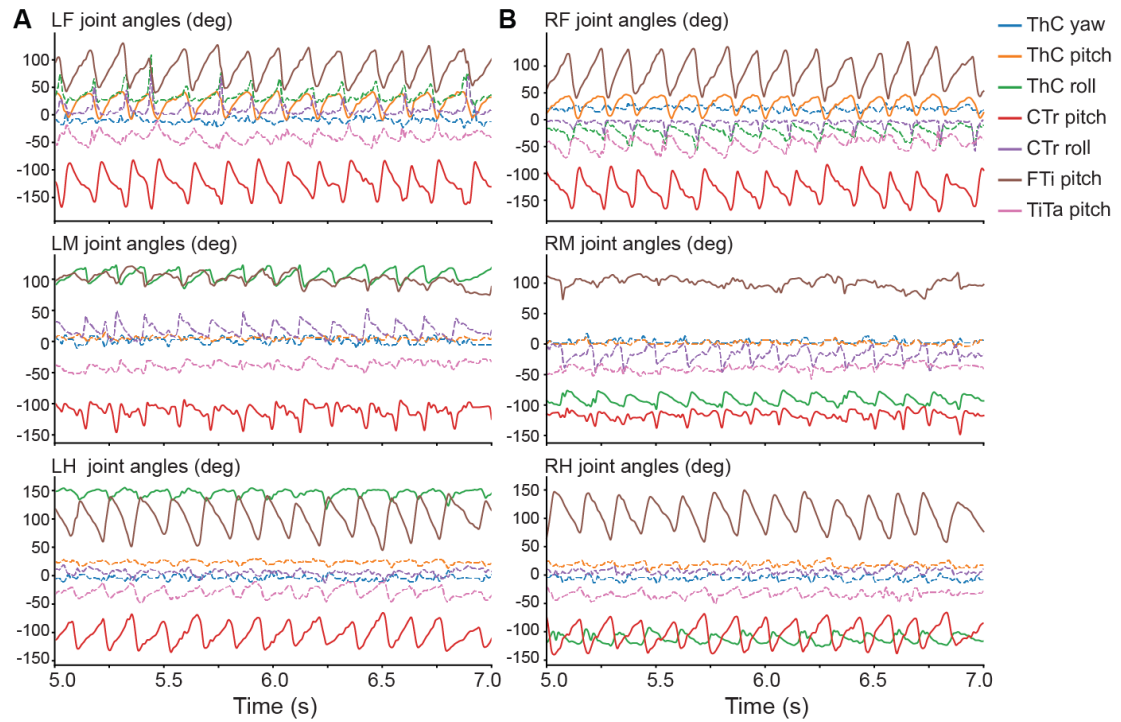
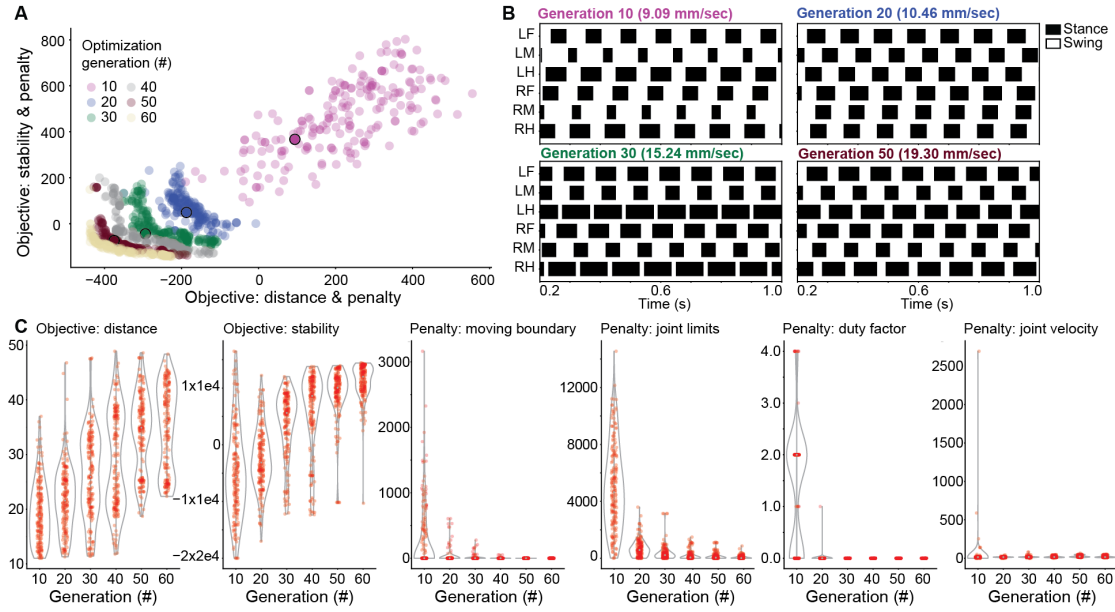


Figure B.13: **Measured joint angles during real forward walking.** Joint angles for the (A) left and (B) right legs measured from a real fly during forward walking. Only the three DoFs with the highest amplitudes (solid lines) were controlled during optimization. These were: for the front legs: ThC pitch, CTr pitch, and FTi pitch; for the middle and hind legs: ThC roll, CTr pitch, and FTi pitch DoFs. The remaining four DoFs (dashed lines) for each leg did not exhibit pronounced angular changes and were fixed to their mean values during optimization.





**Figure B.14: Objectives, penalties, and individual solutions over generations when optimizing for fast and statically stable tethered walking.** (A) Pareto front approximations for six optimization generations. Later generations are more negative because the optimizer aims to minimize the distance and stability objective functions, whose signs are inverted. Four individual solutions dominated by the pareto optimal solutions were selected for more in-depth analysis (10th (purple), 20th (blue), 30th (green), and 50th (dark red); all are outlined in black). (B) Gait diagrams from selected solutions. Stance (black) and swing (white) phases were calculated by reading-out tarsal ground contacts for each leg. Indicated are the velocities of each solution as calculated by averaging the spherical treadmill forward velocity. (C) Progression of weighted objective values (shown without sign inversion) and penalties over the course of 60 generations. Objectives (distance and stability coefficients) increase across generations, while penalties decrease or converge to, or near, zero. The objective distance (mm) is the distance traveled in 2 s. The penalty duty factor is the number of legs violating the duty factor constraint. The remaining penalties are shown in Arbitrary Units.

## B.2 Supplementary Videos

**Video 1: Constructing a data-driven biomechanical model of adult *Drosophila*.**

An adult female fly is encased in resin for x-ray microtomography. The resulting x-ray microtomography data reveals cuticle, muscles, nervous tissues, and internal organs. These data are thresholded to separate the foreground from background. Then the exoskeleton is voxelized into a 3-dimensional polygon mesh. Articulated body segments are separated from one another and then reassembled into a natural pose. Bones are added and rigged to permit actuation. Finally, textures are added to the model for visualization purposes.

<https://www.dropbox.com/s/pkbh4o81bdomx1x/Video1.mov?dl=0>

**Video 2: Visualization of possible additional leg degrees-of-freedom.** NeuroMechFly's left-middle leg is sequentially actuated along DoFs that are later analyzed to test their requirement for accurate replay of real fly leg kinematics. The articulated joint (e.g., 'CTr') and type of movement ('roll') are indicated.

<https://www.dropbox.com/s/8uhi9cyzhdnty4/Video2.mov?dl=0>

**Video 3: The effect of additional degrees-of-freedom on the accuracy of replaying forward walking.** Measured 3D poses (solid lines) and forward kinematic replay (dashed lines) for forward walking. Forward kinematics are determined either (**top-left**) using no additional degrees-of-freedom (Base DoF, dot product), (**top-middle**) instead using inverse kinematics to optimize joint angles and minimize error with only base degrees-of-freedom (Base DoF, inverse kinematics), or (**top-right and bottom row**) by adding a single new DoF (BaseDoF & 'joint' 'DoF'). Legs are color-coded.

<https://www.dropbox.com/s/3f23rdpvz7os640/Video3.mov?dl=0>

**Video 4: The effect of additional degrees-of-freedom on the accuracy of replaying foreleg/antennal grooming.** Measured 3D poses (solid lines) and forward kinematic replay (dashed lines) for foreleg/antennal grooming. Forward kinematics are determined either (**top-left**) using no additional degrees-of-freedom (Base DoF, dot product), (**top-middle**) instead using inverse kinematics to optimize joint angles and minimize error with only base degrees-of-freedom (Base DoF, inverse kinematics), or (**top-right and bottom row**) by adding a single new DoF (BaseDoF & 'joint' 'DoF'). Legs are color-coded.

<https://www.dropbox.com/s/zv860h9ic2r8li2/Video4.mov?dl=0>

**Video 5: Kinematic replay of *Drosophila* forward walking using NeuroMechFly.** (**top-left, 'Raw data'**) A tethered adult fly is shown walking on a spherical treadmill. One of six synchronized camera views is shown. Data are replayed at 0.2x real time. (**bottom-left, '2D tracking'**) 2D poses (filled circles) and connecting 'bones' (lines) are

superimposed for the proximal three legs. (**bottom-right, ‘3D reconstruction’**) These six 2D poses are triangulated to obtain 3D poses. Overlaid are triangulated 3D poses (solid lines) and 3D poses obtained by solving forward kinematics from joint angles (dashed lines). (**top-right, ‘Kinematic replay’**) These 3D joint angles actuate NeuroMechFly leg movements while it walks on a simulated spherical treadmill. Tarsal contacts with the ground are indicated (green). Estimated ground reaction force vectors for the proximal three legs are superimposed on the original video data (**top-left**).

<https://www.dropbox.com/s/iieuwgm8bazzmd/Video5.mov?dl=0>

**Video 6: Kinematic replay of *Drosophila* foreleg/antennal grooming using NeuroMechFly.** (**top-left, ‘Raw data’**) A tethered adult fly is shown grooming on a spherical treadmill. One of six synchronized camera views is shown. Data are replayed at 0.2x real time. (**bottom-left, ‘2D tracking’**) 2D poses (filled circles) and connecting ‘bones’ (lines) are superimposed for the proximal three legs. (**bottom-right, ‘3D reconstruction’**) These six 2D poses are triangulated to obtain 3D poses. Overlaid are triangulated 3D poses (solid lines) and 3D poses obtained by solving forward kinematics from joint angles (dashed lines). (**top-right, ‘Kinematic replay’**) These joint angles actuate NeuroMechFly leg movements while it grooms on a simulated spherical treadmill. Leg segments and antennal collisions are indicated (green). Estimated collision force vectors for the front legs and antennae are subsequently superimposed on the original video data (**top-left**).

<https://www.dropbox.com/s/m3j6wfevzenhfkn/Video6.mov?dl=0>

**Video 7: The influence of leg and antenna morphological detail on collision predictions.** (**top-left, ‘Raw data’**) Real fly grooming as recorded from the front camera. (**top-right, ‘NeuroMechFly’**) NeuroMechFly performing kinematic replay of grooming. (**bottom-left, ‘Stick model legs’**) NeuroMechFly with stick legs but detailed antennae. (**bottom-right, ‘Stick model legs and antennae’**) NeuroMechFly with stick legs and stick antennae.

<https://www.dropbox.com/s/7wpnf2a8s4pzi65/Video7.mov?dl=0>

**Video 8: Kinematic replay of tethered *Drosophila* forward walking using NeuroMechFly on flat terrain without body support.** (**Right**) Pose estimates obtained from a real tethered fly walking on a spherical treadmill are replayed in NeuroMechFly as it walks untethered on flat terrain without body support. (**Left**) Integrated paths are shown for tethered (orange) and flat ground (green) scenarios.

<https://www.dropbox.com/s/e7qvz4tm1exhefl/Video8.mov?dl=0>

**Video 9: Forward walking across optimization generations.** Forward walking for four solutions shown across optimization generations 15, 30, 45 and 60. Tarsal contacts

with the ground are indicated (green). Videos are replayed at 0.1x real time. Solutions shown are: (top-left) a random individual, (top-right) the fastest individual (i.e., with the longest distance traveled), (bottom-left) the most stable individual, and (bottom-right) the best trade-off achieving both high speed and static stability.

<https://www.dropbox.com/s/lizgd3ss2yftlxb/Video9.mov?dl=0>

**Video 10: Replaying real tethered walking kinematics on flat terrain and applying external perturbations.** Pose estimates obtained from a real tethered fly walking on a spherical treadmill are replayed in NeuroMechFly as it walks untethered on flat terrain without body support. Simulated spheres are projected at the model to illustrate perturbations and the possibility of using more complex physical environments in PyBullet.

<https://www.dropbox.com/s/ae6zrejhdwduun/Video10.mov?dl=0>

### B.3 Code and data availability

Data are available at:

<https://doi.org/10.7910/DVN/Y3TAEC>

Code, and documentation are available at:

<https://github.com/NeLy-EPFL/NeuroMechFly>

<https://nely-epfl.github.io/NeuroMechFly>

### B.4 Funding

PR acknowledges support from an SNSF Project Grant (175667), and an SNSF Eccellenza Grant (181239). VLR acknowledges support from the Mexican National Council for Science and Technology, CONACYT, under the grant number 709993. ST acknowledges support from the European Union's Horizon 2020 research and innovation program under grant agreement nos. 720270 (SGA1), 785907 (SGA2). PGO acknowledges support from the Swiss Government Excellence Scholarship for Doctoral Studies. JA acknowledges support from the Human Frontier Science Program (HFSP-RGP0027/2017).

### B.5 Acknowledgments

We thank Stéphanie Clerc Rosset and Graham Knott (Biological Electron Microscopy Facility, EPFL, Lausanne, Switzerland) for preparing *Drosophila melanogaster* samples for X-ray microtomography. We thank Halla Sigurthorsdottir for early work on fly leg

degrees-of-freedom.

## Appendix C

# Supplementary Information : Non-human Primate

### C.1 Muscle spindle and golgi tendon model equations

The equations (4.2), (4.3), and (4.4), in numerical form, were:

$$f_{\text{Ia}} = \max \left\{ 0, \quad 4.3 * \text{sign}(v^M) |v^M|^{0.6} + 2(l^M - l_{\text{opt}}^M) + 50a + 20 \right\}$$

$$f_{\text{Ib}} = \max \left\{ 0, \quad 333 \frac{F^M}{F_{\text{max}}^M} \right\} \tag{A2}$$

$$f_{\text{II}} = \max \{ 0, \quad 13.5 (l^M - l_{\text{opt}}^M) + 20a + 10 \} \tag{A3}$$



# Bibliography

- Ajiboye, A Bolu et al. (May 2017). “Restoration of Reaching and Grasping Movements through Brain-Controlled Muscle Stimulation in a Person with Tetraplegia: A Proof-of-Concept Demonstration”. In: *The Lancet* 389.10081, pp. 1821–1830. ISSN: 0140-6736. DOI: [10.1016/S0140-6736\(17\)30601-3](https://doi.org/10.1016/S0140-6736(17)30601-3).
- Akay, Turgay et al. (Nov. 2014). “Degradation of Mouse Locomotor Pattern in the Absence of Proprioceptive Sensory Feedback”. In: *Proceedings of the National Academy of Sciences* 111.47, pp. 16877–16882. ISSN: 0027-8424, 1091-6490. DOI: [10.1073/pnas.1419045111](https://doi.org/10.1073/pnas.1419045111).
- Alexander, R.Mcn. (1976). “MECHANICS OF BIPEDAL LOCOMOTION”. In: *Zoology*. Elsevier, pp. 493–504. ISBN: 978-0-08-018767-9. DOI: [10.1016/B978-0-08-018767-9.50047-0](https://doi.org/10.1016/B978-0-08-018767-9.50047-0).
- Allen, Vivian, Heather Paxton, and John R. Hutchinson (2009). “Variation in Center of Mass Estimates for Extant Sauropsids and Its Importance for Reconstructing Inertial Properties of Extinct Archosaurs”. In: *The Anatomical Record* 292.9, pp. 1442–1461. ISSN: 1932-8494. DOI: [10.1002/ar.20973](https://doi.org/10.1002/ar.20973).
- Anderson, F. C. and M. G. Pandy (Feb. 2001). “Static and Dynamic Optimization Solutions for Gait Are Practically Equivalent”. In: *Journal of Biomechanics* 34.2, pp. 153–161. ISSN: 0021-9290. DOI: [10.1016/s0021-9290\(00\)00155-x](https://doi.org/10.1016/s0021-9290(00)00155-x).
- Angeli, Claudia A. et al. (Sept. 2018). “Recovery of Over-Ground Walking after Chronic Motor Complete Spinal Cord Injury”. In: *New England Journal of Medicine* 379.13, pp. 1244–1250. ISSN: 0028-4793. DOI: [10.1056/NEJMoa1803588](https://doi.org/10.1056/NEJMoa1803588).
- Aoi, Shinya et al. (Jan. 2019). “Neuromusculoskeletal Model That Walks and Runs across a Speed Range with a Few Motor Control Parameter Changes Based on the Muscle Synergy Hypothesis”. In: *Scientific Reports* 9.1, pp. 1–13. ISSN: 2045-2322. DOI: [10.1038/s41598-018-37460-3](https://doi.org/10.1038/s41598-018-37460-3).
- Arnold, Edith M., Samuel R. Hamner, et al. (June 2013). “How Muscle Fiber Lengths and Velocities Affect Muscle Force Generation as Humans Walk and Run at Different Speeds”. In: *Journal of Experimental Biology* 216.11, pp. 2150–2160. ISSN: 0022-0949. DOI: [10.1242/jeb.075697](https://doi.org/10.1242/jeb.075697).



- Arnold, Edith M., Samuel R. Ward, et al. (Feb. 2010). “A Model of the Lower Limb for Analysis of Human Movement”. In: *Annals of Biomedical Engineering* 38.2, pp. 269–279. ISSN: 0090-6964, 1573-9686. DOI: [10.1007/s10439-009-9852-5](https://doi.org/10.1007/s10439-009-9852-5).
- Ashley-Ross, Miriam A. et al. (Aug. 2013). “Vertebrate Land Invasions—Past, Present, and Future: An Introduction to the Symposium”. In: *Integrative and Comparative Biology* 53.2, pp. 192–196. ISSN: 1540-7063. DOI: [10.1093/icb/ict048](https://doi.org/10.1093/icb/ict048).
- Ausborn, Jessica, Natalia A. Shevtsova, Vittorio Caggiano, et al. (Jan. 2019). *Computational Modeling of Brainstem Circuits Controlling Locomotor Frequency and Gait*. <https://elifesciences.org/articles/43587>. DOI: [10.7554/eLife.43587](https://doi.org/10.7554/eLife.43587).
- Ausborn, Jessica, Natalia A. Shevtsova, and Simon M. Danner (Jan. 2021). “Computational Modeling of Spinal Locomotor Circuitry in the Age of Molecular Genetics”. In: *International Journal of Molecular Sciences* 22.13, p. 6835. DOI: [10.3390/ijms22136835](https://doi.org/10.3390/ijms22136835).
- Azevedo, Anthony W et al. (2020). “A Size Principle for Recruitment of Drosophila Leg Motor Neurons”. In: *eLife* 9.
- Barra, Beatrice et al. (July 2018). “Selective Recruitment of Arm Motoneurons in Non-human Primates Using Epidural Electrical Stimulation of the Cervical Spinal Cord”. In: *Annual International Conference of the IEEE Engineering in Medicine and Biology Society. IEEE Engineering in Medicine and Biology Society. Annual International Conference 2018*, pp. 1424–1427. ISSN: 2694-0604. DOI: [10.1109/EMBC.2018.8512554](https://doi.org/10.1109/EMBC.2018.8512554).
- Bates, Karl T. et al. (Feb. 2009). “Estimating Mass Properties of Dinosaurs Using Laser Imaging and 3D Computer Modelling”. In: *PLoS ONE* 4.2, e4532. ISSN: 1932-6203. DOI: [10.1371/journal.pone.0004532](https://doi.org/10.1371/journal.pone.0004532).
- Beal, D. N. et al. (Feb. 2006). “Passive Propulsion in Vortex Wakes”. In: *Journal of Fluid Mechanics* 549.-1, p. 385. ISSN: 0022-1120, 1469-7645. DOI: [10.1017/S0022112005007925](https://doi.org/10.1017/S0022112005007925).
- Bender, John A, Elaine M Simpson, and Roy E Ritzmann (2010). “Computer-Assisted 3D Kinematic Analysis of All Leg Joints in Walking Insects”. In: *PloS one* 5.10.
- Benitez-Hidalgo, Antonio et al. (2019). “jMetalPy: A Python Framework for Multi-Objective Optimization with Metaheuristics”. In: *Swarm and Evolutionary Computation* 51.
- Bensmaia, Sliman J. (Sept. 2015). “Biological and Bionic Hands: Natural Neural Coding and Artificial Perception”. In: *Philosophical Transactions of the Royal Society of London. Series B, Biological Sciences* 370.1677, p. 20140209. ISSN: 1471-2970. DOI: [10.1098/rstb.2014.0209](https://doi.org/10.1098/rstb.2014.0209).
- Birznieks, Ingvars et al. (Oct. 2001). “Encoding of Direction of Fingertip Forces by Human Tactile Afferents”. In: *Journal of Neuroscience* 21.20, pp. 8222–8237. ISSN: 0270-6474, 1529-2401. DOI: [10.1523/JNEUROSCI.21-20-08222.2001](https://doi.org/10.1523/JNEUROSCI.21-20-08222.2001).
- Bishop, Peter J., Andrew R. Cuff, and John R. Hutchinson (Oct. 2020). “How to Build a Dinosaur: Musculoskeletal Modeling and Simulation of Locomotor Biomechanics in Extinct Animals”. In: *Paleobiology*, pp. 1–38. ISSN: 0094-8373, 1938-5331. DOI: [10.1017/pab.2020.46](https://doi.org/10.1017/pab.2020.46).

- Blickhan, R. and R.J. Full (Nov. 1993). “Similarity in Multilegged Locomotion: Bouncing like a Monopode”. In: *Journal of Comparative Physiology A* 173.5. ISSN: 0340-7594, 1432-1351. DOI: [10.1007/BF00197760](https://doi.org/10.1007/BF00197760).
- Bolaños, Luis A. et al. (Apr. 2021). “A Three-Dimensional Virtual Mouse Generates Synthetic Training Data for Behavioral Analysis”. In: *Nature methods*. ISSN: 1548-7105. DOI: [10.1038/s41592-021-01103-9](https://doi.org/10.1038/s41592-021-01103-9).
- Bonnan, Matthew F. et al. (Mar. 2016). “Forelimb Kinematics of Rats Using XROMM, with Implications for Small Eutherians and Their Fossil Relatives”. In: *PLoS ONE* 11.3. ISSN: 1932-6203. DOI: [10.1371/journal.pone.0149377](https://doi.org/10.1371/journal.pone.0149377).
- Bouton, Chad E. et al. (May 2016). “Restoring Cortical Control of Functional Movement in a Human with Quadriplegia”. In: *Nature* 533.7602, pp. 247–250. ISSN: 1476-4687. DOI: [10.1038/nature17435](https://doi.org/10.1038/nature17435).
- Brill, N. A. et al. (Feb. 2018). “Evaluation of High-Density, Multi-Contact Nerve Cuffs for Activation of Grasp Muscles in Monkeys”. In: *Journal of Neural Engineering* 15.3, p. 036003. ISSN: 1741-2552. DOI: [10.1088/1741-2552/aa8735](https://doi.org/10.1088/1741-2552/aa8735).
- Brown, T. Graham (1911). “The Intrinsic Factors in the Act of Progression in the Mammal”. In: *Proceedings of the Royal Society of London B: Biological Sciences* 84.572, pp. 308–319. ISSN: 0950-1193. DOI: [10.1098/rspb.1911.0077](https://doi.org/10.1098/rspb.1911.0077). eprint: <http://rspb.royalsocietypublishing.org/content/84/572/308.full.pdf>.
- Bruns, Tim M. et al. (Apr. 2013). “Real-Time Control of Hind Limb Functional Electrical Stimulation Using Feedback from Dorsal Root Ganglia Recordings”. In: *Journal of Neural Engineering* 10.2, p. 026020. ISSN: 1741-2552. DOI: [10.1088/1741-2560/10/2/026020](https://doi.org/10.1088/1741-2560/10/2/026020).
- Capogrosso, Marco and Scott F. Lempka (May 2020). “A Computational Outlook on Neurostimulation”. In: *Bioelectronic Medicine* 6.1, p. 10. ISSN: 2332-8886. DOI: [10.1186/s42234-020-00047-3](https://doi.org/10.1186/s42234-020-00047-3).
- Capogrosso, Marco, Tomislav Milekovic, et al. (Nov. 2016). “A Brain–Spine Interface Alleviating Gait Deficits after Spinal Cord Injury in Primates”. In: *Nature* 539.7628, pp. 284–288. ISSN: 1476-4687. DOI: [10.1038/nature20118](https://doi.org/10.1038/nature20118).
- Capogrosso, Marco, Fabien B. Wagner, et al. (Sept. 2018). “Configuration of Electrical Spinal Cord Stimulation through Real-Time Processing of Gait Kinematics”. In: *Nature Protocols* 13.9, pp. 2031–2061. ISSN: 1750-2799. DOI: [10.1038/s41596-018-0030-9](https://doi.org/10.1038/s41596-018-0030-9).
- Capogrosso, Marco, Nikolaus Wenger, et al. (Dec. 2013). “A Computational Model for Epidural Electrical Stimulation of Spinal Sensorimotor Circuits”. In: *The Journal of Neuroscience: The Official Journal of the Society for Neuroscience* 33.49, pp. 19326–19340. ISSN: 1529-2401. DOI: [10.1523/JNEUROSCI.1688-13.2013](https://doi.org/10.1523/JNEUROSCI.1688-13.2013).
- Cardona, Manuel and Cecilia E. Garcia Cena (2019). “Biomechanical Analysis of the Lower Limb: A Full-Body Musculoskeletal Model for Muscle-Driven Simulation”. In: *IEEE Access* 7, pp. 92709–92723. ISSN: 2169-3536. DOI: [10.1109/ACCESS.2019.2927515](https://doi.org/10.1109/ACCESS.2019.2927515).
- Carnevale, Ted et al. (2006). *The NEURON Book*. Cambridge University Press.
- Chaffey, Nigel (2001). *Principles and Techniques of Electron Microscopy: Biological Applications*.

- Chan, Sherwin S and Daniel W Moran (Dec. 2006). “Computational Model of a Primate Arm: From Hand Position to Joint Angles, Joint Torques and Muscle Forces”. In: *Journal of Neural Engineering* 3.4, pp. 327–337. ISSN: 1741-2560, 1741-2552. DOI: [10.1088/1741-2560/3/4/010](https://doi.org/10.1088/1741-2560/3/4/010).
- Charles, James P., Ornella Cappellari, and John R. Hutchinson (2018). “A Dynamic Simulation of Musculoskeletal Function in the Mouse Hindlimb During Trotting Locomotion”. In: *Frontiers in Bioengineering and Biotechnology* 6. ISSN: 2296-4185. DOI: [10.3389/fbioe.2018.00061](https://doi.org/10.3389/fbioe.2018.00061).
- Charles, James P., Ornella Cappellari, Andrew J. Spence, John R. Hutchinson, et al. (Apr. 2016). “Musculoskeletal Geometry, Muscle Architecture and Functional Specialisations of the Mouse Hindlimb”. In: *PLOS ONE* 11.4, e0147669. ISSN: 1932-6203. DOI: [10.1371/journal.pone.0147669](https://doi.org/10.1371/journal.pone.0147669).
- Charles, James P., Ornella Cappellari, Andrew J. Spence, Dominic J. Wells, et al. (2016). “Muscle Moment Arms and Sensitivity Analysis of a Mouse Hindlimb Musculoskeletal Model”. In: *Journal of Anatomy* 229.4, pp. 514–535. ISSN: 1469-7580. DOI: [10.1111/joa.12461](https://doi.org/10.1111/joa.12461).
- Chen, Chin-Lin et al. (2018). “Imaging Neural Activity in the Ventral Nerve Cord of Behaving Adult Drosophila”. In: *Nature communications* 9.1.
- Cheng, E. J. and S. H. Scott (Sept. 2000). “Morphometry of Macaca Mulatta Forelimb. I. Shoulder and Elbow Muscles and Segment Inertial Parameters”. In: *Journal of Morphology* 245.3, pp. 206–224. ISSN: 0362-2525. DOI: [10.1002/1097-4687\(200009\)245:3<206::AID-JMOR3>3.0.CO;2-U](https://doi.org/10.1002/1097-4687(200009)245:3<206::AID-JMOR3>3.0.CO;2-U).
- Chiel, Hillel J and Randall D Beer (1997). “The Brain Has a Body: Adaptive Behavior Emerges from Interactions of Nervous System, Body and Environment”. In: *Trends in neurosciences* 20.12, pp. 553–557.
- CloudCompare - Open Source Project (n.d.).
- Coatham, Samuel J., William I. Sellers, and Thomas A. Püschel (June 2021). “Convex Hull Estimation of Mammalian Body Segment Parameters”. In: *Royal Society Open Science* 8.6, p. 210836. DOI: [10.1098/rsos.210836](https://doi.org/10.1098/rsos.210836).
- Cofer, D. et al. (2010). “Neuromechanical Simulation of the Locust Jump”. In: *Journal of Experimental Biology* 213.7, pp. 1060–1068. ISSN: 0022-0949. DOI: [10.1242/jeb.034678](https://doi.org/10.1242/jeb.034678).
- Cofer, David et al. (Mar. 2010). “AnimatLab: A 3D Graphics Environment for Neuromechanical Simulations”. In: *Journal of Neuroscience Methods* 187.2, pp. 280–288. ISSN: 0165-0270. DOI: [10.1016/j.jneumeth.2010.01.005](https://doi.org/10.1016/j.jneumeth.2010.01.005).
- Cohen, Avis H., Philip J. Holmes, and Richard H. Rand (1982). “The Nature of the Coupling between Segmental Oscillators of the Lamprey Spinal Generator for Locomotion: A Mathematical Model”. In: *Journal of Mathematical Biology* 13.3, pp. 345–369. DOI: [10.1007/bf00276069](https://doi.org/10.1007/bf00276069).
- Collinger, Jennifer L. et al. (Feb. 2013). “High-Performance Neuroprosthetic Control by an Individual with Tetraplegia”. In: *Lancet (London, England)* 381.9866, pp. 557–564. ISSN: 1474-547X. DOI: [10.1016/S0140-6736\(12\)61816-9](https://doi.org/10.1016/S0140-6736(12)61816-9).

- Collins, J. et al. (2021). “A Review of Physics Simulators for Robotic Applications”. In: *IEEE Access* 9, pp. 51416–51431. ISSN: 2169-3536. DOI: [10.1109/ACCESS.2021.3068769](https://doi.org/10.1109/ACCESS.2021.3068769).
- Community, Blender Online (2021). *Blender - a 3D Modelling and Rendering Package*. Manual. Blender Foundation. Stichting Blender Foundation, Amsterdam.
- Coumans, Erwin (2015). “Bullet Physics Simulation”. In: *ACM SIGGRAPH 2015 Courses*.
- Courtine, Grégoire et al. (Oct. 2009). “Transformation of Nonfunctional Spinal Circuits into Functional States after the Loss of Brain Input”. In: *Nature Neuroscience* 12.10, pp. 1333–1342. ISSN: 1546-1726. DOI: [10.1038/nn.2401](https://doi.org/10.1038/nn.2401).
- Cox, S. M. et al. (Jan. 2019). “The Interaction of Compliance and Activation on the Force-Length Operating Range and Force Generating Capacity of Skeletal Muscle: A Computational Study Using a Guinea Fowl Musculoskeletal Model”. In: *Integrative Organismal Biology* 1.1, pp. 1–20. DOI: [10.1093/iob/obz022](https://doi.org/10.1093/iob/obz022).
- Cregg, Jared M. et al. (June 2020). “Brainstem Neurons That Command Mammalian Locomotor Asymmetries”. In: *Nature Neuroscience* 23.6, pp. 730–740. ISSN: 1546-1726. DOI: [10.1038/s41593-020-0633-7](https://doi.org/10.1038/s41593-020-0633-7).
- Cruse, Holk, Volker Dürr, and Josef Schmitz (2007). “Insect Walking Is Based on a Decentralized Architecture Revealing a Simple and Robust Controller”. In: *Philosophical Transactions of the Royal Society A: Mathematical, Physical and Engineering Sciences* 365.1850, pp. 221–250.
- Dallmann, Chris J. et al. (Mar. 2021). “A Leg to Stand on: Computational Models of Proprioception”. In: *Current Opinion in Physiology* 22, p. 100426. ISSN: 2468-8673. DOI: [10.1016/j.cophys.2021.03.001](https://doi.org/10.1016/j.cophys.2021.03.001).
- Danner, Simon M et al. (Nov. 2017). “Computational Modeling of Spinal Circuits Controlling Limb Coordination and Gaits in Quadrupeds”. In: *eLife* 6. Ed. by Ronald L Calabrese, e31050. ISSN: 2050-084X. DOI: [10.7554/eLife.31050](https://doi.org/10.7554/eLife.31050).
- Danner, Simon M., Simon D. Wilshin, et al. (2016). “Central Control of Interlimb Coordination and Speed-Dependent Gait Expression in Quadrupeds”. In: *The Journal of Physiology* 594.23, pp. 6947–6967. ISSN: 1469-7793. DOI: [10.1113/JP272787](https://doi.org/10.1113/JP272787).
- Danner, Simon M., Han Zhang, et al. (2019). “Spinal V3 Interneurons and Left–Right Coordination in Mammalian Locomotion”. In: *Frontiers in Cellular Neuroscience* 0. ISSN: 1662-5102. DOI: [10.3389/fncel.2019.00516](https://doi.org/10.3389/fncel.2019.00516).
- Daun-Gruhn, Silvia (2011). “A Mathematical Modeling Study of Inter-Segmental Coordination during Stick Insect Walking”. In: *Journal of computational neuroscience* 30.2, pp. 255–278.
- De Groote, Friedl et al. (Oct. 2016). “Evaluation of Direct Collocation Optimal Control Problem Formulations for Solving the Muscle Redundancy Problem”. In: *Annals of Biomedical Engineering* 44.10, pp. 2922–2936. ISSN: 1573-9686. DOI: [10.1007/s10439-016-1591-9](https://doi.org/10.1007/s10439-016-1591-9).
- DeAngelis, Brian D, Jacob A Zavatore-Veth, and Damon A Clark (2019). “The Manifold Structure of Limb Coordination in Walking *Drosophila*”. In: *Elife* 8, e46409.
- Deb, Kalyanmoy et al. (2002). “A Fast and Elitist Multiobjective Genetic Algorithm: NSGA-II”. In: *IEEE transactions on evolutionary computation* 6.2, pp. 182–197.

- DeLaurier, April et al. (Sept. 2008). “The Mouse Limb Anatomy Atlas: An Interactive 3D Tool for Studying Embryonic Limb Patterning”. In: *BMC Developmental Biology* 8.1, p. 83. ISSN: 1471-213X. DOI: [10.1186/1471-213X-8-83](https://doi.org/10.1186/1471-213X-8-83).
- Delp, S.L. et al. (Aug. 1990). “An Interactive Graphics-Based Model of the Lower Extremity to Study Orthopaedic Surgical Procedures”. In: *IEEE Transactions on Biomedical Engineering* 37.8, pp. 757–767. ISSN: 1558-2531. DOI: [10.1109/10.102791](https://doi.org/10.1109/10.102791).
- Delp, Scott L. et al. (Nov. 2007). “OpenSim: Open-Source Software to Create and Analyze Dynamic Simulations of Movement”. In: *IEEE transactions on bio-medical engineering* 54.11, pp. 1940–1950. ISSN: 0018-9294. DOI: [10.1109/TBME.2007.901024](https://doi.org/10.1109/TBME.2007.901024).
- Dewan, Ashvin K et al. (Aug. 2010). “Assessing Mechanical Integrity of Spinal Fusion by in Situ Endochondral Osteoinduction in the Murine Model”. In: *Journal of Orthopaedic Surgery and Research* 5, p. 58. ISSN: 1749-799X. DOI: [10.1186/1749-799X-5-58](https://doi.org/10.1186/1749-799X-5-58).
- Dickinson, M. H. (Apr. 2000). “How Animals Move: An Integrative View”. In: *Science* 288.5463, pp. 100–106. ISSN: 00368075, 10959203. DOI: [10.1126/science.288.5463.100](https://doi.org/10.1126/science.288.5463.100).
- Dickson, William B., Andrew D. Straw, and Michael H. Dickinson (2008). “Integrative Model of Drosophila Flight”. In: *AIAA Journal* 46.9, pp. 2150–2164. DOI: [10.2514/1.29862](https://doi.org/10.2514/1.29862).
- Dzeladini, Florin, Jesse van den Kieboom, and Auke Ijspeert (2014). “The Contribution of a Central Pattern Generator in a Reflex-Based Neuromuscular Model”. In: *Frontiers in Human Neuroscience* 8, p. 371. ISSN: 1662-5161. DOI: [10.3389/fnhum.2014.00371](https://doi.org/10.3389/fnhum.2014.00371).
- Edgerton, V. Reggie et al. (Jan. 2008). “Training Locomotor Networks”. In: *Brain Research Reviews* 57.1, pp. 241–254. ISSN: 0165-0173. DOI: [10.1016/j.brainresrev.2007.09.002](https://doi.org/10.1016/j.brainresrev.2007.09.002).
- Edin, B. B. and A. B. Vallbo (June 1990). “Muscle Afferent Responses to Isometric Contractions and Relaxations in Humans”. In: *Journal of Neurophysiology* 63.6, pp. 1307–1313. ISSN: 0022-3077. DOI: [10.1152/jn.1990.63.6.1307](https://doi.org/10.1152/jn.1990.63.6.1307).
- Edwards, Donald H. (July 2010). “Neuromechanical Simulation”. In: *Frontiers in Behavioral Neuroscience* 4. ISSN: 1662-5153. DOI: [10.3389/fnbeh.2010.00040](https://doi.org/10.3389/fnbeh.2010.00040).
- Einevoll, Gaute T et al. (2019). “The Scientific Case for Brain Simulations”. In: *Neuron* 102.4, pp. 735–744.
- Ekeberg, Örjan (Oct. 1993a). “A Combined Neuronal and Mechanical Model of Fish Swimming”. In: *Biological Cybernetics* 69.5, pp. 363–374. ISSN: 1432-0770. DOI: [10.1007/BF00199436](https://doi.org/10.1007/BF00199436).
- (1993b). “A Combined Neuronal and Mechanical Model of Fish Swimming”. In: *Biological cybernetics* 69.5-6, pp. 363–374.
- Ekeberg, Örjan, Marcus Blümel, and Ansgar Büschges (2004). “Dynamic Simulation of Insect Walking”. In: *Arthropod structure & development* 33.3, pp. 287–300.
- Ekeberg, Örjan and Keir Pearson (Dec. 2005). “Computer Simulation of Stepping in the Hind Legs of the Cat: An Examination of Mechanisms Regulating the Stance-to-Swing Transition”. In: *Journal of Neurophysiology* 94.6, pp. 4256–4268. ISSN: 0022-3077. DOI: [10.1152/jn.00065.2005](https://doi.org/10.1152/jn.00065.2005).
- Elliott, Christopher JH and John C Sparrow (2012). “In Vivo Measurement of Muscle Output in Intact Drosophila”. In: *Methods (San Diego, Calif.)* 56.1, pp. 78–86.



- Erwin Coumans and Yunfei Bai (2016). *PyBullet, a Python Module for Physics Simulation for Games, Robotics and Machine Learning*.
- Ethier, C. et al. (May 2012). “Restoration of Grasp Following Paralysis through Brain-Controlled Stimulation of Muscles”. In: *Nature* 485.7398, pp. 368–371. ISSN: 1476-4687. DOI: [10.1038/nature10987](https://doi.org/10.1038/nature10987).
- Falisse, Antoine et al. (Aug. 2019). “Rapid Predictive Simulations with Complex Musculoskeletal Models Suggest That Diverse Healthy and Pathological Human Gaits Can Emerge from Similar Control Strategies”. In: *Journal of The Royal Society Interface* 16.157, p. 20190402. DOI: [10.1098/rsif.2019.0402](https://doi.org/10.1098/rsif.2019.0402).
- Falotico, Egidio et al. (2017). “Connecting Artificial Brains to Robots in a Comprehensive Simulation Framework: The Neurorobotics Platform”. In: *Frontiers in Neurobotics* 11, p. 2. ISSN: 1662-5218. DOI: [10.3389/fnbot.2017.00002](https://doi.org/10.3389/fnbot.2017.00002).
- Featherstone, R. (Mar. 1983). “The Calculation of Robot Dynamics Using Articulated-Body Inertias”. In: *The International Journal of Robotics Research* 2.1, pp. 13–30. ISSN: 0278-3649, 1741-3176. DOI: [10.1177/027836498300200102](https://doi.org/10.1177/027836498300200102).
- Ferreira-Pinto, Manuel J. et al. (Oct. 2018). “Connecting Circuits for Supraspinal Control of Locomotion”. In: *Neuron* 100.2, pp. 361–374. ISSN: 08966273. DOI: [10.1016/j.neuron.2018.09.015](https://doi.org/10.1016/j.neuron.2018.09.015).
- Ferris, G.F. (1950). “External Morphology of the Adult”. In: *Biology of Drosophila*, pp. 368–419.
- Flynn, Peter C and W Reuben Kaufman (2015). “Mechanical Properties of the Cuticle of the Tick Amblyomma Hebraeum (Acari: Ixodidae)”. In: *Journal of Experimental Biology* 218.17, pp. 2806–2814.
- Formento, Emanuele et al. (Dec. 2018). “Electrical Spinal Cord Stimulation Must Preserve Proprioception to Enable Locomotion in Humans with Spinal Cord Injury”. In: *Nature Neuroscience* 21.12, pp. 1728–1741. ISSN: 1546-1726. DOI: [10.1038/s41593-018-0262-6](https://doi.org/10.1038/s41593-018-0262-6).
- Foundation, Blender (2012). *Blender-a 3D Modelling and Rendering Package*.
- Frantsevich, Leonid and Weiyang Wang (2009). “Gimbals in the Insect Leg”. In: *Arthropod structure & development* 38.1, pp. 16–30.
- Fry, Steven N, Rosalyn Sayaman, and Michael H Dickinson (2003). “The Aerodynamics of Free-Flight Maneuvers in *Drosophila*”. In: *Science (New York, N.Y.)* 300.5618, pp. 495–498.
- Fuchs, Einat et al. (2011). “Intersegmental Coordination of Cockroach Locomotion: Adaptive Control of Centrally Coupled Pattern Generator Circuits”. In: *Frontiers in neural circuits* 4, p. 125.
- Full, R.J. and D.E. Koditschek (Dec. 1999). “Templates and Anchors: Neuromechanical Hypotheses of Legged Locomotion on Land”. In: *Journal of Experimental Biology* 202.23, pp. 3325–3332. ISSN: 0022-0949. DOI: [10.1242/jeb.202.23.3325](https://doi.org/10.1242/jeb.202.23.3325).
- Geijtenbeek, T (2013). *Animating Virtual Characters Using Physics-Based Simulation*. Utrecht University. ISBN: 978-94-6182-389-2.

- Geijtenbeek, Thomas (June 2019). “SCONE: Open Source Software for Predictive Simulation of Biological Motion”. In: *Journal of Open Source Software* 4.38, p. 1421. ISSN: 2475-9066. DOI: [10.21105/joss.01421](https://doi.org/10.21105/joss.01421).
- Geurten, Bart R. H. et al. (2014). “Saccadic Body Turns in Walking *Drosophila*”. In: *Frontiers in Behavioral Neuroscience* 8, p. 365. ISSN: 1662-5153. DOI: [10.3389/fnbeh.2014.00365](https://doi.org/10.3389/fnbeh.2014.00365).
- Gewaltig, Marc-Oliver and Markus Diesmann (Apr. 2007). “NEST (NEural Simulation Tool)”. In: *Scholarpedia* 2.4, p. 1430. ISSN: 1941-6016. DOI: [10.4249/scholarpedia.1430](https://doi.org/10.4249/scholarpedia.1430).
- Geyer, Hartmut and Hugh Herr (June 2010). “A Muscle-Reflex Model That Encodes Principles of Legged Mechanics Produces Human Walking Dynamics and Muscle Activities”. In: *IEEE*. ISSN: 1534-4320.
- Geyer, Hartmut, Andre Seyfarth, and Reinhard Blickhan (2006). “Compliant Leg Behaviour Explains Basic Dynamics of Walking and Running”. In: August, pp. 2861–2867. DOI: [10.1098/rspb.2006.3637](https://doi.org/10.1098/rspb.2006.3637).
- Giovanni, Borelli (1685). “De Motu Animalium”. In: *Leiden, The Netherlands: Lugduni* 1.
- Gosgnach, Simon et al. (Nov. 2017). “Delineating the Diversity of Spinal Interneurons in Locomotor Circuits”. In: *Journal of Neuroscience* 37.45, pp. 10835–10841. ISSN: 0270-6474, 1529-2401. DOI: [10.1523/JNEUROSCI.1829-17.2017](https://doi.org/10.1523/JNEUROSCI.1829-17.2017).
- Gosztolai, Adam et al. (2021). “LiftPose3D, a Deep Learning-Based Approach for Transforming Two-Dimensional to Three-Dimensional Poses in Laboratory Animals”. In: *Nature methods* 18.8, pp. 975–981.
- Goulding, Martyn (July 2009). “Circuits Controlling Vertebrate Locomotion: Moving in a New Direction”. In: *Nature Reviews Neuroscience* 10.7, pp. 507–518. ISSN: 1471-0048. DOI: [10.1038/nrn2608](https://doi.org/10.1038/nrn2608).
- Graham, Kirsten M. and Stephen H. Scott (Mar. 2003). “Morphometry of Macaca Mulatta Forelimb. III. Moment Arm of Shoulder and Elbow Muscles”. In: *Journal of Morphology* 255.3, pp. 301–314. ISSN: 0362-2525. DOI: [10.1002/jmor.10064](https://doi.org/10.1002/jmor.10064).
- Gribble, P. L. and D. J. Ostry (Nov. 1999). “Compensation for Interaction Torques during Single- and Multijoint Limb Movement”. In: *Journal of Neurophysiology* 82.5, pp. 2310–2326. ISSN: 0022-3077. DOI: [10.1152/jn.1999.82.5.2310](https://doi.org/10.1152/jn.1999.82.5.2310).
- Grillner, Sten (1981). “Control of Locomotion in Biped, Tetrapods, and Fish”. In: *Handbook of Physiology* Supplement 1.2, pp. 1179–1236. DOI: [10.1002/cphy.cp010226](https://doi.org/10.1002/cphy.cp010226).
- (2011). “Control of Locomotion in Biped, Tetrapods, and Fish”. In: *Comprehensive Physiology*. American Cancer Society, pp. 1179–1236. ISBN: 978-0-470-65071-4. DOI: [10.1002/cphy.cp010226](https://doi.org/10.1002/cphy.cp010226).
- (Feb. 2018). “Evolution: Vertebrate Limb Control over 420 Million Years”. In: *Current Biology* 28.4, R162–R164. ISSN: 0960-9822. DOI: [10.1016/j.cub.2017.12.040](https://doi.org/10.1016/j.cub.2017.12.040).
- Grillner, Sten and Abdeljabbar El Manira (Sept. 2019). “Current Principles of Motor Control, with Special Reference to Vertebrate Locomotion”. In: *Physiological Reviews* 100.1, pp. 271–320. ISSN: 0031-9333. DOI: [10.1152/physrev.00015.2019](https://doi.org/10.1152/physrev.00015.2019).
- Günel, Semih et al. (2019). “DeepFly3D, a Deep Learning-Based Approach for 3D Limb and Appendage Tracking in Tethered, Adult *Drosophila*”. In: *eLife* 8.

- Guo, Shihui et al. (2018). “A Neuro-Musculo-Skeletal Model for Insects with Data-Driven Optimization”. In: *Scientific reports* 8.1, pp. 1–11.
- Gurfinkel, V. S. and M. L. Shik (1974). “The Control of Posture and Locomotion”. In: *Motor Control*. Ed. by Alexander A. Gydikov, Nikolas T. Tankov, and Dimiter S. Kosarov. Boston, MA: Springer US, pp. 217–234. ISBN: 978-1-4613-4502-2. DOI: [10.1007/978-1-4613-4502-2\\_44](https://doi.org/10.1007/978-1-4613-4502-2_44).
- Harding, John D. (Dec. 2017). “Nonhuman Primates and Translational Research: Progress, Opportunities, and Challenges”. In: *ILAR journal* 58.2, pp. 141–150. ISSN: 1930-6180. DOI: [10.1093/ilar/ilx033](https://doi.org/10.1093/ilar/ilx033).
- Herman, Jon and Will Usher (Jan. 2017). “SALib: An Open-Source Python Library for Sensitivity Analysis”. In: *The Journal of Open Source Software* 2.9, p. 97. ISSN: 2475-9066. DOI: [10.21105/joss.00097](https://doi.org/10.21105/joss.00097).
- Hermans, Laura et al. (2021). “Long-Term Imaging of the Ventral Nerve Cord in Behaving Adult *Drosophila*”. In: *bioRxiv : the preprint server for biology*.
- Hines, M. L. and N. T. Carnevale (Aug. 1997). “The NEURON Simulation Environment”. In: *Neural Computation* 9.6, pp. 1179–1209. ISSN: 0899-7667. DOI: [10.1162/neco.1997.9.6.1179](https://doi.org/10.1162/neco.1997.9.6.1179).
- Holinski, B. J. et al. (Oct. 2016). “Intraspinal Microstimulation Produces Over-Ground Walking in Anesthetized Cats”. In: *Journal of Neural Engineering* 13.5, p. 056016. ISSN: 1741-2552. DOI: [10.1088/1741-2560/13/5/056016](https://doi.org/10.1088/1741-2560/13/5/056016).
- Hooper, Scott L. (May 2012). “Body Size and the Neural Control of Movement”. In: *Current Biology* 22.9, R318–R322. ISSN: 09609822. DOI: [10.1016/j.cub.2012.02.048](https://doi.org/10.1016/j.cub.2012.02.048).
- Hooper, Scott L. et al. (Apr. 2009). “Neural Control of Unloaded Leg Posture and of Leg Swing in Stick Insect, Cockroach, and Mouse Differs from That in Larger Animals”. In: *Journal of Neuroscience* 29.13, pp. 4109–4119. ISSN: 0270-6474, 1529-2401. DOI: [10.1523/JNEUROSCI.5510-08.2009](https://doi.org/10.1523/JNEUROSCI.5510-08.2009).
- Hutchinson, John R. (2004). “Biomechanical Modeling and Sensitivity Analysis of Bipedal Running Ability. I. Extant Taxa”. In: *Journal of Morphology* 262.1, pp. 421–440. ISSN: 1097-4687. DOI: [10.1002/jmor.10241](https://doi.org/10.1002/jmor.10241).
- Hutchinson, John R., Jeffery W. Rankin, et al. (June 2015). “Musculoskeletal Modelling of an Ostrich (*Struthio Camelus*) Pelvic Limb: Influence of Limb Orientation on Muscular Capacity during Locomotion”. In: *PeerJ* 3, e1001. ISSN: 2167-8359. DOI: [10.7717/peerj.1001](https://doi.org/10.7717/peerj.1001).
- Hutchinson, John R., Victor Ng-Thow-Hing, and Frank C. Anderson (June 2007). “A 3D Interactive Method for Estimating Body Segmental Parameters in Animals: Application to the Turning and Running Performance of *Tyrannosaurus Rex*”. In: *Journal of Theoretical Biology* 246.4, pp. 660–680. ISSN: 0022-5193. DOI: [10.1016/j.jtbi.2007.01.023](https://doi.org/10.1016/j.jtbi.2007.01.023).
- Ijspeert, Auke Jan (2001). “A Connectionist Central Pattern Generator for the Aquatic and Terrestrial Gaits of a Simulated Salamander”. In: *Biological cybernetics* 84.5, pp. 331–348.



- Ijspeert, Auke Jan et al. (2007). “From Swimming to Walking with a Salamander Robot Driven by a Spinal Cord Model”. In: *Science (New York, N.Y.)* 315.5817, pp. 1416–1420. ISSN: 0036-8075. DOI: [10.1126/science.1138353](https://doi.org/10.1126/science.1138353).
- Iles, J F (Oct. 1976). “Central Terminations of Muscle Afferents on Motoneurons in the Cat Spinal Cord.” In: *The Journal of Physiology* 262.1, pp. 91–117. ISSN: 0022-3751.
- Isakov, Alexander et al. (2016). “Recovery of Locomotion after Injury in *Drosophila Melanogaster* Depends on Proprioception”. In: *Journal of Experimental Biology* 219.11, pp. 1760–1771.
- Ivashko, D.G. et al. (June 2003). “Modeling the Spinal Cord Neural Circuitry Controlling Cat Hindlimb Movement during Locomotion”. In: *Neurocomputing* 52–54, pp. 621–629. ISSN: 09252312. DOI: [10.1016/S0925-2312\(02\)00832-9](https://doi.org/10.1016/S0925-2312(02)00832-9).
- Izquierdo, Eduardo J and Randall D Beer (2018). “From Head to Tail: A Neuromechanical Model of Forward Locomotion in *Caenorhabditis Elegans*”. In: *Philosophical Transactions of the Royal Society B: Biological Sciences* 373.1758.
- Jenett, Arnim et al. (2012). “A GAL4-driver Line Resource for *Drosophila* Neurobiology”. In: *Cell reports* 2.4, pp. 991–1001.
- Jennings, Barbara H. (May 2011). “*Drosophila* – a Versatile Model in Biology & Medicine”. In: *Materials Today* 14.5, pp. 190–195. ISSN: 1369-7021. DOI: [10.1016/S1369-7021\(11\)70113-4](https://doi.org/10.1016/S1369-7021(11)70113-4).
- Jenny, A. B. and J. Inukai (Mar. 1983). “Principles of Motor Organization of the Monkey Cervical Spinal Cord”. In: *The Journal of Neuroscience: The Official Journal of the Society for Neuroscience* 3.3, pp. 567–575. ISSN: 0270-6474.
- Jessell, Thomas M. (Oct. 2000). “Neuronal Specification in the Spinal Cord: Inductive Signals and Transcriptional Codes”. In: *Nature Reviews Genetics* 1.1, pp. 20–29. ISSN: 1471-0064. DOI: [10.1038/35049541](https://doi.org/10.1038/35049541).
- Johnson, Will L. et al. (Jan. 2008). “A Three-Dimensional Model of the Rat Hindlimb: Musculoskeletal Geometry and Muscle Moment Arms”. In: *Journal of Biomechanics* 41.3, pp. 610–619. ISSN: 0021-9290. DOI: [10.1016/j.jbiomech.2007.10.004](https://doi.org/10.1016/j.jbiomech.2007.10.004).
- Kasten, M. R. et al. (Aug. 2013). “Therapeutic Intraspinal Microstimulation Improves Forelimb Function after Cervical Contusion Injury”. In: *Journal of Neural Engineering* 10.4, p. 044001. ISSN: 1741-2552. DOI: [10.1088/1741-2560/10/4/044001](https://doi.org/10.1088/1741-2560/10/4/044001).
- Kibleur, Pierre (2020). “Biomechanical Model of the Primates’ Upper Limb: Design of Stimulation Protocols for the Recovery of Reaching Movements in Tetraplegia”. MA thesis. Switzerland: EPFL.
- Kibleur, Pierre et al. (July 2020). “Spatiotemporal Maps of Proprioceptive Inputs to the Cervical Spinal Cord During Three-Dimensional Reaching and Grasping”. In: *IEEE Transactions on Neural Systems and Rehabilitation Engineering* 28.7, pp. 1668–1677. ISSN: 1558-0210. DOI: [10.1109/TNSRE.2020.2986491](https://doi.org/10.1109/TNSRE.2020.2986491).
- Kiehn, Ole (Feb. 2011). “Development and Functional Organization of Spinal Locomotor Circuits”. In: *Current Opinion in Neurobiology*. Developmental Neuroscience 21.1, pp. 100–109. ISSN: 0959-4388. DOI: [10.1016/j.conb.2010.09.004](https://doi.org/10.1016/j.conb.2010.09.004).

- (Apr. 2016). “Decoding the Organization of Spinal Circuits That Control Locomotion”. In: *Nature reviews. Neuroscience* 17.4, pp. 224–238. ISSN: 1471-003X. DOI: [10.1038/nrn.2016.9](https://doi.org/10.1038/nrn.2016.9).
- Kimura, Ken-ichi et al. (2020). “Framework with Cytoskeletal Actin Filaments Forming Insect Footpad Hairs Inspires Biomimetic Adhesive Device Design”. In: *Communications biology* 3.1, pp. 1–7.
- Kuan, Aaron T et al. (2020). “Dense Neuronal Reconstruction through X-ray Holographic Nano-Tomography”. In: *Nature neuroscience*.
- Kubo, Tai and Michael J. Benton (2009). “Tetrapod Postural Shift Estimated from Permian and Triassic Trackways”. In: *Palaeontology* 52.5, pp. 1029–1037. ISSN: 1475-4983. DOI: [10.1111/j.1475-4983.2009.00897.x](https://doi.org/10.1111/j.1475-4983.2009.00897.x).
- Kuo, Arthur D. (Apr. 2002). “The Relative Roles of Feedforward and Feedback in the Control of Rhythmic Movements”. In: *Motor Control* 6.2, pp. 129–145. ISSN: 1087-1640. DOI: [10.1123/mcj.6.2.129](https://doi.org/10.1123/mcj.6.2.129).
- Lansner, Anders, Jeanette Hellgren Kotaleski, and Sten Grillner (1998). “Modeling of the Spinal Neuronal Circuitry Underlying Locomotion in a Lower Vertebrate”. In: *Annals of the New York Academy of Sciences* 860.1, pp. 239–249.
- Lee, Jeongseok et al. (Feb. 2018). “DART: Dynamic Animation and Robotics Toolkit”. In: *Journal of Open Source Software* 3.22, p. 500. ISSN: 2475-9066. DOI: [10.21105/joss.00500](https://doi.org/10.21105/joss.00500).
- Lee, Seunghwan et al. (July 2019). “Scalable Muscle-Actuated Human Simulation and Control”. In: *ACM Transactions on Graphics* 38.4, pp. 1–13. ISSN: 0730-0301, 1557-7368. DOI: [10.1145/3306346.3322972](https://doi.org/10.1145/3306346.3322972).
- Lewiner, Thomas et al. (2003). “Efficient Implementation of Marching Cubes’ Cases with Topological Guarantees”. In: *Journal of Graphics Tools* 8.2, pp. 1–15.
- Li, Siyuan et al. (2020). “Deformation-Aware Unpaired Image Translation for Pose Estimation on Laboratory Animals”. In: *arXiv*.
- Lloyd, David G. and Thor F. Besier (June 2003). “An EMG-driven Musculoskeletal Model to Estimate Muscle Forces and Knee Joint Moments in Vivo”. In: *Journal of Biomechanics* 36.6, pp. 765–776. ISSN: 0021-9290. DOI: [10.1016/s0021-9290\(03\)00010-1](https://doi.org/10.1016/s0021-9290(03)00010-1).
- Loper, Matthew et al. (2015). “SMPL: A Skinned Multi-Person Linear Model”. In: *ACM transactions on graphics* 34.6, pp. 1–16.
- Loveless, Jane, Konstantinos Lagogiannis, and Barbara Webb (2019). “Modelling the Mechanics of Exploration in Larval *Drosophila*”. In: *PloS computational biology* 15.7.
- Lu, Daniel C. et al. (Nov. 2016). “Engaging Cervical Spinal Cord Networks to Reenable Volitional Control of Hand Function in Tetraplegic Patients”. In: *Neurorehabilitation and Neural Repair* 30.10, pp. 951–962. ISSN: 1552-6844. DOI: [10.1177/1545968316644344](https://doi.org/10.1177/1545968316644344).
- Lundberg, A., K. Malmgren, and E. D. Schomburg (1987). “Reflex Pathways from Group II Muscle Afferents. 3. Secondary Spindle Afferents and the FRA: A New Hypothesis”. In: *Experimental Brain Research* 65.2, pp. 294–306. ISSN: 0014-4819. DOI: [10.1007/BF00236301](https://doi.org/10.1007/BF00236301).

- Macaulay, Sophie, John R. Hutchinson, and Karl T. Bates (2017). “A Quantitative Evaluation of Physical and Digital Approaches to Centre of Mass Estimation”. In: *Journal of Anatomy* 231.5, pp. 758–775. ISSN: 1469-7580. DOI: [10.1111/joa.12667](https://doi.org/10.1111/joa.12667).
- Maimon, Gaby, Andrew D Straw, and Michael H Dickinson (2010). “Active Flight Increases the Gain of Visual Motion Processing in *Drosophila*”. In: *Nature neuroscience* 13.3, p. 393.
- Mamiya, Akira, Pralaksha Gurung, and John C Tuthill (2018). “Neural Coding of Leg Proprioception in *Drosophila*”. In: *Neuron* 100.3, pp. 636–650.
- Manal, Kurt and Thomas S Buchanan (2004). “Subject-Specific Estimates of Tendon Slack Length: A Numerical Method”. In: *Journal of Applied Biomechanics* 20.2, pp. 195–203. DOI: [10.1123/jab.20.2.195](https://doi.org/10.1123/jab.20.2.195).
- Mantziaris, Charalampos, Till Bockemühl, and Ansgar Büschges (2020). “Central Pattern Generating Networks in Insect Locomotion”. In: *Developmental neurobiology* 80.1-2, pp. 16–30.
- Mantziaris, Charalampos, Till Bockemühl, Philip Holmes, et al. (2017). “Intra- and Intersegmental Influences among Central Pattern Generating Networks in the Walking System of the Stick Insect”. In: *Journal of neurophysiology* 118.4, pp. 2296–2310.
- Markin, Sergey N. et al. (2016). “A Neuromechanical Model of Spinal Control of Locomotion”. In: *Neuromechanical Modeling of Posture and Locomotion*. Ed. by Boris I. Prilutsky and Donald H. Edwards. Springer Series in Computational Neuroscience. New York, NY: Springer, pp. 21–65. ISBN: 978-1-4939-3267-2. DOI: [10.1007/978-1-4939-3267-2\\_2](https://doi.org/10.1007/978-1-4939-3267-2_2).
- Mathewson, Margie A et al. (Nov. 2012). “Anatomical, Architectural, and Biochemical Diversity of the Murine Forelimb Muscles”. In: *Journal of Anatomy* 221.5, pp. 443–451. ISSN: 0021-8782. DOI: [10.1111/j.1469-7580.2012.01559.x](https://doi.org/10.1111/j.1469-7580.2012.01559.x).
- Mathis, Alexander, Pranav Mamidanna, Kevin M Cury, et al. (2018a). “DeepLabCut: Markerless Pose Estimation of User-Defined Body Parts with Deep Learning”. In: *Nature neuroscience* 21.9, pp. 1281–1289.
- (Sept. 2018b). “DeepLabCut: Markerless Pose Estimation of User-Defined Body Parts with Deep Learning”. In: *Nature Neuroscience* 21.9, pp. 1281–1289. ISSN: 1546-1726. DOI: [10.1038/s41593-018-0209-y](https://doi.org/10.1038/s41593-018-0209-y).
- McCrea, David A. and Ilya A. Rybak (Jan. 2008). “Organization of Mammalian Locomotor Rhythm and Pattern Generation”. In: *Brain Research Reviews*. Networks in Motion 57.1, pp. 134–146. ISSN: 0165-0173. DOI: [10.1016/j.brainresrev.2007.08.006](https://doi.org/10.1016/j.brainresrev.2007.08.006).
- McMahon T., Cheng G. (1990). “The Mechanism of Running: How Does Stiffness Couple with Speed?” In: *J. Biomech* 23, pp. 65–78. DOI: [10.1016/0021-9290\(90\)90042-2](https://doi.org/10.1016/0021-9290(90)90042-2).
- Mendes, César S et al. (2013). “Quantification of Gait Parameters in Freely Walking Wild Type and Sensory Deprived *Drosophila Melanogaster*”. In: *eLife* 2.
- Merel, Josh, Diego Aldarondo, et al. (2019). “Deep Neuroethology of a Virtual Rodent”. In: *arXiv*.
- Merel, Josh, Matthew Botvinick, and Greg Wayne (Dec. 2019). “Hierarchical Motor Control in Mammals and Machines”. In: *Nature Communications* 10.1, p. 5489. ISSN: 2041-1723. DOI: [10.1038/s41467-019-13239-6](https://doi.org/10.1038/s41467-019-13239-6).

- Michel, O. (2004). "Webots TM : Professional Mobile Robot Simulation". In: *International Journal of Advanced Robotic Systems* 1.1, pp. 39–42. ISSN: 1729-8806. DOI: [10.1.1.86.1278](https://doi.org/10.1.1.86.1278).
- Millard, Matthew et al. (Feb. 2013). "Flexing Computational Muscle: Modeling and Simulation of Musculotendon Dynamics". In: *Journal of Biomechanical Engineering* 135.2, pp. 0210051–02100511. ISSN: 0148-0731. DOI: [10.1115/1.4023390](https://doi.org/10.1115/1.4023390).
- Mochon S., McMahon T. (1980). "Ballistic Walking." In: *J. Biomech* 13, pp. 49–57. DOI: [10.1016/0021-9290\(80\)90007-X](https://doi.org/10.1016/0021-9290(80)90007-X).
- Modenese, Luca et al. (Jan. 2016). "Estimation of Musculotendon Parameters for Scaled and Subject Specific Musculoskeletal Models Using an Optimization Technique". In: *Journal of Biomechanics* 49.2, pp. 141–148. ISSN: 0021-9290. DOI: [10.1016/j.jbiomech.2015.11.006](https://doi.org/10.1016/j.jbiomech.2015.11.006).
- Moore, Richard J.D. et al. (2014). "FicTrac: A Visual Method for Tracking Spherical Motion and Generating Fictive Animal Paths". In: *Journal of Neuroscience Methods* 225, pp. 106–119.
- Moraud, Eduardo Martin et al. (Feb. 2016). "Mechanisms Underlying the Neuromodulation of Spinal Circuits for Correcting Gait and Balance Deficits after Spinal Cord Injury". In: *Neuron* 89.4, pp. 814–828. ISSN: 0896-6273. DOI: [10.1016/j.neuron.2016.01.009](https://doi.org/10.1016/j.neuron.2016.01.009).
- Mu, Jiteng et al. (2020). "Learning from Synthetic Animals". In: *Proceedings of the IEEE/CVF Conference on Computer Vision and Pattern Recognition*, pp. 12386–12395.
- NVIDIA (2022). *NVIDIA PhysX SDK 4.1*. NVIDIA GameWorks.
- O'Neill, Matthew C. et al. (Oct. 2013). "A Three-Dimensional Musculoskeletal Model of the Chimpanzee (Pan Troglodytes) Pelvis and Hind Limb". In: *Journal of Experimental Biology* 216.19, pp. 3709–3723. ISSN: 0022-0949, 1477-9145. DOI: [10.1242/jeb.079665](https://doi.org/10.1242/jeb.079665).
- Oliveira, M. et al. (2011). "Multi-Objective Parameter CPG Optimization for Gait Generation of a Quadruped Robot Considering Behavioral Diversity". In: *2011 IEEE/RSJ International Conference on Intelligent Robots and Systems*, pp. 2286–2291. DOI: [10.1109/IROS.2011.6094819](https://doi.org/10.1109/IROS.2011.6094819).
- OSRF (n.d.). *SDFFormat Home*. <http://sdformat.org/>.
- Pandarínath, Chethan et al. (Feb. 2017). "High Performance Communication by People with Paralysis Using an Intracortical Brain-Computer Interface". In: *eLife* 6. Ed. by Sabine Kastner, e18554. ISSN: 2050-084X. DOI: [10.7554/eLife.18554](https://doi.org/10.7554/eLife.18554).
- Paul, Chandana et al. (Sept. 2005). "Development of a Human Neuro-Musculo-Skeletal Model for Investigation of Spinal Cord Injury". In: *Biological Cybernetics* 93.3, pp. 153–170. ISSN: 0340-1200, 1432-0770. DOI: [10.1007/s00422-005-0559-x](https://doi.org/10.1007/s00422-005-0559-x).
- Pavlou, Hania J and Stephen F Goodwin (2013). "Courtship Behavior in Drosophila Melanogaster: Towards a 'Courtship Connectome'". In: *Current Opinion in Neurobiology* 23.1, pp. 76–83.
- Pearson, K. G. and J. Duysens (1976). "Function of Segmental Reflexes in the Control of Stepping in Cockroaches and Cats". In: *Neural Control of Locomotion*. Ed. by Richard M. Herman et al. Boston, MA: Springer US, pp. 519–537. ISBN: 978-1-4757-0964-3. DOI: [10.1007/978-1-4757-0964-3\\_11](https://doi.org/10.1007/978-1-4757-0964-3_11).

- Pearson, Keir, Örjan Ekeberg, and Ansgar Büschges (Nov. 2006a). “Assessing Sensory Function in Locomotor Systems Using Neuro-Mechanical Simulations”. In: *Trends in Neurosciences* 29.11, pp. 625–631. ISSN: 0166-2236. DOI: [10.1016/j.tins.2006.08.007](https://doi.org/10.1016/j.tins.2006.08.007).
- (2006b). “Assessing Sensory Function in Locomotor Systems Using Neuro-Mechanical Simulations”. In: *Trends in neurosciences* 29.11, pp. 625–631.
- Pereira, Talmo D et al. (2019). “Fast Animal Pose Estimation Using Deep Neural Networks”. In: *Nature methods* 16.1, pp. 117–125.
- Phelps, Jasper S et al. (2021). “Reconstruction of Motor Control Circuits in Adult *Drosophila* Using Automated Transmission Electron Microscopy”. In: *Cell* 184.3, pp. 759–774.
- Pick, Simon and Roland Strauss (2005). “Goal-Driven Behavioral Adaptations in Gap-Climbing *Drosophila*”. In: *Current Biology* 15.16, pp. 1473–1478.
- Popovic, Milos R., Dejan B. Popovic, and Thierry Keller (July 2002). “Neuroprostheses for Grasping”. In: *Neurological Research* 24.5, pp. 443–452. ISSN: 0161-6412. DOI: [10.1179/016164102101200311](https://doi.org/10.1179/016164102101200311).
- Prilutsky, Boris I and Donald H Edwards (2015). *Neuromechanical Modeling of Posture and Locomotion*.
- Prochazka, A. (1999). “Quantifying Proprioception”. In: *Progress in Brain Research* 123, pp. 133–142. ISSN: 0079-6123.
- Prochazka, A. and M. Gorassini (Feb. 1998). “Models of Ensemble Firing of Muscle Spindle Afferents Recorded during Normal Locomotion in Cats”. In: *The Journal of Physiology* 507 ( Pt 1), pp. 277–291. ISSN: 0022-3751. DOI: [10.1111/j.1469-7793.1998.277bu.x](https://doi.org/10.1111/j.1469-7793.1998.277bu.x).
- Prochazka, Arthur and Monica Gorassini (Feb. 1998). “Ensemble Firing of Muscle Afferents Recorded during Normal Locomotion in Cats”. In: *The Journal of Physiology* 507.Pt 1, pp. 293–304. ISSN: 0022-3751. DOI: [10.1111/j.1469-7793.1998.293bu.x](https://doi.org/10.1111/j.1469-7793.1998.293bu.x).
- Proctor, J, RP Kukillaya, and P Holmes (2010). “A Phase-Reduced Neuro-Mechanical Model for Insect Locomotion: Feed-Forward Stability and Proprioceptive Feedback”. In: *Philosophical Transactions of the Royal Society A: Mathematical, Physical and Engineering Sciences* 368.1930, pp. 5087–5104.
- Qian, George and Adam Mahdi (May 2020). “Sensitivity Analysis Methods in the Biomedical Sciences”. In: *Mathematical Biosciences* 323, p. 108306. ISSN: 00255564. DOI: [10.1016/j.mbs.2020.108306](https://doi.org/10.1016/j.mbs.2020.108306).
- R., Blickhan (1989). “The Spring–Mass Model for Running and Hopping.” In: *Journal of Biomechanics* 22, pp. 1217–1227. DOI: [10.1016/0021-9290\(89\)90224-8](https://doi.org/10.1016/0021-9290(89)90224-8).
- Rajagopal, Apoorva et al. (Oct. 2016). “Full-Body Musculoskeletal Model for Muscle-Driven Simulation of Human Gait”. In: *IEEE Transactions on Biomedical Engineering* 63.10, pp. 2068–2079. ISSN: 1558-2531. DOI: [10.1109/TBME.2016.2586891](https://doi.org/10.1109/TBME.2016.2586891).
- Ramachandran, Prabhu et al. (Dec. 2021). “PySPH: A Python-based Framework for Smoothed Particle Hydrodynamics”. In: *ACM Transactions on Mathematical Software* 47.4, pp. 1–38. ISSN: 0098-3500, 1557-7295. DOI: [10.1145/3460773](https://doi.org/10.1145/3460773). arXiv: [1909.04504](https://arxiv.org/abs/1909.04504).



- Ramdy, Pavan et al. (Feb. 2017a). “Climbing Favours the Tripod Gait over Alternative Faster Insect Gaits”. In: *Nature Communications* 8.1, p. 14494. ISSN: 2041-1723. DOI: [10.1038/ncomms14494](https://doi.org/10.1038/ncomms14494).
- (2017b). “Climbing Favours the Tripod Gait over Alternative Faster Insect Gaits”. In: *Nature communications* 8.
- Raspopovic, Stanisa, Marco Capogrosso, and Silvestro Micera (Aug. 2011). “A Computational Model for the Stimulation of Rat Sciatic Nerve Using a Transverse Intrafascicular Multichannel Electrode”. In: *IEEE Transactions on Neural Systems and Rehabilitation Engineering* 19.4, pp. 333–344. ISSN: 1558-0210. DOI: [10.1109/TNSRE.2011.2151878](https://doi.org/10.1109/TNSRE.2011.2151878).
- Rattay, F., K. Minassian, and M. R. Dimitrijevic (Aug. 2000). “Epidural Electrical Stimulation of Posterior Structures of the Human Lumbosacral Cord: 2. Quantitative Analysis by Computer Modeling”. In: *Spinal Cord* 38.8, pp. 473–489. ISSN: 1362-4393. DOI: [10.1038/sj.sc.3101039](https://doi.org/10.1038/sj.sc.3101039).
- Redl, Christian, Margit Gfoehler, and Marcus G. Pandy (Apr. 2007). “Sensitivity of Muscle Force Estimates to Variations in Muscle–Tendon Properties”. In: *Human Movement Science* 26.2, pp. 306–319. ISSN: 01679457. DOI: [10.1016/j.humov.2007.01.008](https://doi.org/10.1016/j.humov.2007.01.008).
- Ríos, Victor Lobato et al. (Nov. 2021). *NeuroMechFly, a Neuromechanical Model of Adult Drosophila Melanogaster*. DOI: [10.1101/2021.04.17.440214](https://doi.org/10.1101/2021.04.17.440214).
- Romero, F. and F. J. Alonso (Jan. 2016). “A Comparison among Different Hill-type Contraction Dynamics Formulations for Muscle Force Estimation”. In: *Mechanical Sciences* 7.1, pp. 19–29. ISSN: 2191-9151. DOI: [10.5194/ms-7-19-2016](https://doi.org/10.5194/ms-7-19-2016).
- Ruder, Ludwig and Silvia Arber (July 2019). “Brainstem Circuits Controlling Action Diversification”. In: *Annual Review of Neuroscience* 42.1, pp. 485–504. ISSN: 0147-006X, 1545-4126. DOI: [10.1146/annurev-neuro-070918-050201](https://doi.org/10.1146/annurev-neuro-070918-050201).
- Ruder, Ludwig, Riccardo Schina, et al. (Feb. 2021). “A Functional Map for Diverse Forelimb Actions within Brainstem Circuitry”. In: *Nature* 590.7846, pp. 445–450. ISSN: 1476-4687. DOI: [10.1038/s41586-020-03080-z](https://doi.org/10.1038/s41586-020-03080-z).
- Rybak, Ilya A, Kimberly J Dougherty, and Natalia A Shevtsova (2015). “Organization of the Mammalian Locomotor CPG: Review of Computational Model and Circuit Architectures Based on Genetically Identified Spinal Interneurons”. In: *ENeuro* 2.5.
- Rybak, Ilya A. et al. (2006). “Modelling Spinal Circuitry Involved in Locomotor Pattern Generation: Insights from Deletions during Fictive Locomotion”. In: *The Journal of Physiology* 577.2, pp. 617–639. ISSN: 1469-7793. DOI: [10.1113/jphysiol.2006.118703](https://doi.org/10.1113/jphysiol.2006.118703).
- Sartori, Massimo et al. (Dec. 2018). “Robust Simultaneous Myoelectric Control of Multiple Degrees of Freedom in Wrist-Hand Prostheses by Real-Time Neuromusculoskeletal Modeling”. In: *Journal of Neural Engineering* 15.6, p. 066026. ISSN: 1741-2552. DOI: [10.1088/1741-2552/aae26b](https://doi.org/10.1088/1741-2552/aae26b).
- Scheffer, Louis K et al. (2020). “A Connectome and Analysis of the Adult Drosophila Central Brain”. In: *bioRxiv : the preprint server for biology*.
- Schiefer, M A et al. (Apr. 2010). “Selective Stimulation of the Human Femoral Nerve with a Flat Interface Nerve Electrode”. In: *Journal of neural engineering* 7.2, p. 26006. ISSN: 1741-2560. DOI: [10.1088/1741-2560/7/2/026006](https://doi.org/10.1088/1741-2560/7/2/026006).

- Schilling, Malte and Holk Cruse (2020). “Decentralized Control of Insect Walking: A Simple Neural Network Explains a Wide Range of Behavioral and Neurophysiological Results”. In: *PLoS computational biology* 16.4.
- Schilling, Malte, Thierry Hoinville, et al. (2013). “Walknet, a Bio-Inspired Controller for Hexapod Walking”. In: *Biological cybernetics* 107.4, pp. 397–419.
- Schindelin, Johannes et al. (2012). “Fiji: An Open-Source Platform for Biological-Image Analysis”. In: *Nature methods* 9.7, pp. 676–682.
- Schirmer, Clemens M. et al. (July 2011). “Heuristic Map of Myotomal Innervation in Humans Using Direct Intraoperative Nerve Root Stimulation”. In: *Journal of Neurosurgery. Spine* 15.1, pp. 64–70. ISSN: 1547-5646. DOI: [10.3171/2011.2.SPINE1068](https://doi.org/10.3171/2011.2.SPINE1068).
- Seeds, Andrew M et al. (2014). “A Suppression Hierarchy among Competing Motor Programs Drives Sequential Grooming in *Drosophila*”. In: *eLife* 3.
- Seelig, Johannes D et al. (2010). “Two-Photon Calcium Imaging from Head-Fixed *Drosophila* during Optomotor Walking Behavior”. In: *Nature methods* 7.7, p. 535.
- Sellers, W. I. et al. (Oct. 2012). “Minimum Convex Hull Mass Estimations of Complete Mounted Skeletons”. In: *Biology Letters* 8.5, pp. 842–845. DOI: [10.1098/rsbl.2012.0263](https://doi.org/10.1098/rsbl.2012.0263).
- Seth, Ajay, Jennifer L Hicks, et al. (2018a). “OpenSim: Simulating Musculoskeletal Dynamics and Neuromuscular Control to Study Human and Animal Movement”. In: *PloS computational biology* 14.7.
- Seth, Ajay, Jennifer L. Hicks, et al. (July 2018b). “OpenSim: Simulating Musculoskeletal Dynamics and Neuromuscular Control to Study Human and Animal Movement”. In: *PLOS Computational Biology* 14.7, e1006223. ISSN: 1553-7358. DOI: [10.1371/journal.pcbi.1006223](https://doi.org/10.1371/journal.pcbi.1006223).
- Shahrokni, Maryam et al. (July 2012). “Design and Biomechanical Evaluation of a Rodent Spinal Fixation Device”. In: *Spinal cord* 50.7, pp. 543–547. ISSN: 1362-4393. DOI: [10.1038/sc.2011.185](https://doi.org/10.1038/sc.2011.185).
- Sherman, Michael A., Ajay Seth, and Scott L. Delp (Jan. 2011). “Simbody: Multibody Dynamics for Biomedical Research”. In: *Procedia IUTAM*. IUTAM Symposium on Human Body Dynamics 2, pp. 241–261. ISSN: 2210-9838. DOI: [10.1016/j.piutam.2011.04.023](https://doi.org/10.1016/j.piutam.2011.04.023).
- (Aug. 2013). “What Is a Moment Arm? Calculating Muscle Effectiveness in Biomechanical Models Using Generalized Coordinates”. In: *Volume 7B: 9th International Conference on Multibody Systems, Nonlinear Dynamics, and Control*. Portland, Oregon, USA: American Society of Mechanical Engineers, V07BT10A052. ISBN: 978-0-7918-5597-3. DOI: [10.1115/DETC2013-13633](https://doi.org/10.1115/DETC2013-13633).
- Sherrington, C S (Apr. 1910). “Flexion-Reflex of the Limb, Crossed Extension-Reflex, and Reflex Stepping and Standing”. In: *The Journal of Physiology* 40.1-2, pp. 28–121.
- Siegler, S., R. Seliktar, and W. Hyman (1982). “Simulation of Human Gait with the Aid of a Simple Mechanical Model”. In: *Journal of Biomechanics* 15.6, pp. 415–425. DOI: [10.1016/0021-9290\(82\)90078-1](https://doi.org/10.1016/0021-9290(82)90078-1).

- Sigvardt, Karen A and William L Miller (1998). “Analysis and Modeling of the Locomotor Central Pattern Generator as a Network of Coupled Oscillators”. In: *Annals of the New York Academy of Sciences* 860.1, pp. 250–265.
- Sims, Karl (July 1994a). “Evolving 3D Morphology and Behavior by Competition”. In: *Artificial Life* 1.4, pp. 353–372. ISSN: 1064-5462. DOI: [10.1162/artl.1994.1.4.353](https://doi.org/10.1162/artl.1994.1.4.353).
- (July 1994b). “Evolving Virtual Creatures”. In: *Proceedings of the 21st Annual Conference on Computer Graphics and Interactive Techniques*. SIGGRAPH '94. New York, NY, USA: Association for Computing Machinery, pp. 15–22. ISBN: 978-0-89791-667-7. DOI: [10.1145/192161.192167](https://doi.org/10.1145/192161.192167).
- Singh, Kan et al. (Mar. 2002). “Morphometry of Macaca Mulatta Forelimb. II. Fiber-type Composition in Shoulder and Elbow Muscles”. In: *Journal of Morphology* 251.3, pp. 323–332. ISSN: 0362-2525. DOI: [10.1002/jmor.1092](https://doi.org/10.1002/jmor.1092).
- Sink, Helen (2006). *Muscle Development in Drosophila*.
- Smith, Russell (2001). *Open Dynamics Engine*.
- Sobol', I. M (Feb. 2001). “Global Sensitivity Indices for Nonlinear Mathematical Models and Their Monte Carlo Estimates”. In: *Mathematics and Computers in Simulation*. The Second IMACS Seminar on Monte Carlo Methods 55.1, pp. 271–280. ISSN: 0378-4754. DOI: [10.1016/S0378-4754\(00\)00270-6](https://doi.org/10.1016/S0378-4754(00)00270-6).
- Soler, Cédric et al. (2004). “Coordinated Development of Muscles and Tendons of the Drosophila Leg”. In: *Development (Cambridge, England)* 131.24, pp. 6041–6051.
- Sreenivasa, Manish, Ko Ayusawa, and Yoshihiko Nakamura (May 2016). “Modeling and Identification of a Realistic Spiking Neural Network and Musculoskeletal Model of the Human Arm, and an Application to the Stretch Reflex”. In: *IEEE Transactions on Neural Systems and Rehabilitation Engineering* 24.5, pp. 591–602. ISSN: 1558-0210. DOI: [10.1109/TNSRE.2015.2478858](https://doi.org/10.1109/TNSRE.2015.2478858).
- Stark, Heiko et al. (May 2021). “A Three-Dimensional Musculoskeletal Model of the Dog”. In: *Scientific Reports* 11.1, p. 11335. ISSN: 2045-2322. DOI: [10.1038/s41598-021-90058-0](https://doi.org/10.1038/s41598-021-90058-0).
- Stein, R B et al. (Nov. 2004). “Coding of Position by Simultaneously Recorded Sensory Neurones in the Cat Dorsal Root Ganglion”. In: *The Journal of Physiology* 560.Pt 3, pp. 883–896. ISSN: 0022-3751. DOI: [10.1113/jphysiol.2004.068668](https://doi.org/10.1113/jphysiol.2004.068668).
- Stimberg, Marcel, Romain Brette, and Dan FM Goodman (Aug. 2019). “Brian 2, an Intuitive and Efficient Neural Simulator”. In: *eLife* 8. Ed. by Frances K Skinner, e47314. ISSN: 2050-084X. DOI: [10.7554/eLife.47314](https://doi.org/10.7554/eLife.47314).
- Strauss, R. and M. Heisenberg (1990). “Coordination of Legs during Straight Walking and Turning in Drosophila Melanogaster”. In: *Journal of Comparative Physiology A* 167.3. DOI: [10.1007/bf00192575](https://doi.org/10.1007/bf00192575).
- Sunshine, Michael D. et al. (Apr. 2013). “Cervical Intraspinal Microstimulation Evokes Robust Forelimb Movements before and after Injury”. In: *Journal of Neural Engineering* 10.3, p. 036001. ISSN: 1741-2552. DOI: [10.1088/1741-2560/10/3/036001](https://doi.org/10.1088/1741-2560/10/3/036001).
- Szczecinski, Nicholas S, Till Bockemühl, et al. (2018). “Static Stability Predicts the Continuum of Interleg Coordination Patterns in Drosophila”. In: *Journal of Experimental Biology* 221.22.



- Szczecinski, Nicholas S, Amy E Brown, et al. (2014). “A Neuromechanical Simulation of Insect Walking and Transition to Turning of the Cockroach *Blaberus Discoidalis*”. In: *Biological cybernetics* 108.1, pp. 1–21.
- Szczecinski, Nicholas S, Joshua P Martin, et al. (2015). “Neuromechanical Model of Praying Mantis Explores the Role of Descending Commands in Pre-Strike Pivots”. In: *Bioinspiration & biomimetics* 10.6.
- Székely, Gy., G. Czéh, and Gy. Vöeös (Aug. 1969). “The Activity Pattern of Limb Muscles in Freely Moving Normal and Deafferented Newts”. In: *Experimental Brain Research* 9.1, pp. 53–62. ISSN: 1432-1106. DOI: [10.1007/BF00235451](https://doi.org/10.1007/BF00235451).
- Szigeti, Balázs et al. (2014). “OpenWorm: An Open-Science Approach to Modeling *Caenorhabditis Elegans*”. In: *Frontiers in computational neuroscience* 8, p. 137.
- Takahashi, Hidetoshi et al. (2017). “Maximum Force Capacity of Legs of a Fruit Fly during Landing Motion”. In: *19th International Conference on Solid-State Sensors, Actuators and Microsystems*, pp. 1061–1064.
- Takeoka, Aya and Silvia Arber (Apr. 2019). “Functional Local Proprioceptive Feedback Circuits Initiate and Maintain Locomotor Recovery after Spinal Cord Injury”. In: *Cell Reports* 27.1, 71–85.e3. ISSN: 22111247. DOI: [10.1016/j.celrep.2019.03.010](https://doi.org/10.1016/j.celrep.2019.03.010).
- Takeoka, Aya, Isabel Vollenweider, et al. (2014). “Muscle Spindle Feedback Directs Locomotor Recovery and Circuit Reorganization after Spinal Cord Injury”. In: *Cell* 159, pp. 1626–1639. DOI: [10.1016/j.cell.2014.11.019](https://doi.org/10.1016/j.cell.2014.11.019).
- Tata Ramalingasetty, Shravan et al. (2021). “A Whole-Body Musculoskeletal Model of the Mouse”. In: *IEEE Access* 9, pp. 163861–163881. ISSN: 2169-3536. DOI: [10.1109/ACCESS.2021.3133078](https://doi.org/10.1109/ACCESS.2021.3133078).
- Thandiackal, Robin et al. (Aug. 2021). “Emergence of Robust Self-Organized Undulatory Swimming Based on Local Hydrodynamic Force Sensing”. In: *Science Robotics* 6.57. ISSN: 2470-9476. DOI: [10.1126/scirobotics.abf6354](https://doi.org/10.1126/scirobotics.abf6354).
- Thelen, Darryl G. (Feb. 2003). “Adjustment of Muscle Mechanics Model Parameters to Simulate Dynamic Contractions in Older Adults”. In: *Journal of Biomechanical Engineering* 125.1, pp. 70–77. ISSN: 0148-0731, 1528-8951. DOI: [10.1115/1.1531112](https://doi.org/10.1115/1.1531112).
- Todorov, Emanuel, Tom Erez, and Yuval Tassa (Oct. 2012). “MuJoCo: A Physics Engine for Model-Based Control”. In: *2012 IEEE/RSJ International Conference on Intelligent Robots and Systems*, pp. 5026–5033. DOI: [10.1109/IROS.2012.6386109](https://doi.org/10.1109/IROS.2012.6386109).
- Toeda, Misaki et al. (Jan. 2020). “Gait Generation and Its Energy Efficiency Based on Rat Neuromusculoskeletal Model”. In: *Frontiers in Neuroscience* 13. ISSN: 1662-4548. DOI: [10.3389/fnins.2019.01337](https://doi.org/10.3389/fnins.2019.01337).
- Toth, Tibor Istvan, Martyna Grabowska, et al. (2013). “A Neuro-Mechanical Model Explaining the Physiological Role of Fast and Slow Muscle Fibres at Stop and Start of Stepping of an Insect Leg”. In: *PloS one* 8.11.
- Toth, Tibor Istvan, Joachim Schmidt, et al. (2013). “A Neuro-Mechanical Model of a Single Leg Joint Highlighting the Basic Physiological Role of Fast and Slow Muscle Fibres of an Insect Muscle System”. In: *PloS one* 8.11.

- Tóth, Tibor I. and Silvia Daun (2019). “A Kinematic Model of Stick-Insect Walking”. In: *Physiological Reports* 7.8, e14080. ISSN: 2051-817X. DOI: [10.14814/phy2.14080](https://doi.org/10.14814/phy2.14080).
- Valle, Giacomo et al. (Oct. 2018). “Biomimetic Intraneural Sensory Feedback Enhances Sensation Naturalness, Tactile Sensitivity, and Manual Dexterity in a Bidirectional Prosthesis”. In: *Neuron* 100.1, 37–45.e7. ISSN: 1097-4199. DOI: [10.1016/j.neuron.2018.08.033](https://doi.org/10.1016/j.neuron.2018.08.033).
- van der Walt, Stéfan et al. (June 2014). “Scikit-Image: Image Processing in Python”. In: *PeerJ* 2. ISSN: 2167-8359.
- Vincent, Julian FV and Ulrike GK Wegst (2004). “Design and Mechanical Properties of Insect Cuticle”. In: *Arthropod structure & development* 33.3, pp. 187–199.
- Wagner, Fabien B. et al. (Nov. 2018). “Targeted Neurotechnology Restores Walking in Humans with Spinal Cord Injury”. In: *Nature* 563.7729, pp. 65–71. ISSN: 1476-4687. DOI: [10.1038/s41586-018-0649-2](https://doi.org/10.1038/s41586-018-0649-2).
- Watson, James T et al. (2002). “Control of Obstacle Climbing in the Cockroach, *Blaberus discoidalis*. I. Kinematics”. In: *Journal of Comparative Physiology A* 188.1, pp. 39–53.
- Webb, Barbara (1999). “A Framework for Models of Biological Behaviour”. In: *International journal of neural systems* 9.05, pp. 375–381.
- Weber, Douglas J. et al. (June 2006). “Decoding Sensory Feedback from Firing Rates of Afferent Ensembles Recorded in Cat Dorsal Root Ganglia in Normal Locomotion”. In: *IEEE transactions on neural systems and rehabilitation engineering: a publication of the IEEE Engineering in Medicine and Biology Society* 14.2, pp. 240–243. ISSN: 1534-4320. DOI: [10.1109/TNSRE.2006.875575](https://doi.org/10.1109/TNSRE.2006.875575).
- Whelan, Patrick J. (Aug. 2010). “Shining Light into the Black Box of Spinal Locomotor Networks”. In: *Philosophical Transactions of the Royal Society B: Biological Sciences* 365.1551, pp. 2383–2395. ISSN: 0962-8436, 1471-2970. DOI: [10.1098/rstb.2009.0322](https://doi.org/10.1098/rstb.2009.0322).
- Wosnitza, Anne et al. (2013). “Inter-Leg Coordination in the Control of Walking Speed in *Drosophila*”. In: *Journal of Experimental Biology* 216.3, pp. 480–491.
- Yakovenko, S., V. Gritsenko, and A. Prochazka (Feb. 2004). “Contribution of Stretch Reflexes to Locomotor Control: A Modeling Study”. In: *Biological Cybernetics* 90.2, pp. 146–155. ISSN: 0340-1200, 1432-0770. DOI: [10.1007/s00422-003-0449-z](https://doi.org/10.1007/s00422-003-0449-z).
- Yakovenko, Sergiy et al. (Mar. 2002). “Spatiotemporal Activation of Lumbosacral Motoneurons in the Locomotor Step Cycle”. In: *Journal of Neurophysiology* 87.3, pp. 1542–1553. ISSN: 0022-3077. DOI: [10.1152/jn.00479.2001](https://doi.org/10.1152/jn.00479.2001).
- Young, Fletcher et al. (Mar. 2019). “Analyzing Moment Arm Profiles in a Full-Muscle Rat Hindlimb Model”. In: *Biomimetics* 4.1, p. 10. DOI: [10.3390/biomimetics4010010](https://doi.org/10.3390/biomimetics4010010).
- Young, R. P., S. H. Scott, and G. E. Loeb (Sept. 1993). “The Distal Hindlimb Musculature of the Cat: Multiaxis Moment Arms at the Ankle Joint”. In: *Experimental Brain Research* 96.1, pp. 141–151. ISSN: 0014-4819, 1432-1106. DOI: [10.1007/BF00230447](https://doi.org/10.1007/BF00230447).
- Zajac, F. (1989). “Muscle and Tendon: Properties, Models, Scaling, and Application to Biomechanics and Motor Control.” In: *Crit Rev Biomed Eng* 17.4, pp. 359–411.

- Zajac, Felix E, Richard R Neptune, and A Kautz (2003). “Biomechanics and Muscle Coordination of Human Walking Part II : Lessons from Dynamical Simulations and Clinical Implications”. In: 17.
- Zill, Sasha N et al. (2017). “Effects of Force Detecting Sense Organs on Muscle Synergies Are Correlated with Their Response Properties”. In: *Arthropod structure & development* 46.4, pp. 564–578.
- Zimmermann, Jonas B., Kazuhiko Seki, and Andrew Jackson (Oct. 2011). “Reanimating the Arm and Hand with Intraspinal Microstimulation”. In: *Journal of Neural Engineering* 8.5, p. 054001. ISSN: 1741-2552. DOI: [10.1088/1741-2560/8/5/054001](https://doi.org/10.1088/1741-2560/8/5/054001).
- Zuffi, Silvia et al. (2017). “3D Menagerie: Modeling the 3D Shape and Pose of Animals”. In: *Proceedings of the IEEE Conference on Computer Vision and Pattern Recognition*, pp. 6365–6373.

# Shravan T. Ramalingasetty

BioROBOTICS ENGINEER

26A, Chemin De Beree, Lausanne, Switzerland - 1010

☎ (+41) 78-697-8947 | ✉ shravan.tataramalingasetty@epfl.ch | 📱 ShravanTata | 📧 Shravi1113

*"Take Risks in Life, If you Win you Can Lead! If you Lose you Can Guide!"*

## Education

### EPFL (École polytechnique fédérale de Lausanne)

Luusanne, Switzerland

DOCTORAL STUDENT, BioROB

Oct. 2016 - Jan, 2022

- "Neuromechanical modeling and simulation of multi-legged terrestrial locomotion" - **Prof Auke Ijspeert**

### TU Delft (Delft University of Technology) - 8

Delft, Netherlands

M.Sc IN MECHANICAL ENGINEERING, BIO ROBOTICS

Aug. 2014 - Sept. 2016

- Master Thesis : "Cerebellum Inspired Computational Models for Robot Control" - **Prof.dr.ir. P.P. Jonker**

### MIT (Manipal Institute of Technology) - 9.5

Manipal, India

B.E IN MECHATRONICS ENGINEERING

Aug. 2019 - May. 2013

- Bachelor Thesis : "Human Motion Analysis using Inertial Sensors" - **Dr. S.N. Omkar**

## Skills

**Programming** C, C++, Python, ROS, MATLAB, LaTeX

**Software** Catia V5, Mac OS X, Linux

**Simulation tools** MuJoCo, Webots, PyBullet, V-REP, Gazebo, OpenSim

**Languages** English, Telugu, Kannada, French (Basic)

## Experience

### DCSC Systems and Controls, TU Delft

Delft, Netherlands

TEACHING ASSISTANT <CONTROL METHODS FOR ROBOTICS>

Feb. 2016 - May. 2016

- Design assignments for students to test different control strategies introduced during the course
- Use of MATLAB and VREP interface for simulating and control of robots
- Simulation environment for control of 8 DOF robotic Arm
- Simulation environment for control of R-Hex robots
- Simulation environment for control of Quadrotor race arena
- Assist in evaluation of student exams and assignments

### DCSC Systems and Controls, TU Delft

Delft, Netherlands

SOFTWARE & ELECTRONICS <ZEBRO-ART : WHEN ROBOTS MEET ART >

Sep. 2015 - Aug. 2016

- To design R-Hex robot that can carry a statue in a dynamic office environment
- Raspberry Pi powered ROS framework for control, navigation and localization
- Challenges involve in designing robot that can co-exist in an environment with people in close proximity
- Capability to climb stairs while carrying a statue
- Use of Lidar and Depth cameras for SLAM

### RENESAS Electronics Europe GmbH

Paris, France

TRAINEE <EVALUATION OF CONVOLUTION NEURAL NETWORKS FOR AUTOMOTIVE APPLICATIONS>

Sep. 2015 - Nov. 2015

- Set-Up the Caffe frame work
- Pedestrian detection using Convolution Neural Networks(CNN) based on Daimler dataset
- Adapt network configuration to increase detection rate and also meet real time requirements
- Extend detection framework using HoG based window scanning
- Extend the framework for Road Sign Classification and Detection
- Create data set for full scene semantic labeling
- CNN networks for learning pixel level semantic labeling

179

## Multimedia Computing Group, TU Delft

RESEARCH ASSISTANT

*Delft, Netherlands*

*Jun. 2015 - Aug. 2015*

- Set-Up the experimental interface for Image aesthetics and Quality assessment experiment
- Use of psychophysics toolbox in MATLAB for interface design

## Computational Intelligence Lab, Indian Institute of Science

JUNIOR RESEARCH FELLOW, DEPT. OF AEROSPACE ENGINEERING

*Bangalore, India*

*May. 2013 - Jul. 2014*

- Worked on design and analysis of lower body human exo-skeleton suit using LifeMod software and Inertial Sensors.
- Analysed Human swing phase of walking with exoskeleton using LifeMod and Inertial Sensors.
- Analysis of the dynamic visco-elastic properties of human arm-hand experienced by a martial artist while breaking a brick using lumped parameter model.
- Developed an On board (UDOO-Python) vision based Quadcopter stabilisation using Fuzzy Controller.

## Computational Intelligence Lab, Indian Institute of Science

TEACHING ASSISTANT <BASICS OF DESIGN AND DEVELOPMENT OF FIXED WING RC PLANES AND QUADCOPTER'S>

*Bangalore, India*

*Feb. 2014 - Apr. 2014*

- Use of MultiWii autopilot for RC planes.
- Basics of Flying a Quadcopter.

## Computational Intelligence Lab, Indian Institute of Science

PROJECT INTERN <HUMAN MOTION ANALYSIS USING INERTIAL SENSORS>, DEPT. OF AEROSPACE ENGINEERING

*Bangalore, India*

*Dec. 2012 - May. 2013*

- Exposure to Inertial measurement units for motion capture.
- Exposure to EEG sensors for capturing muscle activity.
- Digital Signal Processing tools: Short time Fourier Transform, Wigner-Ville Transform, Hilbert Huang Transform.
- Quantification of yoga postures and exercises.

## Bosch Pvt. Limited

INDUSTRIAL TRAINEE, BOSCH CRDI

*Bangalore, India*

*Jun. 2012 - Jul. 2012*

- Understanding of Bosch production system, which is manifestation of Lean Manufacturing system.
- Understanding the application of Bosch Production systems in the manufacturing of PF pumps (mainly PF 51 and PF 45), exposure to pump's assembly process including testing and calibration.
- Worked on programmable logic controller for automating CRDI systems.
- Trained to operate a 6 DOF, ABB robotic arm.

## Publications

### A whole-body musculoskeletal model of the mouse

*IEEE Access*

AUTHORS: SHRAVAN TATA RAMALINGASETTY, SIMON M. DANNER, JONATHAN ARREGUIT, SERGEY N. MARKIN, DIMITRI

*Dec 2021*

RODARIE, CLAUDIA KATHE, GRÉGOIRE COURTINE, ILYA A. RYBAK, AUKE IJSPEERT

- The paper describes the development of the first whole body 3D mouse musculoskeletal model. Both the forelimbs and hindlimb musculature was modeled as hill-type muscles with all the parameters appropriately estimated. We then describe influence of muscle moments and moment-arms on joint motion in a comprehensive manner.

### Spatiotemporal Maps of Proprioceptive Inputs to the Cervical Spinal Cord During Three-Dimensional Reaching and Grasping

*International Journal of  
Biomechanics and Biomedical  
Robotics*

AUTHORS: PIERRE KIBLEUR, SHRAVAN R TATA\*, NATHAN GREINER\*, SARA CONTI, BEATRICE BARRA, KATIE ZHUANG,

*Jul 2020*

MELANIE KAESER, AUKE IJSPEERT, MARCO CAPOGROSSO

- The paper describes the methodology to generate spatiotemporal maps of spinal proprioceptive inputs during voluntary movements using experimental recordings and biomechanical simulations. The results indicate that reproducing the proprioceptive information flow to the cervical spinal cord requires complex spatio-temporal modulation of each spinal root. Our model can support the design of neuroprosthetic technologies as well as in-silico investigations of the primate sensorimotor system.

## Computational modelling of musculoskeletal to predict the human response with exoskeleton suit

*International Journal of  
Biomechanics and Biomedical  
Robotics*  
Jul 2020

AUTHORS: GOVINDA A, SHRAVAN.T.R, OMKAR.S.N, INDRAJIT MUKHERJEE, SIVAKUMAR R

- The paper concentrates on the biomechanical aspect of human Stand-to-Sit motion and also evaluating the muscle activity of a subject driven by an exoskeleton. The analysis is performed using State of the Art biomechanical software LifeMod. The analyzed results can be used to design control systems for lower limb exoskeleton and also establish a frame work for study of behavior of muscle activation while performing various activities driven by wearable exoskeleton.

## Scale Adaptive Object Tracker with Occlusion Handling

*International Journal of Image,  
Graphics and Signal Processing  
(IJIGSP)*  
Jul 2015

AUTHORS: K.M.RAM ARAVIND, SHRAVAN.T.R, OMKAR.S.N

- This paper proposes a different approach to solve two typical issues existing in tracking algorithms like mean shift: (1) adaptively estimating scale of the object and (2) handling occlusions. The log likelihood function is used to extract object pixels and estimate the scale of the object. Extreme learning machine is applied to train the radial basis function neural network to search for objects in case of occlusion or local convergence of mean shift.

## Wireless Performance Evaluation Of Sun Salutation Using Body Mount Accelerometers.

*International Journal of Yoga and  
Allied Sciences*  
Dec 2014

AUTHORS: SHRAVAN.T.R, OMKAR.S.N

- This paper a methodology that can be used in everyday environment to analyze and evaluate the performance of Sun Salutation exercise. Body orientations and accelerations at selected points on the body are acquired from the accelerometers developed by Shimmer®. From statistical analysis, the evaluated results are represented in a form that is understandable by both the instructor and the performer himself. The technique can be utilized to develop a wireless system that is used to evaluate exercises which involve repeatable performance with grace.

## Honors & Awards

2016	<b>Cum laude</b> , This predicate is meant for the fastest students with the highest grades	<i>TU Delft, Delft</i>
2014	<b>Felicitation</b> , Academic Excellency in engineering by Arya Vysya Mahasabha.	<i>Karnataka, India</i>
2013	<b>Topper</b> , Medal of Honor from the Dept. of Mechatronics 2009-2013	<i>MIT, India</i>
2012	<b>Winner</b> , Junkyard Wars competition held at Techatva (National level technical fest)	<i>Manipal, India</i>
2009	<b>Scholarship</b> , MHRD Karnataka State Scholarship for Excellence in 12th	<i>Bangalore, India</i>

## Extra Activity

### BEST (Board of European Students of Technology)

*Delft, Netherlands*  
Feb. 2016 - PRESENT

MEMBER

- Organizational skills for hosting international events like exchange courses
- Work in a multi-national environment

### Bangalore Institute of Movement and Research Analysis

*Bangalore, India*  
Jan. 2014

ATTENDEE

- Introduction to 2D & 3D gait analysis from a medical context
- Interaction with leading doctors involved in Movement research

### Indian Institute of Technology

*Bombay, India*  
Jul. 2012

WORKSHOP

- Design and Development of a 4-Degree of freedom Haptic controlled robotic arm

### Texas Instruments®

*Manipal, India*  
Sep, 2012

WORKSHOP

- Programming MSP430 microcontroller (Assembly and Embedded C programming)

